Technische Universität München
Max-Planck-Institut für Quantenoptik

Algorithms for Hamiltonian Quantum Field Theories

Patrick Emonts

Vollständiger Abdruck der von der Fakultät für Physik der Technischen Universität München zur Erlangung des akademischen Grades eines

Doktors der Naturwissenschaften (Dr. rer. nat.)

genehmigten Dissertation.

Vorsitz: Prof. Dr. Stefan Filipp

Prüfer der Dissertation: Hon-Prof. Dr. J. Ignacio Cirac
Prof. Dr. Johannes Knolle

Die Dissertation wurde am 10.05.2022 bei der Technischen Universität München eingereicht und durch die Fakultät für Physik am 23.09.2022 angenommen.

ABSTRACT

Quantum field theories and in particular gauge theories are at the base of our understanding of modern physics. In the Standard Model of Particle Physics, they explain three of the four fundamental interaction known in nature. The evaluation of quantum field theories (QFT), however, is quite involved. While weakly coupled QFT can be studied with perturbation theory in the continuum, strongly coupled theories like quantum chromodynamics are usually discretized. Even after a discretization on a lattice, certain regions of the phase diagram of the standard model cannot be explored with traditional Monte Carlo methods. The path to the finite-density regime of the standard model is blocked due to the sign problem in Monte Carlo and time dynamics cannot be explored since the action formalism has no explicit notion of time.

Here, we explore new algorithms for QFT in the continuum and on the lattice. Instead of the action formalism, we focus on the Hamiltonian formulation of QFT. The combination of Hamiltonian formalism and new algorithms enables us to explore which were inaccessible with prior methods.

The thesis is structured into four main parts which focus on different combinations of algorithms and systems. All projects are grouped along two axes: the type of the algorithm and the discretization of the system. The first two chapters give an increasingly technical introduction into the topic and present the methods which are used throughout. We review recent advances and show where we connect to the known state of the field.

The first project investigates a pure $\mathbb{Z}_3$ lattice gauge theory with a tensor network based ansatz, gauged Gaussian projected entangled pair states (GGPEPS) in two spatial dimensions. While the gauge field can be integrated out in one dimension, the two-dimensional case is more involved due to the self-interactions of the gauge fields. GGPEPS are locally gauge invariant by design and explore only the physically relevant part of the Hilbert space. In a first explorative, numerical study, we benchmark the performance of the states and investigate their viability.

In the second project, we change from tensor networks to a periodic Gaussian Ansatz to simulate compact quantum electrodynamics (cQED) on the lattice. We stay with the lattice formulation in two spatial dimensions, while adapting the states. Extending previous work to complex periodic Gaussian states, we simulate the first time-evolution after quenches in two-dimensional cQED. In this thesis, we focus on the formulation of the Ansatz and computational challenges.

The third project changes the focus from lattice gauge theories to QFT in the continuum while returning to tensor network based states. We choose to work with Gaussian continuous tensor network states (GCTNS), a restriction of general continuous tensor networks. The Gaussian character lets us treat most of the calculations analytically, such that the numerical investigation can focus on the actual match of the states to the true ground state. GCTNS capture the ground states of Gaussian theories excellently, and we can explore their limitations with quartic theories like the Lieb-Liniger model. We prove the numerical viability of CTNS as a numerical tool to investigate theories

directly in the continuum.

Finally, we turn to the last remaining combination: a study of QFT (without discretization) without tensor networks. The computation of entanglement entropies in quantum field theories directly in the continuum is challenging since the usually used momentum basis does not allow for a trivial bipartition in real space. In the framework of Hamiltonian truncation, we devise the first algorithm to numerically investigate arbitrary entanglement measures for quantum field theories. By splitting the system into two subsystems, and mapping the full fields onto fields on the partitions, we are able to explicitly compute the reduced density matrix, giving access to many entanglement related quantities. We verify the procedure on the massive Klein-Gordon and obtain interesting new results on the interacting sine-Gordon model.

ZUSAMMENFASSUNG

Quantenfeldtheorien bilden die Grundlage für unser Verständnis der modernen Physik. Im Standardmodell der Teilchenphysik formulieren sie drei der vier bekannten fundamentalen Wechselwirkungen in der Natur. Die Auswertung von Quantenfeldtheorien (QFT) ist jedoch kompliziert. Während schwach gekoppelte QFT mit Hilfe von Störungsrechnung direkt im Kontinuum berechnet werden können, müssen stark gekoppelte Theorien üblicherweise auf einem Gitter dargestellt werden. Selbst nach einer Diskretisierung auf einem Gitter, können bestimmte Regionen des Phasendiagramms des Standardmodells nicht mit traditionellen Monte-Carlo-Methoden erforscht werden. Aufgrund des Vorzeichenproblems in Monte Carlo Algorithmen, können Regionen mit endlichem chemischen Potenzial im Standardmodells nicht simuliert werden. Die Berechnung von Zeitdynamik scheitert an der Formulierung der Theorie im Aktionsformalismus.

In dieser Dissertation untersuchen wir neue Algorithmen für QFT im Kontinuum und auf dem Gitter. Anstelle des Aktionsformalismus konzentrieren wir uns auf die Hamiltonsche Formulierung von QFT. Die Kombination aus Hamiltonformalismus und neuen Algorithmen ermöglicht uns das Studium neuer Phänomene, die mit früheren Methoden unzugänglich waren.

Die Arbeit ist in vier Hauptteile gegliedert, die sich auf verschiedene Kombinationen von Algorithmen und Systemen konzentrieren. Alle Projekte sind entlang zweier Achsen gruppiert: die Art des Algorithmus und die Diskretisierung des Systems. Die ersten beiden Kapitel geben eine zunehmend technische Einführung in das Thema und stellen die verwendeten Methoden vor. Wir geben einen Überblick über die jüngsten Fortschritte und zeigen, wo wir den Anschluss an den bekannten Stand des Feldes finden.

Das erste Projekt untersucht eine reine $\mathbb{Z}_3$-Gittereichtheorie mit tensornetzwerkbasierten Zuständen, geeichten Gaußschen verschränkten Paarzuständen (GGPEPS), in zwei Raumdimensionen. Während das Eichfeld in einer Dimension ausintegriert werden kann, ist dies im zweidimensionale Fall aufgrund der Selbstwechselwirkung der Eichfelder nicht möglich. GGPEPS sind per Definition eichinvariant und erforschen nur den physikalisch relevanten Teil des Hilbert-Raums. In einer ersten explorativen, numerischen Studie vergleichen wir die Qualität der Zustände und untersuchen weitere Möglichkeiten zur Anwendung.

Im zweiten Projekt wechseln wir von Tensornetzwerken zu einem periodischen Gaußschen Ansatz, um kompakte Quantenelektrodynamik (cQED) auf dem Gitter zu simulieren. Wir bleiben bei der Gitterformulierung in zwei räumlichen Dimensionen, passen aber die Zustände an. Indem wir frühere Arbeiten auf komplexe periodische Gaußsche Zustände ausdehnen, können wir die erste Zeitentwicklung nach Quenches in zweidimensionaler cQED simulieren. In dieser Arbeit konzentrieren wir uns auf die Formulierung des Ansatzes und numerische Herausforderungen.

Das dritte Projekt wechselt den Fokus von Gittereichtheorien zu kontinuierlichen QFT und kehrt gleichzeitig zu tensornetzwerkbasierten Zuständen zurück. Wir arbeiten

mit Gaußschen kontinuierlichen Tensornetzwerkzuständen (GCTNS), einer Einschränkung allgemeiner kontinuierlicher Tensornetzwerke. Der Gaußsche Charakter macht die meisten Berechnungen analytisch behandelbar, sodass sich die numerische Untersuchung auf die tatsächliche Übereinstimmung der Zustände mit dem wahren Grundzustand konzentrieren kann. GCTNS erfassen die Grundzustände von Gaußschen Theorien hervorragend, und wir können ihre Grenzen mit quartischen Theorien wie dem Lieb-Liniger-Modell erkunden. Wir zeigen die Perspektive von CTNS als numerisches Werkzeug zur Untersuchung von Theorien direkt im Kontinuum.

Schließlich wenden wir uns der letzten verbleibenden Kombination zu: einer Untersuchung von QFT (ohne Diskretisierung) ohne Tensornetzwerke. Die Berechnung von Verschränkungsentropien von QFT direkt im Kontinuum ist komplex, da die üblicherweise verwendete Impulsbasis keine einfache Zweiteilung in Ortskoordinaten zulässt. Im Rahmen von Hamiltonscher Trunkierung entwickeln wir den ersten Algorithmus, um beliebige Verschränkungsmaße für Quantenfeldtheorien numerisch zu untersuchen. Die Zweiteilung des Systems ermöglicht die Abbildung der Felder des ganzen Systems auf Felder auf den Partitionen, sodass wir in der Lage sind die reduzierte Dichtematrix explizit zu berechnen. Sie gibt uns Zugang zu Verschränkungsmaßen wie der von Neumann Entropie oder Rényi Entropien sowie deren Dynamik. Wir testen das Verfahren am massiven Klein-Gordon und erhalten interessante neue Ergebnisse für das wechselwirkende Sinus-Gordon-Modell.

LIST OF PUBLICATIONS

PUBLICATIONS RELATED TO THIS THESIS

[1] *Variational Monte Carlo simulation with tensor networks of a pure $\mathbb{Z}_3$ gauge theory in (2+1) D*
P. Emonts, M. C. Bañuls, J. I. Cirac, and E. Zohar
Phys. Rev. D 102, 074501 (2020).
Copyright 2020 by the American Physical Society. See chapter 3.

[2] *Real-time dynamics in 2 + 1D compact QED using complex periodic Gaussian states*
J. Bender, **P. Emonts**, E. Zohar, and J. I. Cirac
Phys. Rev. Research 2, 043145 (2020).
Copyright 2020 by the American Physical Society. See chapter 4.

[3] *Gaussian continuous tensor network states for simple bosonic field theories*
T. D. Karanikolaou, **P. Emonts**, and A. Tilloy
Phys. Rev. Research 3, 023059 (2021).
Copyright 2020 by the American Physical Society. See chapter 5.

[4] *Reduced density matrix and entanglement in interacting quantum field theory with Hamiltonian truncation*
P. Emonts and I. Kukuljan
arXiv:2202.11113 (2022).
See chapter 6.

FURTHER PUBLICATIONS

[5] *Monte Carlo study of the discontinuous quantum phase transition in the transverse-field Ising model on the pyrochlore lattice*
P. Emonts and S. Wessel
Physical Review B 98, (2018).

[6] *Gauss law, minimal coupling and fermionic PEPS for lattice gauge theories*
P. Emonts and E. Zohar
SciPost Phys. Lect. Notes 12 (2020).

Contents

1 INTRODUCTION

At the beginning of the last century, two discoveries fundamentally changed our understanding of physics: the principle of relativity and quantum mechanics. While the first deals with phenomena at very high velocity (special relativity) or the motion of stars (general relativity), the other is concerned with the structure of atoms and the entanglement of different parties. Contrary to the first impression, these two fields are closely related when describing the fundamental forces of nature.

The principle of relativity changed the understanding of mechanics and gravity. Special relativity dictates that information cannot be transmitted faster than the speed of light [7]. Before the discovery of relativity, Newtonian mechanics was used and according to this theory objects could travel at an arbitrary speed. Relativity manages to reconcile the principle of locality with gravity. The idea of locality is omnipresent in classical mechanics: objects can only interact if they are in direct contact (or via gravity) – a spring moves a weight because it is connected to it. In contrast, Newtonian gravity did not have any notion of locality; the interaction is instantaneous between arbitrarily remote particles which implies a communication at arbitrary speed. This is similar to two charges when considering Coulomb's law. According to Coulomb's law, two opposite charges attract each other, while identical charges interact repulsively. Coulomb's law, however, does not answer how one charge gets the information that it should be pushed or pulled by another one and in which direction. The instantaneous communication required in Coulomb's law violates the principle of relativity since information is transmitted faster than light. In order to preserve locality, the notion of a field is introduced to transmit the information. In electromagnetism, local interactions are ensured via a classic field theory formulated as Maxwell's equations. Here, electric and magnetic fields are present everywhere in space. They moderate the interaction between charged particles and all interactions are local. In analogy with the single spring that we discussed as an example for classical mechanics, we can now think of small springs at every point in space that interact with our charge. The information about a change in charge can only travel with the speed of light. After considering the example of two charges, we can return to the case of gravity. The problem of non-local interactions occurs also when two masses attract each other and the theory of general relativity solves the problem by reconciling locality with gravity.

Physics on the atomic and molecular scale works manifestly different from our everyday experience. Motivated by effects like black-body radiation [8] and the photoelectric effect [9], physicists realized that light is not only a wave but exhibits a particle-like character at the same time. Light is quantized into particles, better known as photons and the classical world discovered quantum mechanics and experienced the *first quantum revolution*. In the quantum realm, the Heisenberg principle of uncertainty dictates that velocity and position cannot be measured with arbitrary accuracy anymore [10]. Whereas, in a classical setting it is possible to measure speed and position precisely at the same time. Additionally, quantum mechanics cannot be reconciled with the idea of locality, leading to the EPR-paradox [11]. If one of the biggest successes of the century is to make gravity local and causal (eliminating faster-than-light communication), then it is quite surprising if quantum mechanics does not follow the same guidelines. In particular, it turns out that quantum mechanics hosts manifestly non-local correlations and is not just a bad approximation of a hidden theory. This statement is formulated in testable terms in the Bell inequalities [12] and by now, they have been experimentally tested [13].

A priori, quantum mechanics and relativity are two independent theories. One describes the interaction at low energies for atoms and molecules while the other one usually speaks about velocities close to the speed of light. However, there are particles, that combine those two qualities, like fast electrons. They are quantum mechanical in nature, travel close to the speed of light and interact electromagnetically. Quantum field theory (QFT) manages the feat to unify both theories, relativity and quantum mechanics, into one framework. It describes interactions in a local fashion while preserving the non-local effects of quantum mechanics. Quantum field theories are immensely successful in describing nature, but they are notoriously hard to evaluate. They are usually easy to formulate, in the sense of writing them down, but hard to compute in relevant settings, *i.e.* to calculate a prediction for an experiment.

In the last century, not only science, also technology developed at a rapid pace. The advent of the first digital computers transformed our capability to analyze and compute data; computer simulation had a vast impact on physics. Problems that cannot be solved on a piece of paper, can now be solved or approximated with computers. Despite the rapid growth of computing power, some problems remain challenging even with the most advanced computers; among them the simulation of problems in quantum physics.

Since the invention of computers, physicists have been exploring theories and predictions using computers. Some of the first large scale computers were purposefully designed to evaluate lattice gauge theories, a formulation of a quantum field theory that can be treated numerically. Lattice gauge theories are usually simulated with Monte Carlo algorithms [14, 15], a heuristic procedure to approximate the actual value of a function. These algorithms, however, are limited to certain regimes where the approximation works well. Naturally, there is an interest to explore the unknown parts of the theory with new algorithms.

In the last few years, we are witnessing a *second quantum revolution* [16]: technology allows us to control quantum systems to an extent that we can use them as more advanced computers. The idea to use a well-controlled quantum system as a quantum computer was brought up by Feynman in the 1980s [17–19]. The idea of quantum information processing is born, and this new paradigm opens new pathways to solving formerly hard problems. The essential challenge of classical simulation is the complexity of the quantum system. It is inherently hard to map a quantum system to a classical computer. Intuitively, a quantum system does not have to store explicitly all the superpositions that a quantum system can be in. It is a quantum system itself and can deal with superpositions more naturally. For a classical computer, it is hard to keep track of the state of the quantum system. In recent years the implementation of the idea to employ quantum computers gets within reach of experimental systems. The actual mapping to a quantum system is performed in different ways, mainly two approaches are pursuit – analog and digital simulation. Analog quantum simulation describes the idea to simulate a system of interest with another system that is easier to control. This is a purpose-built quantum simulator to understand a specific system. An orthogonal approach is a universal (digital) quantum simulator. In contrast to analog quantum simulators, a digital simulator can simulate arbitrary quantum systems (within boundaries) but it must approximate the original system with customized operations. While simulators are often not yet refined enough to keep up with classical simulations, they show promise at exploring uncharted territory. In particular, quantum field theories are currently considered as targets for digital and analog simulations.

The idea to enrich the spectrum of algorithms for the simulation of quantum field theories is the guiding theme of this thesis. When using new technologies like quantum simulation – digital or analog –, the need for verification of the new method arises. Quantum simulators excel at computing time dynamics, a task among others that traditional Monte Carlo frameworks [15, 20] cannot help with. Thus, new classical methods are in demand. We focus on the simulation of quantum field theories in the Hamiltonian formalism, a formulation of quantum systems that is usually used in quantum simulation. Here, we address the issue from different directions. On the one hand, we explore continuous and discretized systems with tensor networks, a class of ansätze motivated by quantum information processing. On the other hand, we develop new algorithms for Hamiltonian QFT, in the continuum and on the lattice, independently of the framework of tensor networks.

The present work represents a valuable contribution to the exploration of quantum field theories by adding new computational methods.

1.1 OUTLINE

This thesis explores new numerical methods to investigate quantum field theories in the Hamiltonian formalism. The projects presented in this thesis can be grouped along two axes: methods and discretization. An overview of the projects is given in fig. 1.1.

The choice of the ansatz determines the subsequent capabilities and limitations of the computations. In two projects, we explore tensor network based ansätze, both in the continuum and on the lattice. This introduces directly the second dimension of the classification: discretization. Two projects were undertaken in the continuum, while the other two used a lattice regularization.

All four combinations of the two categories on each axis are explored in four different projects. Each chapter of the thesis explores one of the projects.

In chapter 2, we lay the foundation for subsequent chapters. Concepts like Hamiltonian QFT and lattice gauge theories are introduced in more detail. We also give an overview of tensor networks and other methods used in the thesis.

Chapter 3 starts in the top-left corner of the overview with a tensor-network based simulation of a lattice gauge theory. We evaluate a $\mathbb{Z}_3$ gauge theory with a tensor network based ansatz, more precisely with gauged Gaussian projected entangled pair states (GGPEPS). The project focuses on the computation of ground-state quantities to obtain a first benchmark for GGPEPS. In contrast to prior projects, the computation is performed in two spatial dimensions. Here, the computation is more involved than in one dimension since the gauge field is dynamic and cannot be integrated out as in the one dimensional case.

In chapter 4, we stay on the topic of lattice gauge theories, but consider a different ansatz. Introducing periodic complex Gaussian states, we investigate the confinement behavior in compact Quantum Electrodynamics, a $U(1)$ gauge theory. It is the first

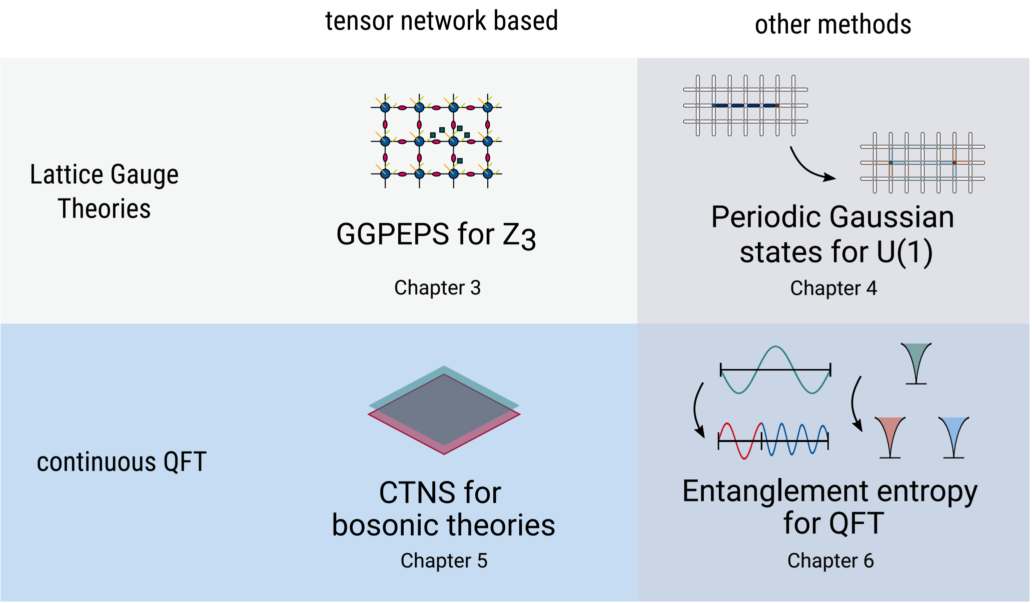

Figure 1.1: Overview of the different projects in this thesis. The projects are ordered along two axes: methods and systems. They all investigate Hamiltonian quantum field theories from different angles.

computation of time dynamics of quantum electrodynamics on the lattice. The chapter in this thesis focuses on the computational aspects of the project.

Chapter 5 changes both the method and the description of the theory with regard to chapter 4, and we use tensor networks to investigate several quantum field theories in the continuum. We limit the class of continuous tensor network states (CTNS) to the Gaussian submanifold and check their numerical performance. The work with tensor networks in the continuum has been explored very little so far. We show that continuous tensor networks are a viable ansatz to be further investigated.

Finally, we change the computational method while remaining in the continuum. In chapter 6, we focus on the entanglement properties of QFT and devise an algorithm to compute reduced density matrices in the framework of Hamiltonian truncation. The model-independent algorithm enables us to compute entanglement measures and their time dynamics directly in the continuum. The algorithm benchmarked with the massive Klein-Gordon model, and we obtain new results for the interacting sine-Gordon model.

2 PRELIMINARIES

This chapter provides an overview of the systems and methods used throughout the thesis. We do not attempt to give an extensive introduction into all subjects, but rather would like to familiarize the reader with the concepts that are explored in detail in subsequent chapters.

2.1 TENSOR NETWORKS

The simulation of quantum many-body systems is a computationally challenging task since we have to battle against two exponentials. Firstly, the number of states in a many-body system, also a classical one, grows exponentially with the system size. A classical spin system experiences an exponential growth of configurations just as a quantum system. In the case of a quantum system, however, the description of the state in a given basis will take exponentially many coefficients as well. This second exponential does not exist in a classical system, since a classical system cannot be in a superposition of different states.

Computational methods try to circumvent the problem of exponential scaling in different ways. Variational approaches are one option to achieve this goal. Instead of considering the whole Hilbert space, these methods consider a parameterized submanifold of the Hilbert space. The goal is to find the best approximation of the ground state $|\psi\rangle$ of the system in the given manifold. The ansatz states $|\psi_\alpha\rangle$ are parameterized by a set of parameters α which are adapted to minimize the expectation value of the energy

$$\min_\alpha E_\alpha = \frac{\langle\psi_\alpha|H|\psi_\alpha\rangle}{\langle\psi_\alpha|\psi_\alpha\rangle}\,, \tag{2.1}$$

where H is the Hamiltonian of the system. While the variational principle guarantees that the energy of the approximated can never be smaller than the actual ground state, the quality of the approximation depends crucially on the choice of ansatz states.

In the following section, we will construct tensor networks, a class of ansatz states, in one and two spatial dimension since they are an important building block for chapters 3 and 5. We start with a short introduction about matrix product states (MPS) [21, 22] in section 2.1.1. In section 2.1.2, we formulate the two-dimensional analog to MPS, projected entangled pair states (PEPS) [23–25]. As a preparation for chapter 5, we introduce continuous tensor networks in section 2.1.3.

2.1.1 MATRIX PRODUCT STATES

As with many other variational approaches, the basic idea of tensor network states is to reduce the number of parameters that describe a state. In one spatial dimension, matrix product states have become one of the most powerful methods to study many-body phenomena in and out of equilibrium [26].

This section provides only an overview of the most relevant features of MPS that we need for subsequent chapters. For more information, we refer the reader to introductions [27, 28] and reviews [26, 29] on tensor networks.

As the name suggests, MPS are parameterized by a set of matrices (or more generally, tensors) that define the state. The idea of the decomposition predates the name MPS and was used numerically in the density matrix renormalization group (DMRG) [26, 30]. In math and computer science, a similar concept called tensor trains [31–33] is used for example for data compression.

We consider a general quantum state ψ for an N particle system that is written in a computational basis $|\sigma\rangle$

$$|\psi\rangle = \sum_{\sigma_1 \dots \sigma_N} c^{\sigma_1,\sigma_2 \dots \sigma_N} |\sigma_1 \sigma_2 \dots \sigma_N\rangle \, . \tag{2.2}$$

Here, we use a shorthand notation for the tensor product $|\sigma_1, \dots, \sigma_N\rangle = |\sigma_1\rangle \otimes |\sigma_2\rangle \otimes \dots \otimes |\sigma_N\rangle$. The number of states in the product Hilbert space of N particles scales exponentially. Consequently, the number of components in $c^{\sigma_1,\dots,\sigma_N}$ scales exponentially, as well. As an example, we consider N two-level systems with internal states $|0\rangle$ and $|1\rangle$. The state of each particle lives in $d = 2$ dimensional Hilbert space and the size of the tensor $c^{\sigma_1,\dots,\sigma_N}$ scales as 2^N with the system size N. This exponential scaling makes the numerical treatment of large systems impossible.

The idea of matrix product states is to approximate the tensor $c^{\sigma_1,\dots,\sigma_N}$ with a product of matrices. We rewrite eq. (2.2) as

$$|\Psi\rangle = \sum_{\sigma_1 \dots \sigma_N} \underbrace{\sum_{a_1,\dots,a_{N-1}} A^{\sigma_1}_{1,a_1} A^{\sigma_2}_{a_1,a_2} \cdots A^{\sigma_{N-1}}_{a_{N-2},a_{N-1}} A^{\sigma_N}_{a_{N-1},1}}_{c^{\sigma_1,\sigma_2 \dots \sigma_N}} |\sigma_1 \sigma_2 \dots \sigma_N\rangle \, , \tag{2.3}$$

where $A^{\sigma}_{a_i,a_{i+1}}$ are tensors with three indices. To distinguish between the different indices, we call the indices σ physical indices (here with $d = 2$ dimensions) and a_i virtual indices of dimension D. While the indices σ relate to the physical system, the a_i are introduced in the construction and are traced out at the end. The first and the last tensor in eq. (2.3) have a special form since we chose open boundary conditions. The index 1 is only an artificial dimension that is added to ensure the compatibility with other tensors. In the case of periodic boundary conditions, the first and last index would be contracted

$$|\Psi\rangle = \sum_{\sigma_1 \dots \sigma_N} \underbrace{\sum_{a_1,\dots,a_N} A^{\sigma_1}_{a_N,a_1} A^{\sigma_2}_{a_1,a_2} \cdots A^{\sigma_{N-1}}_{a_{N-2},a_{N-1}} A^{\sigma_N}_{a_{N-1},a_N}}_{c^{\sigma_1,\sigma_2 \dots \sigma_N}} |\sigma_1 \sigma_2 \dots \sigma_N\rangle \, . \tag{2.4}$$

Without any further approximations, the scaling of the number of parameters with system size does not change. However, the matrix product structure enables us to truncate the matrices $A_{a_i,a_{i+1}}$ to lower rank versions. This is equivalent to restricting the virtual bond dimension to a maximum dimension D. Thus, adding a new particle adds $D \times D$ parameters instead of multiplying the number the parameter by d. The original scaling of the tensors c of $O\left(2^N\right)$ is reduced to $O\left(NdD^2\right)$ since each tensor has dD^2 coefficients.

In practical computations, the transformation of the multi-index tensor $c^{\sigma_1,\dots,\sigma_N}$ into the three-dimensional tensors is performed via singular value decompositions (SVD). Further details about the decomposition can be found in [26–28].

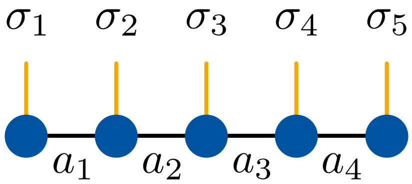

Figure 2.1: Graphical tensor network notation. Vertical (yellow) indices are physical indices with physical bond dimension d. Horizontal (black) legs are virtual legs of bond dimension D. Connected legs are contracted.

The construction based on SVD takes a top-down approach in the sense that we start with the full tensor $c^{\sigma_1,\dots,\sigma_N}$ and decompose it into smaller (rank-3) tensors. In some scenarios, as we will see below, it is more convenient to start with local constituents and build the tensor network bottom-up. We start the construction with a set of maximally entangled pairs on neighboring sites

$$|\Phi\rangle = \sum_{j=0}^{D-1} |jj\rangle \ . \tag{2.5}$$

These states ”live” in a Hilbert space of dimension D, the virtual bond dimension introduced above. In order to obtain the same state that we defined via SVD before, we project neighboring, unentangled sites together with

$$\omega = \sum_{\sigma,\alpha,\beta} A^{\sigma}_{\alpha,\beta} |\sigma\rangle \langle \alpha\beta| \ . \tag{2.6}$$

The states $|\sigma\rangle$ are the computational basis used in eq. (2.3) and $A^{\sigma}_{\alpha,\beta}$ is the same tensor as above. Here, we formulated the system as translational invariant by using identical tensors A on all sites, but the same construction holds with different tensors. Since the construction is commonly used to build the AKLT state [26, 28, 34], an $SO(3)$ symmetric state constructed from entangled pairs, we will sometimes refer to this construction as AKLT construction. As the construction uses entangled pairs as a starting point, it is in a way a one-dimensional PEPS. The construction builds the basis for fermionic PEPS and gauged Gaussian PEPS (cf. chapter 3).

GRAPHICAL NOTATION

Since the matrix notation of tensor networks can be cumbersome, a graphic notation is commonly used. Tensor are represented as circles (or squares) and indices are depicted by lines (so-called legs) attached to the circles. By convention, vertical(horizontal) legs represent physical(virtual) indices. Figure 2.1 shows an MPS in graphical notation. Legs that are connected are contracted, *i.e.* summed over. The MPS in fig. 2.1 is defined with open boundary conditions, *i.e.* the first and the last leg are not contracted.

One key criterion for variational states is the computational efficiency of physical quantities like norms, expectation values and correlators. In the case of MPS, these quantities can be efficiently computed due to the canonical form [26]. Since not all MPS represent a different physical state [35], a gauge transformation can be applied to the virtual legs in the form of an invertible matrix. The transformation works by inserting a $D \times D$ matrix M and its inverse M^{-1} between to tensors and absorb them into the two neighboring tensors. In MPS, we can always find transformations that render certain contractions trivial, bringing the state into canonical form. This enables the efficient minimization and computation of observables with MPS. Note that this gauge transformation is fundamentally different from the gauge transformations discussed in chapter 3. When we are constructing a canonical form, the gauge transformations do not have any physical significance. They act on the virtual degrees of freedom which are traced out in the end of the construction. In the case of gauged Gaussian PEPS, the invariance under the gauge transformation is warranted by the physical system. Physical degrees of freedom are involved in the invariance and it is not only an insertion of a matrix and its inverse. Further details about canonical forms can be found in [35].

ENTANGLEMENT AND AREA LAW

The success of MPS in simulating condensed matter systems is rooted in their entanglement properties. A typical measure for entanglement entropy between two partitions A and B of a system is the von Neumann entropy

$$S_{\mathrm{vN}} = -\operatorname{Tr}\left(\rho_A \log \rho_A\right) \tag{2.7}$$

with the reduced density matrix $\rho_A \equiv \operatorname{Tr}_B \rho$, where ρ is the density matrix of the full system. Since the logarithm in eq. (2.7) is numerically difficult to compute, it is convenient to study Rényi entropies

$$S_A^{(\alpha)} = \frac{1}{1-\alpha} \log \operatorname{Tr}\left(\rho_A^{\alpha}\right) \tag{2.8}$$

from which the $\alpha \to 1$ limit recovers the von Neumann entropy. The special case of S_0 is called entanglement rank and is the logarithm of the number of non-zero singular values for a given bipartition. For general states in a one-dimensional system, the entanglement entropy depends on the size of subsystem, *i.e.* it follows a volume law. Ground states of local, gapped Hamiltonians, however, are special states [36]. Their entropy is bounded for any bisection such $S_0 < \log c$ for some number c, *i.e.* the states follows an area law instead of a volume law. Such a state can be expressed (exactly) with an MPS using $O(dNc^2)$ parameters. Thus, MPS can approximate ground states of gapped local Hamiltonians with polynomially many parameters in system size.

2.1.2 PROJECTED ENTANGLED PAIR STATES

Although MPS have been used for the simulation of two-dimensional systems [26], the one-dimensional structure of the state leads to a mismatch between locality on the Hamiltonian and the state level. If we want to cover a two-dimensional system with an MPS, the most common option is to use a snake-pattern through the system (cf. fig. 2.2). While interactions in one direction act on neighboring sites, interactions in the second direction act on sites removed by the system size in the MPS.

Alternatively, MPS can be extended to the second dimension by adding direct couplings between all neighboring sites to build PEPS (cf. right panel of fig. 2.2). While PEPS match better in terms of locality, the introduction of loops in the construction leads to much higher numerical cost. Even simple PEPS can only be contracted efficiently if post-selected quantum computing can be classically simulated [37]. In practice, however, many algorithms actively use PEPS in the finite [38] and infinite case [39, 40] using approximate methods to contract the states [38, 39, 41–43].

The problem of increasing numerical cost can be tackled in different ways. One approach to circumvent the expensive scaling of PEPS is to consider loop-free tensor networks [44, 45]. Alternatively, the complexity of contraction can be reduced by restricting the PEPS manifold to a smaller one, *e.g.* a Gaussian one. The consequences of a such a restriction will be analyzed in depth in chapter 3.

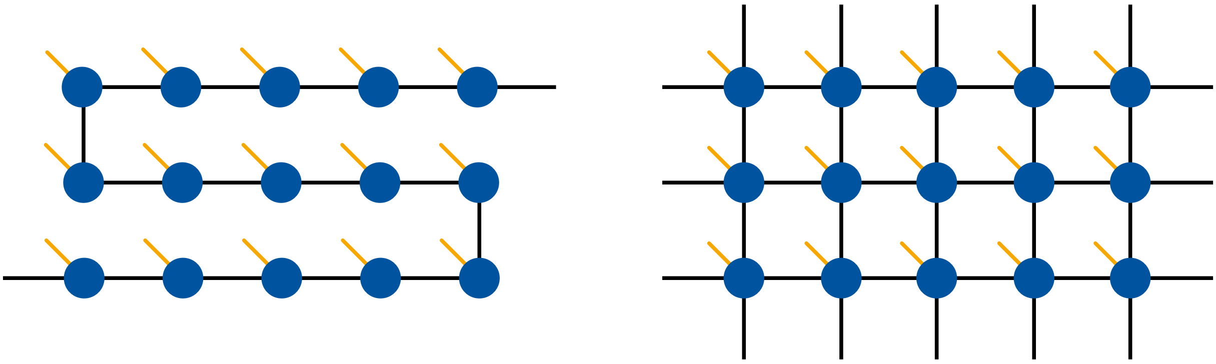

Figure 2.2: MPS (left) and PEPS (right) for two-dimensional systems. As above, vertical (yellow) legs are physical indices and the horizontal (black) connections are virtual indices.

While the construction of PEPS resembles the AKLT construction of MPS, some features like the contraction complexity are manifestly different. In addition to the different complexity, the scaling of correlations differs between the two formulations. While MPS can only host exponentially decaying correlation functions, PEPS can host algebraically decaying correlations. Thus, PEPS are a priori more suitable to describe critical systems. However, the vast majority of PEPS hosts exponentially decaying correlation functions [46]. If critical systems are of interest, a more specialized ansatz like the multiscale entanglement renormalization ansatz (MERA) might be more suitable [47].

FERMIONIC PEPS

PEPS are commonly formulated in terms of a spin basis. Since many condensed matter systems of interest host fermions, a formulation in terms of fermionic degrees of freedom is desirable. In one dimension, a Jordan-Wigner transformation maps fermions to spins (and vice versa) while keeping interactions local. In two (and higher) spatial dimensions, however, the existence of loops renders the mapping non-local which renders simulation more challenging.

One formulation of fermionic PEPS (fPEPS) is derived in [48]. The key idea is to reformulate the PEPS construction in terms of fermionic modes. On-site operators create entangled pairs of fermions which are then projected to the physical subspace. This is in close correspondence to the PEPS construction for spins. Similar constructions are used as a building block to tackle lattice gauge theory systems [49] (cf. chapter 3). In parallel, fermionization ideas from the multiscale entanglement renormalization ansatz [47, 50, 51] computations were transferred to PEPS [52] to simulate condensed matter systems.

2.1.3 CONTINUOUS TENSOR NETWORKS

Since tensor networks have been undeniably successful on the lattice, it is tempting to try to formulate tensor networks in the continuum. There are two possible scenarios: one can either discretize continuum theories to the lattice or bring tensor networks to the continuum. The first scenario is much more common and is so far unmatched in its efficiency [53–55]. Bringing tensor network states to the continuum can be done rather straightforwardly in $d = 1$ space dimension, with the so-called continuous matrix product states (cMPS) [56]. They have been applied successfully to several QFT [57–59]. A formulation in $d \geq 2$ space dimensions has proved more difficult due to differences in the continuum limit. In one space dimension, the continuum limit can be obtained by successive blocking of local tensors [56, 60]. While the physical bond dimension increases in this procedure, the virtual bond dimension stays constant. The same blocking procedure does not work in two dimensions, since it increases also the virtual bond dimension in spatial dimensions $d > 1$. Thus, a different prescription has to be found for the virtual bond dimension on the links.

Recently, two candidates for higher dimensional tensor network states in the continuum were presented [61, 62]. Both of them are limits of lattice tensor network states which are extended to the continuum. In the following, we focus on the continuous tensor network(CTN) formulation [61], since it will be used for numerical simulations in chapter 5.

A continuous tensor network state (CTNS) is a quantum state $|V, \alpha\rangle$, belonging to the Fock space $\mathcal{F}[L^2(\mathbb{R}^d)]$. It is defined by the functional integral [61]

$$|V,\alpha\rangle \equiv \int \mathcal{D}\phi \exp\left\{-\int \mathrm{d}^d x \frac{1}{2}\|\nabla\phi(x)\|^2 + V[\phi(x)] - \alpha[\phi(x)]\psi^\dagger(x)\right\} |\mathrm{vac}\rangle\Big\} , \qquad (2.9)$$

where $|\mathrm{vac}\rangle$ is the "physical" Fock vacuum state, $(\psi^\dagger, \psi)$ are the canonical bosonic creation-annihilation operators on this Fock space, satisfying the canonical commutation relation $[\psi(x), \psi^\dagger(y)] = \delta^d(x - y)$. The "auxiliary" field ϕ that is integrated over has D components, $\phi = [\phi_k]_{k=1}^D$, and $\|\nabla\phi\|^2 := \sum_k \nabla\phi_k \cdot \nabla\phi_k$. The number D is the (field) bond dimension, and it is analog of the bond dimension of discrete tensor networks in the continuous case [cf. section 2.1.1]. Here, we restrict the discussion to the translation invariant case and take the thermodynamic limit, eliminating the discussion of boundary effects. The state as written in eq. (2.9) is not normalized, and not all choices of functions V and α yield a state at all, *e.g.* if $V[\phi] = -\phi^2$. We assume functions V and α such that the functional integral in eq. (2.9) at least formally makes sense.

The state is parameterized by two complex functions $V[\phi]$ and $\alpha[\phi]$, which means that there is an infinite number of parameters even for a fixed number D of auxiliary fields. In practice, we can expand both functions as polynomials in the fields

$$\begin{aligned} V[\phi] &= V^{(0)} + V_j^{(1)}\phi_j + V_{jk}^{(2)}\phi_j\phi_k + V_{jk\ell}^{(3)}\phi_j\phi_k\phi_\ell + \dots , \\ \alpha[\phi] &= \alpha^{(0)} + \alpha_j^{(1)}\phi_j + \alpha_{jk}^{(2)}\phi_j\phi_k + \alpha_{jk\ell}^{(3)}\phi_j\phi_k\phi_\ell + \dots . \end{aligned}$$

The maximum degrees κ_V, κ_α of these two expansions, together with D, then give a measure of the expressiveness. Formally, the coefficients in the expansion are also tensors, recovering the simple idea that a tensor network state should associate a quantum state to a few elementary low-rank tensors.

Before starting with the actual formulation, we can try to give some intuition of the connection between the CTNS ansatz in eq. (2.9) and discrete TNS (cf. section 2.1). As described in section 2.1, a tensor network state is obtained by taking a product of elementary tensors and contracting a fraction of their indices (the virtual bond indices) along the edges of a lattice. For CTNS, the equivalent of the product of tensors is the exponential of the integral over the auxiliary fields ϕ. Analogously, the product of integrals over auxiliary fields is the equivalent to the contraction of discrete indices. The product of integrals becomes a functional integral in the limit [61]. The gradient square term in eq. (2.9) connects the tensors to their nearest neighbors.

GENERATING FUNCTIONAL

To compute expectation values of local observables with a CTNS, the most straightforward method is to introduce the generating functional $\mathcal{Z}_{j',j}$ for the normal ordered correlation functions

$$\mathcal{Z}_{j',j} = \frac{\langle V,\alpha|\exp\left(\int j'\,\psi^\dagger\right)\exp\left(\int j\,\psi\right)|V,\alpha\rangle}{\langle V,\alpha|V,\alpha\rangle}\,. \tag{2.10}$$

For example, it can be used to compute the simple two-point function

$$\begin{aligned}\langle\psi^\dagger(x)\psi(y)\rangle_{V,\alpha} :=& \frac{\langle V,\alpha|\psi^\dagger(x)\psi(y)|V,\alpha\rangle}{\langle V,\alpha|V,\alpha\rangle} \\ =& \frac{\delta}{\delta j'(x)}\frac{\delta}{\delta j(y)}\mathcal{Z}_{j',j}\Big|_{j,j'=0}\,.\end{aligned} \tag{2.11}$$

Using the Baker-Campbell-Hausdorff formula to commute the two exponentials in eq. (2.10) and then using the formula for the overlap of unnormalized field coherent states, one obtains [61]:

$$\begin{aligned}\mathcal{Z}_{j',j} = \frac{1}{\mathcal{N}}\int \mathcal{D}\phi\mathcal{D}\phi'\,\exp\Big\{-\int \frac{\|\nabla\phi\|^2+\|\nabla\phi'\|^2}{2} + V[\phi] + V^*[\phi'] - \alpha^*[\phi']\alpha[\phi] \\ - j\alpha[\phi] - j'\alpha^*[\phi']\Big\}\,.\end{aligned} \tag{2.12}$$

It is important to note that powers of the field in the expansion of α come multiplied and connect together the two auxiliary fields coming from bra and ket, as in a Schwinger-Keldysh functional integral. In general, if arbitrary powers of the field appear, the functional integral eq. (2.12) might be diverging. Assuming that the divergences can be properly subtracted, then actually *computing* correlation functions remains difficult non-perturbatively. Apart from Monte-Carlo techniques, a boundary cMPS method was suggested in [61].

2.2 HAMILTONIAN QUANTUM FIELD THEORY

Quantum field theory allows treatment of quantum mechanics and special relativity in one framework. Some quantum field theories, like quantum electrodynamics, are only weakly interacting and can be treated with perturbative methods [63]. If the coupling is small, higher order terms contribute to an increasingly small degree.

Gauge theories, a special class of quantum field theories, are one of the fundamental building blocks of modern physics. The standard model of particle physics is a gauge theory including the gauge groups $SU(3) \times SU(2) \times U(1)$. It unifies quantum chromodynamics (QCD) in the strong interaction [$SU(3)$], the weak interaction and electromagnetism [spontaneously broken $SU(2) \times U(1)$] and describes the interaction of (fermionic) matter with gauge bosons mediating the forces [63–65]. Gauge theories are also often considered as effective theories in condensed matter, *e.g.* in the form of an Ising gauge theory [66, 67].

In contrast to Abelian gauge theories like quantum electrodynamics [$U(1)$], the strong interaction in the standard model is a non-Abelian theory [$SU(3)$]. Due to the non-Abelian character, QCD experiences a phenomenon called asymptotic freedom at high energy scale. The coupling constant decreases as the energy scale increases, thus the high energy part of the theory can be treated with perturbation theory [68, 69]. In the low-energy regime, however, the coupling constant increases and non-perturbative methods are required [63]. The regime of high-coupling is analytically not accessible and only the introduction of lattice gauge theories allowed first numerical studies of the confinement of quarks [70]. Quarks are said to be confined since they are only observed in terms of baryons (three quarks) and mesons (two quarks). This is in stark contrast to the asymptotic freedom that is expected at high energies. Only numerical studies [70, 71] were a first convincing evidence that QCD could indeed explain the experimentally observed confinement. Even today, there is no analytic derivation of confinement from first principles [72].

In the following section, we introduce lattice gauge theories, a lattice regularization of quantum field theories that is commonly used numerically. We focus on compact quantum electrodynamics (cQED), a $U(1)$ gauge theory, and a subgroup of $U(1)$, the $\mathbb{Z}_3$ lattice gauge theory which share features like confinement with QCD. We will not attempt to give a full systematic review of quantum field theories, but rather present the models that are investigated in subsequent chapters. For a more systematic introduction into quantum field theory, we refer to [63, 73].

2.2.1 LATTICE GAUGE THEORIES

The traditional approach to lattice gauge theories is a formulation in terms of an action S which depends on a field configuration at every space point. Since we will consider quantum electrodynamics later as a theory on the lattice in section 2.2.1, we will introduce it in the continuum here. For the sake of simplicity, we start by formulating the theory for the fields without any charges. The action of pure QED is

$$S_{QED}[A_\mu] = -\frac{1}{4}\int \mathrm{d}x^\alpha F_{\mu\nu}(x^\alpha)F^{\mu\nu}(x^\alpha)\,, \tag{2.13}$$

where A_μ is the electromagnetic four-potential and $F_{\mu\nu} = \partial_\mu A_\nu(x^\alpha) - \partial_\nu A_\mu(x^\alpha)$. To avoid unnecessary sums, the Einstein summation convention is assumed over repeated indices. Greek indices are summed over all four spacetime dimension $\mu, \nu = \{0, 1, 2, 3\}$, where we implicitly assume a Minkowski metric with the signature $(-+++)$. The local gauge symmetry under $U(1)$ transformations is described by $A_\mu \to A_\mu + \partial_\mu \alpha(x)$ where $\alpha(x)$ is a scalar function.

The goal of our study is the computation of expectation values. In the path integral formalism [63, 65, 74] expectation values are computed by integrating over all possible field configurations at all spacetime points. The observable is weighted by the exponential of the action at a given point. In the case of QED, we integrate over all field configurations $A_\mu(x^\alpha)$ of the four-vector. The expectation value for an observable O is defined as

$$\langle \Omega | O | \Omega \rangle = \frac{\int \mathcal{D}A O[A_\mu] e^{iS_{QED}[A_\mu]}}{\int \mathcal{D}A e^{iS_{QED}[A_\mu]}} , \tag{2.14}$$

where Ω is the vacuum and $\mathcal{D}A$ denotes the functional measure of the path integral.

Equation (2.14) is not convenient to evaluate in its current form since the exponential in the numerator is heavily oscillating. Additionally, the expression is problematic from a mathematical standpoint since the measure $\mathcal{D}A$ of the gauge field is mathematically ill-defined. By changing the metric from a Minkowski metric to a Euclidean metric with a signature of $(++++)$, time is treated on the same footing as all other coordinates. This transformation is called Wick rotation, $t \to i\tau$. The change between the metric transforms the problem into a statistical mechanics problem with one additional dimension. We change from a Minkowski action S_M to a Euclidean action S_E by a change of variables in the integral

$$e^{iS_M} \equiv e^{i \int \mathrm{d}x_M^\alpha \mathcal{L}(x_M^\alpha)} = e^{-\int \mathrm{d}x_E^\alpha \mathcal{L}(x_E^\alpha)} \equiv e^{-S_E} , \tag{2.15}$$

where $\mathcal{L}_M$ and $\mathcal{L}_E$ are the Lagrangian density in the Minkowski and Euclidean formulation, respectively. The Euclidean metric leads to a more favorable behavior in the exponent since it is now decaying with increasing action instead of oscillating. On the other hand, the evaluation of time-dependent quantities becomes more difficult requiring analytic continuation of the sampled data.

In the case of QED, we do not have to resort to Monte Carlo computations on the lattice. Since the interaction vertex of QED is weighted with the fine structure constant $\alpha = 1/137$, we can use perturbation theory, *e.g.* in terms of Feynman diagrams. Each order of interaction is weighted with α and high orders of perturbation are heavily suppressed. Perturbation theory relies on the weight of the interaction vertex to be small. With changing energy scales, the coupling constant α; a behavior described by the beta function

$$\beta(g) = \mu \frac{\mathrm{d}g}{\mathrm{d}\mu} = \frac{\mathrm{d}g}{\mathrm{d}\ln\mu} , \tag{2.16}$$

where μ is the considered energy scale. In the case of QED, the beta function is positive which positive and the coupling increases with increasing energy. The growth, however, is rather small and the existence of a Landau pole, *i.e.* an infinite coupling at finite energy, is not finally settled.

Unfortunately, the non-Abelian gauge theory of quantum chromodynamics (QCD), which describes the strong interaction between quarks, exhibits a running coupling [75] with negative beta function. In contrast to QED, the coupling increases with decreasing energy scale in QCD. For high energies, quarks are asymptotically free and the coupling of quarks and gluons $\alpha_{gl} \ll 1$ such that perturbative methods are valid. At low energies, however, the coupling increases to $\alpha_{gl} \approx 1$ and perturbative methods break down. In order to explore the low energy behavior of QCD, new, non-perturbative methods have to be used.

One option is lattice gauge theories, a lattice regularization of the continuum QFT [70]. The formulation on a lattice has several advantages: a lattice renders the number of points finite, which makes the representation on a computer possible. Additionally, the lattice acts as a UV cut-off to the theory [70], and thus regulates possible UV divergences of the theory. Since perturbative methods break down at low-energy scales, LGT enables the numerical study of confinement. On the other hand, the theory is not represented in the continuum anymore and a continuum limit must be taken at the end of the calculation. We will consider the continuum limit in more detail at the end of the section.

Although, we could solve QED with perturbation theory, we will use it as an example for the discretization procedure. As we will see, the discretized version of QED shares some features with the $SU(3)$ description that makes it worth to study. Introducing a square lattice geometry was first considered by Wilson in his seminal paper *Confinement of Quarks* [70]. The gauge fields of the theory reside on the links of the lattice and the fermions are pinned to the vertices. We will add the fermions in a second step and focus on the gauge fields for the moment.

More concretely, we change from a continuous spacetime described by the continuous four-vector x^α to a four-dimensional lattice with spacing a described with a discrete four dimensional vector $\mathbf{x}$. The fermionic matter of the theory resided on the vertices and the gauge fields moderating the interaction ”live” on the links. The description of the gauge field changes from $A_\mu(x^\alpha)$ in terms of a Lie algebra (in our case $\mathfrak{u}(1)$) to $U_{\mathbf{x},\mu} = e^{iaA_{\mathbf{x},\mu}}$ which is an element of the group $U(1)$. We use the notation $\mathbf{x},\mu$ to identify a link emanating from vertex $\mathbf{x}$ in direction $\mu \in \{0,1,2,3\}$. The field in the continuum is the generator of the group on the lattice.

We choose to work with compact QED, *i.e.* $A_{\mathbf{x},\mu} \in [-\pi,\pi)$. In principle, we could also work with non-compact QED. However, cQED shares interesting features like confinement with non-Abelian theories [76].

The goal is to find an action on the lattice that agrees with the continuum action in the limit of vanishing lattice spacing ($a \to 0$). The most common choice is the Wilson action [70]

$$S_{\text{cQED}}\left(U_{x,\mu}\right) = \frac{1}{g^2}\sum_x \sum_{\mu<\nu} \operatorname{Re}\operatorname{Tr}\left(1 - W^{1\times1}_{\mu,\nu}\right) \tag{2.17}$$

where $W^{1\times1}_{\mu,\nu}$ is the simplest Wilson loop on a single plaquette

$$\begin{aligned} W^{1\times1}_{\mu,\nu} &= U_\mu(x)U_\nu(x+\hat{\mu})U_\mu(x+\hat{\nu})^\dagger U_\nu(x)^\dagger && (2.18)\\ &= \exp\left(iag\left[A_\mu(x+\hat{\mu}/2) + A_\nu(x+\hat{\mu}+\nu/2) - A_\mu(x+\hat{\nu}+\hat{\mu}/2) - A_\nu(x+\hat{\nu}/2)\right]\right). && (2.19)\end{aligned}$$

Greek letter with hats $\hat{\mu}$ represent the unit vector in direction μ on the lattice. The last line re-expresses the Wilson action on the lattice in the corresponding variables of the continuous theory. In the $a \to 0$, we recover the continuum action of pure QED that we originally wanted to simulate.

The gauge invariance of the continuous case is preserved on the lattice with $U_\mu(x) \to e^{i\phi(x)}U_\mu(x)e^{i\phi(x+\hat{\mu})}$, where $\phi(x) \in [-\pi,\pi)$. Once the lattice is introduced, we can rewrite the expectation value (2.14) in terms of the lattice action in Euclidean spacetime

$$\langle O[U]\rangle = \frac{\int \mathcal{D}U O[U] e^{-S_E[U]}}{\int \mathcal{D}U e^{-S_E[U]}}, \tag{2.20}$$

where $\mathcal{D}U = \prod_{x,\mu} \mathrm{d}U_\mu(x)$ is formulated in terms of the group's Haar measure which is well-defined in contrast to the measure $\mathcal{D}A$ in eq. (2.14). One advantage of the Wilson action (2.17) are the local interactions. If we want to evaluate the change of the action upon changing a gauge field, the total action changes only with respect to the neighboring plaquettes of the gauge field. This allows a local evaluation of the action which is computationally advantageous [77–79].

In contrast to eq. (2.14), eq. (2.20) is amenable to numerical treatment. The second part in the numerator and the denominator can be interpreted as a probability distribution

$$p(U) = \frac{e^{-S_E[U]}}{\int \mathcal{D}U e^{-S_E[U]}}\,, \tag{2.21}$$

if the $S_E[U] \in \mathbb{R} \forall U$. The high-dimensional integral in eq. (2.20) is well-suited for Monte Carlo sampling [14] and the expectation value of an observable is computed as

$$\langle O \rangle \approx \frac{1}{N} \sum_{i=1}^{N} O[U_i]\,, \tag{2.22}$$

where i is the index of a sampled gauge field configuration.

In practice, more involved algorithms like hybrid Monte Carlo and refinements thereof are employed [15]. The success of Monte Carlo computations for static quantities in high energy physics is unparalleled. The masses of hadronic particles agree with the experimental measures with astonishing precision [20]. However, the action formalism comes with one drawback. Since the action is expressed in Euclidean spacetime, real-time evolution becomes almost impossible to compute. If we want to study dynamic phenomena like string-breaking in a confining theory, other methods have to be used.

Until now, we have considered a pure theory without any matter content. To include fermions, we add the fermionic action S_{fer} to the exponent

$$\begin{aligned} S_{\text{fer}}[\psi, \bar{\psi}, U] &= m \sum_x \bar{\psi}(x)\psi(x) + \frac{1}{2a}\bar{\psi}(x) \sum_\mu \gamma_m u \left[U_\mu(x)\psi(x+\hat{\mu}) - U\mu^\dagger(x-\hat{\mu})\psi(x-\hat{\mu}) \right] \\ &\equiv \sum_x \bar{\psi}(x) M_{xy}[U] \psi(y)\,, \end{aligned} \tag{2.23}$$

where we introduced the interaction matrix M of the fermions

$$M_{i,j}[U] = m\delta_{ij} + \frac{1}{2a} \sum_\mu \left[\gamma_\mu U_{i,\mu} \delta_{i,j-\mu} - \gamma_\mu U^\dagger_{i-\mu,\mu} \delta_{i,j+\mu} \right]\,, \tag{2.24}$$

with the Euclidean γ_μ matrices. The first term in eq. (2.24) is the mass term of the fermions with mass m. The last two terms are the interaction of the fermions with the gauge field. We obtain for the expectation value

$$\begin{aligned} \langle O \rangle &= \frac{\int \mathcal{D}U \mathcal{D}\psi \mathcal{D}\bar{\psi} O[U] e^{-S_E[U] - S_{\text{fer}}[\psi,\bar{\psi},U]}}{\int \mathcal{D}U \mathcal{D}\psi \mathcal{D}\bar{\psi} e^{-S_E[U] - S_{\text{fer}}[\psi,\bar{\psi},U]}} \\ &= \frac{\mathcal{D}U O[U] \det(M[U]) e^{-S_E[U]}}{\mathcal{D}U \det(M[U]) e^{-S_E[U]}} \\ &= \frac{\int \mathcal{D}O[U] p(U)}{\int \mathcal{D}p(U)}\,, \end{aligned} \tag{2.25}$$

where we integrated out the fermions from the first line to the second using Grassmann integral identities

$$\int \mathcal{D}\bar{\Psi}\mathcal{D}\Psi e^{-\bar{\Psi}M[U]\Psi} = \det(M[U]) \tag{2.26}$$

and the probability distribution is modified to

$$p(U) \equiv \frac{\det\left(M[U]\right) e^{-S_E[U]}}{\int \mathcal{D}U \det\left(M[U]\right) e^{-S_E[U]}}\,. \tag{2.27}$$

The crucial requirement for Monte Carlo simulation is the interpretation of a part of the equation as a probability distribution $p(U)$. In the case of finite chemical potential μ or an odd number of fermion flavors in the system, the determinant of the coupling matrix $M[U] \in \mathbb{C}$. This leads to the infamous sign-problem [80] and the convergence of the Monte Carlo approximation breaks down. Instead of a convergence to the true mean in $\mathcal{O}\left(1/\sqrt{N}\right)$, the convergence gets exponentially slow.

The introduction of the lattice is a modification of the system that was necessary to obtain a computationally viable procedure. With Monte Carlo sampling, we obtain expectation values of observables $\langle O(g(a), a, L)\rangle$ which depend on the lattice spacing a, the size of the lattice L and the parameters of the theory g. The coupling depends explicitly on the lattice spacing, since the coupling of the theory is usually scale dependent. At the end of the computation, however, we are interested in results that are on infinite systems and on infinitely small lattice spacings, *i.e.* in the continuum. The first limit, is the thermodynamic limit $N \to \infty$ and it is usually obtained by extrapolating the data from large lattices to an infinite lattice. Since the coupling does not change with the system size, it is mainly a computational challenge to obtain data for large enough lattices to perform a reliable extrapolation. The second limit, the continuum limit $a \to 0$, is more challenging, because the coupling of the theory depends on the length-scale of the problem. In general, the functional dependence $g(a)$ is not known which makes the continuum limit much more challenging. Multiple works on one-dimensional lattice gauge theories have explored the continuum limit with matrix product states in more detail [81, 82]. In this thesis, we work at a fixed lattice spacing of $a = 1$ (in chapters 3 and 4) since we do not focus on the continuum limit but on the description of confinement on the lattice.

In addition to the continuum limit, fermions on the lattice exhibit a problem called fermion doubling. Instead of considering the full theory, we will demonstrate the issue and common solutions using the example of a free fermion. The Dirac equation of a free, massless fermion in one dimension is given by

$$i\partial_t \psi(x) = i\alpha\partial_x \psi(x)\,, \tag{2.28}$$

where $\psi = (\psi_1\ \psi_2)^T$ is the two-component Dirac spinor, and the Dirac matrices are given by

$$\gamma_0 = \begin{pmatrix} 1 & \\ & -1 \end{pmatrix} \quad \alpha = \begin{pmatrix} 0 & 1 \\ 1 & 0 \end{pmatrix}. \tag{2.29}$$

The problem of fermion doubling appears upon introducing a lattice with spacing a and coordinate $x = na$ for the nth. We can formulate eq. (2.28) on the lattice by replacing the spatial derivative by a finite differences

$$i\partial_t \psi(n) = i\alpha \frac{1}{2a}\left[\psi(n+1) - \psi(n-1)\right]\,, \tag{2.30}$$

where we replaced the continuous variable by the lattice index n. In both cases, we can compute the dispersion law and we obtain for the continuous theory

$$\omega = \alpha k, \quad -\infty < k < \infty \tag{2.31}$$

and

$$\omega = \alpha \frac{\sin(l)}{a}, \quad -\pi \leq l \leq \pi \tag{2.32}$$

for the discrete theory. The dispersion relation in the continuum [cf. eq. (2.31)] shows the expected linear dispersion for a relativistic particle. On the lattice, the frequency changes as $1/a$ except for special points $l \to ka$, $l - \pi \to ka$ and $l + \pi \to ka$ due to the sine term in eq. (2.32). In the limit, we obtain finite frequencies for around $l = 0$ and around $l = \pm\pi$. The modes at $l = 0$ can be identified with linear dispersion relation of the continuum modes. The gapless modes at $l = \pm\pi$, however, pose a problem since they allow finite momentum excitations of the system with zero energy cost. In the limit of $a \to 0$, these modes will carry infinite momentum which is significantly different from the continuum case that we started from. While we can choose to only populate the zero momentum modes ($l = 0$) in the free theory, an interaction can populate the modes around $l = \pi$. The effect of multiple roots of the dispersion relation is called fermion doubling.

Two well-known solutions to fermion doubling are Wilson fermions and staggered fermions. The basic idea of Wilson fermions is to shift the dispersion relation at the points $l = \pm\pi$ up by modifying the Hamiltonian of the system [70]. Thus, only the modes at $l = 0$ are gapless excitations and as long as the gap of at $l = \pm\pi$ is bigger than the energy scale that we are interested in, there will be no influence on the physics. The other option are staggered fermions as presented in [83, 84]. Instead of full two-component spinors, only one component of the spinor is placed on a given lattice point, *e.g.* ψ_1 on even and ψ_2 on odd sites. This construction effectively doubles the lattice spacing which leads to a shrinking of the Brillouin zone by a factor of two. Thus, we only observe the $l = 0$ node in the first Brillouin zone. While the procedure of staggering eliminates fermion doubling in one dimension, the issue is more involved in higher dimensions since not all doublers can be eliminated. In chapter 3, we will use an ansatz formulated in terms of staggered fermions to facilitate the inclusion of physical fermions. A more detailed presentation of staggering and fermion doubling in one and three dimensions is given in [84]. The need for a modification of the naive discretization of fermions can be also derived from the Nielsen-Ninomiya no-go theorem for lattice gauge theorems [85].

Motivated by the distinct problems of the action formalism, the main ones being the sign-problem and difficulties in the simulation of time dynamics, it is worth to explore other formulations of lattice gauge theories. One formulation, that lends itself also well to experimental implementation, is the Hamiltonian formalism [83]. Here, time is kept continuous, while space is discretized. Since time keeps its special role and is not Wick-rotated, real-time evolution is possible in this framework. The transition from an action $S[U_\mu(x)]$ to a Hamiltonian is performed by taking the limit $a_\tau \to 0$ for the lattice spacing in the temporal direction and using the temporal gauge $U_0 \equiv 0$. The temporal gauge implies that all gauge field on temporal links are set to 0 and it allows to use canonical quantization in subsequent steps [83, 86].

In the Hamiltonian formulation, a Hamiltonian operator explicitly acts on a Hilbert space. Thus, the Hilbert space has to be treated numerically. This is in stark contrast to the action formalism, where the problem is reduced to a statistical mechanics problem with a scalar action. If the gauge group is a compact Lie group, like $U(1)$ or $SU(3)$, the Hilbert space of each link becomes infinite dimensional. One formulation, that we focus on in this thesis, is based on the Hamiltonian formulation proposed by Kogut and Susskind [83]. Other formulations in the Hamiltonian picture include the quantum link model [87–90] or the prepotential approach [91].

In the following sections, we introduce the Kogut-Susskind Hamiltonian for the gauge groups $U(1)$ and $\mathbb{Z}_3$ in more detail. One-dimensional lattice gauge theories present a special case since the fermionic matter content fully determines the gauge fields. There are no loops and the gauge fields are only influenced from the two neighboring sites. The gauge field cannot interact with itself in the form of loops, since a one-dimensional system does not contain loops. Upon integrating out the gauge degrees of freedom, the theory only contains the fermionic degrees of freedom. Details on the classic computations in one dimension are summarized in section 2.2.2.

Chapters 3 and 4 focus on systems in $(2+1)$ dimensions. Here, the gauge cannot be integrated out and the self-interaction of the gauge field (in the form of loops) plays a major role. We consider the Kogut-Susskind Hamiltonian in $(2+1)$ dimensions for cQED, the $U(1)$ gauge theory treated above. Additionally, we introduce the $\mathbb{Z}_3$ since we explore it in chapter 3.

$(2+1)$-DIMENSIONAL COMPACT QED

Additional to a short review of the general formulation presented in section 2.2.1, we introduce a new set of variables on the plaquettes to reduce the degrees of freedom. We consider $(2+1)$-dimensional cQED on an $L \times L$ square lattice with periodic boundary conditions. As described above, the gauge fields reside on the links; $U_{\mathbf{x},i}$ denotes the gauge field operator on the link emanating from site $\mathbf{x}$ in direction $\mathbf{e}_i$. The notation changed from $U_\mu(x)$ to $U_{\mathbf{x},i}$ since we are now considering a two-dimensional spatial lattice and not a four dimensional spacetime lattice. The Hamiltonian in lattice units as proposed by Kogut and Susskind [83] takes the form

$$H_{KS} = \frac{g^2}{2} \sum_{\mathbf{x},i} E^2_{\mathbf{x},i} + \frac{1}{2g^2} \sum_{\mathbf{p}} \left[2 - \left(U_{\mathbf{p}} + U^\dagger_{\mathbf{p}}\right)\right], \tag{2.33}$$

where g^2 is the coupling constant and $U_{\mathbf{p}} \equiv U_{\mathbf{x},1} U_{\mathbf{x}+\mathbf{e}_1,2} U^\dagger_{\mathbf{x}+\mathbf{e}_2,1} U^\dagger_{\mathbf{x},2}$ where $\mathbf{x}$ is the bottom left corner of plaquette $\mathbf{p}$. $U_{\mathbf{x},i}$ is in the fundamental representation of $U(1)$; and we write it in terms of an angle $\theta_{\mathbf{x},i}$, $U_{\mathbf{x},i} = e^{i\theta_{\mathbf{x},i}}$ with $-\pi < \theta_{\mathbf{x},i} \leq \pi$. As mentioned above, the theory is called compact QED due to the restriction of the gauge field to the compact interval $\theta_{\mathbf{x},i} \in (\pi, \pi]$. It causes interesting features such as confinement in contrast to the non-compact theory [76]. $E_{\mathbf{x},i}$ is the electric field operator fulfilling the commutation relations

$$[E_{\mathbf{x},i}, U_{\mathbf{y},j}] = \delta_{\mathbf{x},\mathbf{y}} \delta_{i,j} U_{\mathbf{x},i} \quad \text{and} \tag{2.34}$$

$$[\theta_{\mathbf{x},i}, E_{\mathbf{y},j}] = i \delta_{\mathbf{x},\mathbf{y}} \delta_{i,j}\,. \tag{2.35}$$

Since we work in the temporal gauge, there is a residual spatial gauge symmetry defined by the Gauss law operators $G_{\mathbf{x}}$. All physical states must be eigenstates of $G_{\mathbf{x}}$

$$G_{\mathbf{x}} \left|\text{phys}\right\rangle = \sum_{i=1}^{2} \left(E_{\mathbf{x},i} - E_{\mathbf{x}-\mathbf{e}_i,i}\right) \left|\text{phys}\right\rangle = Q_{\mathbf{x}} \left|\text{phys}\right\rangle \quad \forall\, \mathbf{x}, \tag{2.36}$$

where the eigenvalue $Q_{\mathbf{x}}$ are determined by the static charge configuration at $\mathbf{x}$.

These local constraints put severe restrictions on the choice of variational states. Following [92], we thus change to a different set of variables that incorporates gauge invariance up to a global constraint. We split the electric field $E_{\mathbf{x},i}$ on a link into its dynamic, transversal part $E^T_{\mathbf{x},i}$ and a longitudinal part $E^L_{\mathbf{x},i}$ fixed by the static charge configuration. The transversal field in direction i is given by

$$E_i^T(\mathbf{x}) = \nabla^{(-)} \times \varepsilon \equiv \epsilon_{ij} \nabla_j^{(-)} \varepsilon(\mathbf{x}) \,, \tag{2.37}$$

where $\nabla^{(-)} f(\mathbf{x}) = f(\mathbf{x}) - f(\mathbf{x} - \mathbf{e}_i)$ is the backward lattice derivative in direction i. The electric field ε is defined on the plaquette whose bottom-left corner is the vertex $\mathbf{x}$. The longitudinal component

$$E_i^L(\mathbf{x}) = -\nabla^{(+)} \phi(\mathbf{x}) \equiv -\left(\phi(\mathbf{x} + \mathbf{e}_i) - \phi(\mathbf{x})\right) \tag{2.38}$$

is defined by the forward derivative $\nabla^{(+)}$ of a scalar field ϕ defined on the vertices and ϵ_{ij} is the antisymmetric Levi-Civita symbol. The scalar field ϕ is fixed by the static charge configuration that we impose. For a full reformulation of the electric energy in terms of transversal and longitudinal fields, we refer to Appendix A of [2]. Since the transversal part of the electric field can be expressed by a plaquette field $L_{\mathbf{p}}$ (the lattice analog of a solenoidal vector field), the remaining dynamical degrees of freedom $\left\{L_{\mathbf{p}}, U_{\mathbf{p}} = e^{i\theta_{\mathbf{p}}}\right\}$ reside on plaquettes. They have the same Hilbert space structure and fulfill the same commutation relations as the link variables

$$[L_{\mathbf{p}}, U_{\mathbf{p}'}] = \delta_{\mathbf{p},\mathbf{p}'} U_{\mathbf{p}'} \quad \text{and} \tag{2.39}$$

$$[\theta_{\mathbf{p}}, L_{\mathbf{p}'}] = i\delta_{\mathbf{p},\mathbf{p}'} \,. \tag{2.40}$$

The operator $U_{\mathbf{p}}$ creates an electric flux excitation around plaquette $\mathbf{p}$. Not the difference between the operator $U_{\mathbf{x},\mu}$ acting on a link and $U_{\mathbf{p}}$ acting on a plaquette. To construct all possible gauge-invariant flux configurations, two global non-contractible flux loops around the torus (one for each spatial direction) are required. Their operators are denoted by $\{\theta_1, L_1\}$ and $\{\theta_2, L_2\}$ specifying the topological sector of the flux configuration. L_1 and L_2 commute with the Hamiltonian, and we restrict ourselves to the topological sector with $L_1 = L_2 = 0$ which corresponds to no electric flux loops winding around the torus. For more details see [93] or Appendix A of [2].

Writing the Hamiltonian in terms of these new variables, we obtain

$$H_{KS} = E_C + \frac{1}{g^2} \sum_{\mathbf{p}} \left(1 - \cos\theta_{\mathbf{p}}\right) + \frac{g^2}{2} \sum_{\mathbf{p}} \sum_{i=1}^{2} \left(L_{\mathbf{p}} - L_{\mathbf{p}-\hat{\mathbf{e}}_i} + \epsilon_{\mathbf{p}} - \epsilon_{\mathbf{p}-\hat{\mathbf{e}}_i}\right)^2 \,, \tag{2.41}$$

where E_C is an energy offset given by the lattice Coulomb energy and $\epsilon_{\mathbf{p}}$ accounts for the transversal part of the electric field caused by the static charges only, *i.e.* $\epsilon_{\mathbf{p}} = 0$ in case of no static charges. Even in this formulation there is one remaining global constraint left which is intuitively clear since raising the electric flux around all plaquettes should return the same state due to the periodic boundary conditions. Thus,

$$\prod_{\mathbf{p}} U_{\mathbf{p}} \left|\text{phys}\right\rangle = \left|\text{phys}\right\rangle \,, \tag{2.42}$$

for all physical states $|\text{phys}\rangle$. For further details on this formulation, we refer to [92, 93].

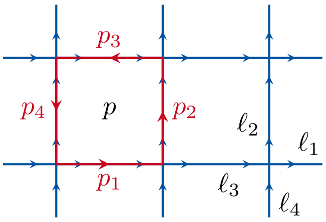

Figure 2.3: Convention for labeling the links of a plaquette. The red arrows indicate the orientation of the plaquette. The blue arrows show the convention for the calculation of a divergence on the lattice.

$(2+1)$-DIMENSIONAL $\mathbb{Z}_N$ THEORY

In the following section, we focus on Abelian lattice gauge theories with finite gauge groups ($\mathbb{Z}_N$), without dynamical matter, i.e. pure gauge theories. As in the $U(1)$ case, we consider a two-dimensional $L \times L$ lattice with periodic boundary conditions. Thus, the only degrees of freedom of the theory reside on the links. There are no static charges or dynamic fermions in the model used in chapter 3. Both extension will be considered in future works.

As described in Ref. [94], the $N \to \infty$ limit of $\mathbb{Z}_N$ reproduces $U(1)$, and hence $\mathbb{Z}_N$ lattice gauge theories flow, in the large N limit, to cQED [86].

We write the Hamiltonian of a pure $\mathbb{Z}_N$ gauge theory as

$$\begin{aligned} H &= H_E + H_B \\ &= \frac{g^2}{2}\sum_{\mathbf{x},i}\left[2-(P_{\mathbf{x},i}+P^\dagger_{\mathbf{x},i})\right] + \frac{1}{2g^2}\sum_p\left[2-(Q_{p_1}Q_{p_2}Q^\dagger_{p_3}Q^\dagger_{p_4}+\text{H.c.})\right], \end{aligned} \tag{2.43}$$

where p is a plaquette [94]. The indices p_j refer to one of the four links of plaquette p as indicated in fig. 2.3. The terms H_E and H_B are referred to as electric and magnetic part of the Hamiltonian, respectively [83].

The operators in eq. (2.43) obey the $\mathbb{Z}_N$ algebra given by

$$\begin{aligned} P_\ell^N &= Q_\ell^N = 1 \qquad P_\ell^\dagger P_\ell = Q_\ell^\dagger Q_\ell = 1 \\ P_\ell^\dagger Q_\ell P_\ell &= e^{i\delta} Q_\ell \qquad \delta = \frac{2\pi}{N}, \end{aligned} \tag{2.44}$$

where we introduced the shorthand $\ell = (\mathbf{x}, i)$ for the link variables. Operators that act on different links commute with each other.

The Hamiltonian eq. (2.43) is invariant under the action of the local unitary operators

$$\Theta(\mathbf{x}) = P_{\mathbf{x},1}\,P_{\mathbf{x},2}\,P^\dagger_{\mathbf{x}-\hat{\mathbf{e}}_1,1}\,P^\dagger_{\mathbf{x}-\hat{\mathbf{e}}_2,2}\,. \tag{2.45}$$

This local gauge invariance implies that $\Theta(\mathbf{x})$ commutes with the Hamiltonian on each site

$$[\Theta(\mathbf{x}), H] = 0 \quad \forall\,\mathbf{x}\,. \tag{2.46}$$

Due to the generators of local symmetry [given in eq. (2.45)], we know that the physical states of the system obey the symmetry

$$\Theta(\mathbf{x})\,|\Psi\rangle = |\Psi\rangle \quad \forall\,\mathbf{x}\,. \tag{2.47}$$

Equation (2.47) holds since we do not consider static charges in chapter 3.

Given the group $\mathbb{Z}_N$, we define a set of group element states $|q(\ell)\rangle$ labeled by integers $q = 0, \dots, N-1$, which span the local gauge field Hilbert space on link ℓ. They correspond to group elements with the discrete angles $\phi(\ell) = q\delta$ [δ is defined in eq. (2.44)]. In contrast to the $U(1)$ theory presented in section 2.2.1, the angle does not take continuous values in $Z(N)$. The group element states form an orthonormal basis for the local Hilbert space $\langle q|q'\rangle = \delta_{q,q'}$.

These states are eigenstates of the Q operators, with

$$Q\,|q\rangle = e^{i\delta q}\,|q\rangle\ . \tag{2.48}$$

They are lowered by the P operators, periodically as

$$P\,|q\rangle = |q-1\rangle\ . \tag{2.49}$$

We will actively use the two formulations of the Kogut-Susskind Hamiltonian in chapters 3 and 4.

2.2.2 CLASSICAL SIMULATION OF HAMILTONIAN LATTICE GAUGE THEORIES

The first works to consider tensor networks for lattice gauge theories are formulated in one spatial dimension. A typical test bench in one spatial dimension is one-dimensional QED, *i.e.* the Schwinger model [95, 96]. The match of highly efficient MPS algorithms and the possibility to integrate out the gauge field, makes them a perfect candidate for new algorithms. In [97], the Schwinger model is evaluated with DMRG which is equivalent to a treatment with MPS. In order to use MPS algorithms, the Schwinger model is formulated as a Kogut-Susskind Hamiltonian in terms of staggered fermions [83] and then transformed to a spin Hamiltonian [98]. This formulation can be directly treated with MPS methods. In subsequent works, the mass spectrum [99, 100], the behavior at finite temperature [101] and the time-evolution of string breaking [102] were studied in more detail. In [81], the Schwinger model is treated at finite density, a setting that cannot be treated with Monte Carlo methods due to the sign problem.

With Abelian $U(1)$ successfully mastered in one dimension, the focus shifted to non-Abelian theories. In [103], an MPS formulation for SU(2) is presented.

As discussed above, lattice gauge theories change dramatically when changing from one to two dimensions. In addition, the contraction of PEPS states becomes more difficult (cf. section 2.1.2). In [104], a $(2+1)$-dimensional iPEPS simulation shows the possibilities of PEPS. Here, gauge invariance is enforced during the optimization and not explicitly encoded in the state. An alternative approach where gauge invariance is encoded in a finite PEPS state is presented in chapter 3. The prohibitively high cost during the contractions originates from the loop structure in fully connected PEPS. As an alternative, a loop-less tensor network construction was proposed [45] which can be extended to more than one dimension while keeping contractions efficient.

The exploration of lattice gauge theories is not limited to tensor network states. A generalization of Gaussian states has proven suitable [105] to describe one dimensional theories. As an alternative, we present a new class of Gaussian states, complex periodic Gaussian states, in chapter 4.

Machine learning (ML) plays an increasingly prominent role when defining ansatz states in condensed matter [106, 107]. The local constraints in form of the Gauss law have so far precluded the direct application of ML methods to lattice gauge theories. In [108, 109], first approaches have been explored to use gauge-invariant machine-learning states for lattice gauge theories.

An alternative formulation to the Kogut-Susskind Hamiltonian are quantum link models [87–90, 110]. The basic idea is to replace the gauge fields on the links by bilinear operators with additional constraints, the number of link particles must be conserved. This formulation renders the Hilbert space finite dimensional even for continuous groups like $U(1)$, making the model amenable for exact diagonalization. On the other hand, the formulation limits the number of electric field occupations that can be represented. Beyond the simulation of lattice gauge theories with high energy or experiments [111, 112] in mind, quantum link models have been used recently to explore many-body effects like localization [113–115].

All prior ideas are based on the variational principle – an ansatz state is formulated to control the exponential growth of parameters – or on exact diagonalization. Alternatively, we can try to model a quantum system using partition sums in statistical mechanics. The product structure of a partition sum can be interpreted as a contraction of local tensors. Tensor renormalization group (TRG) approaches large system sizes by repeatedly contracting tensors [116] to coarse-grain the system following a renormalization group idea. Typically, properties like phase transitions can be studied. TRG methods have been transferred to lattice gauge theories [117–119].

2.2.3 QUANTUM SIMULATION OF HAMILTONIAN LATTICE GAUGE THEORIES

High energy physics systems are usually difficult to manipulate since high energies and big experiments like the Large Hadron Collider (LHC) are necessary. Quantum simulations – digital or analog – can offer the possibility to probe a system with the same physical properties as the original in a table-top experiment. Analog simulation describes the idea of purpose-built experiments that emulate another physics system while being easier to manipulate and to measure. If we can understand the behavior of the simulating experiment, we can transfer the results to the actual system.

Digital simulation is a more general approach to quantum simulation. A given simulator uses a stroboscopic time-evolution expressed in terms of gates to simulate another quantum system. The generality of simulating an arbitrary system requires the approximation of a stroboscopic evolution.

Both approaches do not imply that colliders are not needed anymore. Quantum simulations can only explore physics that we understand to the degree that we are able to formulate it in equations. The exploration of the actual system can still lead to fundamentally new insights.

The following sections explore the current state-of-the art in digital and analog quantum simulation of lattice gauge theories. Naturally, the ideas presented here are only an overview. For more details, we refer to reviews on the subject [120–122].

ANALOG QUANTUM SIMULATION

Since the analog simulator is a quantum system itself, there is no computational overhead comparable to the classical simulation of quantum systems. Even the time-evolution of the quantum system, a challenging task in classical computing, is directly accessible, since the model system follows the same dynamics as the original system. In recent years, different platforms have been proposed to simulate lattice gauge theories, *e.g.* cold atoms [123–125], trapped ions [112] and superconducting circuits [126]. To make cold atoms amenable for well controlled manipulations the atoms are trapped in a light field created by counter-propagating laser beams. The beams create a lattice that is strong enough to fix the atoms at given positions. Conceptually, this is already very close to a lattice gauge theory. Some proposals were recently realized in cold atom experiments, like the quantum simulation of an Abelian $\mathbb{Z}_2$ double-well in [127] or a demonstration of U(1) gauge invariance in Bose-Einstein condensates [128]. Due to experimental constraints, the systems are currently limited to low spatial dimensions and cannot yet compete with the most sophisticated classical simulations.

In the upcoming years, we expect to see experiments for both, more involved gauge groups like non-Abelian gauges and simulations in higher dimensions.

DIGITAL QUANTUM SIMULATION

Since fully fault-tolerant digital quantum simulators are not available yet, simulations are either formulated for noisy intermediate scale quantum devices (NISQ devices) [129] or the algorithms are proposals for future machines.

In [130], the authors present a quantum algorithm for a fault-tolerant quantum computer to evaluate the scattering amplitudes of the interacting ϕ^4 theory. The algorithm is polynomial in the number of particles, their energy and the desired precision. Thus, it presents an exponential speed-up in comparison to the best classical algorithms [131–133].

An orthogonal approach to the development of a pure quantum algorithm, is the idea to use a hybrid quantum-classical approach. The ansatz is implemented in terms of an n-qubit circuit parameterized by classical variables. These variables are adapted by a classical optimizer. By iterating the procedure many times until convergence, the algorithm obtains an approximate solution for the ground sate. In the case of classical combinatorics, the approach is named Quantum Approximate Optimization Algorithm (QAOA). If it is applied to a quantum problem, it is called variational quantum eigensolver (VQE). In [134] the VQE algorithm is implemented on a photonic device to demonstrate the performance in computing ground states of nuclei like helium.

Digital simulators cannot only be implemented in photonics, but also in cold atom arrays and trapped ions experiments. In [135] a digital simulation of the Schwinger model with trapped ions is performed. The algorithm is demonstrated with four ions and a gate sequence of more than 200 gates. Since it is a digital simulation, the time-evolution is trotterized [136].

A simulation of LGT in superconducting qubits was proposed in [137] for the non-Abelian $SU(2)$ theory. Experimental realizations of non-Abelian theories, however, are more challenging than Abelian ones and have yet to be performed.

Finally, Rydberg atoms are considered to be a promising platform for universal quantum computation. Rydberg simulators are based on the idea to excite neutral atoms in an optical lattice to highly excited states. Due to the so-called Rydberg blockade, very strong interactions between spatially separated atoms can be introduced. The interactions between atoms enable the implementation of gates and cold atoms can be used for digital quantum computation. Several proposals [138–142] point out that a fully gauge-invariant simulation of gauge theories can be achieved with Rydberg atoms.

2.3 HAMILTONIAN TRUNCATION

In the last part of the preliminary materials, we move from lattice theories back to the continuum. Hamiltonian Truncation (HT) is a numerical method to study strongly interacting QFT directly in the continuum. It was first introduced by Yurov and Zamolodchikov [143, 144] in the 1990s. Instead of finding an ansatz state for the ground state (as in section 2.1), HT is closer to exact diagonalization in spirit. The idea is to represent the Hamiltonian of a field theory defined on a compact domain as

$$H = H_0 + V\,, \tag{2.50}$$

where H_0 is the solvable part of the Hamiltonian and V is a perturbing potential. Traditionally, the conformal field theory (CFT) of the UV fixed point of the theory was used as solvable H_0. More modern approaches consist of using other solvable theories like free massless and massive theories [145, 146]. In contrast to perturbation theory, the perturbing potential V does not need to be small which gives HT the power to capture non-perturbative effects.

The method proceeds with representing the Hamiltonian operator H as a matrix in the Hilbert space of H_0, the space $\mathcal{H}_0$ as

$$H_{ij} = \langle i| H |j\rangle \ . \tag{2.51}$$

Since H_0 is solvable, we know the orthogonal eigenstates $|i\rangle$ that diagonalize H_0. In order to explore the spectrum of the theory, we want to diagonalize the Hamiltonian. Until now, this method is identical with exact diagonalization (ED) which consists of diagonalizing a matrix representation of the Hamiltonian. In order to speed up the computation, it is common to exploit quantum numbers that split the Hamiltonian into sectors. These sectors are diagonalized separately which reduces the complexity of the problem [147]. In the case of a continuous quantum field theory, however, the Hilbert space is infinite dimensional and the Hilbert space cannot be diagonalized a priori; we have to introduce a truncation to make the Hilbert space finite.

The following presentation of the method follows [145] in spirit and notation. Ideally, we could solve the actual eigenvalue problem of the infinite dimensional system

$$H\left|\psi\right\rangle = \mathcal{E}\left|\psi\right\rangle \,, \tag{2.52}$$

where $\mathcal{E}$ are the exact eigenvalues of the Hamiltonian H and $\left|\psi\right\rangle$ are infinite dimensional energy eigenvectors. The crucial step of HT is to introduce a high energy cutoff, keeping only the low energy states of H_0 which renders the matrices finite and enables numerical computations. Thus, we split the Hilbert space into two subspaces $\mathcal{H}_l$, the low-energy sector of the Hilbert space, and $\mathcal{H}_h$, the high-energy sector

$$\mathcal{H} = \mathcal{H}_l \oplus \mathcal{H}_h\,. \tag{2.53}$$

The low-energy subspace $\mathcal{H}_l$ is finite dimensional and will be treated numerically, while the sector $\mathcal{H}_h$ contains infinitely many states that we discarded.

Given the splitting of the Hilbert space, we can rewrite eq. (2.52) and obtain

$$H_{ll}\,|\psi_l\rangle + H_{lh}\,|\psi_h\rangle = \mathcal{E}|\psi_l\rangle \tag{2.54}$$

$$H_{hl}\,|\psi_l\rangle + H_{hh}\,|\psi_h\rangle = \mathcal{E}|\psi_h\rangle\ , \tag{2.55}$$

where we defined $|\psi\rangle = |\psi_l\rangle \oplus |\psi_h\rangle$ to split the low-energy part of the eigenvector from the high-energy part. Note, that we do not know the exact value for $\mathcal{E}$ or $|\psi\rangle$. Additionally, we defined the projected Hamiltonians $H_{\alpha,\beta} \equiv P_\alpha H P_\beta$ where P_α is the projector the low- or high-energy subspace with $\alpha \in \{l, h\}$.

Since we are interested in computing the low-energy sector of the spectrum numerically, we use eq. (2.55) to eliminate $|\psi_h\rangle$ in eq. (2.54)

$$\left[H_{ll} - H_{lh}\left(H_{hh} - \mathcal{E}\right)^{-1} H_{hl}\right]|\psi_l\rangle = \mathcal{E}c_l\,. \tag{2.56}$$

While eq. (2.56) has the structure of an eigenvalue problem in the low-energy sector, it contains the unknown energies $\mathcal{E}$ of the true problem. Since H_0 is diagonal and cannot couple the low- to the high-energy sector of the spectrum, we identify $H_{lh} \equiv V_{lh}$, $H_{hl} \equiv V_{hl}$, and $H_{hh} \equiv V_{hh}$. This transforms eq. (2.56) to

$$\begin{aligned}\left[H_{\text{trunc}} + \Delta H\right]|\psi_l\rangle &= \mathcal{E}|\psi_l\rangle\ ,\\ \Delta H &= -V_{lh}\left(H_0 + V_h h - \mathcal{E}\right)^{-1} V_{hl}\,.\end{aligned} \tag{2.57}$$

Here, we identified $H_{ll} \equiv H_0$.

Until now, all modifications to the equations have been exact. In order to proceed, we start to expand ΔH in V_{hh}

$$\Delta H = -V_{lh}\left(H_0 - \mathcal{E}\right)^{-1} V_{hl} + \cdots\ . \tag{2.58}$$

For more details on a possible inclusion of higher order terms, we refer to [145]. The formulation of ΔH in eq. (2.58) is entirely in $\mathcal{H}_l$ now, the matrix elements, however contain contributions from the high-energy spectrum still

$$(\Delta H)_{ij} = -\sum_{k:E_k>E_{\text{max}}} \frac{V_{ik}V_{kj}}{E_k - \mathcal{E}_*}\,, \tag{2.59}$$

where we introduce a reference energy $\mathcal{E}_*$ since we do not know the true value of $\mathcal{E}$ that enters into the computation of ΔH.

As presented in [145, 148], ΔH can be rewritten without infinite sums and the reference energy can be eliminated as well. Finally, we obtain a matrix in the low-energy sector that contains some information about the coupling to the high-energy sector via ΔH.

The method of Hamiltonian truncation converges if the perturbation V does not mix significantly the low energy sector of $\mathcal{H}_0$ with the higher energy sectors, *i.e.* that $V_l h$ does not strongly couple low-energy states to high-energy states. All excitations from $\mathcal{H}_0$ into the high energy sector are lost. In case of an expansion around the CFT point, this is guaranteed by the renormalization group theory for relevant perturbations V. If computed for several high enough cutoffs the results of an HT simulation can often be extrapolated to obtain the infinite cutoff value. Alternatively, a numerical renormalization group algorithm can be used [149].

We use HT in chapter 6 to study the entanglement properties of quantum field theories directly in the continuum.

3 GAUGED-GAUSSIAN PROJECTED ENTANGLED PAIR STATES

3.1 MOTIVATION

Gauge theories appear in many fundamental physical contexts, *e.g.* the standard model of particle physics, where gauge fields act as force carriers. In particular, the standard model includes quantum chromodynamics (QCD), the theory of the strong nuclear force, which, as a non-Abelian gauge theory [63], has a running coupling with negative beta function. In QCD, asymptotic freedom [68] gives rise to asymptotically weak couplings for high energy scales (*e.g.* collider experiments), and therefore perturbation theory could be used in these physical regimes. On the other hand, at low energy QCD is a strongly coupled model, requiring non-perturbative treatment.

As described in the preliminary material [cf. section 2.2.1], lattice gauge theories are a common approach to access regimes where non-perturbative methods break down. They provide a gauge invariant regularization of gauge theories on the lattice, discretizing either spacetime [70] or only space (leaving time continuous) [83]. While extremely successful for static studies (such as the hadronic spectrum), Monte Carlo methods face two major difficulties, the calculation of time dynamics and the sign problem at finite chemical potential [80]. This limitation blocks the way to important phases of the QCD phase diagram [150].

Motivated by the success of tensor networks in condensed matter physics, they have been generalized and applied to particle physics problems, in particular to lattice gauge theories (LGT) [121]. In one space dimension, matrix product states (MPS) have been very successful in finding ground states and describing time dynamics (see Ref. [121] and references therein). In higher dimensions, MPS are generalized to projected entangled pair states (PEPS), whose contraction is in general very costly. This hinders the application of variational PEPS algorithms in higher dimensions, although state-of-the-art algorithms can handle all terms in a gauge theory [151] and a first numerical study for a pure gauge theory has been recently presented in [104]. Earlier numerical studies used less general tensor networks for two-dimensional lattice gauge theories, either purely gauge [152] or including fermions [153].

Analytical approaches have developed faster, with the formulation of gauge invariant pure gauge PEPS [154], and more general gauging mechanisms including matter for arbitrarily dimensional PEPS [49, 155]. In these works, the global symmetry of a matter-only PEPS (without gauge fields) is lifted to a local symmetry by introducing a gauge field, in a way analogous to minimal coupling. This gauging method is used to construct gauged Gaussian fermionic PEPS (GGPEPS) [156, 157], where the initial matter state is a free (Gaussian) fermionic state, in a manner analogous to minimal coupling of a Hamiltonian [6]. The restriction to GGPEPS enables the efficient contraction of the states with Monte Carlo techniques [158]. Since the sampling probability of the algorithm depends only on the norm of the state, the Monte Carlo algorithm cannot suffer from the sign problem. Furthermore, the construction allows for a natural and efficient extension to higher bond dimensions which is numerically very expensive in general PEPS calculations. However, until now, these states have only been used to compute observables of toy models – either exact contractions, showing relevant physical behavior [156, 157] or a demonstration of the feasibility of the Monte Carlo contraction of the PEPS, but for given states, without variational techniques [158]. The next logical step is the numerical evaluation of GGPEPS as a variational ansatz state.

The content of this chapter is based on Ref. [1].

3.2 EXECUTIVE SUMMARY

Gauge theories lie at the heart of our understanding of particle physics. Since direct evaluations of the quantum field theory in the continuum is analytically impossible, lattice regularization are a common tool to treat these theories numerically [15, 20, 70]. The restrictions of Monte Carlo computations motivate the development of new algorithms [80].

A direct treatment of QCD is difficult since the theory is non-Abelian. The non-commutativity of gauge fields creates further difficulties in the computational method. Instead of full QCD, we consider a $\mathbb{Z}_3$ theory in $(2+1)$ spacetime dimensions, a theory which shares some key features with QCD. The confinement properties of non-Abelian $SU(N)$ theories are intimately related to the $\mathbb{Z}_N$ center of the gauge group [159–164]. Thus, the Abelian $\mathbb{Z}_3$ theory is a step towards understanding color confinement in QCD. The $\mathbb{Z}_3$ theory exhibits a (first-order) phase transition between a confining and non-confining phase, and thus constitutes a non-trivial test bench [78]. Furthermore, extensive Monte Carlo studies have been performed on $\mathbb{Z}_N$ theories, which enable a benchmark of our results against known results [165]. Our goal is to demonstrate the expressibility of the ansatz presented in Ref. [158] and how it can be applied to study gauge theories. We use gauged Gaussian PEPS (GGPEPS) as an ansatz to compute the ground state energy. Due to the symmetries encoded in the state, the number of parameters is strongly restricted. To increase the expressive power of the ansatz, we couple several GGPEPS to the same gauge field. We call each independently parameterized GGPEPS that builds the full state a layer. Since all layers can be evaluated independently, the complexity scales linearly in the number of layers.

The next step, required for demonstrating the credibility and feasibility of the method, is the actual energy minimization procedure of a real lattice gauge theory Hamiltonian: a numerical verification that the such ansatz states can converge to true ground states. In this chapter, we present the application of fermionic GGPEPS[49, 156–158] as ansatz states in a variational Monte Carlo (VMC) procedure [166–168].

Figure 3.4 shows an initial benchmark of the state. For small systems, the GGPEPS can be contracted exactly and compared with the exact ground state (obtained via exact diagonalization). With a single layer, *i.e.* two parameters, only the high-coupling part of the theory matches due to the construction of the state. With an increasing number of layers, the correspondence between the two methods increases also for the low-coupling regime.

The computation is not limited to small systems. By using Monte Carlo computations instead of exact contractions, we can also obtain results for larger systems (cf. fig. 3.5). However, precisely locating the phase transition remains challenging, even with an increased number of layers (cf. fig. 3.6). The main obstacle is the expensive evaluation of a Pfaffian that appears in the calculation of the electric energy. It has to be calculated in every Monte Carlo step during the energy minimization. We show that the GGPEPS are promising states to study gauge theories in higher dimensions. The next steps include increasing the spatial dimension to three space dimension and to include physical fermions.

The rest of the chapter is structured as follows: In section 3.3, we construct the ansatz states and introduce the numerical method used in the minimization. The results of the variational procedure are presented in section 3.4. Finally, we discuss our findings and further research directions in section 3.5.

3.3 THEORETICAL FRAMEWORK

Expressing a lattice gauge theory in terms of a Hamiltonian implies that we have to work with a Hilbert space. This problem is elegantly avoided in the path integral formalism. The path integral does not need an explicit formulation of the Hilbert space; instead, the path integral is directly sampled via Monte Carlo.

In the case of a general lattice gauge theory with fermions and gauge fields, we have to consider two Hilbert spaces: one for the fermions on the vertices and one for the gauge fields on the links. One problem of numerically simulating a lattice gauge theories with compact Lie groups [even the Abelian $U(1)$] is the infinite dimension of each Hilbert space on the links. This can be approached by truncating the local Hilbert spaces, either by introducing a cutoff to the electric field, allowing one to restore the full theory by extending the cutoff [156] or integrating over an extra dimension [87–89], or by sampling group elements [94] from the gauge group, which form a subgroup. Due to the construction of our states (see section 3.3.1), we chose the second approach, *i.e.* instead of simulating the full $U(1)$ theory, we consider a $\mathbb{Z}_N$ subgroup that serves as an approximation for $U(1)$. Since we restrict ourselves to a pure gauge theory, we will not treat the fermionic Hilbert spaces on the vertices. Further details about $\mathbb{Z}_N$ lattice gauge theories are provided in section 2.2.1.

3.3.1 CONSTRUCTION OF GGPEPS

The original GGPEPS construction [49, 156, 158] builds the basis for the numerical ansatz. We enlarge the family of variational states by using several GGPEPS coupled to the same gauge field. Each GGPEPS is called a *layer* and has an independent set of parameters. We start by describing the construction of a single layer and combine them in a second step.

CONSTRUCTION WITH A SINGLE LAYER

Products of local group element states define the configuration of gauge fields on the lattice. Such product states, $|\mathcal{G}\rangle = \otimes_\ell |q(\ell)\rangle$ with $\ell = (\mathbf{x}, i)$ form an orthonormal basis, and we use it to expand every state in the gauge field Hilbert space

$$|\psi\rangle = \sum_{\mathcal{G}} \psi(\mathcal{G})\, |\mathcal{G}\rangle \;, \tag{3.1}$$

where the sum runs over all possible gauge field configurations on the links and $\psi(\mathcal{G})$ is a gauge field dependent wave function of the configuration $\mathcal{G}$. This expression is a special case of the more general formulation presented in [158], where $\psi(\mathcal{G})$ can be a quantum state of the dynamical (fermionic) matter, $|\psi(\mathcal{G})\rangle$, instead of the wave function we have in the pure gauge case.

As described in section 2.2.1, not every state that can be expressed with eq. (3.1) is physically relevant, *i.e.* fulfills the local symmetry in eq. (2.45). Thus, the wave function $\psi(\mathcal{G})$ has to be chosen such that the full state $|\psi\rangle$ obeys the correct symmetries. Additionally, the state that we pick should allow for efficient numerical calculations of observables and gradients. Following the general construction in [158], we choose a gauged Gaussian projected entangled pair state (GGPEPS) as an ansatz. For details and further motivation, we refer to Refs. [6, 156].

Following the idea of the PEPS construction presented in section 2.1.2, we build the GGPEPS out of local constituents which help us to impose the symmetry. The local parts are entangled during the construction to form the final wave function. The elementary building blocks for the wave function are auxiliary (or virtual) fermionic modes that are attached to each leg of the vertices of the lattice. They are chosen to be fermionic to enable a consistent coupling to fermionic matter which obeys the correct statistics [158]. Although, for the description of a pure gauge theory, the coupling to matter is not necessary.

Before we construct the variational ansatz state in full detail, we give a general overview of the process. The construction of a GGPEPS consists of three essential parts (cf. fig. 3.1). First, the *fiducial operators* $\mathcal{A}(\mathbf{x})$ create virtual fermionic states with modes associated to each site. These fermionic states are constructed in a way that guarantees virtual gauge invariance. The virtual invariance is used in general PEPS constructions to impose global symmetries. This step of the construction can be readily extended to include more virtual fermions, in a similar spirit that the bond dimension of a PEPS can be increased. Details for a construction with multiple layers are given below. In a second step, some of the virtual modes on each site are rotated with respect to the physical gauge fields of the theory, in a particular way that lifts the virtual symmetries to physical ones [158]. This is done by gauging operators $\mathcal{U}_{\mathcal{G}}$ acting on the virtual fermions and controlled by the gauge field configuration. Finally, the pairs of virtual fermionic modes on the two sides of each link are projected onto maximally entangled states by projection operators ω_ℓ. That contracts the state from its local constituents and introduces correlations to the state.

The wave function can thus be written as

$$\psi(\mathcal{G}) = \langle \Omega_v | \prod_{\ell} \omega_\ell \prod_{\ell} \mathcal{U}_{\mathcal{G}}(\ell) \prod_{\mathbf{x}} \mathcal{A}(\mathbf{x}) \, |\Omega_v\rangle \, , \tag{3.2}$$

where the products are over all links ℓ of the lattice and $|\Omega_v\rangle$ is the fermionic Fock vacuum. In the following, we will treat the three main components of the construction $\mathcal{A}$, $\mathcal{U}_{\mathcal{G}}$, and ω in more detail, and see how to make sure that $\psi(\mathcal{G})$ obeys the right symmetry properties. Furthermore, we aim for a wave function that enables an efficient computation of norms and expectation values. We choose to pick a Gaussian formulation for $\psi(\mathcal{G})$, thus all its constituents must be Gaussian too.

After the intuitive overview of the full process, we describe the details in the following paragraphs. On each vertex $\mathbf{x}$ of the two-dimensional lattice, we define eight virtual fermionic modes, two associated to each leg – left, right, up and down. On each leg we label the two modes by $\pm$, and sort them into two groups: $a_i = \{l_+, r_-, u_-, d_+\}$ (which we call the negative modes) and $b_i = \{l_-, r_+, u_+, d_-\}$ (positive modes). The modes obey the Dirac anti-commutation relation $\{c(\mathbf{x}), c^\dagger(\mathbf{y})\} = \delta_{\mathbf{x},\mathbf{y}}$ and $\{c(\mathbf{x}), c(\mathbf{y})\} = \{c^\dagger(\mathbf{x}), c^\dagger(\mathbf{y})\} = 0$, where $\mathbf{x}, \mathbf{y}$ are vertices on the lattice and c is a fermionic mode.

We define the virtual electric fields

$$E_0(\mathbf{x}, k) = (-1)^{\mathbf{x}} (k_+^\dagger(\mathbf{x}) k_+(\mathbf{x}) + k_-^\dagger(\mathbf{x}) k_-(\mathbf{x})) \tag{3.3}$$

with $k \in \{r, l, u, d\}$ and the generator of the gauge transformation on the virtual degrees of freedom,

$$G_0(\mathbf{x}) = E_0(\mathbf{x}, r) + E_0(\mathbf{x}, u) - E_0(\mathbf{x}, l) - E_0(\mathbf{x}, d) \, . \tag{3.4}$$

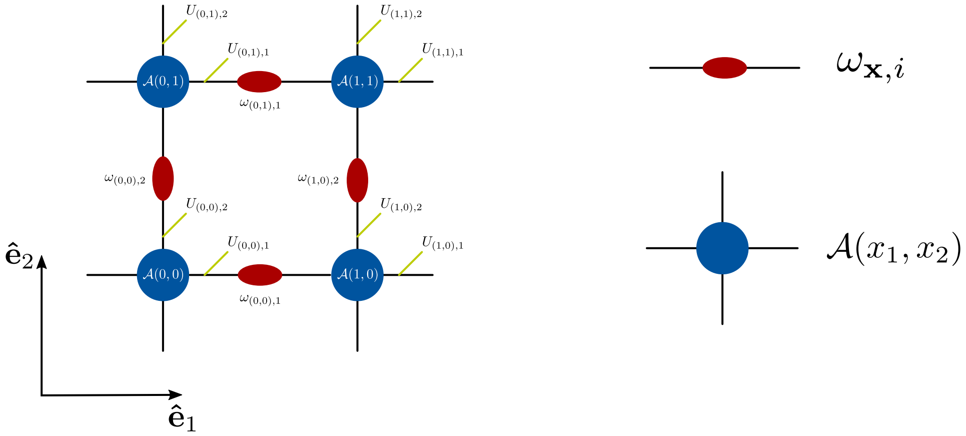

Figure 3.1: Illustration of the state's construction. The blue circles with four legs are created by the fiducial operator $\mathcal{A}$. The four black legs mark virtual modes in the different directions. The red ellipses between the virtual modes illustrate the unnormalized projectors ω. The gauge fields on the links between the sites are depicted as green lines. They couple to the respective virtual mode that the green line emanates from.

This can be seen as a version of a Gauss law operator: the divergence of the virtual electric fields at the vertex. The staggering is introduced to accommodate the general case with physical fermions [158] (aiming at the problem of physical fermion doubling [84] which we do not encounter in the pure gauge case). It is taken care of already on the level of electric fields [cf. eq. (3.3)] and thus the rest of the equations can be stated without explicit reference to staggering.

The fiducial operator $\mathcal{A}(\mathbf{x})$ creates the modes out of the vacuum and has to be Gaussian to ensure the Gaussian character of $\psi(\mathcal{G})$. Additionally, it must be invariant under transformation generated by $G_0(\mathbf{x})$. Hence, it is given by [6, 156]

$$\mathcal{A}(\mathbf{x}) = \exp\left(\sum_{ij} T_{ij} a_i^\dagger(\mathbf{x}) b_j^\dagger(\mathbf{x})\right), \tag{3.5}$$

where T_{ij} is a 4×4 matrix containing all parameters of the ansatz. $\mathcal{A}$ is a Gaussian operator by construction. It obeys the correct symmetry property since positive modes are only coupled to negative ones, thus

$$\exp(i\alpha G_0(\mathbf{x}))\mathcal{A}(\mathbf{x}) \exp(-i\alpha G_0(\mathbf{x})) = \mathcal{A}(\mathbf{x}) \tag{3.6}$$

is satisfied for every angle α, hence forming a $U(1)$ parameterization. As such, it contains also the $\mathbb{Z}_N$ cases, with a discrete choice of angles. Due to other symmetry considerations (*e.g.* lattice rotation invariance), only two independent parameters in T_{ij} of initially sixteen remain, y and z. They couple different modes in a given vertex: y couples right(up) and left(down) modes in a vertex, z couples modes that are building corners, *e.g.* right and up modes. The exact form of T and a motivation of the symmetries can be found in appendix 3.A.

For now, we will formulate the ansatz with eight virtual fermions per vertex. One set of eight virtual fermions is referred to as one *layer*. In a second step, we will enlarge the number of variational parameters by adding more layers, *i.e.* more virtual fermions to the links. Each layer gets an independent set of parameters y and z. Increasing the

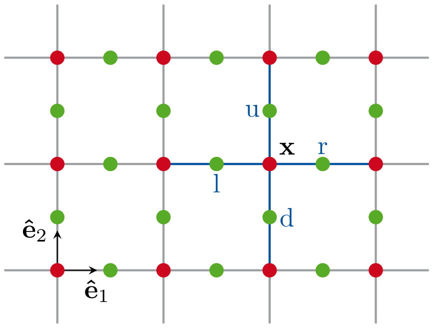

Figure 3.2: Arrangement of vertices and gauge fields in a lattice gauge theory. Vertices are indicated in red, gauge fields are shown in green. The convention for labeling links around a vertex **x** is indicated in blue.

number of layers is the analogue to increasing the virtual bond dimension in a non-fermionic PEPS.

In a second step, we entangle the virtual fermions on the links with physical gauge fields on the links. The gauging operator for a given gauge field configuration $\mathcal{G}$ takes the form

$$\mathcal{U}_{\mathcal{G}}\left(\ell\right) = \begin{cases} e^{i(-1)^{\mathbf{x}} q(\ell)\delta E_0(\mathbf{x},r)} & \ell \text{ horizontal} \\ e^{i(-1)^{\mathbf{x}} q(\ell)\delta E_0(\mathbf{x},u)} & \ell \text{ vertical}, \end{cases} \tag{3.7}$$

where $q(\ell)$ parameterizes the group element on the link ℓ in the configuration $\mathcal{G}$. The local gauge transformation changes only the modes in the up and right direction. Modifying the left and bottom modes as well would undo the gauge transformation due to the staggering. For a detailed overview of the gauging procedure in terms of PEPS operators, *i.e.* in graphical notation, we refer to Refs. [6, 49, 156].

In order to create more than a product state, we project the virtual, fermionic modes adjacent to each link onto maximally entangled states. The unnormalized projectors

$$\begin{aligned} \omega_{\mathbf{x},1} = & \exp\left(l_+^\dagger\left(\mathbf{x}+\hat{\mathbf{e}}_1\right) r_-^\dagger\left(\mathbf{x}\right) + l_-^\dagger\left(\mathbf{x}+\hat{\mathbf{e}}_1\right) r_+^\dagger\left(\mathbf{x}\right)\right) \Omega_\ell \times \\ & \times \exp\left(r_-\left(\mathbf{x}\right) l_+\left(\mathbf{x}+\hat{\mathbf{e}}_1\right) + r_+\left(\mathbf{x}\right) l_-\left(\mathbf{x}+\hat{\mathbf{e}}_1\right)\right) \end{aligned} \tag{3.8}$$

$$\begin{aligned} \omega_{\mathbf{x},2} = & \exp\left(u_+^\dagger\left(\mathbf{x}\right) d_-^\dagger\left(\mathbf{x}+\hat{\mathbf{e}}_2\right) + u_-^\dagger\left(\mathbf{x}\right) d_+^\dagger\left(\mathbf{x}+\hat{\mathbf{e}}_2\right)\right) \Omega_\ell \times \\ & \times \exp\left(d_-\left(\mathbf{x}+\hat{\mathbf{e}}_2\right) u_+\left(\mathbf{x}\right) + d_+\left(\mathbf{x}+\hat{\mathbf{e}}_2\right) u_-\left(\mathbf{x}\right)\right), \end{aligned} \tag{3.9}$$

connect the left(upper) and right(lower) modes of neighboring sites. Here, Ω_ℓ is the projector to the virtual vacuum on link ℓ and $\hat{\mathbf{e}}_i$ is the unit vector in direction i. Similar to the fiducial operators $\mathcal{A}$, the projectors ω are Gaussian and commute among each other since they are products of fermionic modes on different links. The projectors link the virtual modes of one site with the virtual modes of the next site in the horizontal and the vertical direction, respectively. It is essential that the projectors are unnormalized since the norm of a state will serve as a transition probability between different gauge field configurations in the Monte Carlo algorithm.

Combining $\mathcal{A}$, ω, and $\mathcal{U}_{\mathcal{G}}$, we get the wave function in eq. (3.2). Now, we can show that the construction is indeed gauge invariant and fulfills eq. (2.47). We act with

$\Theta(\mathbf{x})$ on $|\psi\rangle$ explicitly, on some given vertex $\mathbf{x}$:

$$
\begin{aligned}
\Theta(\mathbf{x})\,|\psi\rangle &= \sum_{\mathcal{G}} \psi(\mathcal{G}) P_{\mathbf{x},u} P_{\mathbf{x},r} P^{\dagger}_{\mathbf{x}-\hat{\mathbf{e}}_1,r} P^{\dagger}_{\mathbf{x}-\hat{\mathbf{e}}_2,u}\,|\mathcal{G}\rangle \\
&= \sum_{\mathcal{G}} \psi(\mathcal{G})\,|q(\ell_1)-1, q(\ell_2)-1, q(\ell_3)+1, q(\ell_4)+1\rangle \otimes |\tilde{q}\rangle \\
&= \sum_{\mathcal{G}} \psi(\underbrace{q(\ell_1)+1, q(\ell_2)+1, q(\ell_3)-1, q(\ell_4)-1, \tilde{q}}_{\equiv \mathcal{G}'})\,|\mathcal{G}\rangle\,,
\end{aligned}
\tag{3.10}
$$

where $\tilde{q}$ are all gauge fields that are not affected by the gauge transformation, *i.e.* that are not adjacent to $\mathbf{x}$. To shorten notation, we named the different links according to the labels defined in the left panel of fig. 3.2. The third line is linked to the second one by a change of variables in q. The gauge invariance holds if $\psi(\mathcal{G}) = \psi(\mathcal{G}')$. We can write the wave function $\psi(\mathcal{G}')$ as

$$
\begin{aligned}
\psi(\mathcal{G}') =& \langle \Omega_v| \prod_{\ell} \omega_\ell \prod_{\tilde{\ell}} \mathcal{U}_{\mathcal{G}}(\tilde{\ell}) e^{\pm i\delta(q_1+1)E_0(\mathbf{x},r)} e^{\pm i\delta(q_2+1)E_0(\mathbf{x},u)} e^{\mp i\delta(q_3-1)E_0(\mathbf{x}-\hat{\mathbf{e}}_1,r)} \\
& \qquad e^{\mp i\delta(q_4-1)E_0(\mathbf{x}-\hat{\mathbf{e}}_2,u)} \prod_{\mathbf{x}} \mathcal{A}(\mathbf{x})\,|\Omega_v\rangle \\
=& \langle \Omega_v| \prod_{\ell} \omega_\ell \prod_{\tilde{\ell}} \mathcal{U}_{\mathcal{G}}(\tilde{\ell}) e^{\pm i\delta(E_0(\mathbf{x},r)+E_0(\mathbf{x},u)-E_0(\mathbf{x},l)-E_0(\mathbf{x},d))} \prod_{\mathbf{x}} \mathcal{A}(\mathbf{x})\,|\Omega_v\rangle \\
=& \psi(\mathcal{G})\,,
\end{aligned}
\tag{3.11}
$$

where $\tilde{\ell}$ are all links that are unaffected by the gauge transformation and Ω_v is the vacuum of all virtual modes. The notation of multiple signs shows the transformation for an even (top sign) and an odd (bottom sign) vertex at the same time. We used the invariance of the fiducial operator (3.6) in the last line. In order to transform the virtual electric field from the adjacent vertices $\mathbf{x}-\hat{\mathbf{e}}_1$ and $\mathbf{x}-\hat{\mathbf{e}}_2$ to vertex $\mathbf{x}$, we use the invariance of the projectors ω:

$$
\begin{aligned}
\omega_{\mathbf{x}-\hat{\mathbf{e}}_1,1} e^{i\delta E_0(\mathbf{x}-\hat{\mathbf{e}}_1,r)} &= \omega_{\mathbf{x}-\hat{\mathbf{e}}_1,1} e^{-i\delta E_0(\mathbf{x},l)} \\
\omega_{\mathbf{x}-\hat{\mathbf{e}}_2,2} e^{i\delta E_0(\mathbf{x}-\hat{\mathbf{e}}_2,u)} &= \omega_{\mathbf{x}-\hat{\mathbf{e}}_2,2} e^{-i\delta E_0(\mathbf{x},d)}\,.
\end{aligned}
\tag{3.12}
$$

All operators employed in the construction ($\mathcal{A}$, ω, and $\mathcal{U}_{\mathcal{G}}$) are Gaussian operators. Since products of Gaussian operators are Gaussian [169], the wave function $\psi(\mathcal{G})$ can be efficiently described with covariance matrices. As detailed in [158], there are multiple ways of combining the operators to covariance matrices. We choose to group the gauging operators and the projectors together into $\Gamma_{\mathrm{in}}(\mathcal{G})$, a covariance matrix that depends on the gauge. The fiducial operators are summarized in a second covariance matrix D. The relation between the covariance matrices and the gauged ansatz state can be summarized as

$$
\psi(\mathcal{G}) = \underbrace{\langle \Omega_v| \prod_{\mathbf{x}} \omega(\mathbf{x}) \prod_{\ell} \mathcal{U}_{G(\ell)}}_{\Gamma_{\mathrm{in}}(\mathcal{G})} \underbrace{\prod_{\mathbf{x}} \mathcal{A}(\mathbf{x})\,|\Omega_v\rangle}_{D}\,.
\tag{3.13}
$$

For further details about the formulation of Gaussian operators in terms of covariance matrices, we refer to appendix 3.C. The covariance matrices or parts of them allow the efficient calculation of the Monte Carlo transition probability [cf. eq. (3.18)].

CONSTRUCTION WITH MULTIPLE LAYERS

Although the ansatz wave function with a single layer, *i.e.* two variational parameters, captures the high coupling regime very well, the low coupling regime is challenging for a single layer (cf. fig. 3.4). Upon increasing the number of layers, the agreement between exact diagonalization data and the variational PEPS approach improves dramatically. In order to increase the number of variational parameters, we add more virtual fermions to the construction. Each layer carries an independent set of parameters, *i.e.* the matrix T in the fiducial operator $\mathcal{A}$ is different for each layer, while the states are coupled to the same gauge field. This ensures that all states fulfill the Gauss law. The virtual fermions of different layers on the links do not interact. The complexity of the computation scales linearly in the number of layers because the state can be contracted as independent layers of equally sized PEPS. Further details about the contraction and the changes to the calculation of observables are explained in appendix 3.B.

3.3.2 COMPUTATIONAL EVALUATION

The ansatz defined above characterizes a family of states that depends on two parameters per layer. In order to find the ground state of the Hamiltonian (2.43) for $N = 3$, we have to adapt the parameters such that the energy is minimized. By computing expectation values of observables and gradients with respect to the parameters via sampling, we circumvent the unfavorable scaling of PEPS contractions. The variational Monte Carlo technique works in a two-step procedure: first, the energy and the gradients are sampled for a given set of parameters α. In the second step, the parameters are changed $\alpha \to \alpha'$ according to the gradients and a minimization algorithm.

CALCULATION OF EXPECTATION VALUES

The Hamiltonian (2.43) consists of two terms, the electric energy and the magnetic energy. Due to translational invariance of the states and the Hamiltonian, it is sufficient to calculate the energy of a single plaquette and a single link,

$$\langle H \rangle = n_{\text{links}} \left(2 - \left\langle P_\ell + P_\ell^\dagger \right\rangle\right) + n_{\text{plaq}} \left(2 - \left\langle Q_{p_1} Q_{p_2} Q_{p_3}^\dagger Q_{p_4}^\dagger + \text{H.c.} \right\rangle\right) , \tag{3.14}$$

where $n_{\text{plaq}} = L^2$, $n_{\text{links}} = 2n_{\text{plaq}}$ and L is the linear extent of the quadratic lattice (number of vertices). In the equation above, ℓ is a freely chosen link. If not stated otherwise, we choose the link at $\mathbf{x} = 0$ in the horizontal direction. Calculating the magnetic energy is a special case of the expectation value of a Wilson loop. The Wilson loop operator is defined as

$$W(R_1, R_2) = \prod_{\ell \in C} Q_\ell , \tag{3.15}$$

where C is an oriented, rectangular curve of length R_1 in the horizontal and R_2 in the vertical direction. The operator Q_ℓ is picked as is or daggered according to whether the link is traversed in the direction of the blue arrows (cf. fig. 3.3) or against them. The Wilson loop operator does not only play a role for the calculation of the energy, but can be used as an indicator for confinement in the theory (cf. section 3.4). Given

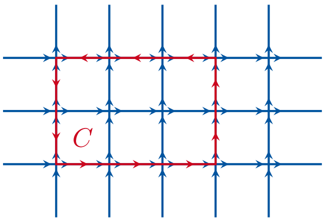

Figure 3.3: Illustration of a Wilson loop. The operator Q_ℓ is chosen as is if the red path follows the direction of the blue arrows and daggered if it traverses the blue arrows in the opposite direction.

the state defined in eq. (3.1), the expectation value of a Wilson loop is

$$\begin{aligned}\langle W(R_1,R_2)\rangle &= \sum_{\mathcal{G}} \mathcal{F}_{W(R_1,R_2)}(\mathcal{G})p(\mathcal{G}) \\ &= \left\langle \mathcal{F}_{W(R_1,R_2)} \right\rangle_{\mathrm{MC}} ,\end{aligned} \tag{3.16}$$

where the estimator $\mathcal{F}_{W(R_1,R_2)} = \prod_{\ell\in C} \exp(\pm i\phi(\ell))$ is a complex number and the sampling probability is

$$p(\mathcal{G}) = \frac{|\psi(\mathcal{G})|^2}{\sum_{\mathcal{G}'} |\psi(\mathcal{G}')|^2} . \tag{3.17}$$

While the expression $\langle\cdot\rangle$ is the expectation value of an operator, the expression $\langle\cdot\rangle_{\mathrm{MC}}$ is a $p(\mathcal{G})$-weighted average over complex numbers. Since the norm of a state is always real and larger than zero, this formulation of a Monte Carlo procedure cannot suffer from the sign problem.

The Monte Carlo procedure requires a transition probability between different configuration states of the gauge field. In our case, this is the squared norm of the state. While the norm of a PEPS is a difficult quantity to compute in the general case, the Gaussian nature of $\psi(\mathcal{G})$ enables the efficient computation. Using the covariance matrices defined in eq. (3.13) for Majorana fermions (cf. appendix 3.C), we can write the squared norm of the wave function as a determinant

$$|\psi(\mathcal{G})|^2 = \sqrt{\det\left(\frac{1 - \Gamma_{\mathrm{in}}(\mathcal{G})D}{2}\right)} . \tag{3.18}$$

In our Monte Carlo scheme, we use the Metropolis algorithm [14] with eq. (3.17) as a transition probability. In each step, one gauge field is randomly selected and updated according to the transition probability. The gauge field is initialized with state $|0\rangle$ everywhere and warmed up without measurements for a fixed number of iterations. After the warm-up phase, each iteration includes a measurement of the observables.

In contrast to the magnetic energy, the electric energy is not diagonal in the gauge field basis. Instead of evaluating the full electric energy H_E, we focus on the expectation value $\langle P_\ell\rangle$. P_ℓ acts as a lowering operator on the gauge field states. Thus, we have to evaluate an expression that has a modified gauge field on one link. We can transfer that modification to the covariance matrices by evaluating the integrals in Grassmann variables directly. The estimator for $\langle P_\ell\rangle$ in a $\mathbb{Z}_3$ gauge theory is

$$\mathcal{F}_{\mathrm{el}}(G) = \frac{1}{4}\frac{\mathrm{Pf}\left(\tilde{\Gamma}_{\mathrm{in}} - D^{-1}\right)}{\sqrt{\det\left(D^{-1} - \Gamma_{\mathrm{in}}\right)}} , \tag{3.19}$$

where $\tilde{\Gamma}_{\text{in}}$ is a modified version of Γ_{in} that differs from the original one on a single link ℓ. Further details about the calculation are provided in appendix 3.D.

EVALUATION OF GRADIENTS

The evaluation of gradients with respect to the parameters in T enables the efficient minimization of observables. Instead of directly tracking the derivative of the parameters through the state construction, we derive the matrix equations obtained for the covariance matrices with respect to the variational parameters. The covariance matrix of the fiducial state D does not change during the Monte Carlo computation, and it is the only covariance matrix that contains variational parameters $\alpha \in \{y, z\}$. Thus, we can calculate the gradient for an arbitrary observable O whose estimator $\mathcal{F}_O(D)$ can depend on the covariance matrix D of the fiducial operator explicitly

$$\begin{aligned}\frac{\partial}{\partial\alpha}\langle O\rangle =& \frac{\partial}{\partial\alpha}\langle\mathcal{F}_O(D)\rangle_{\text{MC}} \\ =& \left\langle\frac{\partial}{\partial\alpha}\mathcal{F}_O(D)\right\rangle_{\text{MC}} + \left\langle\mathcal{F}_O(D)\frac{\frac{\partial}{\partial\alpha}|\psi(\mathcal{G})|^2}{|\psi(\mathcal{G})|^2}\right\rangle_{\text{MC}} \\ &- \langle\mathcal{F}_O(D)\rangle_{\text{MC}}\left\langle\frac{\frac{\partial}{\partial\alpha}|\psi(\mathcal{G})|^2}{|\psi(\mathcal{G})|^2}\right\rangle_{\text{MC}} .\end{aligned} \tag{3.20}$$

Since we aim to find the best ground state approximation with our ansatz, we calculate the gradients of the energy. They consist of two parts, the gradient of the magnetic and the gradient of the electric energy. In the case of the magnetic energy, the first term on the right-hand side of eq. (3.20) vanishes since the gauge field has no explicit dependence on the parameters. It remains to calculate the expression $\frac{\partial}{\partial\alpha}|\psi(\mathcal{G})|^2$ since we know the form of $|\psi(\mathcal{G})|^2$ from the evaluation of the transition probability (3.17) already. Using Jacobi's formula

$$\frac{\mathrm{d}}{\mathrm{d}\alpha}\det A(\alpha) = \operatorname{Tr}\left(\operatorname{Adj}(A(\alpha))\frac{\mathrm{d}A(\alpha)}{\mathrm{d}\alpha}\right), \tag{3.21}$$

we obtain

$$\begin{aligned}\frac{\partial}{\partial\alpha}|\psi(\mathcal{G})|^2 &= \frac{\partial}{\partial\alpha}\sqrt{\det\left(\frac{1-\Gamma_{\text{in}}(\mathcal{G})D}{2}\right)} \\ &= -\frac{1}{2^{N+1}}\sqrt{\det(1-\Gamma_{\text{in}}(\mathcal{G})D)}\operatorname{Tr}\left(\Gamma_{\text{in}}(\mathcal{G})\frac{\partial D}{\partial\alpha}^{-1}\right).\end{aligned} \tag{3.22}$$

Combining eq. (3.18) and eq. (3.22), we find

$$\begin{aligned}\frac{\frac{\partial}{\partial\alpha}|\psi(\mathcal{G})|^2}{|\psi(\mathcal{G})|^2} &= \frac{\frac{\partial}{\partial\alpha}|\psi(\mathcal{G})|^2}{\sqrt{\det\left(\frac{1-\Gamma_{\text{in}}(\mathcal{G})D}{2}\right)}} \\ &= -\frac{1}{2}\operatorname{Tr}\left(\Gamma_{\text{in}}(\mathcal{G})\frac{\partial D}{\partial\alpha}(1-\Gamma_{\text{in}}(\mathcal{G})D)^{-1}\right),\end{aligned} \tag{3.23}$$

where $\frac{\partial D}{\partial \alpha}$ is the explicit derivative of the covariance matrix of the virtual modes with respect to parameter α. This expression can be derived analytically.

In contrast to the magnetic energy, the electric energy depends explicitly on the parameters of the ansatz. Thus, the first term on the right-hand side of eq. (3.20) does not vanish. The explicit form of the gradient is stated in appendix 3.D.

VARIATIONAL MINIMIZATION

For small systems ($L = 2$), we can substitute the Monte Carlo step with an exact contraction (EC) of the PEPS. Each possible gauge field configuration on the lattice is sampled and the individual contributions of the different states are summed up. For the $L = 2$ lattice, there are 8 links and thus $3^8 = 6561$ possible gauge field states. In the case of exact calculations of the gradients and observables, we used the Broyden-Fletcher-Goldfarb-Shanno (BFGS) algorithm [170] to adapt the parameters of the state. If the gradients and the observables are calculated with Monte Carlo sampling, the inherent error of the estimates makes the use of a line search based algorithm like BFGS difficult. The fluctuations of the estimate lead to inconsistencies during the line-search which cause the termination of the algorithm. Thus, we decided to work with a simple gradient descent algorithm if the expectation values are estimated with Monte Carlo. After estimating the energy and the gradients, we adapt the set of parameters in the opposite direction of the gradient,

$$\alpha' = \alpha - \xi(i) \frac{\partial \langle H \rangle}{\partial \alpha}, \tag{3.24}$$

where $\xi(i)$ is the weight for the gradient in dependence of the step. We used $\xi(i) = 0.01 \cdot 0.99^i$ in our simulation. The choice of parameters and the schedule of $\xi(i)$ may be further optimized.

3.4 RESULTS

Applying the ansatz developed in Ref. [158] to a physical Hamiltonian, we want to ensure that we are able to capture relevant physics despite the small number of parameters of the states. In particular, our goal is to demonstrate that a higher number of layers leads to an improved expressibility.

As a first step, we compare to a small system with $L = 2$, *i.e.* four plaquettes, which can be solved with exact diagonalization (cf. fig. 3.4). Due to the small lattice size, we can contract the GGPEPS exactly by summing over all configurations of the gauge field explicitly. Since we do not use Monte Carlo, we can separate the statistical errors from the Monte Carlo simulation from the expressibility problems of the state. A mismatch in energy after exact contraction must be a problem of the state. Figure 3.4 and the inset therein show good agreement for states at high couplings where the electric energy is the dominant contribution in the Hamiltonian (2.43). The ground state of the electric Hamiltonian is the state with no electric excitations, *i.e.* the electric field is zero on all links. We expect to approximate it well because it is the state that we obtain if the operator $\mathcal{A}$ is equal to the identity. This happens if both parameters $y = z = 0$: $T(y = 0, z = 0) = \mathbb{1}$. We observed that the values of y and z indeed approach zero as the coupling increases.

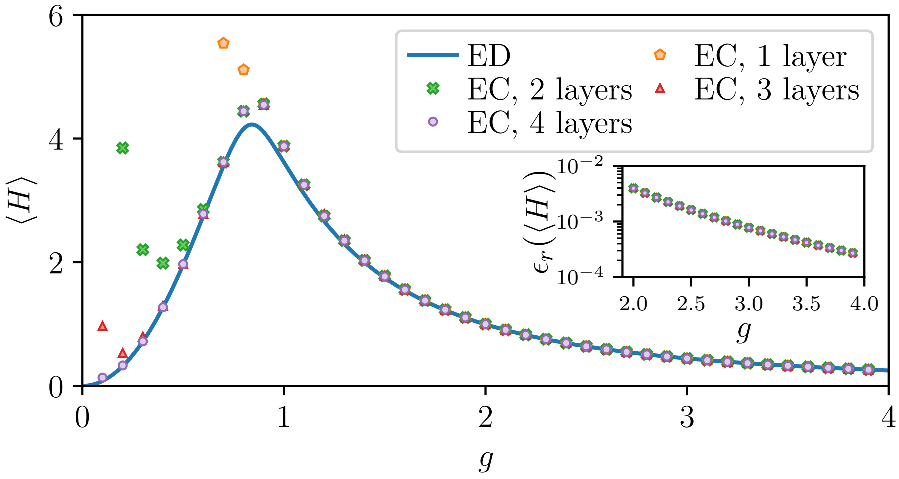

Figure 3.4: Convergence of the energy for an $L = 2$ system. The solid blue line is the exact diagonalization (ED) result. The colored dots are exact contractions (EC) of the ansatz state with varying number of layers of virtual fermions on the links. The inset displays the relative error ϵ_r of the energy with respect to the exact diagonalization results at high coupling.

While the high coupling regime matches well to the exact values, the low coupling regime, which is dominated by the magnetic energy, is more challenging. States with few layers show a divergent behavior at low couplings. The quadratic divergence is caused by a lack of expressibility of states with few layers: The parameters approach a constant for low coupling and the $1/g^2$ term in the Hamiltonian leads to the divergence. An increase in the number of layers helps to systematically improve the states while only linearly affecting the run-time.

The error around the transition $g \approx 1$ does not decrease when additional layers are used. We attribute this behavior to the specific ansatz that we are using. We do not expect a Gaussian PEPS based ansatz to hold at criticality.

Figure 3.5 shows the energy density of the system for different lattice sizes for three layers of the parameters. Due to the larger system sizes, we cannot contract the GGPEPS exactly. The Monte Carlo estimation uses 10^4 steps for the warm-up phase that is performed without measurement and 10^5 steps for the sampling. Since the Monte Carlo simulation has to be performed for each variational minimization step, the number of Monte Carlo steps with measurements is kept rather small. Especially the calculation of the electric energy, which features a Pfaffian, is expensive.

The estimates agree very well with the ED data for an $L = 2$ system over a large range of the coupling. The deviations at the phase transition due to the ansatz as described above. The deviation at very low coupling for large system sizes originates from the fact that the minimization becomes increasingly costly. Especially the calculation of the Pfaffian in the electric energy is computationally expensive. While all determinants that appear in the calculation of norms can be calculated by updating previous results if the gauge field is changed, the Pfaffian has to be recalculated in every step. The Pfaffian is the single most expensive step in the algorithm. Since we are plotting the energy density in relation to an $L = 2$ system, deviations can be either finite size effects (in which case the MC points would be more correct than ED) or errors due to the Monte Carlo sampling procedure.

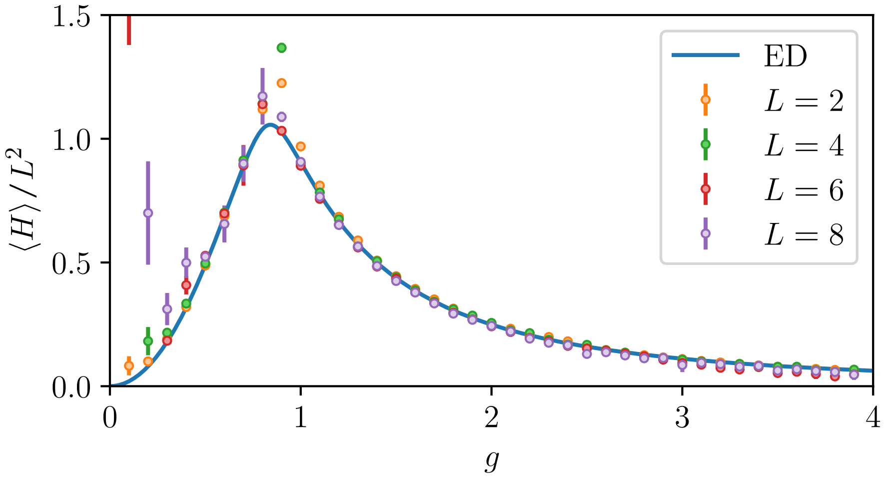

Figure 3.5: Finite size effects for different system sizes. The blue line is the exact data for an $L = 2$ system. All data points are computed with VMC for different system sizes using with three layers in the construction of the state.

Following previous works, we expect the theory to have two phases [86, 94]. According to Elitzur's theorem [171], the expectation value of any operator that is not gauge invariant will vanish, and thus a local order parameter is ruled out. Instead, following Wegner and Wilson [66, 70], we can analyze the correlation in the different phases by studying the Wilson loop. The corresponding operator is gauge invariant and shows different scaling in the different phases of $\mathbb{Z}_N$ theories. In the low-coupling regime, which is dominated by the magnetic part H_B of the Hamiltonian, the expectation value of the Wilson loop follows a perimeter law which, to the lowest order in perturbation theory [86], reads

$$\langle W(R_1, R_2)\rangle \sim \exp\big(-\kappa_p 2(R_1 + R_2)\big)\,. \tag{3.25}$$

Here, κ_p is a constant and $2(R_1 + R_2)$ is the perimeter of the Wilson loop. The scaling changes in the high coupling regime, where the electric energy is the dominant contribution to the total energy and the Wilson loop operator scales with the area of the curve. The area scaling reads to the lowest order in perturbation theory [86],

$$\langle W(R_1, R_2)\rangle \sim \exp(-\sigma R_1 R_2)\ , \tag{3.26}$$

where σ is the string tension. Since the potential of static charges, *i.e.* charges that are not dynamically coupled to the gauge fields in the Hamiltonian, increases linearly with the distance in this phase, it costs an infinite amount of energy to separate two static charges. The two static charges are confined.

We can use the states that we obtained using the VMC procedure for an $L = 6$ lattice to evaluate the scaling behavior in the different regimes (cf. fig. 3.6). Here, we used three layers in the minimization. The Wilson loop expectation values are recomputed for the minimal parameters with 10^4 warm-up steps and 10^6 sampling steps. By fitting eq. (3.26) to different Wilson loops $W(R_1, R_2)$ of a maximal size of $L/2$ and $|R_1 - R_2| < 1$, we can obtain the string tension of the states. The result of the fits for different couplings is shown in fig. 3.6. The $\mathbb{Z}_3$ gauge theory can be mapped to a three state Potts model [78] and the first order phase transition has been studied with Monte

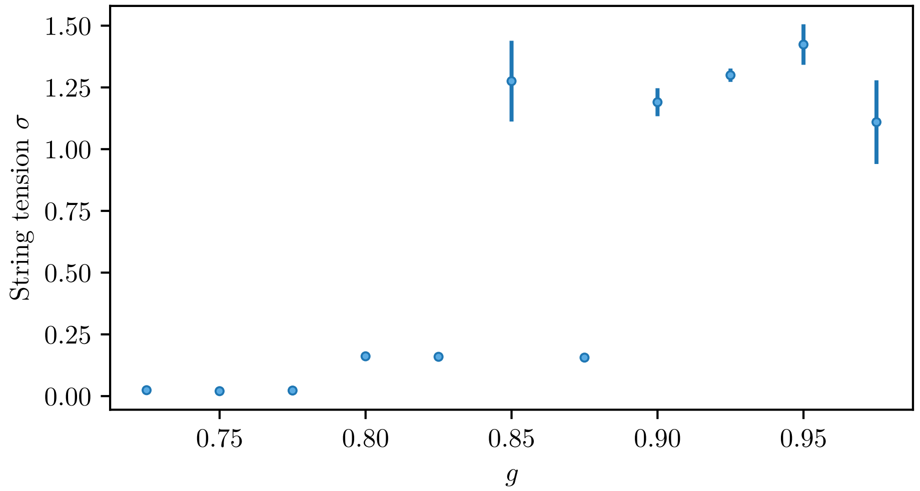

Figure 3.6: String tension for different value of the coupling. The string tension is extracted by fitting the area law expectation to Wilson loops of different size. The state is constructed with three layers of virtual fermions.

Carlo [165]. The plot shows that the string tension is almost zero in the low-coupling phase and rises to a finite value in the high-coupling, confining phase. Around the transition region, the minimization becomes difficult due to the ansatz we are using. Thus, results in direct vicinity to the transition region might not be obtained for the ground state and one has to be careful to use them for an interpretation of confining or non-confining behavior [172]. The range of accessible couplings is limited from above since the Wilson loop decays exponentially with size and coupling. The Monte Carlo procedure cannot reliably resolve the expectation value of the Wilson loop in the high coupling regime.

3.5 Discussion

We show that GGPEPS are promising ansatz states for $\mathbb{Z}_N$ lattice gauge theories in two spatial dimensions. Since the transition probability between two configurations of the gauge field is given by the squared norm of a state, the sign problem is avoided. The norm as well as the gradients for a given set of parameters can be efficiently computed with the covariance matrix formalism leading to a scalable algorithm.

By contracting small systems exactly we show that the states themselves capture the relevant physics well, although they are based only on a few parameters. We demonstrate a systematic improvement of the energy by increasing the number of virtual fermions on the links while impacting the run-time only linearly.

The variational optimization with Monte Carlo is very successful for large couplings, but gets increasingly difficult for smaller couplings and larger lattices. In this regime, the states have to approximate states dominated by the magnetic interaction in the Hamiltonian. Since the ansatz is based on the electric vacuum on the links, this regime is challenging. Additionally, larger lattices lead to higher run-times, especially in the calculation of the Pfaffian in the electric energy.

We expect to be able to improve the results of the Monte Carlo simulation further by changing to a more advanced sampling scheme. Currently, the algorithm updates only one gauge field at a time, which leads to a smaller relative change if the system size increases. The usage of collective cluster updates [173, 174] or hybrid Monte Carlo techniques [15] may lead to better convergence.

Additionally, the ansatz introduced in Ref. [158] allows for static charges and dynamic fermions. The introduction of static charges allows to measure the string tension directly as an observable between two opposite charges and leads to another measure of confinement which is especially beneficial at large couplings. Simulating dynamic fermions presents the interesting possibility to study the behavior of mesonic strings.

Finally, the optimization in the weak coupling regime could be improved by starting from a different initial state on the links. If the state on the links is more suited for the magnetic Hamiltonian, the physics of the magnetic phase might be easier to capture with fewer layers.

APPENDIX

3.A DERIVATION OF T

The fiducial operator (3.5) used in the GGPEPS construction (3.2) determines the symmetries of the state $|\psi\rangle$. We demand rotational invariance by $\pi/2$, translational invariance when shifting by two sites due to the staggering and charge conjugation invariance if we shift by one site. Since the parameterization was originally developed to accommodate a $U(1)$ gauge theory [156], the formulation obeys, additionally, a global $U(1)$ symmetry. Here, we state only the result

$$T = \begin{pmatrix} 0 & y & z/\sqrt{2} & z/\sqrt{2} \\ -y & 0 & -z/\sqrt{2} & z/\sqrt{2} \\ -z/\sqrt{2} & z/\sqrt{2} & 0 & y \\ -z/\sqrt{2} & -z/\sqrt{2} & -y & 0 \end{pmatrix}, \tag{3.27}$$

with $y, z \in \mathbb{C}$. y and z are the only two independent parameters that remain. The matrix is given in the mode order $\{l, r, u, d\}$. The rows correspond to the modes $\{l_+, r_-, u_-, d_+\}$, and the columns to $\{l_-, r_+, u_+, d_-\}$. In this work, we restrict ourselves to $y, z \in \mathbb{R}$.

3.B FORMALISM WITH MULTIPLE LAYERS

We achieve a higher expressibility of the ansatz states by increasing the number of virtual fermions on the links. Different layers of virtual fermions do not interact with each other and have independent sets of parameters $y^{(i)}$ and $z^{(i)}$, where i is the index of the layer. Each layer can be seen as an independent PEPS coupled to the same gauge field. Since the layers are independent, the norm of the state $|\psi\rangle$ is the product of the norms of its layers $|\psi_i\rangle$:

$$\langle\psi|\psi\rangle = \prod_i \langle\psi_i|\psi_i\rangle \,, \tag{3.28}$$

where i is the index of the layer and runs from 1 to the number of layers. This construction leads to a linear scaling with the bond dimension. The matrix size of the covariance matrices stays unchanged because we do not add the parameters to the T matrix. Instead, we consider multiple covariance matrices generated by different parameter matrices T_i. Thus, we have to perform parts of the calculation multiple times with varying covariance matrices of the same size.

Since we layer only the virtual fermions, the computation of diagonal observables in the gauge field does not change. Observables like the electric energy, however, need more consideration. Due to the product structure of the ansatz state, we can write the estimator of the electric energy as a product $\mathcal{F}_{\text{el}} = \prod_i \mathcal{F}_{\text{el}}^{(i)}$, where i is again the index of the layer. Each $\mathcal{F}_{\mathrm{el}}^{(i)}$ involves only the covariance matrices of layer i and can be calculated with eq. (3.40).

Finally, the gradients for the squared norm and the explicit derivative of the electric energy have to be adapted. The derivative of the squared norm enters the equations only as a fraction of the squared norm [cf. eq. (3.20)], we only have to adapt the expression

$$\begin{aligned}\frac{\frac{\partial}{\partial\alpha_i}\prod_j\left\langle\psi_j(\mathcal{G})\middle|\psi_j(\mathcal{G})\right\rangle}{\prod_j\left\langle\psi_j(\mathcal{G})\middle|\psi_j(\mathcal{G})\right\rangle} &= \frac{\sum_i\prod_{i\neq j}\left\langle\psi_j(\mathcal{G})\middle|\psi_j(\mathcal{G})\right\rangle\frac{\partial}{\partial\alpha_i}\left\langle\psi_i(\mathcal{G})\middle|\psi_i(\mathcal{G})\right\rangle}{\prod_j\left\langle\psi_j(\mathcal{G})\middle|\psi_j(\mathcal{G})\right\rangle} \\ &= \frac{\frac{\partial}{\partial\alpha_i}\left\langle\psi_i(\mathcal{G})\middle|\psi_i(\mathcal{G})\right\rangle}{\left\langle\psi_i(\mathcal{G})\middle|\psi_i(\mathcal{G})\right\rangle}\,.\end{aligned} \tag{3.29}$$

Here, we move the derivative with respect to parameter $\alpha_i \in \{y, z\}$ of layer i to the respective layer i since all other parameters are independent of α_i.

The gradient of the electric energy is adapted similarly because the derivative acts only on one of the layers.

3.C GAUSSIAN FORMALISM

Given a Dirac mode c, we can construct the corresponding Majorana operators $\gamma^{(1)}$ and $\gamma^{(2)}$ as

$$\begin{aligned}\gamma^{(1)} &= c + c^{\dagger} \\ \gamma^{(2)} &= i(c - c^{\dagger})\,.\end{aligned} \tag{3.30}$$

The Majorana modes obey the anti-commutation relation $\{\gamma_a, \gamma_b\} = 2\delta_{a,b}$. The construction in eq. (3.2) uses only Gaussian operators, thus, we can formulate it in terms of covariance matrices. We define the covariance matrix of a Gaussian state $|\Phi\rangle$ in terms of Majorana modes as

$$\Gamma_{a,b} = \frac{i}{2}\langle[\gamma_a, \gamma_b]\rangle = \frac{i}{2}\frac{\langle\Phi|\,[\gamma_a, \gamma_b]\,|\Phi\rangle}{\langle\Phi|\Phi\rangle}\,. \tag{3.31}$$

The construction of the Gaussian state is divided into two covariance matrices. We separate the covariance matrix of the fiducial operators D from the covariance matrix of the gauged projectors $\Gamma_{\mathrm{in}}(\mathcal{G})$. This allows us to calculate the squared norm of the state with eq. (3.32). During one Monte Carlo simulation, D stays constant and can be calculated during the initialization. Changing the gauge field value on a link only alters $\Gamma_{\mathrm{in}}(\mathcal{G})$. We refer to Ref. [158] for more details on the Gaussian mapping.

In order to calculate the squared norm of the wave function, we use the following identities [169]:

$$\begin{aligned}&\int D\theta \exp\left(\frac{i}{2}\theta^T M\theta\right) = i^n\,\mathrm{Pf}\,(M) \\ &\int D\theta \exp\left(\eta^T\theta + \frac{i}{2}\theta^T M\theta\right) = i^n\,\mathrm{Pf}\,(M)\exp\left(-\frac{i}{2}\eta^T M^{-1}\eta\right) \\ &\mathrm{Tr}(XY) = (-2)^n\int D\theta D\mu e^{\theta^T\mu}[X]_{G,\theta}[Y]_{G,\mu}\,,\end{aligned} \tag{3.32}$$

where M is a complex antisymmetric $2n\times 2n$ matrix and $[X]_{G,\theta}$ is the Grassmann representation of the operator X in terms of Grassmann variables θ. Equation (3.18) follows directly from eq. (3.32).

3.D CALCULATION OF THE ELECTRIC ENERGY AND ITS GRADIENT FOR Z_N

Since the electric energy is not diagonal in the group element basis, we cannot use the equivalent of eq. (3.16) directly. We have to consider the computation of expectation values for the electric energy more carefully.

3.D.1 CALCULATION OF THE EXPECTATION VALUE OF THE ELECTRIC ENERGY

Due to the translational invariance of the states and the Hamiltonian, it is sufficient to calculate the expectation value of the electric energy over one link ℓ. The notation for $\psi(\mathcal{G})$ introduced in eq. (3.2) is changed to distinguish between the group element q on link ℓ and all other group elements G to $\psi(q, G)$. In the following, we focus on the calculation of the expectation value $\langle P_\ell \rangle$; the extension to $\left\langle P_\ell + P_\ell^\dagger \right\rangle$ which appears in the Hamiltonian (2.43) follows directly by complex conjugation. Since we are only considering a single, fixed link for the rest of the calculation, we drop the index ℓ:

$$\begin{aligned}
\langle P \rangle &= \frac{\langle \psi | P | \psi \rangle}{\langle \psi | \psi \rangle} \\
&= \sum_{q,q',G} \langle q' | P | q \rangle \frac{\psi^*(G, q')\psi(G, q)}{|\psi(\mathcal{G})|^2} p(G, q) \\
&= \sum_{q,G} \frac{\psi^*(G, q-1)\psi(G, q)}{|\psi(\mathcal{G})|^2} p(G, q) \\
&= \sum_{q,G} \mathcal{F}_{\text{el}}(G, q) p(G, q) \,,
\end{aligned} \tag{3.33}$$

where $\mathcal{F}_{\text{el}}(G)$ is the Monte Carlo estimator of the electric energy. From the second line to the third line we use that P acts as a lowering operator on the gauge field states. The remaining expression is the product of two wave functions that differ in terms of the gauge field on one link. Using the explicit formulation of the state, we obtain [product symbols as in eq. (3.2)]

$$\begin{aligned}
\psi^*(G, q')\psi(G, q) &= \langle \Omega_\nu | \mathcal{A}^\dagger \mathcal{U}^\dagger_{(q',G)} \omega \mathcal{U}_{(q,G)} \mathcal{A} | \Omega_\nu \rangle \\
&= \langle \Omega_\nu | \mathcal{A}^\dagger \mathcal{U}^\dagger_{(q,G)} \mathcal{U}_{(\tilde{q})} \omega \mathcal{U}_{(q,G)} \mathcal{A} | \Omega_\nu \rangle \,.
\end{aligned} \tag{3.34}$$

Thus, we calculate the expectation value of the new operator $\mathcal{U}_{(\tilde{q})}\omega$ with the density matrix resulting from the original wave function $\psi(\mathcal{G})$. Since we gauge only the right and upper modes, we can focus on the gauging transformation $\mathcal{U}_{(q')} = \exp\left(i\Phi r_+^\dagger r_+\right) = \exp\left(i\Phi r^\dagger r\right)$ with $\Phi = \pm\delta$. Without loss of generality, we choose a right mode for the computation. We consider only positive modes r_+ for simplicity. The negative modes r_- are gauged with the same expression where Φ is substituted by $-\Phi$. For increased readability, we will skip the plus and minus signs of the modes in the following calculation:

$$\begin{aligned}
\mathcal{U}_{(\tilde{q})}\omega &= e^{i\Phi r^\dagger r}(1 + l^\dagger l) r r^\dagger l l^\dagger (1 + lr) \\
&= rl + rr^\dagger l l^\dagger + e^{i\Phi} l^\dagger l r^\dagger r + e^{i\Phi} l^\dagger r^\dagger \,.
\end{aligned}$$

We use the Majorana modes in eq. (3.30) to rewrite $\mathcal{U}_{(\tilde{q})}\omega$ with $p = 1 + e^{i\Phi}$ and $m = e^{i\Phi} - 1$:

$$\mathcal{U}_{(\tilde{q})}\omega = \frac{1}{4}p\left[1 - \frac{m}{p}r_1l_1 - ir_1l_1 + \frac{m}{p}r_2l_2 - ir_2l_1 + i\frac{m}{p}r_1r_2 + i\frac{m}{p}l_1l_2\right] + \frac{1}{4}p\left[-r_1r_2l_1l_2\right]. \tag{3.35}$$

Following [169], we replace the Majorana operators with Grassmann variables, to calculate the overlap:

$$[\mathcal{U}_{(\tilde{q})}\omega]_G = \left(-\frac{m}{p}\theta_{r_1}\theta_{l_1}\right)\left(\frac{m}{p}\theta_{r_2}\theta_{l_2}\right) + \left(-i\theta_{r_1}\theta_{l_2}\right)\left(-i\theta_{r_2}\theta_{l_1}\right) + \left(i\frac{m}{p}\right)^2\theta_{r_1}\theta_{r_2}\theta_{l_1}\theta_{l_2}. \tag{3.36}$$

Finally, we can formulate eq. (3.36) as a matrix for the full operator $U_{(\tilde{q})}\omega$:

$$U_{(\tilde{q})}\omega = \frac{1}{4}(1 + e^{i\Phi})\exp\left(\frac{i}{2}(\theta_{r_1}\,\theta_{r_2}\,\theta_{l_1}\,\theta_{l_2})\underbrace{\begin{pmatrix} 0 & it & -t & -1 \\ -it & 0 & -1 & t \\ t & 1 & 0 & it \\ 1 & -t & -it & 0 \end{pmatrix}}_{M(\Phi)}\begin{pmatrix}\theta_{r_1}\\ \theta_{r_2}\\ \theta_{l_1}\\ \theta_{l_2}\end{pmatrix}\right), \tag{3.37}$$

where $t = \tan\left(\frac{\Phi}{2}\right)$. The covariance matrix $M(\Phi)$ in eq. (3.37) of the r and l modes replaces a part of the original covariance matrix Γ_{in}that belongs to the link that $\mathcal{U}_{(\tilde{q})}$ acts on. Since one link consists of positive and negative modes, we will have to substitute the single link with the direct sum $M(\Phi) \oplus M(-\Phi)$.

Due to the modification of the original covariance matrix for the projectors, we have to adapt the calculation for the overlap of two wave functions. While the identities (3.32) still hold, eq. (3.18) cannot be used. Instead, we calculate the overlap using

$$\operatorname{Tr}(XY) = 2^{-n}\operatorname{Pf}(\Gamma_X)\operatorname{Pf}\left(\Gamma_Y - \Gamma_X^{-1}\right) \tag{3.38}$$

which follows from eq. (3.32). Here, X and Y are operators and Γ_X and Γ_Y are the covariance matrices of X and Y in terms of Grassmann variables. If the operators are Gaussian, these representations coincide with the covariance matrices in terms of Majorana fermions.

The Grassmann representation of the involved operators is

$$\begin{aligned} [\rho]_{G,\mu} &= \frac{1}{2^n}\exp\left(\frac{i}{2}\mu^T D\mu\right) \\ [\mathcal{U}_q^\dagger\omega]_{G,\theta} &= \frac{1}{2}(1 + \cos(\Phi))\frac{1}{2^n}\exp\left(\frac{i}{2}\theta^T\left(\bigoplus_{l}^{n_{\text{links}}-2\,\text{copies}}\Gamma_{\text{in}}(\ell)\right)\theta\right) \\ &\quad\times\exp\left(\frac{i}{2}\theta^T M(\Phi)\theta\right)\exp\left(\frac{i}{2}\theta^T M(-\Phi)\theta\right). \end{aligned} \tag{3.39}$$

Here, $\Gamma_{\text{in}}(\ell)$ is the covariance matrix of link ℓ. Thus, we have to use an adapted prefactor for eq. (3.38):

$$\operatorname{Tr}\left(\mathcal{U}_q^\dagger\omega\rho\right) = \frac{1}{2}(1 + \cos(\Phi))2^{-n}\operatorname{Pf}(D)\operatorname{Pf}\left(\tilde{\Gamma}_{\text{in}} - D^{-1}\right),$$

where $\tilde{\Gamma}_{\text{in}}$ is the modified covariance matrix of the links as defined in eq. (3.39). In the case of a $\mathbb{Z}_3$ gauge, we know that $\cos(\Phi) = -\frac{1}{2}$ and obtain

$$\operatorname{Tr}\left(\mathcal{U}_g^{\dagger} \omega \rho\right) = \frac{1}{4} 2^{-n} \operatorname{Pf}(D) \operatorname{Pf}\left(\tilde{\Gamma}_{\text{in}} - D^{-1}\right). \tag{3.40}$$

This expression can be further simplified since the Monte Carlo estimator in eq. (3.33) divides by the square of the norm, and we obtain

$$\mathcal{F}_{\text{el}}(G) = \frac{1}{4} \frac{\operatorname{Pf}\left(\tilde{\Gamma}_{\text{in}} - D^{-1}\right)}{\sqrt{\det\left(D^{-1} - \Gamma_{\text{in}}\right)}}. \tag{3.41}$$

This is the expression stated in the main text as eq. (3.19). In the case of a pure gauge theory, eq. (3.41) can be further simplified with $D^{-1} = -D$.

3.D.2 CALCULATION OF THE GRADIENT OF THE ELECTRIC ENERGY

In contrast to the calculation of the gradient of the Wilson loop, we cannot neglect the first term in eq. (3.20). The estimator of the electric energy depends explicitly on the parameters of the ansatz. Thus, we have to build the derivative of $\mathcal{F}_{\text{el}}$ in eq. (3.41), the estimator of the electric energy, with respect to the parameters $\alpha \in \{y, z\}$.

$$\begin{aligned} \frac{\partial}{\partial \alpha} \mathcal{F}_{\text{el}}(\mathcal{G}, D) = \frac{1}{2} \mathcal{F}_{\text{el}}(\mathcal{G}, D) \Bigg[& \operatorname{Tr}\left(D^{-1} \frac{\partial D}{\partial \alpha}\right) + \operatorname{Tr}\left(\left(\tilde{\Gamma}_{\text{in}} - D^{-1}\right)^{-1} D^{-1} \frac{\partial D}{\partial \alpha} D^{-1}\right) \\ & + \operatorname{Tr}\left(\Gamma_{\text{in}} \frac{\partial D}{\partial \alpha} D^{-1} \left(D^{-1} - \Gamma_{\text{in}}\right)^{-1}\right) \Bigg]. \end{aligned} \tag{3.42}$$

As stated in the main text, the expression for $\frac{\partial D}{\partial \alpha}$ is an analytical expression. Since D is a covariance matrix of Majorana fermions in a pure gauge theory, $D^{-1} = D^{\dagger} = -D$ holds. Thus, the first trace of eq. (3.42) is zero.

4 NON-GAUSSIAN VARIATIONAL STATES

4.1 MOTIVATION

Gauged Gaussian PEPS (cf. chapter 3) are one possible ansatz state to variationally treat lattice gauge theories. In this chapter, we will change the focus towards a different class of states while staying on the lattice.

As we discussed in chapters 2 and 3, the evaluation of gauge theories in the continuum is often challenging, and a lattice regularization enables the numerical evaluation of observables. The evaluation of lattice gauge theories in the action formalism with Monte Carlo methods reaches its limits if a chemical potential [80] is introduced or time dynamics are considered. The Hamiltonian formalism, however, keeps a notion of time and enables the explicit time-evolution of states.

Following the idea of a Hamiltonian approach, we explored a tensor network approach in two spatial dimensions in chapter 3. While the capabilities of finding the ground state are promising, a caveat of tensor networks is the scaling of entanglement during time evolution. Since excited states do not follow the area-law of the ground state, the bond dimension has to grow to capture time evolution accurately. Due to the logarithmic connection between entanglement and virtual bond dimension, the bond dimension must grow exponentially for a polynomially growing entanglement [175–177]. This limits tensor network simulation for time dynamics typically to small times. Other variational states do not necessarily have this restriction.

Here, we introduce complex periodic Gaussian states, a generalization of periodic Gaussian states, first proposed in [92] to prove confinement in the weak-coupling limit of $2+1$d compact QED. We use them to study $(2+1)$-dimensional compact quantum electrodynamics (compact QED), a $U(1)$ theory similar to the theory studied in chapter 3. The theory is good starting point for the study of higher dimensional lattice gauge theories since it shares some features with $(3+1)$-dimensional quantum chromodynamics, *i.e.* it is in a confined phase for all values of the coupling constant [172].

The content of this chapter is based on Ref. [2]. Here, we focus on the computational aspects of the publication. The physical implications are discussed in detail in the publication and will be part of Julian Bender's PhD thesis.

4.2 EXECUTIVE SUMMARY

Since exact diagonalization methods become infeasible in higher dimensions for reasonable system sizes, in particular due to the infinite local Hilbert space of the gauge field, it seems unavoidable to use variational techniques. In $(1+1)$ dimensions the infinite dimension can be avoided either by integrating out the gauge field non-locally [103, 178, 179] or by using the natural restriction of gauge symmetry which makes the dimensions finite [180].

In this chapter, we introduce complex periodic Gaussian states and study compact quantum electrodynamics in $(2+1)$ dimensions. Here, the gauge field cannot be integrated out, and we have to consider it explicitly in our ansatz. As expectation values with respect to periodic Gaussian states cannot be evaluated analytically, the authors of reference [92] used Feynman diagram techniques to evaluate all relevant quantities in the weak-coupling regime. In contrast to that approach, we develop a numerical approximation scheme to evaluate these states for the whole coupling region. Furthermore, the extension of the variational manifold to complex periodic Gaussian states enables the study of real-time dynamics. Importantly, the states do not require any truncation in Hilbert space. Thus, we can explicitly study truncation effects which are occurring in other approaches and give estimates in which coupling regimes the truncations are justified.

In [2], we benchmark the energy convergence of the states and study real-time dynamics after quenches. We establish the existence of one confining phase for all couplings also in the Hamiltonian picture (after it had been proven in the action formalism [172]). Static charges provide a direct probe for the string tension and work as an additional indicator for confinement at large coupling. At low coupling, the string tension can be computed with high accuracy from the Wilson loop.

In this chapter, we focus on the numerical approximation scheme and its implementation. Depending on the coupling region, the variational parameters in the state demand a different evaluation strategy. For small couplings, the infinite sums in the periodic Gaussian formulation can be split into orders, similar to perturbation scheme. For large couplings, however, the negative exponents of the terms become small and convergence is faster with an inverse scheme in the exponentials. Both schemes are presented and their respective range of applicability is benchmarked in fig. 4.3.1. Figure 4.3.2 shows an explicit comparison of the ansatz with exact results for a single plaquette. The physical results are presented in detail in [2] and the thesis by Julian Bender.

The chapter is structured as follows: In section 4.3, we introduce the variational ansatz. The model is introduced as part of the preliminaries in section 2.2.1. In section 4.4, we detail the numerical evaluation of the ansatz. In section 4.5, we discuss the implications of the evaluation. For further details, we refer to Ref. [2].

4.3 THEORETICAL FRAMEWORK

In the preliminary material (cf. section 2.2.1), we presented a formulation of compact QED in terms of plaquette variables. The main idea is to split the electric field into a transverse and a longitudinal component. Subsequently, the $U(1)$ gauge theory can be reformulated in terms of plaquette variables that obey only one global constraint (cf. eq. (2.42)) instead of many local ones. Our ansatz is based on this formulation in terms of $\theta_{\mathbf{p}}$ since a global constraint is easier to handle than many local ones.

The ansatz is used for two distinct tasks in the simulation. First, we need to find the ground state of the U(1) Kogut-Susskind Hamiltonian. In a second step, we will analyze the behavior of observables after quenches from one coupling to another. The construction is based on a periodic Gaussian state [92], and we enhance the expressibility by adding an imaginary part to the wave function to treat the real-time dynamics in the second step. For now, we start with a complex Gaussian (CG)

$$\psi_{CG}\left(\{x_{\mathbf{p}}\}\right) \equiv \exp\left(-\frac{1}{2}\sum_{\mathbf{p},\mathbf{p}'} x_{\mathbf{p}} A_{\mathbf{p}\mathbf{p}'} x_{\mathbf{p}'} - i\sum_{\mathbf{p}} \epsilon_{\mathbf{p}} x_{\mathbf{p}}\right) \tag{4.1}$$

with $x_{\mathbf{p}} \in \mathbb{R}$ and $\mathbf{p} = (p_1, p_2), p_1, p_2 \in [0, .., L-1]$.

As a part of the confinement analysis, we use static charges in the system directly access the string tension. The static charge configuration in the system fixes the linear part in the exponent, *i.e.* $\epsilon_{\mathbf{p}}$ (for further details see section 2.2.1 and Appendix A of [2]). The coupling matrix $A_{\mathbf{p}\mathbf{p}'}$ in eq. (4.1) is defined by the variational parameters

$$A_{\mathbf{p}\mathbf{p}'} \equiv \frac{1}{\pi L^2}\sum_{k_1,k_2=0}^{L-1} \exp\left(2\pi i \frac{(p_1-p_1')\,k_1 + (p_2-p_2')\,k_2}{L}\right)\left(\gamma_{\mathbf{k}}^R + i\gamma_{\mathbf{k}}^I\right), \tag{4.2}$$

where $\{\gamma_{\mathbf{k}}^R\}$ couples to the real part and $\{\gamma_{\mathbf{k}}^I\}$ couples to the imaginary part. For the rest of this chapter, we introduce the shorthand notation $\mathbf{pk} \equiv 2\pi\frac{p_1k_1+p_2k_2}{L}$ (inspired by a scalar product). The factor of $1/\pi$ in eq. (4.2) is chosen for later convenience.

If we consider the system without static charges, it is translational invariant. This invariance is broken when static charges are introduced. Since this influence is already taken care of by $\epsilon_{\mathbf{p}}$, the quadratic part A is assumed to stay translationally invariant.

Given the translational invariance, we can treat the system using Fourier components $x_{\mathbf{k}} = \frac{1}{L}\sum_{\mathbf{p}} e^{i\mathbf{pk}} x_{\mathbf{p}}$ and the quadratic coupling in the exponential becomes

$$\sum_{\mathbf{p},\mathbf{p}'} x_{\mathbf{p}} A_{\mathbf{p}\mathbf{p}'} x_{\mathbf{p}'} = \frac{1}{\pi}\sum_{\mathbf{k}} |x_{\mathbf{k}}|^2 \left(\gamma_{\mathbf{k}}^R + i\gamma_{\mathbf{k}}^I\right). \tag{4.3}$$

In order to guarantee convergence of the ansatz wave function ψ_{CG}, we require $\gamma_{\mathbf{k}}^R > 0\,\forall\mathbf{k}$. Since $|x_{\mathbf{k}}|^2 = |x_{-\mathbf{k}}|^2$ after the Fourier transform, we can eliminate some redundancy in the variational parameters $\gamma_{\mathbf{k}}^{R/I}$ and $\gamma_{-\mathbf{k}}^{R/I}$. The R/I notation is a shorthand to avoid writing the equations for the parameters γ^I and γ^R separately.

We define the equivalence relation

$$\begin{aligned} \mathbf{k} \sim_k \mathbf{k}' \quad \text{if} \quad & k_1 = -k_1' \pmod{L} \\ \text{and} \quad & k_2 = -k_2' \pmod{L} \end{aligned} \tag{4.4}$$

and use the quotient set $\mathcal{K} \equiv \left\{[0,..,L-1]^2 \;\; (0,0)\right\}/\sim_k$ to define a new set of independent variational parameters, $\left\{\gamma_{\mathbf{k}}^{R/I}\right\}_{\mathbf{k}\in\mathcal{K}}$. The independence of the variational parameters will enable us later to apply the time dependent variational principle (see section 4.3.1) for time-evolution after quenches.

To construct the actual ansatz state for compact $U(1)$ gauge fields ($\theta_{\mathbf{p}} \in [-\pi,\pi]$), we sum over infinitely many complex Gaussian states, thus ensuring periodicity

$$\psi_{CPG}\left(\{\theta_{\mathbf{p}}\}\right) \equiv \prod_{\mathbf{p}}\left(\sum_{N_{\mathbf{p}}=-\infty}^{+\infty}\right)\psi_{CG}\left(\{\theta_{\mathbf{p}}-2\pi N_{\mathbf{p}}\}\right)\delta\left(\sum_{\mathbf{p}}\theta_{\mathbf{p}}-2\pi N_{\mathbf{p}}\right). \tag{4.5}$$

The delta function needs to be included in order to satisfy condition (2.42) for physical states. To shorten notation, we will denote the product over infinite sums $\prod_{\mathbf{p}}\sum_{N_{\mathbf{p}}=-\infty}^{+\infty}$ by $\sum_{\{N_{\mathbf{p}}\}}$ and the product over integrals $\prod_{\mathbf{p}}\int_{-\pi}^{\pi}d\theta_{\mathbf{p}}$ by $\int_{-\pi}^{\pi}D\theta$.

The name of periodic Gaussian states can be slightly misleading. Although the construction of the state features Gaussian parts in the sum, the resulting state ψ_{CPG} is not Gaussian since a sum of Gaussian is not Gaussian itself. Thus, we expect that the descriptive power of the state is not limited to free theories.

The Gaussian nature of parts of the wave function, however, is exploited when computing expectation values of observables O. We combine the integral over 2π with one of the two infinite sums to an integration over the real axis

$$\langle\psi_{CPG}|O|\psi_{CPG}\rangle = \sum_{\{N_{\mathbf{p}}\}}\delta\left(\sum_{\mathbf{p}}N_{\mathbf{p}}\right)f_O(\{N_{\mathbf{p}}\}) \tag{4.6}$$

with

$$f_O(\{N_{\mathbf{p}}\}) \equiv \int_{-\infty}^{+\infty}D\theta\,\overline{\psi_{CG}}\left(\theta_{\mathbf{p}}-2\pi N_{\mathbf{p}}\right)O\left(\theta_{\mathbf{p}}\right)\psi_{CG}\left(\theta_{\mathbf{p}}\right)\delta\left(\sum_{\mathbf{p}}\theta_{\mathbf{p}}\right). \tag{4.7}$$

The integral $f_O(\{N_{\mathbf{p}}\})$ can be calculated analytically, while the remaining infinite sum needs to be evaluated numerically. The evaluation of the infinite sum is the main topic in section 4.4.

Exemplary, we demonstrate the procedure for the norm of the state $\langle\psi_{CPG}|\psi_{CPG}\rangle$. The computation of observables follows analogously; further details are presented in Appendix C of [2]. After calculating the integrals analytically, the remaining function $f_{\mathbb{1}}\left(\{N_{\mathbf{p}}\}\right)$ is

$$f_{\mathbb{1}}(\{N_{\mathbf{p}}\}) = \prod_{\mathbf{k}\neq 0}\sqrt{\frac{\pi}{\gamma_{\mathbf{k}}^R}}\exp\left(2\pi i\sum_{\mathbf{p}}\epsilon_{\mathbf{p}}N_{\mathbf{p}}\right)\exp\left(-\pi\sum_{\mathbf{k}}\gamma_{\mathbf{k}}|N_{\mathbf{k}}|^2\right) \tag{4.8}$$

where $N_{\mathbf{k}} \equiv \frac{1}{L}\sum_{\mathbf{p}}\exp\left(i\mathbf{pk}\right)N_{\mathbf{p}}$ is the discrete Fourier transform of $N_{\mathbf{p}}$ and $\gamma_{\mathbf{k}} \equiv \gamma_{\mathbf{k}}^R + \left(\gamma_{\mathbf{k}}^I\right)^2\left(\gamma_{\mathbf{k}}^R\right)^{-1}$. The parameters $\gamma_{\mathbf{k}}$ determine the prefactor of the exponential decay of terms in eq. (4.6) with increasing $|N_{\mathbf{k}}|^2$.

The rest of the computation is a numerical problem. The goal is to evaluate the sum in eq. (4.8) as precisely as possible. One benefit of the sum is that higher order terms in $|N_{\mathbf{k}}|$ are suppressed exponential.

In a first step, we analyze the structure of the terms. The configurations $N_{\mathbf{p}}$ can be ordered such that within each order configurations only change up to permutations.

Although $N_{\mathbf{p}} \in \mathbb{Z}$, we notice that all relevant configurations contain mostly zeros. For better readability, we identify orders by their non-zero elements, *e.g.* $\{N\}_1$ is the set of all permutations of the configuration N' defined by $N'_{\mathbf{p}=0} = 1$ and $N'_{\mathbf{p}\neq 0} = 0$, i.e. $\{N\}_1 \equiv S_{N'}$. Orders with more non-zero terms are exponentially suppressed due to the form of eq. (4.8).

An evaluation of the full sum (including all terms) is not possible on a computer since it includes infinitely many terms. In principle, there are multiple ways to deal with a sum. On option would be a heuristic approach like Monte Carlo sampling. By defining a weight for each configuration, we can obtain an estimator for the full sum. Here, we decided to use a truncation strategy instead. Since we know that higher orders are exponentially suppressed, we can avoid the statistical error of Monte Carlo sampling and sum instead the important contributions at low orders completely. The quality of the approximation when truncating the sum depends on the parameters $\gamma_{\mathbf{k}}$. With increasing values of $\gamma_{\mathbf{k}}$, the sum can be approximated well by orders with small Euclidean norm, $\left\|N_{\mathbf{p}}\right\|_2^2 = \sum_{\mathbf{p}} \left|N_{\mathbf{p}}\right|^2 = \|N_{\mathbf{k}}\|_2^2$. The argument is actually slightly more involved. On one hand, terms of higher orders are suppressed due to the decaying exponential. In contrast, higher orders have more combinations in the permutations. The higher number of permutations, however, cannot compensate for the exponential suppression (this would not be the case if the $\gamma_{\mathbf{k}}$ were arbitrarily small).

Thinking in terms of orders of non-zero contributions in N, the constraint $\delta\left(\sum_{\mathbf{p}} N_{\mathbf{p}}\right)$ is essential as it excludes many orders, *e.g.* $\{N\}_1$ or $\{N\}_{-1}$. The first order with non-zero norm is $\{N\}_{1,-1}$. Upon closer inspection, the sum in eq. (4.6) can be expanded in orders containing only pairs of $1, -1$:

$$\begin{aligned} \langle \psi_{CPG} | \psi_{CPG} \rangle &= \prod_{\mathbf{k}\neq 0} \sqrt{\frac{\pi}{\gamma^R_{\mathbf{k}}}} \sum_{\{N_{\mathbf{k}=0}=0\}} e^{2\pi i \sum_{\mathbf{p}} \epsilon_{\mathbf{p}} N_{\mathbf{p}}} e^{-\pi \sum_{\mathbf{k}} |N_{\mathbf{k}}|^2 \gamma_{\mathbf{k}}} \\ &= \prod_{\mathbf{k}\neq 0} \sqrt{\frac{\pi}{\gamma^R_{\mathbf{k}}}} \left(1 + \sum_{\{N\}_{1,-1}} e^{2\pi i \sum_{\mathbf{p}} \epsilon_{\mathbf{p}} N_{\mathbf{p}}} e^{-\pi \sum_{\mathbf{k}} |N_{\mathbf{k}}|^2 \gamma_{\mathbf{k}}} \right. \\ &\qquad \left. + \sum_{\{N\}_{1,1,-1,-1}} e^{2\pi i \sum_{\mathbf{p}} \epsilon_{\mathbf{p}} N_{\mathbf{p}}} e^{-\pi \sum_{\mathbf{k}} |N_{\mathbf{k}}|^2 \gamma_{\mathbf{k}}} + \dots \right) . \end{aligned} \tag{4.9}$$

Here, $\sum_{\{N_{\mathbf{k}=0}=0\}}$ denotes the sum over the set of all $N_{\mathbf{p}}$ configurations with $N_{\mathbf{k}=\mathbf{0}} = 0$, *i.e.* fulfilling the global constraint. If the parameters of the wave function $\gamma_{\mathbf{k}}$ become sufficiently large, higher orders of the type $\{N\}_{2,-2}$ or $\{N\}_{-2,1,1}$ are exponentially suppressed as well as orders with many $1, -1$ pairs. Thus, the above expansion can be truncated after the first few terms. The remaining orders are evaluated numerically. The fact that configurations only change up to permutations within one order can be used to highly parallelize the computation. Further details about the parallelization scheme is presented in section 4.4. On an 8×8 lattice we are able to compute the first three orders exactly. This procedure works well for configurations of variational parameters with $\gamma_{\mathbf{k}} \gtrsim 1$. However, in the intermediate regime $\gamma_{\mathbf{k}} \approx 1$ more orders are required to obtain good convergence since the exponential suppression is not as pronounced. In these cases, higher orders are included with a uniform sampling approach. Since in all of our numerical simulations $\gamma_{\mathbf{k}}$ parameters are of the same order of magnitude and the $N_{\mathbf{p}}$ configurations only change up to a permutation within an order, a uniform probability distribution is a good ansatz for the exponential in eq. (4.8). This is only the case for sampling within one order; it will fail if we try to sample the whole sum since exponentials from different will contribute with a different weight. This combined approach of exact evaluation of the truncated sum and uniform sampling has the advantage that it introduces almost no error for most of the variational manifold (up to truncated orders which are exponentially suppressed). Even for regions where uniform sampling is required the error is still suppressed since the approach is only used to evaluate higher order contributions. For a detailed analysis of the errors resulting from sampling and truncation, see section 4.4.

The analysis above is based on the assumption that higher order contributions are strongly exponentially suppressed due to $\gamma_{\mathbf{k}} \gtrsim 1$. When the parameters become small, the approximation fails. However, we can exploit that $\langle \psi_{CPG} | \psi_{CPG} \rangle$ can be identified with a multidimensional Riemann theta function [181]

$$\theta(z|\Omega) = \sum_{N \in \mathbb{Z}^g} e^{2\pi i (z \cdot N + \frac{1}{2} N \cdot \Omega \cdot N)} \tag{4.10}$$

where $z \in \mathbb{C}^g$, $\Omega \in \mathbb{C}^{g \times g}$, such that $\Omega = \Omega^T$ and $\mathrm{Im}(\Omega)$ is strictly positive definite. By rewriting the delta function as the limit of a Gaussian, we can bring $\langle \psi_{CPG} | \psi_{CPG} \rangle$ into this form and exchange the limit with the infinite sum due to uniform convergence. We exploit the invariance of the Riemann theta function under modular transformations, in particular the following relation holds (for details see [181])

$$\theta\left(z|\Omega\right) = \frac{1}{\sqrt{\det\left(-i\Omega\right)}} e^{-i\pi z \cdot \Omega \cdot z} \theta\left(\Omega^{-1} z | -\Omega^{-1}\right) . \tag{4.11}$$

Combining the two equations, we obtain

$$\begin{aligned} \langle \psi_{CPG} | \psi_{CPG} \rangle &= \prod_{\mathbf{k} \neq 0} \sqrt{\frac{\pi}{\gamma_{\mathbf{k}}^R \gamma_{\mathbf{k}}}} \sum_{\{N_{\mathbf{p}}\}} \exp\left(-\pi \sum_{\mathbf{k}} \left| N_{\mathbf{k}} - \epsilon_{\mathbf{k}} \right|^2 \gamma_{\mathbf{k}}^{-1} \right) \\ &\equiv \sum_{\{N_{\mathbf{p}}\}} f_{\mathrm{inv},1}\left(\{ N_{\mathbf{k} \neq 0} \} \right) \end{aligned} \tag{4.12}$$

with $\gamma_{\mathbf{0}}^{-1} = 0$.

In comparison to the earlier formulation, the exponential weight depends now on $\gamma_{\mathbf{k}}^{-1}$. In principle, it allows to approximate the sum with a limited number of orders for sufficiently small $\gamma_{\mathbf{k}}$. However, the sum is not well-defined since all constant configurations $N_{\mathbf{p}} = c(1, 1, ..., 1)$ have weight one for $c \in \mathbb{Z}$. Fortunately, all $f_{\mathrm{inv},O}(\{N_{\mathbf{k} \neq 0}\})$ are independent of $N_{\mathbf{k}=\mathbf{0}}$ (as a result of the global constraint on physical states), and all these configurations can be factored out such that they cancel when calculating expectation values. We formulate this more rigorously by defining an equivalence relation for $N_{\mathbf{p}}$ configurations

$$N_{\mathbf{p}} \sim_1 N'_{\mathbf{p}} \quad \text{if} \quad \exists \quad c \in \mathbb{Z} \quad \text{s.t.} \quad N_{\mathbf{p}} - N'_{\mathbf{p}} = c(1, 1, ..., 1) . \tag{4.13}$$

When calculating expectation values of observables only a sum over representatives of this equivalence relation is required

$$\frac{\langle \psi_{CPG} | O | \psi_{CPG} \rangle}{\langle \psi_{CPG} | \psi_{CPG} \rangle} = \frac{\sum_{\{N_{\mathbf{p}}\}/\sim_1} f_{\mathrm{inv},O}(\{N_{\mathbf{k} \neq 0}\})}{\sum_{\{N_{\mathbf{p}}\}/\sim_1} f_{\mathrm{inv},1}(\{N_{\mathbf{k} \neq 0}\})} . \tag{4.14}$$

If we choose the representative to be the one closest in norm to the $N_{\mathbf{p}} = \mathbf{0}$ configuration, we can expand the sum again in orders having mostly 0's. In this case we have no constraint so that all orders must be taken into account.

Now, we have two ways to evaluate the sum, one in the large parameter regime and one in the low parameter regime. Depending on the parameters, we can adapt the evaluation method. To check the validity of both numerical approximation schemes, we ensure that they agree in the parameter region $\gamma_{\mathbf{k}} \approx 1$.

To illustrate that both approximation schemes complement each other, we give the variational energy of ψ_{CPG} with respect to the Kogut-Susskind Hamiltonian given in eq. (2.41), written both in the infinite sum representation for high and for low $\gamma_{\mathbf{k}}$

$$\begin{aligned}\frac{\langle\psi_{CPG}|H_{KS}|\psi_{CPG}\rangle}{\langle\psi_{CPG}|\psi_{CPG}\rangle} =&E_C + \frac{g^2}{4\pi}\sum_{\mathbf{k}}\gamma_{\mathbf{k}}\left(4 - 2\cos\left(\frac{2\pi k_1}{L}\right) - 2\cos\left(\frac{2\pi k_2}{L}\right)\right)\\ &-\frac{g^2}{2}\sum_{\mathbf{k}}\gamma_{\mathbf{k}}^2\left(4 - 2\cos\left(\frac{2\pi k_1}{L}\right) - 2\cos\left(\frac{2\pi k_2}{L}\right)\right)\left\langle|N_{\mathbf{k}}|^2\right\rangle\\ &+\frac{1}{g^2}\sum_{\mathbf{p}}\left(1 - e^{-\frac{\pi}{4L^2}\sum_{\mathbf{k}\neq\mathbf{0}}\left(\gamma_{\mathbf{k}}^R\right)^{-1}}\left\langle(-1)^{N_{\mathbf{p}}}\cosh\left(\pi\sum_{\mathbf{k}}\mathrm{Re}\left(N_{\mathbf{k}}b_{\mathbf{k}}^{\mathbf{p}}\right)\right)\right\rangle\right)\end{aligned} \tag{4.15}$$

with $b_{\mathbf{k}}^{\mathbf{p}} = \frac{1}{L}\gamma_{\mathbf{k}}^I\left(\gamma_{\mathbf{k}}^R\right)^{-1}e^{-i\mathbf{pk}}$. In eq. (4.15), we use the following expressions for the norm

$$\begin{aligned}\left\langle|N_{\mathbf{k}}|^2\right\rangle \equiv&\frac{\sum_{\{N_{\mathbf{k}=\mathbf{0}}=0\}}\exp\left(2\pi i\sum_{\mathbf{p}}\epsilon_{\mathbf{p}}N_{\mathbf{p}}\right)\exp\left(-\pi\sum_{\mathbf{k}'}|N_{\mathbf{k}'}|^2\gamma_{\mathbf{k}'}\right)|N_{\mathbf{k}}|^2}{\sum_{\{N_{\mathbf{k}=\mathbf{0}}=0\}}\exp\left(2\pi i\sum_{\mathbf{p}}\epsilon_{\mathbf{p}}N_{\mathbf{p}}\right)\exp\left(-\pi\sum_{\mathbf{k}'}|N_{\mathbf{k}'}|^2\gamma_{\mathbf{k}'}\right)}\\ =&\frac{1}{2\pi}\gamma_{\mathbf{k}}^{-1}\left(4 - 2\cos\left(\frac{2\pi k_1}{L}\right) - 2\cos\left(\frac{2\pi k_2}{L}\right)\right)\\ &-\gamma_{\mathbf{k}}^{-2}\frac{\sum_{\{N_{\mathbf{p}}\}/\sim_1}\exp\left(-\pi\sum_{\mathbf{k}'}|N_{\mathbf{k}'}-\epsilon_{\mathbf{k}'}|^2\gamma_{\mathbf{k}'}^{-1}\right)|N_{\mathbf{k}}-\epsilon_{\mathbf{k}}|^2}{\sum_{\{N_{\mathbf{p}}\}/\sim_1}\exp\left(-\pi\sum_{\mathbf{k}'}|N_{\mathbf{k}'}-\epsilon_{\mathbf{k}'}|^2\gamma_{\mathbf{k}'}^{-1}\right)}\end{aligned} \tag{4.16}$$

and the expectation value of the hyperbolic cosine

$$\begin{aligned}&\left\langle(-1)^{N_{\mathbf{p}}}\cosh\left(\pi\sum_{\mathbf{k}}\mathrm{Re}\left(N_{\mathbf{k}}b_{\mathbf{k}}^{\mathbf{p}}\right)\right)\right\rangle\\ &=\frac{\sum_{\{N_{\mathbf{k}=\mathbf{0}}=0\}}(-1)^{N_{\mathbf{p}}}\cosh\left(\pi\sum_{\mathbf{k}}\mathrm{Re}\left(N_{\mathbf{k}}b_{\mathbf{k}}^{\mathbf{p}}\right)\right)\exp\left(2\pi i\sum_{\mathbf{p}}\epsilon_{\mathbf{p}}N_{\mathbf{p}}\right)\exp\left(-\pi\sum_{\mathbf{k}}|N_{\mathbf{k}}|^2\gamma_{\mathbf{k}}\right)}{\sum_{\{N_{\mathbf{k}=\mathbf{0}}=0\}}\exp\left(2\pi i\sum_{\mathbf{p}}\epsilon_{\mathbf{p}}N_{\mathbf{p}}\right)\exp\left(-\pi\sum_{\mathbf{k}}|N_{\mathbf{k}}|^2\gamma_{\mathbf{k}}\right)}\\ &=\frac{\sum_{\{N_{\mathbf{p}}\}/\sim_1}e^{-\pi\sum_{\mathbf{k}}\left(\left|N_{\mathbf{k}}-\epsilon_{\mathbf{k}}-\frac{1}{2}{}^{\mathbf{p}}_{\mathbf{k}}\right|^2-\frac{1}{4}|b_{\mathbf{k}}^{\mathbf{p}}|^2\right)\gamma_{\mathbf{k}}^{-1}}\cos\left(\pi\sum_{\mathbf{k}}\gamma_{\mathbf{k}}^{-1}\mathrm{Re}\left[\left(N_{\mathbf{k}}-\epsilon_{\mathbf{k}}-\frac{1}{2}{}^{\mathbf{p}}_{\mathbf{k}}\right)b_{\mathbf{k}}^{\mathbf{p}}\right]\right)}{\sum_{\{N_{\mathbf{p}}\}/\sim_1}\exp\left(-\pi\sum_{\mathbf{k}}|N_{\mathbf{k}}-\epsilon_{\mathbf{k}}|^2\gamma_{\mathbf{k}}^{-1}\right)}\end{aligned} \tag{4.17}$$

with $\frac{1}{2}{}^{\mathbf{p}}_{\mathbf{k}} = \frac{1}{2L}e^{-i\mathbf{pk}}$. Finally, we can set $\gamma_{\mathbf{k}}^I = 0\,\forall\mathbf{k}$ in the expressions for high $\gamma_{\mathbf{k}}^R$, *i.e.* with the sums $\sum_{\{N_{\mathbf{k}=\mathbf{0}}=0\}}$. The resulting expression agrees with the computations given in [92] up to redefinitions. This is expected since $\gamma_{\mathbf{k}}^I = 0\,\forall\mathbf{k}$ leads back to periodic Gaussian states with real coefficients.

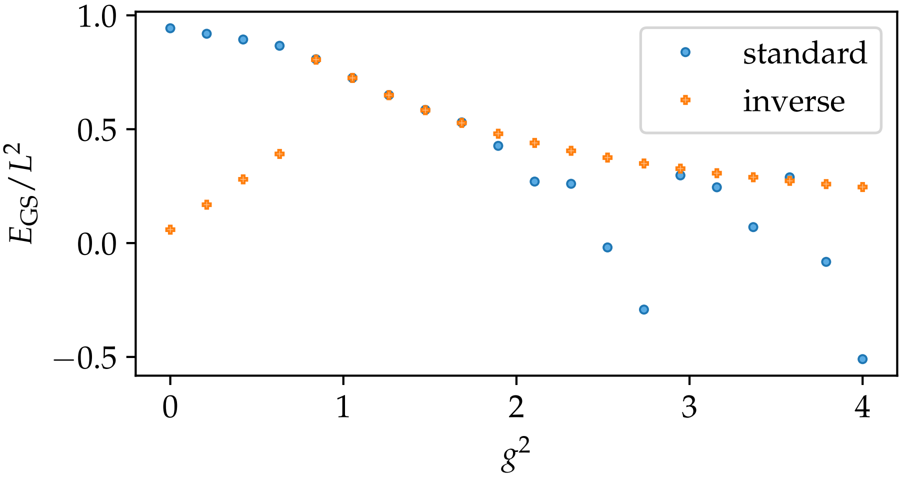

Figure 4.3.1: Evaluation of the complex periodic Gaussian states in different coupling regimes on a 6 × 6 lattice. The standard method performs best at small couplings when the coefficients $\gamma_{\mathbf{k}}$ are big. At large couplings, the inverse method yields more reliable results.

In fig. 4.3.1, we compare the different evaluation methods in different coupling regimes. The idea to use a complex periodic Gaussian state as an Ansatz is a variational method implying that it should be impossible to energies smaller than the true ground state energy of the system. However, this implication requires the correct evaluation of the state. As described above, the standard approximation (blue dots in fig. 4.3.1) in orders breaks down if the coefficients $\gamma_{\mathbf{k}}$ are becoming too small (at couplings $g^2 \leq 1.1$). For small couplings, the standard evaluation method works well because higher order have a negligible contribution. At larger couplings, however, the contributions become sizable and the evaluation of the Ansatz becomes unreliable. In this coupling region, *i.e.* for small values of $\gamma_{\mathbf{k}}$, the inverse scheme (orange plus signs in fig. 4.3.1) is preferable. In the intermediate regions of couplings around $g^2 \approx 1.1$ both evaluation schemes agree, as we would expect.

To check the validity of the mixed evaluation scheme, we compare against an exact solution. A single plaquette of the system can be solved exactly in terms of Mathieu functions (for details see [2]). In fig. 4.3.2, we see excellent agreement between the exact solution and the complex periodic Gaussian state. At intermediate couplings around $g^2 \approx 1.1$, which are challenging for both the standard and the inverse method, the deviations reach a maximal deviation of $\approx 0.5\%$. The evaluation of the state works reliable, since we never reach energies smaller than the exact solution.

The convergence of the infinite sums, and subsequently the ansatz, is determined by $\gamma_{\mathbf{k}} = \gamma^R_{\mathbf{k}} + \left(\gamma^I_{\mathbf{k}}\right)^2 \left(\gamma^R_{\mathbf{k}}\right)^{-1}$ or $\gamma_{\mathbf{k}}^{-1}$, respectively. For real-time evolutions, e.g. a quantum quench, $\left(\gamma^I_{\mathbf{k}}\right)^2$ will typically become large and so will $\gamma_{\mathbf{k}}$, irrespective of the real part $\gamma^R_{\mathbf{k}}$. This allows a truncation of the expansion in eq. (4.9) already after the first term such that everything can be evaluated without resorting to sampling. Thus, the ansatz is well suited for real-time evolution compared with other methods where computational hurdles make it difficult to reach long times.

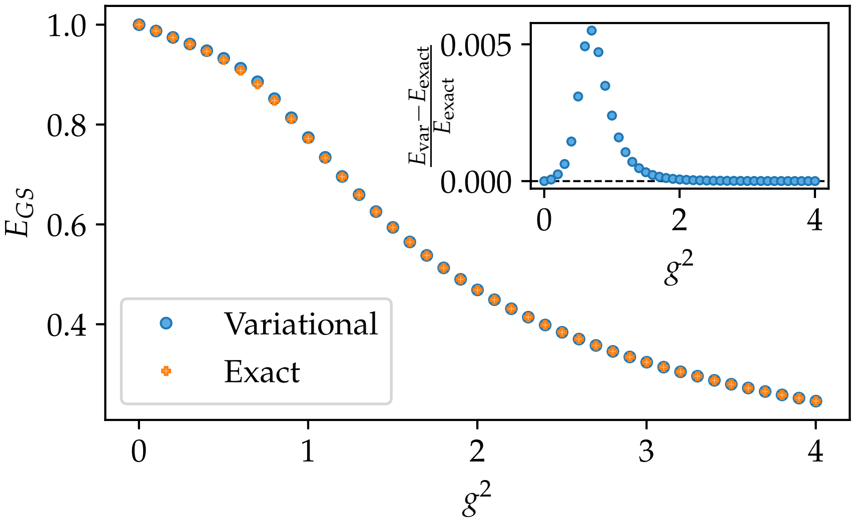

Figure 4.3.2: Comparison of the exact ground state energy of one plaquette and the approximation with a complex periodic Gaussian state. The inset shows the relative error of the Ansatz.

4.3.1 TIME-DEPENDENT VARIATIONAL PRINCIPLE

In addition to static phenomena, we aim to study the time evolution of the system after quenches. One option to perform time evolution is the time-dependent variational principle (TDVP). Here, the equations of motion are projected onto the tangent plane of our variational manifold. For every variational parameter $\gamma_{\mathbf{k}}^{R/I}$, we define a corresponding tangent vector $\left|\psi_{\mathbf{k}}^{R/I}\right\rangle \equiv \mathbb{P}_{\psi}\left(\frac{\partial}{\partial\gamma_{\mathbf{k}}^{R/I}}\left|\psi_{CPG}\right\rangle\right)$ where $\mathbb{P}_{\psi}$ ensures orthogonality to $\left|\psi_{CPG}\right\rangle$

$$\mathbb{P}_{\psi}\left(|\psi\rangle\right) \equiv |\psi\rangle - \langle\psi_{CPG}|\psi\rangle\,|\psi_{CPG}\rangle\ . \tag{4.18}$$

By restricting the momenta $\mathbf{k}$ of the variational parameters to the set $\mathcal{K}$ defined in eq. (4.4), all tangent vectors become linearly independent. This independence enables us to invert the Gram matrix $G_{\mathbf{k}'\mathbf{k}} \equiv \left\langle\psi_{\mathbf{k}'}^{R}|\psi_{\mathbf{k}}^{R}\right\rangle$ with $\mathbf{k},\mathbf{k}' \in \mathcal{K}$. Having a well-defined inverse is not always the case for the Gram matrix. If the parameters are not independent of each other, one has to resort to approximate methods to obtain an approximate inverse like the minimal residual method. Since our variational manifold is Kähler, we can express the time evolution of the variational parameters $\gamma_{\mathbf{k}}^{R/I}$ $(\mathbf{k} \in \mathcal{K})$ [182]

$$i\left(\dot\gamma_{\mathbf{k}}^{R} + i\dot\gamma_{\mathbf{k}}^{I}\right) = \frac{1}{2}\sum_{\mathbf{k}'\in\mathcal{K}}\left(G^{-1}\right)_{\mathbf{k}\mathbf{k}'}\left(\frac{\partial E}{\partial\gamma_{\mathbf{k}'}^{R}} + i\frac{\partial E}{\partial\gamma_{\mathbf{k}'}^{I}}\right) \tag{4.19}$$

with $E \equiv \frac{\langle\psi_{CPG}|H_{KS}|\psi_{CPG}\rangle}{\langle\psi_{CPG}|\psi_{CPG}\rangle}$ the variational energy in eq. (4.15) and $\dot\gamma \equiv \frac{\partial\gamma}{\partial t}$. The formula for the calculation of the Gram matrix and the gradient of the variational energy can be found in Appendix C of [2].

4.4 COMPUTATIONAL CONSIDERATIONS

In this section, we review the numerical evaluation of complex periodic Gaussian states in more detail. As stated above, the region with $\gamma_{\mathbf{k}} = \gamma^R_{\mathbf{k}} + \left(\gamma^I_{\mathbf{k}}\right)^2 \left(\gamma^R_{\mathbf{k}}\right)^{-1} \approx 1$ is the most difficult to evaluate since the exponential decays slowly in both formulations (direct and inverse in $\gamma_{\mathbf{k}}$). Since the variational ground state with $\gamma^I_{\mathbf{k}} = 0$ varies from high $\gamma^R_{\mathbf{k}}$ for low couplings to low $\gamma^R_{\mathbf{k}}$ for large couplings, there is a transition region at $g^2 \sim 1.1$ where $\gamma_{\mathbf{k}} \approx 1$. Thus, we choose this regime to study the quality of the approximations of the infinite sums in this regime. Concretely, we analyze the convergence of the ground state energy (4.15) on an 8×8 lattice without static charges at for two couplings. First, we consider $g^2 = 1.1$ which is the highest coupling where the high $\gamma_{\mathbf{k}}$ approximation is used. Second, we study the convergence for $g^2 = 1.2$ which is the lowest coupling for we use the low $\gamma_{\mathbf{k}}$ approximation. For all other considered couplings the contributions to infinite sums decay faster with higher orders compared to one of the two examples discussed below.

Using $\gamma^I_{\mathbf{k}} = 0$ and $\epsilon_{\mathbf{p}} = 0$, the expressions for the variational ground state at $g^2 = 1.1$ simplifies to

$$I_{\text{el}} \equiv \sum_{\{N_{\mathbf{k}=\mathbf{0}}=0\}} e^{-\pi \sum_{\mathbf{k}} |N_{\mathbf{k}}|^2 \gamma^R_{\mathbf{k}}} \sum_{\mathbf{k}} \left(\gamma^R_{\mathbf{k}}\right)^2 |N_{\mathbf{k}}|^2 \left(4 - 2\cos\left(\frac{2\pi k_1}{L}\right) - 2\cos\left(\frac{2\pi k_2}{L}\right)\right) \tag{4.20}$$

for the electric energy,

$$I_{\text{mag}} \equiv \sum_{\{N_{\mathbf{k}=\mathbf{0}}=0\}} e^{-\pi \sum_{\mathbf{k}} |N_{\mathbf{k}}|^2 \gamma^R_{\mathbf{k}}} \sum_{\mathbf{p}} (-1)^{N_{\mathbf{p}}} \tag{4.21}$$

for the magnetic energy and the normalization

$$I_0 = \sum_{\{N_{\mathbf{k}=\mathbf{0}}=0\}} e^{-\pi \sum_{\mathbf{k}} |N_{\mathbf{k}}|^2 \gamma^R_{\mathbf{k}}} . \tag{4.22}$$

In total, we include orders with $N_{\mathbf{p}}$ configurations of up to 8 pairs of $\{1, -1\}$ and the rest zeros. The first three orders are computed exactly and the remaining five by uniform sampling. Additionally, we compute exactly the orders $\{N\}_{2,-1,-1}$ and $\{N\}_{-2,1,1}$ to show they have negligible contributions. The configuration of orders like $\{N\}_{2,-1,-1}$ and $\{N\}_{-2,1,1}$ differ only by a minus sign, and they can be evaluated together by computing for every permutation not only the contribution of $N_{\mathbf{p}}$ but also of $-N_{\mathbf{p}}$. Therefore, from now on orders which are not closed under reflection will also include all their permutations multiplied by minus one. This is heavily used in the low $\gamma_{\mathbf{k}}$ approximation.

The exact evaluation of orders is based on an algorithm which iteratively generates new permutations of a multi-set in $O(1)$ time [183], i.e. the time to generate a new permutation is independent of the permutation size. It is much smaller than the time needed to do computations with a permutation which allows to highly parallelize the process and reach higher orders. The algorithm uses a combination of generators [184] and the multiprocessing [185]. In Python, the global interpreter lock [186] prevents the execution of multithreaded code. Thus, we use process-based parallelism instead of thread-based parallelism.

Before forking the processes, we assign a range of configurations to each process. Since the generation of samples is cheap, we allocate an independent generator for

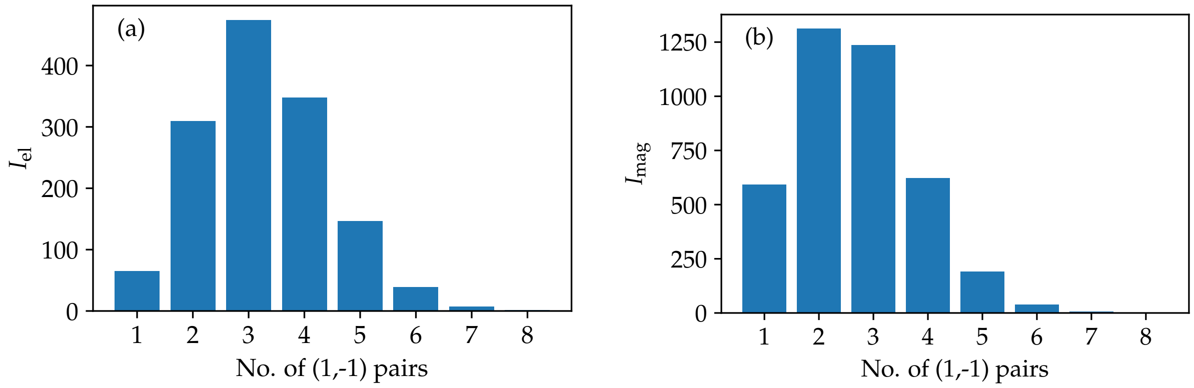

Figure 4.4.1: Contributions of different orders of $N_{\mathbf{p}}$ configurations to the infinite sums I_{el} (a) and I_{mag} (b) appearing in the high $\gamma_{\mathbf{k}}$ approximation of the variational energy. Every bar represents the summed contributions of all $N_{\mathbf{p}}$ configurations containing a certain number of (1,-1) pairs and the remaining entries zero. Orders which are not of this type have a negligible contribution, *e.g.* $\{N\}_{-2,1,1}$ has a summed contribution to I_{el} of 0.076 and a summed contribution to I_{mag} of 0.23.

each process and move the generator to the beginning of the assigned interval. When the process has evaluated all configurations, the results is added to a value in shared memory. Thus, the amount of communication among the processes in minimized and the respective computation can run independently. The major advantage of using a generator instead of computing all permutations beforehand is memory-efficiency. By generating the configurations during the computation, we never have to store all configurations in main memory.

The evaluation of an observable with respect to a set of permutations $\{N\}$ with uniform sampling is based on the approximation:

$$\sum_{N_{\mathbf{p}}\in\{N\}} O(N_{\mathbf{p}}) \approx \frac{p}{s} \sum_{N_{\mathbf{p}}\in S} O(N_{\mathbf{p}}) \tag{4.23}$$

where S is a set of s randomly drawn $N_{\mathbf{p}}$ configurations from $\{N\}$ and p the number of permutations within this order. For all orders which are computed with uniform sampling we use $s = 10^8$ in the high $\gamma_{\mathbf{k}}$ approximation and $s = 10^7$ in the low $\gamma_{\mathbf{k}}$ approximation. The contributions to I_{el} and I_{mag} for the high $\gamma_{\mathbf{k}}$ approximation are displayed in fig. 4.4.1. We do not show this analysis for the normalization since its contributions decay faster than the ones for I_{el} and I_{mag}. The errors due to uniform sampling are too small to be shown in the plot, the biggest error occurs in the order with four pairs of $\{1,-1\}$ which has a contribution of 347.54(15) to I_{el} and of 622.70(24) to I_{mag}.

As a second example, we consider the evaluation method of inverse $\gamma_{\mathbf{k}}$. For the variational ground state at $g^2 = 1.2$, the infinite sums in eq. (4.15) reduce to

$$J_{\mathrm{el}} = \sum_{\{N_{\mathbf{p}}\}/\sim_1} e^{-\pi \sum_{\mathbf{k}} |N_{\mathbf{k}}|^2 (\gamma_{\mathbf{k}}^R)^{-1}} \sum_{\mathbf{k}} \left(4 - 2\cos\left(\frac{2\pi k_1}{L}\right) - 2\cos\left(\frac{2\pi k_2}{L}\right)\right) |N_{\mathbf{k}}|^2 \tag{4.24}$$

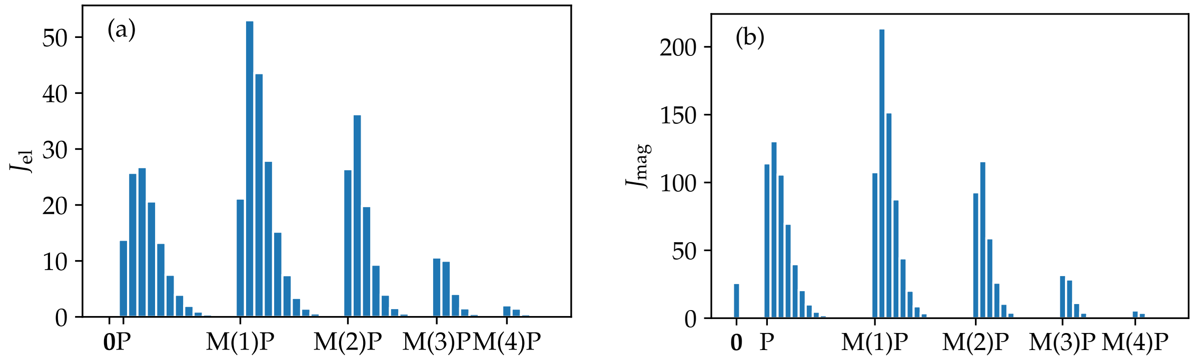

Figure 4.4.2: Contributions of different orders of $N_{\mathbf{p}}$ configurations to the infinite sums J_{el} (a) and J_{mag} (b) appearing in the low $\gamma_{\mathbf{k}}$ approximation of the variational energy. Due to absence of a constraint, all $N_{\mathbf{p}}$ configurations need to be considered. For better overview, the orders are organized in groups: P denotes orders which contain a growing number of 1's. Since $N_{\mathbf{p}}$ and $-N_{\mathbf{p}}$ are evaluated together, P also represents orders with a growing number of -1's. $M(1)P$ contains orders whose non-zero elements are a single -1 and a growing number of 1's. The first order in $M(1)P$ contains a pair of (1,-1) as non-zero elements. $M(2)P$ is structured in the same way as $M(1)P$ but with two -1's. Analogously for the other groups. The $N_{\mathbf{p}} = \mathbf{0}$ configuration (denoted as **0**) has vanishing contribution to J_{el} but a non-zero contribution to J_{mag}.

for the computation of the electric energy,

$$J_{\mathrm{mag}} = \sum_{\{N_{\mathbf{p}}\}/\sim_1} \sum_{\mathbf{p}} e^{-\pi \sum_{\mathbf{k}} \left|N_{\mathbf{k}} - \frac{1}{2}{}^{\mathbf{p}}_{\mathbf{k}}\right|^2 (\gamma^R_{\mathbf{k}})^{-1}} \tag{4.25}$$

with $\frac{1}{2}{}^{\mathbf{p}}_{\mathbf{k}} = \frac{1}{2L} e^{-i\mathbf{pk}}$ for the computation of the magnetic energy and

$$J_0 = \sum_{\{N_{\mathbf{p}}\}/\sim_1} e^{-\pi \sum_{\mathbf{k}} |N_{\mathbf{k}}|^2 (\gamma^R_{\mathbf{k}})^{-1}} \tag{4.26}$$

for the normalization. Since we do not have a global constraint in the low $\gamma_{\mathbf{k}}$ approximation, more orders contribute to the infinite sums. The contributions to J_{el} and J_{mag} of different orders are given in fig. 4.4.2. The errors are again too small to be displayed, the biggest one occurs in the order $\{N\}_{-1,1,1,1,1,1}$ with contributions of 15.22(1) to J_{el} and of 44.07(4) to J_{mag}.

Both approximation schemes decay reasonably well with higher orders and the truncation of even higher orders can be justified. Moreover, the errors introduced due to uniform sampling are small, in particular since the lowest orders were still calculated exactly. The algorithm we applied during computations to decide with which approximation method an expectation value should be evaluated was to select higher orders and compute them by uniform sampling with a low sample size of $s = 10^5$. This allowed us to choose the scheme which had a better decay with higher orders.

4.5 DISCUSSION

We introduced a new class of variational states, complex periodic Gaussian states, to study ground state properties and real-time dynamics in a $(2+1)$-dimensional $U(1)$ lattice gauge theory. The evaluation of expectation values can only partially be done analytically, an infinite sum remains to be computed numerically. The sum is numerically approximated for all variational parameters on an 8×8 lattice and for the weak-coupling regime up to a lattice size of 20×20. This allows us to study the variational ground state of these states over the whole coupling region and extract the thermodynamic limit.

The physical results are presented in detail in [2]. Here, we summarize the results concisely. The implementation was checked by comparing the ansatz against a well-known approximation for the ground state energy in the single plaquette case. The confinement of the ground state for all couplings was verified with a direct computation of the string tension between two charges and a fit to the area law of Wilson loops. We see confining behavior for all couplings g^2.

Finally, the time-dependent variational principle enables the investigation of quantum quenches in the coupling constant. The implementation of the time-evolution was verified with exact diagonalization data from a $\mathbb{Z}_3$ system. Subsequently, we studied the equilibration of observables after quenches in the coupling constant. For all considered quenches, we observe equilibrating behavior of the observables up to times when boundary effects start to play a role.

As a perspective, it would be interesting to compare the equilibrated expectation values to thermal expectation values. The thermal expectation values can be obtained with Monte Carlo techniques in the action formalism [187, 188]. Another application for Monte-Carlo methods could be numerical evaluation of the variational ansatz by approximating the infinite sums. This could potentially enable the simulation of larger system sizes. The new evaluation scheme would replace the current truncation procedure. The accuracy of these simulations would need to be high in order to carry out the evolution over reasonable time scales while ensuring energy conservation.

A natural extension is the treatment of $(3+1)$-dimensional compact QED. By generalizing an idea in Ref. [92] to complex Gaussian states, a variational ansatz can be designed for $3+1$ dimensions. However, due to additional local constraints appearing in $3+1$ dimensions (compared to one global constraint in $2+1$ dimensions), a new numerical approximation scheme would be required. It would be especially interesting to combine the $(3+1)$-dimensional formulation with the new Monte Carlo evaluation mentioned above.

Finally, dynamical matter could be included into the system. To couple the gauge degrees of freedom to matter, it is essential to find a formulation of such a theory, which admits the same gauge-invariant variables as used in this work for static matter. Recently, such a formulation has been proposed in Ref. [189].

5 CONTINUOUS TENSOR NETWORKS

5.1 MOTIVATION

Quantum field theories are difficult to solve out of the perturbative regime with deterministic techniques. One common option are lattice Monte Carlo algorithms [20, 70, 77, 78] in the action formalism. These algorithms, however, rely heavily on the action formalism and need a lattice discretization.

A complementary option are variational algorithms to solve strongly coupled QFT. The central idea is to guess a suitable manifold $\mathcal{M}$ of states $|\psi_\nu\rangle$ described by a manageable number of parameters ν and to minimize the energy $\langle\psi_\nu|H|\psi_\nu\rangle$ over this class $\mathcal{M}$. We hope that the answer is close enough to the real ground state $|0\rangle$. In contrast to Monte Carlo techniques, variational approaches are highly dependent on the choice of the manifold $\mathcal{M}$. If the manifold does not contain the ground state or states that are very similar, the minimization is bound to fail. The main idea was noted by Feynman already [190], finding such a good manifold for typical QFT is a highly non-trivial task. In particular, apart from simple Gaussian states such as free ground states, it seems impossible to have a sparsely parameterized state with easily computable local observables $\langle\psi_\nu|\mathcal{O}(x_1)\cdots\mathcal{O}(x_n)|\psi_\nu\rangle$ while keeping an extensive ansatz – the latter requirement excluding *e.g.* simple expansions in the particle number basis.

The last two chapters focused on lattice formulations of gauge theories and different Ansatz states in the discrete setting. In particular, in chapter 3, we explored a special class of gauged tensor network states, GGPEPS. Motivated by the success of discrete tensor networks, several proposals for continuous tensor networks have been made in the last years [56, 61, 62]. Since continuous tensor networks are working directly in the continuum, a continuum limit can be avoided when applying them to quantum field theories. Continuous matrix product states (cMPS) [56] are a continuous extension of discrete matrix product state. They have been successfully applied to quantum field theories [57–59]. In this chapter, we focus on the dimension-independent proposal [61] for continuous tensor network states (CTNS). They are proposed as a variational ansatz for ground states of quantum field theories. While CTNS show promising analytical properties, their numerical performance has not been tested.

The content of this chapter is based on Ref. [3].

5.2 EXECUTIVE SUMMARY

Discrete tensor networks are undeniably successful in describing quantum field theories on the lattice [1, 100, 104, 191]. Motivated by their success, we numerically explore the capabilities of continuous tensor network states (CTNS) for quantum field theories directly in the continuum.

In this chapter, we use a Gaussian submanifold of CTNS, Gaussian CTNS (GCTNS), to benchmark the states on quadratic and quartic Hamiltonians. Restricting to the manifold to Gaussian states enables the analytic calculation of expectation values and correlators. We numerically minimize the energy of different Hamiltonians to obtain the ground state of the respective model. As benchmark models, we use the free boson, a quadratic Hamiltonian, and the Lieb-Liniger model, a quartic Hamiltonian. Both models have exact solutions in terms of Bogoliubov transformations or Bethe ansatz, respectively. We compare the variational ground state of the one- and two-dimensional systems with exact results and find excellent agreement (cf. figs. 5.4.1 and 5.4.3). In addition to the energy, the correlations of the states match the exact results as well. Following the intuition borrowed from discrete tensor network, the results improve with increasing virtual bond dimension D.

In a second step, we compare the variational results of GCTNS with Bethe ansatz calculations for the Lieb-Liniger model. Given the non-Gaussian ground state of the model, we do not expect to match the ground state exactly. For small couplings, where the theory approaches a Gaussian ground state, we match well (cf. fig. 5.4.5). Interestingly, we are able to capture most of the Gaussian features already with a small bond dimension of $D = 1$.

The benchmark shows that CTNS are a promising ansatz for quantum field theories and further research into more general CTNS can lead to interesting results.

The following chapter is organized as follows: section 5.3 presents the Gaussian submanifold and the models used for the benchmark. Furthermore, it provides details about the variational optimization procedure and the renormalization that is necessary in two space dimensions. The benchmarking results are shown in section 5.4. Finally, we discuss possible research directions in section 5.5.

5.3 THEORETICAL FRAMEWORK

5.3.1 GAUSSIAN APPROXIMATION

Continuous tensor networks [61] are hard to evaluate in their full generality. If no restrictions are placed on the function V and α in the functional integral in eq. (2.12), the evaluation of observables and states cannot be done analytically. The integral of the virtual field (in the exponent) can be evaluated with Monte Carlo techniques for certain choices of V and α. Since we want to test rather the manifold of states than the contraction in the exponent, we focus here on the analytically contractible case. Expectation values and correlations can be computed exactly if the expansions of V and α are truncated to quadratic and linear order respectively [1]:

$$\begin{aligned} V[\phi] &= V^{(0)} + V_j^{(1)}\phi_j + V_{jk}^{(2)}\phi_j\phi_k\,, \\ \alpha[\phi] &= \alpha^{(0)} + \alpha_j^{(1)}\phi_j\,. \end{aligned}$$

Due to the restriction to quadratic order, we call these states Gaussian CTNS. Since the state are Gaussian, we can carry out the Gaussian integral directly in the state definition (2.9) and obtain:

$$|V,\alpha\rangle = \exp\left\{\int \psi^\dagger G\,\psi^\dagger + \beta\,\psi^\dagger\right\}|\mathrm{vac}\rangle\ , \tag{5.1}$$

where

$$G = \alpha^{(1)\,T}\left(-\frac{\nabla^2}{2}\mathbb{1} + V^{(2)}\right)^{-1}\alpha^{(1)} \tag{5.2}$$

$$\beta = \alpha^{(0)} - \frac{1}{2}\left[V^{(1)\,T}\left(-\frac{\nabla^2}{2}\mathbb{1} + V^{(2)}\right)^{-1}\alpha^{(1)} + \alpha^{(1)\,T}\left(-\frac{\nabla^2}{2}\mathbb{1} + V^{(2)}\right)^{-1}V^{(1)}\right]. \tag{5.3}$$

Equation (5.3) demonstrates some redundancies in the parameterization. We observe that $V^{(0)}$ does not appear because it only changes the state's normalization and during the computation, we do not actively track the normalization of the state. Instead, we normalize the state numerically when we evaluate expectation values. Additionally, we notice that the second term in eq. (5.3) can be incorporated into $\alpha^{(0)}$, and thus we may fix $V^{(1)} = 0$ without lack of generality. From an intuitive standpoint, we can interpret the redefinition as a compensation of one term with another. A non-zero expectation value of an auxiliary field can be compensated by a constant source. Finally, under the mild assumption that $V^{(2)}$ is diagonalizable $V^{(2)} = U^{-1}(M/2)U$, we have a straightforward rewriting:

$$G = \frac{1}{2}\sum_\ell \underbrace{\left[\sum_{jk}\alpha_j^{(1)}U_{j\ell}U_{\ell k}^{-1}\alpha_k\right]}_{:=A_\ell}\Big(-\nabla^2 + M_{\ell\ell}\Big)^{-1}. \tag{5.4}$$

Equation (5.4) can be obtained directly by taking $V^{(2)} = M/2$ diagonal and $\alpha_k^{(1)}$ a complex square root of A_k. Thus, without lack of generality, we can now assume that we have diagonal "mass" matrix $M := \mathrm{diag}(m_1, \dots, m_D)$ for the auxiliary field. In the

---

[1] Beware of the factor of 2 difference in the definition of $V^{(2)}$ compared to [61]

end, a GCTNS is parameterized by two complex vectors $\alpha^{(1)}$ and m, and a scalar $\alpha^{(0)}$, *i.e.* $2D+1$ complex parameters, where D is the dimension of the virtual fields.

With these simplifications in mind, we now go back to the computation of the generating functional (2.12). As above, we can perform the Gaussian integration, yielding

$$\mathcal{Z}_{j',j} = \exp\Big(\int \frac{1}{2} J(j,j')^T K J(j,j') + j\alpha^{(0)} + j'\alpha^{(0)*} \Big),$$

where the operator K fulfills

$$\begin{pmatrix} -\nabla^2 + M & -\alpha^{(1)}\alpha^{(1)*T} \\ -\alpha^{(1)*}\alpha^{(1)T} & -\nabla^2 + M^* \end{pmatrix} K(x,y) = \mathbb{1}\,\delta(x-y)\,,$$

and $J(j,j')^T = \big(\alpha^{(1)}[j+\alpha^{(0)*}], \alpha^{(1)*}[j'+\alpha^{(0)}]\big)$. Because of translation invariance $K(x,y) = K(x-y)$, and it is convenient to formulate the equation in Fourier space:

$$K(x-y) = \int \frac{\mathrm{d}^d p}{(2\pi)^d} K(p)\, \mathrm{e}^{ip(x-y)} \tag{5.5}$$

which yields $K(p) = \big(p^2\,\mathbb{1} + W\big)^{-1}$ with

$$W = \begin{pmatrix} M & -\alpha^{(1)}\alpha^{(1)*T} \\ -\alpha^{(1)*}\alpha^{(1)T} & M^* \end{pmatrix}. \tag{5.6}$$

This formulation allows us to compute various expectation values of the state, for example the two-point functions using eq. (2.11).

5.3.2 MODELS

In the following section, we test GCTNS for two models in $d=1$ and $d=2$. First, we consider a quadratic, bosonic model in one and two space dimensions. While the energy density is finite in the one-dimensional case, we have to renormalize it in two space dimensions. In a second step, we consider a quartic model in one space dimension which does not have a Gaussian ground state.

We first consider a non-relativistic model with a Hamiltonian quadratic in bosonic creation and annihilation operators ψ

$$H = \int_{\mathbb{R}^d} \nabla\psi^\dagger\nabla\psi + \mu\,\psi^\dagger\psi + \lambda\left[\psi^\dagger\psi^\dagger + \psi\,\psi\right]. \tag{5.7}$$

Since it is quadratic in bosonic operators, it has a Gaussian ground state. In fact, for a single species of spinless bosons and the usual non-relativistic kinetic term, it is essentially the most general one can write. Such a Hamiltonian can be obtained as the mean field approximation of a weakly interacting Bose gas, but we take it as an exact starting point here. We can also interpret the same Hamiltonian as the regularized Hamiltonian of the relativistic free boson [58]

$$H_{\text{fb}}^{\Lambda} = \frac{1}{2}\int_{\mathbb{R}^d} \pi^2 + (\nabla\phi)^2 + m^2\phi^2 + \underbrace{\frac{1}{\Lambda^2}(\nabla\pi)^2}_{\text{regulator}}, \tag{5.8}$$

where π, ϕ are the traditional canonically conjugate fields $[\phi(x), \pi(y)] = i\delta^d(x-y)$, and Λ is a non-relativistic momentum cutoff. The Hamiltonian H_{fb}^{Λ} in eq. (5.8) reduces to eq. (5.7) with the field mapping

$$\phi = \sqrt{\frac{1}{2\Lambda}}(\psi + \psi^\dagger) \tag{5.9}$$

$$\pi = \sqrt{\frac{\Lambda}{2}}\,(\psi - \psi^\dagger) \tag{5.10}$$

and the parameters

$$\mu = \frac{\Lambda^2 + m^2}{2}, \tag{5.11}$$

$$\lambda = \frac{\Lambda^2 - m^2}{4}. \tag{5.12}$$

The closing the gap at $\lambda/\mu \to f_c = 1/2$ is equivalent to lifting the non-relativistic regulator ($m \ll \Lambda$).

The model (5.7) is exactly solvable, and we find (see appendix 5.A) the ground state energy density

$$\mathbf{e}_0 = \frac{1}{2}\int \frac{\mathrm{d}^d p}{(2\pi)^d}\left[\sqrt{(p^2+\mu)^2 - 4\lambda^2} - (p^2+\mu)\right], \tag{5.13}$$

which is infinite when $d \geq 2$. Consequently, we have to treat the system in one dimension differently from the system in higher dimensions. While the optimization of the energy is directly possible in $d = 1$, we will have to renormalize away the divergent part in $d = 2$. The corresponding two-point functions can also be computed exactly, and we have *e.g.*

$$\begin{aligned} \langle 0|\,\psi^\dagger(x)\psi(y)\,|0\rangle &= \int \frac{\mathrm{d}^d p}{(2\pi)^d} C_0(p) \mathrm{e}^{ip(x-y)} \\ \text{with}\ \ C_0(p) &= \frac{1}{2}\left(\frac{p^2+\mu}{\sqrt{(p^2+\mu)^2 - 4\lambda^2}} - 1\right). \end{aligned} \tag{5.14}$$

In addition to the quadratic models in $d = 1$ and $d = 2$, we consider a quartic model, the Lieb-Liniger model. It is one of the simplest models for interacting bosons in $d = 1$ and is given by the Hamiltonian

$$H_{\text{LL}} = \int_{\mathbb{R}} \partial_x\psi^\dagger\partial_x\psi + c\,\psi^\dagger\psi^\dagger\psi\psi, \tag{5.15}$$

where c is the strength of the coupling. The Hamiltonian preserves the number of particles. The filling is controlled by the particle density $\rho = \langle\psi^\dagger\psi\rangle$. The physics of the model depends on the adimensional coupling $\gamma = c/\rho$. The model is integrable, and it is possible to write an exact equation for the energy density in the ground state with the Bethe ansatz. It can be solved numerically to essentially arbitrary precision or expanded in a power series at weak and strong coupling [192, 193]. We use these expansions to evaluate the performance of our method.

The ground state of the Lieb-Liniger model is not a Gaussian state. As a result a GCTNS cannot approximate it with arbitrary precision even for large D, because we restricted the CTNS to be Gaussian. However, it is possible for a GCTNS to give reasonable approximation in some regime, which is what we aim to explore here. We compare the GCTNS results with two other simple approximation techniques: classical solution and mean field. The classical solution is the result of a minimization of the energy in the space of coherent states, or equivalently a GCTNS with $D = 0$. The mean-field approximation corresponds to the ground state of a different Hamiltonian, namely the mean field quadratic Hamiltonian of the same model. In section 5.B.2, we explain how to deal with the quartic terms and how to obtain the mean field Hamiltonian.

Our analysis can be seen as the continuum analogue of the one carried recently for the Bose-Hubbard model [194], where a generic Gaussian state approximation was compared with standard classical and mean field solutions. In our case, aside from dealing with the continuum, we have the refinement that we do not use the most general Gaussian states in the first place (which would anyway require infinitely many parameters), but a tower of more and more expressive submanifolds indexed by D.

5.3.3 VARIATIONAL OPTIMIZATION

The goal of our analysis is to numerically check whether CTNS are a promising ansatz for ground state computations in QFT. Thus, we have to numerically find the ground state for a given Hamiltonian. We now summarize the strategy to variationally optimize GCTNS in practice.

In what follows, we will study models specified by a local bosonic Hamiltonian:

$$H = \int_{\mathbb{R}^d} \mathrm{d}^d x \, h\left(\psi^\dagger, \psi\right)(x) \, , \tag{5.16}$$

where $h\left(\psi^\dagger, \psi\right)(x)$ contains product of the operators $\psi, \psi^\dagger$ and its derivatives. More concretely, we will consider the free boson in one and two space dimensions and the Lieb-Liniger model in one space dimension. For a GCTNS $|V, \alpha\rangle$ we introduce the associated energy density

$$\langle h \rangle_{V,\alpha} := \frac{\langle V, \alpha | h(\psi^\dagger, \psi) | V, \alpha\rangle}{\langle V, \alpha | V, \alpha \rangle} \, . \tag{5.17}$$

Our objective is to minimize it to find an approximation to the ground state $|0\rangle$ and an upper bound to the ground energy density $\mathbf{e}_0$:

$$|0\rangle \simeq |V, \alpha\rangle = \operatorname{argmin} \, \langle h \rangle_{V,\alpha} \, , \tag{5.18}$$

$$\mathbf{e}_0 \leq \min_{V,\alpha} \, \langle h \rangle_{V,\alpha} \, . \tag{5.19}$$

To minimize the energy, we must compute $\langle h \rangle_{V,\alpha}$ [cf. eq. (5.17)], which reduces to the computation of a sum of correlation functions of $\psi, \psi^\dagger$, which we know how to compute in general from the generating functional (see appendix 5.B). The numerical minimization can be sped up significantly by also providing the (analytic) gradient of the energy density with respect to the $2D + 1$ complex parameters. Since we have explicit expressions for all correlation functions, the gradients can be computed analytically. Details can be found in appendix 5.B.

In $d = 2$ space dimensions, several two point functions of interest diverge when taken at equal points. In particular, the kinetic energy $\nabla\psi^\dagger\nabla\psi$ and $\psi\psi + \psi^\dagger\psi^\dagger$ terms diverge when evaluated on GCTNS. This can be traced back to the fact that the corresponding momentum integrals (see appendix 5.B) diverge logarithmically.

This divergence can be renormalized. First, we introduce a hard momentum cutoff Λ such that correlation functions are finite. We then observe that the energy density evaluated on a GCTNS changes to

$$\langle h\rangle_{V,\alpha} = \langle h\rangle_{\mathrm{r}} + \frac{1}{4\pi}\ln(\Lambda^2)\,\langle h\rangle_{\mathrm{div}} + o(1)\,, \tag{5.20}$$

such that the energy can be split into a regular and log divergent part. For the quadratic Hamiltonian (5.7), the log divergent part can be evaluated exactly and we find

$$\langle h\rangle_{\mathrm{div}} = \left[\sum_{j=1}^{D}\alpha_j^2\right]\left[\sum_{j=1}^{D}\alpha_j^2\right]^* + \lambda\sum_{j=1}^{D}\left(\alpha_j^2+\alpha_j^{*2}\right), \tag{5.21}$$

where we used the simplified notation $\alpha_j^{(1)} = \alpha_j$. Importantly, $\langle h\rangle_{\mathrm{div}}$ can be made negative and minimized exactly, yielding the condition

$$\sum_{j=1}^{D}\alpha_j^2 = -\lambda. \tag{5.22}$$

This condition defines a submanifold of "maximally divergent energy" GCTNS on which the parameters can be numerically tuned to minimize the remaining finite part $\langle h\rangle_{\mathrm{r}}$. The remaining numerical challenge is to minimize the regular part of the energy in this submanifold.

We obtained the condition (5.22) in a variational way by only asking that the energy is minimal and taking the cutoff to infinity. As a welcome surprise, it provides the same divergence of the energy density as the exact solution! The energy density diverges as $-\lambda^2\ln\Lambda^2/(\pi)$ [cf. eq. (5.13)], exactly as for GCTNS on the submanifold defined by eq. (5.22). Thus, a GCTNS can not only capture the UV behavior of the exact ground state, it captures it *exactly* upon optimization.

5.4 RESULTS

We start by presenting the results for the quadratic Hamiltonian in one and two space dimensions. Since we can solve it exactly with a Bogoliubov transformation, we use it as a benchmark for the GCTNS computations. In a second part, we detail our findings for the Lieb-Liniger model in one space dimension. To compute the ground state energy with our ansatz, we compute the energy density, its gradient with respect to the parameters, and use a standard BFGS solver [170] to find the point yielding the minimal energy. In this setting, we can use the more advanced BFGS solver in contrast to the stochastic gradient that we used for the minimization of GGPEPS in chapter 3. Energies and gradients are computed by evaluating analytic formulas which leads to deterministic results instead of results with statistical error as in the Monte Carlo case. The use of BFGS facilitates the minimization of the energy.

The results for the one-dimensional, quadratic model are shown in fig. 5.4.1. We observe that for parameter values of order 1 away from the gap closing (*e.g.* $f = \lambda/\mu = 0.25 = f_c/2$), the convergence to the exact value is extremely fast in D – to the point that it is difficult to probe large values of D because of machine precision issues. Note that the plots in fig. 5.4.1 display the relative error of the energy density and not the

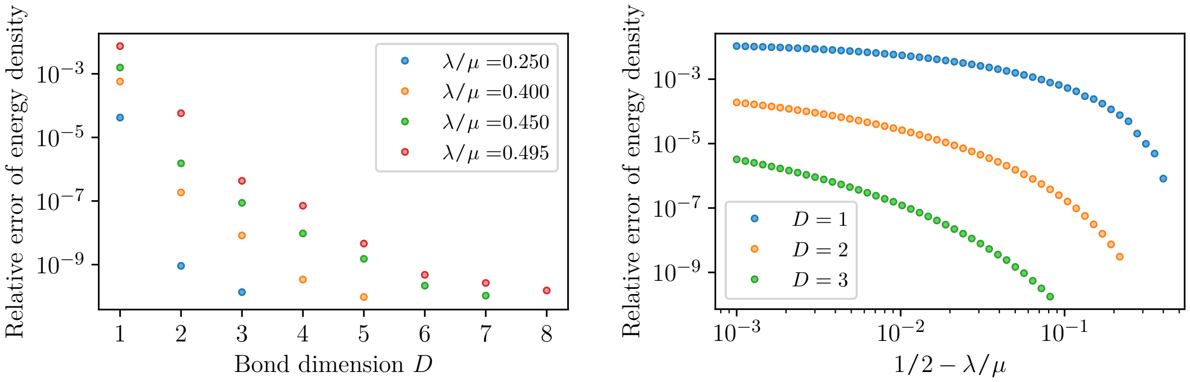

Figure 5.4.1: Convergence of the energy density in $d = 1$. Left – Relative error in the energy density $\langle h \rangle_{V,\alpha} / \mathbf{e}_0 - 1$ as a function of the field bond dimension D. Right – Relative error as a function of the distance $1/2 - \lambda/\mu$ from the gap closing point for $D = 1, 2, 3$.

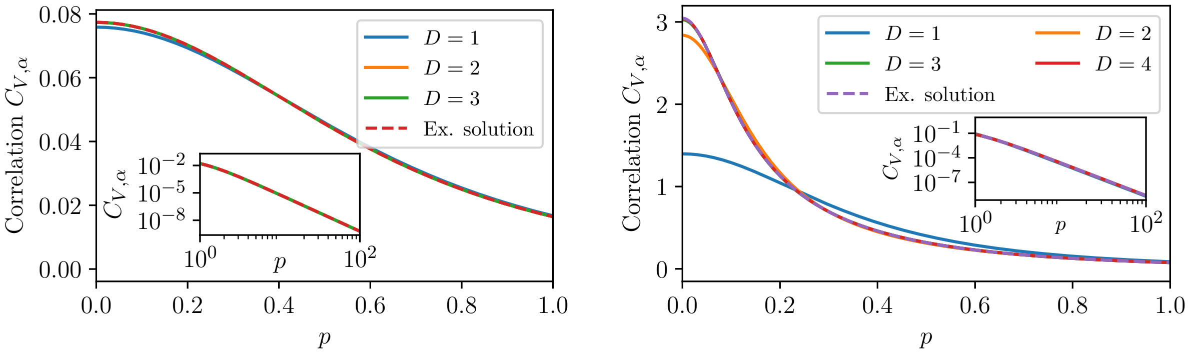

Figure 5.4.2: Convergence of the correlation function in $d = 1$. Two-point correlation function in momentum space $C_{V,\alpha}(p)$ for $\mu = 1$ away from the gap closing for $\lambda = 0.25$ (left) and near the gap closing for $\lambda = 0.495$ (right). The GCTNS correlation function converges uniformly to the exact one as D is increased, but larger values of D are required as the gap closes.

absolute error. As we get closer to the parameters of the gap closing, the convergence becomes slower, but moderate values of D still give accurate values, even for $\lambda/\mu = 0.99 f_c$. This is compatible with the tensor network interpretation that gapped systems can be precisely approximated with low bond dimension. However, larger values of the bond dimension are needed closer to a critical point.

In QFT, one might worry that optimizing the energy does not give a fast convergence of the state itself (summarized by its two-point functions in the Gaussian case). Here, because the theory is regular (or equivalently non-relativistic), this is not the case, and we observe a fast uniform convergence of the two-point function, at least away from the gap closing (see fig. 5.4.2).

Before we move on to the more involved $d = 2$ space dimensions case, it is helpful to understand better the structure of GCTNS correlation functions and compare them to the exact one (5.14). Using the expression for the generating functional, we notice that $C_{V,\alpha}(p)$, the Fourier transform of $\langle\psi^\dagger(x)\psi(0)\rangle_{V,\alpha}$, is of the form

$$C_{V,\alpha}(p) = \sum_{k=1}^{2D} \frac{a_k}{p^2 + w_k}, \tag{5.23}$$

where w_k are the complex eigenvalues of W defined in eq. (5.6) and a_k are complex coefficients (see appendix 5.B for more detail). Bringing all the fractions in eq. (5.23) on the same denominator shows that $C_{V,\alpha}(p)$ is an even rational function of degree at most $4D$. It is impossible to capture $C_0(p)$ exactly for a finite D, since it contains a square root. However, using the identity

$$(1-x)^a = \sum_{n=0}^{\infty} \binom{a}{n} x^n, \tag{5.24}$$

we obtain that

$$C_0(p) = \frac{1}{2}\sum_{n=1}^{+\infty} \binom{-\frac{1}{2}}{n} \left[\frac{4\lambda^2}{(p^2+\mu)^2}\right]^n, \tag{5.25}$$

with uniform convergence for all p as long as $\lambda/\mu < 1/2$. This is the same structure as a GCTNS correlation function, except that the expansion in rational functions is truncated at order $4D$ in p for GCTNS.

At short distances, $p \to +\infty$, only the first term in the expansion matters. It can be reproduced exactly already by a GCTNS with $D = 1$, which means the UV behavior of the QFT can be captured by the simplest non-trivial GCTNS. At long distances, $p \simeq 0$, the series (5.25) is still absolutely convergent with an error decreasing exponentially with the number of terms. Hence, for a GTCNS the error should be dominated by the infrared and at most $\mathcal{O}([2\lambda/\mu]^{2D})$.

In our method, we perform a variational optimization of the energy and not a perturbative term by term optimization of the two-point function. As a result the error obtained in practice could scale differently. Indeed, we observe in fig. 5.4.1 that the error decreases faster than naively expected for small D.

In what follows and for comparison, we consider only the renormalized part of the energy density $\langle h\rangle_\mathrm{r} := \lim_{\Lambda\to\infty}\langle h\rangle - \lambda^2\ln(\Lambda^2)/(4\pi)$. For the exact solution it gives the "renormalized" energy density

$$\mathbf{e}_0^R = \int \frac{\mathrm{d}^2p}{(2\pi)^2}\left(\varepsilon_0(p) + \frac{\lambda^2}{(p^2+\mu)}\right) + \frac{\lambda^2}{4\pi}\ln(\mu), \tag{5.26}$$

which is of course finite and which we can compare to $\langle h\rangle_\mathrm{r}$ since the counter terms used in both cases (the divergent parts) are identical. Again, we insist that this optimization procedure and the associated renormalization of the energy density do not require knowing the exact solution.

Results are shown in fig. 5.4.3, and we observe that the convergence for the renormalized energy density and two point function is qualitatively as good as in the $d = 1$ case.

After considering the quadratic model, we turn to the more involved case of the quartic model. We do not expect to match the ground state exactly (since it is not Gaussian). In practice, we minimize the energy density of the model over GCTNS of fixed D keeping $\rho = 1$ fixed with gradient descent. Since we are working in a special submanifold with $\rho = 1$, we do not use the BFGS algorithm here. As GCTNS are

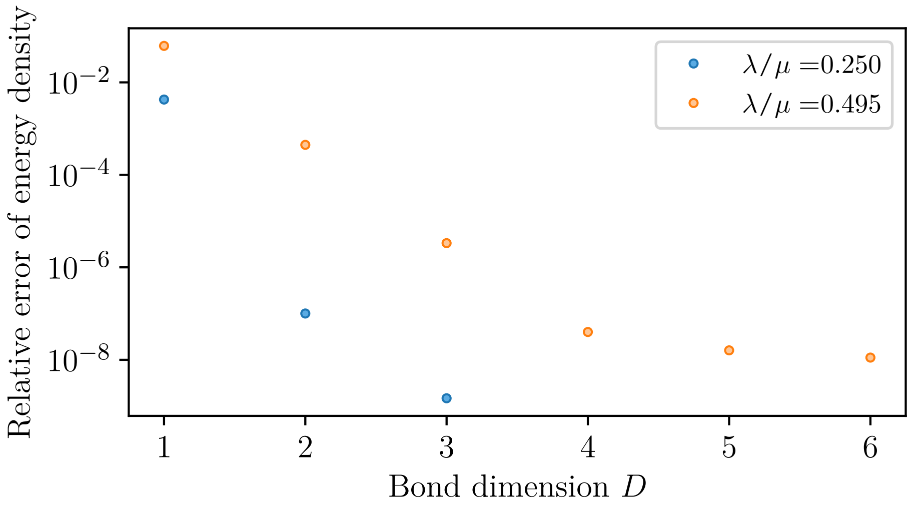

Figure 5.4.3: Convergence of the energy density in $d = 2$. Relative error in the energy density as a function of the bond field dimension D for $\lambda/\mu = 0.25$ (away from the gap closing) and $\lambda/\mu = 0.495$ (close to the gap closing).

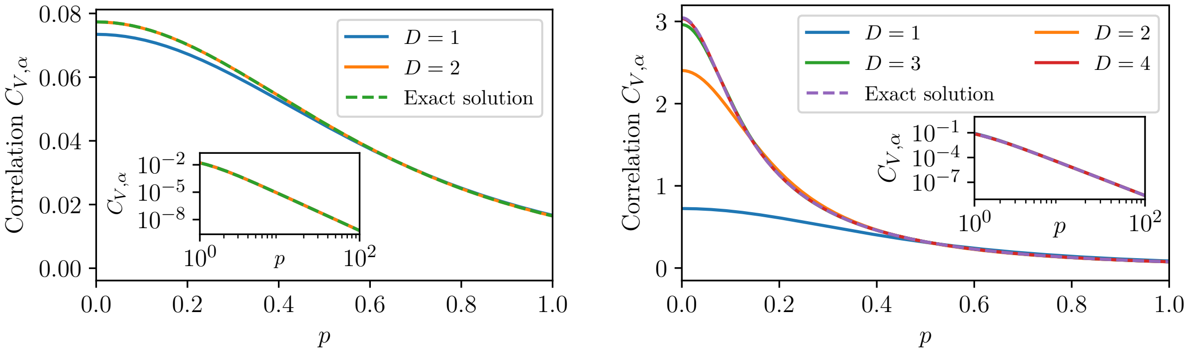

Figure 5.4.4: Convergence of the correlation function in $d = 2$. Two-point correlation function in momentum space $C_{V,\alpha}(p)$ for $\mu = 1$ away from the gap closing for $\lambda = 0.25$ (left) and near the gap closing for $\lambda = 0.495$ (right). As in $d = 1$, the GCTNS correlation function converges uniformly to the exact one as D is increased in two space dimensions.

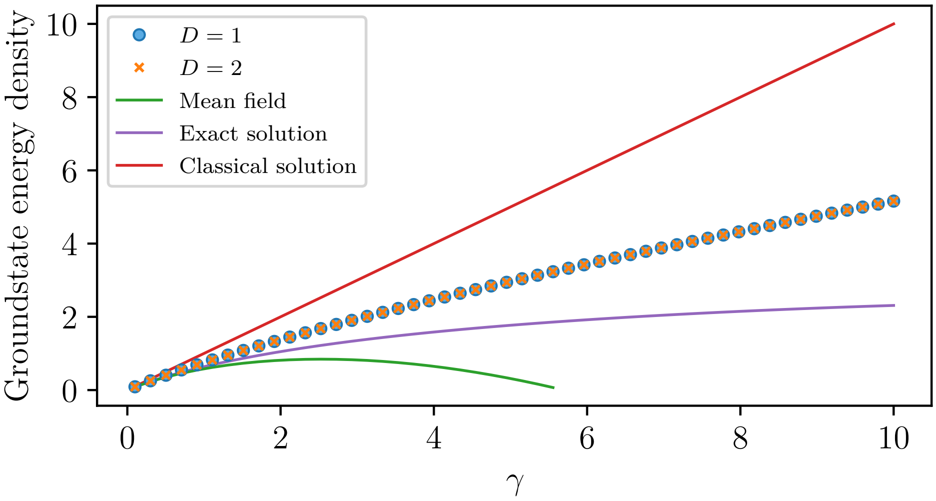

Figure 5.4.5: Energy density of the Lieb-Liniger model ground state as a function of the coupling strength $\gamma = c/\rho$. At $\gamma = 0$ the theory becomes Gaussian and the GCTNS matches the ground state energy very well. For larger values of γ the theory becomes increasingly non-Gaussian and the match between the ansatz and the true ground state energy deteriorates.

Gaussian states, the expectation value of the quartic term is simply computed with Wick's theorem (see appendix 5.B), and thus the energy density and its gradient are easily evaluated.

In fig. 5.4.5, we can see that the upper bound provided by GCTNS approaches the exact ground energy as the coupling γ gets smaller. This is expected: the ground state of a weakly interacting Bose gas becomes Gaussian when the coupling approaches zero.

What is remarkable is that the simplest GCTNS ansatz for $D = 1$ is already sufficient to get all the expressive power of Gaussian states in this case. Almost all the improvement from the classical solution $D = 0$ is reached for $D = 1$. The refinements obtained with larger D are not necessary in the sense that they bring improvements in the energy density much smaller than the distance between the best Gaussian energy density and the true energy density. This is rather intuitive: if a Gaussian state is not the exact solution, we do not gain much by getting the best Gaussian state; an approximation of the best Gaussian state can do qualitatively as well.

5.5 DISCUSSION

In summary, we are mainly interested in knowing if CTNS can be a promising trial wave functions for quantum field theories, coming close to the efficiency of discrete lattice tensor networks. Our aim is to benchmark the performance of the states and not of the numeric algorithm that we used. Thus, we focused on a subclass of analytically tractable CTNS, Gaussian CTNS. The optimizing of GCTNS on a simple non-relativistic quadratic Hamiltonian matches well with the exact solution, both for the energy density and the state itself (parameterized by its two point function). In two space dimensions, the renormalization of the Gaussian theory becomes necessary. GCTNS show the correct divergence in the UV to enable exact renormalization of the divergent. Importantly, the renormalization is performed entirely variationally, *i.e.* without knowing the exact solution. Upon increasing the bond dimension of GCTNS to moderate values of D, we can even approximate the regime where the gap closes, corresponding to the relativistic limit of the theory. Hence, GCTNS have exactly the right UV properties to approximate non-relativistic QFT.

Many-body Hamiltonians are usually interacting and their ground state is not Gaussian. In general, we cannot expect a GCTNS to approximate the ground state of a non-Gaussian theory with good precision. It is, however, worthwhile to see how GCTNS perform in comparison to other approximation methods like mean-field approximation. We chose to test GCTNS on the Lieb-Liniger model, a simple quartic model. At low coupling, GCTNS provide a good approximation to the energy since the theory becomes Gaussian if the coupling drops to zero. The approximation is largely independent of the bond dimension D, and the lowest bond dimension of $D = 1$ already captures essentially everything that general Gaussian states (with an infinite number of parameters) can capture. Thus, we are able to drastically compress the number of parameters needed for a similar approximation quality. All these results show that GCTNS are a viable approximation and deserve to be studied in more detail.

The work can be extended in multiple directions, even when keeping the Gaussian character of the states. If the Hamiltonian includes fermions, even quadratic Hamiltonian can yield richer physics. Additionally, the exploration of topological phases becomes possible if multiple species of bosons or fermions are included. Following the ideas for geometric methods in [182, 194], GCTNS could be used to explore real-time dynamics and spectral properties. Finally, entanglement properties have been a key to our understanding of discrete tensor network algorithms. A similar analysis in the case of GCTNS could shed new light on the performance of the states.

In addition to considering Gaussian states, we could leave the Gaussian setting and deal with genuinely interacting theories. Since a sum of Gaussian states is not Gaussian anymore, a sum of GCTNS could be first step into a non-Gaussian direction. As we saw above, low field bond dimensions yield already a good description of the best Gaussian states. This efficient parameterization would enable large sums of GCTNS to be considered as an Ansatz. A similar idea would be numerically unfeasible due to the large number of parameters of generic Gaussian states. In line with the work chapter 6, GCTNS are an interesting starting point to create a better basis of states for Hamiltonian truncation. With GCTNS, the commonly used free Fock space basis could be replaced by the Fock space built from the excitations above a GCTNS optimized on the interacting Hamiltonian, leading possibly to a better convergence for a given cut-off.

When leaving the environment of GCTNS altogether, exact computations of correlation functions become impossible. In particular, there is no exact expression for the energy density that we aim to minimize. The needed correlations could be evaluated with Monte-Carlo or perturbatively. The most appealing option and the one closest to discrete tensor network methods would be an evaluation of the correlation functions of a CTNS in 2 dimensions using the transfer matrix method in 1 dimension as proposed in [61]. In 1 space dimension, cMPS algorithms [60] can evaluate the largest eigenstate of an operator, in this case the transfer matrix. The problem of minimizing a CTNS is reduced to optimizing a cMPS. Ultimately, although a lot of challenges remain to be solved to make CTNS a viable numerical ansatz for interacting QFT, we hope that the present work offers motivation to further explore CTNS.

APPENDIX

5.A EXACT DIAGONALIZATION OF H

Since it is quadratic, the Hamiltonian (5.7) can be diagonalized exactly using a Fourier and a Bogoliubov transformation. The Fourier transformation yields

$$H = \int \frac{\mathrm{d}^d p}{(2\pi)^d} \left(p^2 + \mu\right) \psi_p^\dagger \psi_p + \lambda \left(\psi_p^\dagger \psi_{-p}^\dagger + \psi_p \psi_{-p}\right). \tag{5.27}$$

A subsequent Bogoliubov transformation consists in introducing new creation annihilation operators $(b_p^\dagger, b_p)$ linearly related to the original ones

$$\psi_p = u_p b_p + v_p b_{-p}^\dagger \tag{5.28}$$

$$\psi_p^\dagger = u_p^* b_p^\dagger + v_p^* b_{-p}\,, \tag{5.29}$$

where $|u_p|^2 - |v_p|^2 = 1$ to ensure the canonical commutation relations remain valid. The Hamiltonian (5.27) becomes diagonal if

$$u_p v_p = \frac{\lambda}{p^2 + \mu}\left(u_p^2 + v_p^2\right)\,, \tag{5.30}$$

which is solved by

$$u_p = \sqrt{\frac{p^2 + \mu}{2\sqrt{\left(p^2 + \mu\right)^2 - 4\lambda^2}} + \frac{1}{2}}\,, \tag{5.31}$$

$$v_p = -\sqrt{\frac{p^2 + \mu}{2\sqrt{\left(p^2 + \mu\right)^2 - 4\lambda^2}} - \frac{1}{2}}\,. \tag{5.32}$$

Finally, the diagonalized Hamiltonian reads:

$$H = \int \frac{\mathrm{d}^d p}{(2\pi)^d}\, \varepsilon_1(p)\, b_p^\dagger b_p + \varepsilon_0(p), \tag{5.33}$$

with

$$\varepsilon_1(p) = \sqrt{(p^2 + \mu)^2 - 4\lambda^2} \tag{5.34}$$

$$\varepsilon_0(p) = \frac{1}{2}\left[\varepsilon_1(p) - (p^2 + \mu)\right]. \tag{5.35}$$

The associated ground state energy density $\mathbf{e}_0$, which will be useful for benchmarks, is

$$\mathbf{e}_0 = \int \frac{\mathrm{d}^d p}{(2\pi)^d}\, \varepsilon_0(p)\,. \tag{5.36}$$

For large p, $\varepsilon_0(p)$ decays as p^{-2} and thus the ground energy density is infinite for $d \geq 2$.

Expressing ψ_p as a function of the b_p, we get the ground state two-point function:

$$\left\langle \psi_p^\dagger \psi_q \right\rangle = \left(\frac{p^2 + \mu}{2\,\varepsilon_1(p)} - \frac{1}{2}\right) \delta(p - q). \tag{5.37}$$

5.B CORRELATION FUNCTIONS AND THEIR GRADIENTS

5.B.1 TWO-POINT FUNCTIONS

The expectation values of GCTNS are computed as functional derivatives of the generating functional $\mathcal{Z}_{j',j}$ given in eq. (5.5)

$$\langle\psi^\dagger(x)\psi(y)\rangle_{V,\alpha} = \frac{\delta}{\delta j'(x)}\frac{\delta}{\delta j(y)}\mathcal{Z}_{j',j}\Big|_{j,j'=0} . \tag{5.38}$$

Since all two point functions can be computed in the same way, we focus on the computation of the correlation function given above. Using the expression for $\mathcal{Z}_{j',j}$ we obtain:

$$\langle\psi^\dagger(x)\psi(y)\rangle_{V,\alpha} = \int\frac{\mathrm{d}^d p}{(2\pi)^d}C_{V,\alpha}(p)e^{ip(x-y)} \tag{5.39}$$

with

$$C_{V,\alpha}(p) = (0,\alpha^{(1)*})K(p)(\alpha^{(1)},0)^T + \left\langle\psi_p^\dagger\right\rangle\left\langle\psi_p\right\rangle\delta(p) . \tag{5.40}$$

Here, $(\alpha^{(1)},0)$ and $(0,\alpha^{(1)*})$ are $2D$ vectors, $K(p) = \left(p^2\,\mathbb{1} + W\right)^{-1}$ (see eq. (5.6)) and only the second term (the zero mode) depends on $\alpha^{(0)}$

$$\left\langle\psi_p^\dagger\right\rangle = \alpha^{(0)}\left[\left(\alpha^{(1)},\alpha^{(1)*}\right)K(p)\left(\alpha^{(1)},0\right)^T\right] . \tag{5.41}$$

Note that in the models we are considering one can choose the gauge where $a^{(0)}\in\mathbb{R}$. We set

$$C_{V,\alpha}(p)\big|_{\alpha^{(0)}=0} = \left(0,\alpha^{(1)*}\right)K(p)\left(\alpha^{(1)},0\right)^T \tag{5.42}$$

because it corresponds to the $C_{V,\alpha}$ when $\alpha^{(0)} = 0$.

In order to compute the energy density, we now compute the real space correlation function at equal points. As the momentum integral of the zero mode is trivial, we focus on the contribution from $C_{V,\alpha}(p)|_{\alpha^{(0)}=0}$. In a first step, we diagonalize matrix $K(p)$ with a unitary $2D\times 2D$ matrix U, such that $W = U^{-1}LU$ and L is a $2D\times 2D$ diagonal matrix with eigenvalues $\lambda_1,\lambda_2,\ldots,\lambda_{2D}$. The matrix W needs to be positive definite for the state to be physical, thus $\mathrm{Re}[\lambda_i] > 0$. We obtain

$$K(p) = U^{-1}\left(p^2\cdot\mathbb{1} + L\right)^{-1}U, \tag{5.43}$$

and hence

$$C_{V,\alpha}(p)\big|_{\alpha^{(0)}=0} = \left(0,\alpha^{(1)*}\right)U\left(p^2\cdot\mathbb{1}+L\right)^{-1}U^{-1}\left(\alpha^{(1)},0\right)^T . \tag{5.44}$$

This allows to find the equal point 2-point function

$$\langle\psi^\dagger(x)\psi(x)\rangle\big|_{\alpha^{(0)}=0} = \sum_{i=1}^{2D}\left[\left(0,\alpha^{(1)*}\right)U\right]_i I_1(\lambda_i)\left[U^{-1}(\alpha^{(1)},0)^T\right]_i \tag{5.45}$$

with the integral

$$I_1(\lambda_i) = \int\frac{\mathrm{d}^d p}{(2\pi)^d}\frac{1}{p^2+\lambda_i} .$$

The integral is convergent in $d = 1$ and logarithmically divergent in $d = 2$. However, the divergences cancel each other in the sum (5.45) as they do not depend on λ_i and thus the particle density is finite in $d = 2$ space dimensions (and in fact even in $d = 3$).

We can proceed in the same way to compute the other correlation functions $\langle \psi(x)\psi(x)\rangle$ and $\langle \psi^\dagger(x)\psi^\dagger(x)\rangle$. For these, the logarithmic divergences do not cancel each other in $d = 2$ and contribute to the divergence of the energy density. The renormalization procedure is explained in the main text.

To compute the kinetic energy density, we take the derivative of the two point function $\lim_{x\to y} \partial_x \partial_y \langle \psi^\dagger(x)\psi(y)\rangle$. Ultimately, this yields the same formula as before with the replacement of I_1 by

$$I_{1\mathrm{kin}}(\lambda_i) = \int \frac{\mathrm{d}^d p}{(2\pi)^d} \frac{p^2}{p^2 + \lambda_i} . \tag{5.46}$$

This latter integral is linearly divergent in $d = 1$, but again this divergent part is independent of λ_i and thus cancels in the expression for the kinetic energy. In $d = 2$, the leading divergence is quadratic and cancels in the sum but a subleading logarithmic divergence remains in the expression of the kinetic energy density, as well as in $\langle \psi(x)\psi(x)\rangle$ and $\langle \psi^\dagger(x)\psi^\dagger(x)\rangle$, contributing to the overall logarithmic divergence of the energy density.

5.B.2 FOUR-POINT FUNCTION

The Lieb-Liniger Hamiltonian contains quartic terms and, as a result, evaluating its energy density requires computing a 4-point function. As our states are Gaussian, we can use Wick's theorem or the expression for the generating functional $\mathcal{Z}_{j',j}$ to get:

$$\begin{aligned} \langle \psi^\dagger\psi^\dagger\psi\psi\rangle = {} & |\langle\psi\rangle|^4 + 4\,|\langle\psi\rangle|^2\, \langle\psi^\dagger\psi\rangle\big|_{\alpha^{(0)}=0} + |\langle\psi\rangle|^2\, \{\langle\psi^\dagger\psi^\dagger\rangle + \langle\psi\psi\rangle\}\big|_{\alpha^{(0)}=0} \\ & + 2\,\langle\psi^\dagger\psi\rangle\big|_{\alpha^{(0)}=0} \langle\psi^\dagger\psi\rangle\big|_{\alpha^{(0)}=0} + \langle\psi^\dagger\psi^\dagger\rangle\big|_{\alpha^{(0)}=0} \langle\psi\psi\rangle\big|_{\alpha^{(0)}=0} , \end{aligned} \tag{5.47}$$

where all the operators are taken in the same point x which we omitted since the problem is translation invariant. We have also split the 2-point functions into a part that does not depend on $\alpha^{(0)}$ and the zero mode contribution:

$$\langle\psi\rangle := \langle\psi(x)\rangle = \frac{1}{(2\pi)^d} \left\langle \psi_{p=0} \right\rangle . \tag{5.48}$$

The latter corresponds to the condensed fraction in the Lieb-Liniger model. Taking the mean field approximation is equivalent to neglecting the last two lines in eq. (5.47) as one assumes that the zero mode $\langle\psi\rangle$ dominates.

5.B.3 GRADIENTS

To carry the optimization efficiently, we need the gradient of $\langle h\rangle_{V,\alpha}$ with respect to the $2D + 1$ complex coefficients parameterizing the state. The coefficients include D complex parameters from M, D complex parameters from $\alpha^{(1)}$ vector and one parameter from $\alpha^{(0)}$. We present the computations for one 2-point function, $\langle \psi^\dagger(x)\psi(x)\rangle$, as the rest of the gradients are computed in the same manner. The derivative of the Fourier transformed 2-point function $C_{V,\alpha}(p)$ with respect to some GCTNS parameter a is given by

$$\frac{\partial C_{V,\alpha}(p)}{\partial a} = \left.\frac{\partial C_{V,\alpha}(p)}{\partial a}\right|_{\alpha^{(0)}=0} + \left\langle \psi_p^\dagger \right\rangle \frac{\partial \left\langle \psi_p \right\rangle}{\partial a} \delta(p) + \frac{\partial \left\langle \psi_p^\dagger \right\rangle}{\partial a} \left\langle \psi_p \right\rangle \delta(p)\,. \tag{5.49}$$

We start by computing the first term. Using

$$\frac{\mathrm{d}K^{-1}}{\mathrm{d}x} = -K^{-1}\frac{\mathrm{d}K}{\mathrm{d}x}K^{-1} \tag{5.50}$$

for a matrix K depending on a parameter x and $U^{-1}K^{-1}U = \left(p^2+L\right)^{-1}$, we obtain the derivative with respect to parameters of the mass matrix M

$$\left.\frac{\partial C_{V,\alpha}(p)}{\partial \mathrm{Re}(m_j)/i\mathrm{Im}(m_j)}\right|_{\alpha^{(0)}=0} = -\left(0,\alpha^{(1)*}\right) U \left(p^2+L\right)^{-1} F^{R/I}(j) \left(p^2+L\right)^{-1} U^{-1} \left(\alpha^{(1)},0\right)^T \tag{5.51}$$

where $F(j)$ is $2D \times 2D$ a complex matrix with elements

$$F^R_{lk}(j) = U^{-1}_{lj}U_{jk} + U^{-1}_{l,j+D}U_{j+D,k} \tag{5.52}$$

$$F^I_{lk}(j) = U^{-1}_{lj}U_{jk} - U^{-1}_{l,j+D}U_{j+D,k}\,. \tag{5.53}$$

The derivative with respect to the parameters of $\alpha^{(1)}$ yields

$$\begin{aligned}\left.\frac{\partial C_{V,\alpha}(p)}{\partial \mathrm{Re}(\alpha_j)/i\mathrm{Im}(\alpha_j)}\right|_{\alpha^{(0)}=0} &= -\left(0,\alpha^{(1)*}\right) U \left(p^2+L\right)^{-1} U^{-1} G^{R/I}(j) U \left(p^2+L\right)^{-1} U^{-1} \left(\alpha^{(1)},0\right)^T \\ &\quad + \left[\left(0,\alpha^{(1)*}\right) U \left(p^2+L\right)^{-1} U^{-1}\right]_j \pm \left[U \left(p^2+L\right)^{-1} U^{-1} \left(\alpha^{(1)},0\right)\right]_{j+D}\end{aligned} \tag{5.54}$$

where $G^R(j)$ and $G^I(j)$ are $2D \times 2D$ matrices

$$G^{R/I}(j) = -\left[e_j \cdot \left(0,\alpha^{(1)*}\right) \pm e_{j+D} \cdot \left(\alpha^{(1)},0\right) + \left(0,\alpha^{(1)*}\right)^T \cdot e_j^T \pm \left(\alpha^{(1)},0\right)^T \cdot e_{j+D}^T\right] \tag{5.55}$$

with e_j the $2D$ column vector with the j-th coefficient 1 and zero otherwise. To go get the equal point correlation functions in real space, we need to integrate over momenta, which means we need to compute the integral

$$I_2(\lambda_i,\lambda_j) = \int \frac{\mathrm{d}^d p}{(2\pi)^d} \frac{1}{p^2+\lambda_i} \frac{1}{p^2+\lambda_j}\,, \tag{5.56}$$

which is well-behaved in the dimensions we consider and given in appendix 5.C. The gradient of the kinetic term is obtained in the same way and adds a p^2 term in the previous integral

$$I_{2\mathrm{kin}}(\lambda_i,\lambda_j) = \int \frac{\mathrm{d}^d p}{(2\pi)^d} \frac{p^2}{p^2+\lambda_i} \frac{1}{p^2+\lambda_j}\,. \tag{5.57}$$

The zero mode terms in the gradient (5.49) are computed in the same way and the integration over p is then immediate because of the Dirac δ in eq. (5.49) (only the zero mode contributes).

5.C A FEW (REGULATED) MOMENTUM INTEGRALS

In one dimension, we can compute $I_1(\lambda)$ with the theorem of residues or using the fact that arctan is an explicit primitive of the integrand to get

$$I_1(\lambda_i) = \int \frac{\mathrm{d}p}{2\pi}\frac{1}{p^2+\lambda} = \frac{1}{2\sqrt{\lambda}}\,.$$

The integral $I_{1\text{kin}} = \int \mathrm{d}p/(2\pi)1-\lambda I_1$ clearly diverges. With a UV regulator Λ (unrelated to the non-relativistic regulator of section 5.3.2) we obtain

$$\begin{aligned}
I_{1\text{kin}}(\lambda) &= \int_{-\Lambda}^{\Lambda} \frac{\mathrm{d}p}{2\pi}\frac{p^2}{p^2+\lambda} \qquad (5.58)\\
&= \frac{\Lambda}{\pi} - \frac{\sqrt{\lambda}}{\pi}\arctan\left(\Lambda/\sqrt{\lambda}\right) \qquad (5.59)\\
&= \frac{\Lambda}{\pi} - \frac{\sqrt{\lambda}}{2} + o(1)\,. \qquad (5.60)
\end{aligned}$$

The integrals $I_2(\lambda_i,\lambda_j)$ and $I_2(\lambda_i,\lambda_j)$ are convergent and computed with the theorem of residues which yields

$$\begin{aligned}
I_2(\lambda_i,\lambda_j) &= \int \frac{\mathrm{d}p}{2\pi}\frac{1}{p^2+\lambda_i}\frac{1}{p^2+\lambda_j} \qquad (5.61)\\
&= \frac{1}{2(\sqrt{\lambda_i}+\sqrt{\lambda_j})(\sqrt{\lambda_i}\sqrt{\lambda_j})} \qquad (5.62)
\end{aligned}$$

and

$$\begin{aligned}
I_{2\text{kin}}(\lambda_i,\lambda_j) &= \int \frac{\mathrm{d}p}{2\pi}\frac{p^2}{p^2+\lambda_i}\frac{1}{p^2+\lambda_j} \qquad (5.63)\\
&= \frac{1}{2(\sqrt{\lambda_i}+\sqrt{\lambda_j})}\,. \qquad (5.64)
\end{aligned}$$

In two dimensions, I_1 already requires a UV regulator $\|p\| \leq \Lambda$

$$\begin{aligned}
I_1(\lambda) &= \int_{\|p\|\leq\Lambda} \frac{\mathrm{d}^2p}{(2\pi)^2}\frac{1}{p^2+\lambda}\\
&= \int_0^{\Lambda^2} \frac{\mathrm{d}(p^2)}{4\pi}\frac{1}{p^2+\lambda_i}\\
&= \frac{1}{4\pi}\ln\left(\Lambda^2+\lambda\right) - \frac{1}{4\pi}\ln(\lambda) \qquad (5.65)\\
&= \frac{1}{4\pi}\ln\left(\Lambda^2\right) - \frac{1}{4\pi}\ln(\lambda) + o(1)\,. \qquad (5.66)
\end{aligned}$$

Using the relation between I_1 and $I_{1\text{kin}}$ as in $d=1$, we obtain

$$\begin{aligned}
I_{1\text{kin}}(\lambda) &= \int_{\|p\|\leq\Lambda} \frac{\mathrm{d}^2p}{(2\pi)^2}\frac{p^2}{p^2+\lambda_i}\\
&= \frac{1}{4\pi}\left[\Lambda^2 - \lambda\ln\left(\Lambda^2+\lambda\right) + \lambda\ln(\lambda)\right]. \qquad (5.67)
\end{aligned}$$

The integral I_2 is convergent in $d = 2$ and computed with the theorem of residues

$$\begin{aligned} I_2(\lambda_i, \lambda_j) &= \int \frac{\mathrm{d}^2 p}{(2\pi)^2} \frac{1}{p^2 + \lambda_i} \frac{1}{p^2 + \lambda_j} \\ &= \begin{cases} \frac{\ln\left(\lambda_i / \lambda_j\right)}{4\pi(\lambda_i - \lambda_j)}, \text{for } \lambda_i \neq \lambda_j \\ \frac{1}{4\pi\lambda_i}, \text{for } \lambda_i = \lambda_j \end{cases} \quad . \end{aligned} \tag{5.68}$$

Finally, $I_{2\text{kin}}$ needs to be regulated. Using $I_{2\text{kin}}(\lambda_i, \lambda_j) = I_1(\lambda_j) - \lambda_i I_2(\lambda_i, \lambda_j)$, we get

$$I_{2\text{kin}}(\lambda_i, \lambda_j) = \int_{\|p\| \leq \Lambda} \frac{\mathrm{d}^2 p}{(2\pi)^2} \frac{p^2}{p^2 + \lambda_i} \frac{1}{p^2 + \lambda_j} = \frac{1}{4\pi} \ln\left(\Lambda^2\right) - \frac{\lambda_i \ln(\lambda_i) - \lambda_j \ln\left(\lambda_j\right)}{4\pi(\lambda_i - \lambda_j)} + o(1) \, . \tag{5.69}$$

6 ENTANGLEMENT ENTROPY FOR QUANTUM FIELD THEORIES

6.1 MOTIVATION

Entanglement is one of the key feature that distinguishes quantum from classical systems. In an entangled system, the constituents of the system cannot be described independently of all other parts – in other words, the state of the system is not separable. The interest in entanglement is driven by the rise of quantum technologies [195], where the entanglement acts as a resource, and the improved understanding of numerical Ansatz states like tensor networks. The computation of entanglement quantities like the Neumann or the Rényi entropy demand access to a partial density matrix of the system (cf. section 2.1). The evaluation of partial traces is very natural in lattice systems (like tensor networks) where the Hilbert space inherently has a local tensor product structure.

The calculation of entanglement properties is much more challenging in the case of continuous field theories. Here, the number of degrees of freedom is infinite, and the reduced density matrix can only be defined through the path integral formalism and entropies only become meaningfully defined after the introduction of an ultraviolet (UV) cutoff. A widely used approach to compute entanglement entropies is the replica trick [196] which can be carried out for free [197], integrable [198], and conformal field theories (CFT) [199]. It has been argued that some results apply also to the general non-integrable case [200], yet it remains an open question. Another field theoretical approach consists of the covariance matrix formalism where the entanglement entropies are computed from the correlation functions of Gaussian states [197, 201]. Finally, the field theory can be approximated with a lattice system and discrete methods tensor networks can be used to compute the entanglement measures. This has been extremely successful for computing equilibrium properties [26, 121] but is suffering from severe limitations when computing non-equilibrium dynamics due to the exponentially increasing bond dimension during time evolution [26].

The spectrum of current methods leaves room for a numerical method that works directly in the continuum and gives access to the reduced density matrix. A powerful class of numerical methods for quantum field theory (QFT) are Hamiltonian truncation (HT) based methods [202]. HT does not require to approximate the field theory with a lattice system and to take the continuum limit in the end. The method works directly in the continuum.

While HT is very successful at computing spectral properties and non-equilibrium time evolution, it has not been the most convenient choice for computing entanglement related quantities. In preceding works [203, 204], HT was used to calculate matrix elements between higher excited states. By using analytic replica techniques, correlation functions of twist fields and other entanglement related objects for those states were calculated. While such approaches proved useful at computing low Rényi entropies, the calculation of vN entropies and entanglement negativity remained out of reach.

We aim to combine the possibilities of Hamiltonian truncation with direct access to the reduced density matrix to compute entanglement related quantities.

The content of this chapter is based on Ref. [4].

6.2 EXECUTIVE SUMMARY

Entanglement entropy is one of the guiding principles of numerical and analytical development when considering quantum systems. The computation of entanglement related quantities for quantum field theories directly in the continuum, however, is difficult.

In this work, we develop a general way to construct reduced density matrices with Hamiltonian Truncation (HT). The algorithm splits the system explicitly into two subsystems and maps the original fields onto the two partitions. The output of the method is the reduced density matrix of a state explicitly represented in a computational basis which is a tensor product of the basis of the left and right subsystems. The tensor product structure enables the direct computation of almost any entanglement related quantity: von Neumann entropy, entanglement negativity, and mutual information. Additional, the method allows the direct study of the entanglement Hamiltonian and of the reduced density matrix of an interacting field theory. The method is model-independent and can be widely used on top of any HT code that uses expansions in free bases (see section 2.3) which is a common choice in modern applications [145, 205–208]. This enables us to take full advantage of the power of HT for real time evolution of a wide range of interacting QFT and study the whole spectrum of entanglement related quantities without needing to approximate the theory with a lattice system. It gives access to the entanglement properties of ground, excited and time dependent non-equilibrium states as well as thermodynamic entropies of thermal states.

As an initial test for the method, we benchmark it with the massive Klein-Gordon model. Since the Klein-Gordon model is a Gaussian model, its entanglement properties can be computed analytically with the covariance matrix formalism. e see excellent agreement between the HT based method and exact results for the von Neumann entropy in the ground and in thermal states (cf. figs. 6.4.2 and 6.4.3). Additionally, the time evolution of quenches between different masses agrees with the analytical prediction (cf. fig. 6.4.4). In a second step, we consider the sine-Gordon model, an interacting quantum field theory. We find good agreement with previous works when considering the time dynamics of the system (cf. fig. 6.4.6). The frequencies present in the time-evolution (cf. fig. 6.4.7) correspond to even breather frequencies as predicted in earlier works [209].

The method has the potential to provide new insights into interacting field theories directly in the continuum.

The chapter is organized as follows: In section 6.3 we present our method for computing reduced density matrices. We begin in section 6.3.1 with the theoretical construction and continue in section 6.3.2 outlining an efficient algorithm for the numerical implementation. In section 6.4 we present the results and a comparison against analytical predictions. Section 6.4.1 focuses on the results for the Klein Gordon model. These results are used a benchmark for the method. Section 6.4.2 details the results for the interacting sine Gordon model. We conclude in section 6.5 with an overview, discussion and the scope for the future work.

6.3 THEORETICAL FRAMEWORK

Our main goal is the construction of reduced density matrices for truncated Hamiltonian methods. We consider a field theory defined on a finite interval $F = [0, L]$ (full) with open boundary conditions and are interested in computing the entanglement between two subsystems $L = [0, \ell]$ (left) and $R = [\ell, L]$ (right). The letter L is used in this chapter as a label for a subsystem and for the length of the system; its interpretation will be clear from the context. Using HT, we can compute the density matrix ρ of a ground, excited, thermal or non-equilibrium state of the theory expressed in the Hilbert space $\mathcal{H}_F$ of the full interval F. However, tracing out a spatial part of the system is difficult in the full (momentum) basis. If we express ρ as ρ_{LR} in a Hilbert space $\mathcal{H}_L \otimes \mathcal{H}_R$ built out of Hilbert spaces $\mathcal{H}_L$ and $\mathcal{H}_R$ on the intervals L and R, we can trace one part of the system directly. We thus need to construct $\mathcal{H}_F$, $\mathcal{H}_L$ and $\mathcal{H}_R$ and find the unitary transformation

$$U_T : \mathcal{H}_F \to \mathcal{H}_L \otimes \mathcal{H}_R \tag{6.1}$$

to compute

$$\rho_{LR} = U_T \rho U_T^\dagger. \tag{6.2}$$

The idea of the method is visualized in fig. 6.3.1.

6.3.1 SPLITTING THE SYSTEM

FIELDS AND HILBERT SPACES

We start with the construction of the Hilbert space on the full interval $\mathcal{H}_F$. We expand the fields of the free theory (massless or massive) in terms of momentum modes. The Fock space generated by the mode creation operators serves as the computational basis. For concreteness, we choose an expansion around a massless free bosonic field theory with Dirichlet boundary conditions ($\phi(0) = \phi(L) = 0$) at the edges. The procedure is easily generalizable to expansions around massive free theories and other boundary conditions and could by construction be applied also in dimensions $d > (1+1)$.

The field expansion can be written as

$$\phi(x,t) = \sqrt{\frac{1}{L}} \sum_{k=1}^{\infty} \frac{1}{\sqrt{p_k}} \left(A_k e^{-ip_k t} + A_k^\dagger e^{ip_k t} \right) \sin(p_k x), \tag{6.3}$$

with $p_k = k\frac{\pi}{L}$ and A_k the bosonic modes on the full interval fulfilling the commutation relations $[A_k, A_l] = \left[A_k^\dagger, A_l^\dagger\right] = 0$ and $\left[A_k, A_l^\dagger\right] = \delta_{k,l}$. We refer to the modes A_k as full modes in the rest of the text.

The full modes A_k span the Hilbert space $\mathcal{H}_F$

$$|\vec{n}_F\rangle \equiv |n_1, n_2, \ldots\rangle \equiv \frac{1}{N_F} \prod_{k>0} \left(A_k^\dagger\right)^{n_k} |0\rangle \tag{6.4}$$

with n_k the bosonic occupation numbers, the normalization $N_F = \prod_{k>0} \sqrt{n_k!}$ and $|0\rangle$ the vacuum of the massive free boson theory.

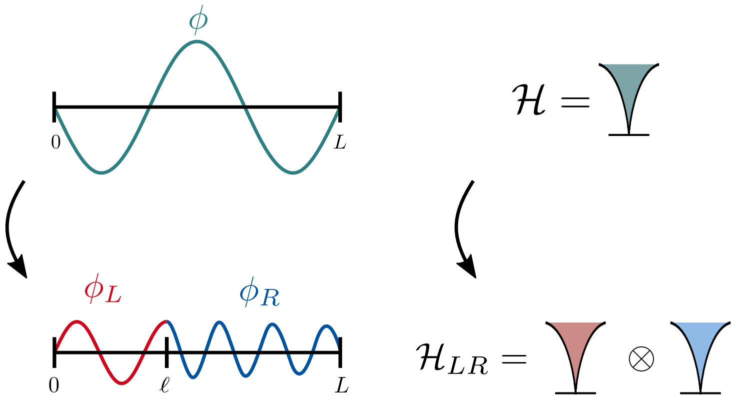

Figure 6.3.1: Schematic drawing of the algorithm. *Left* – We split the system on the top by representing the field ϕ living on the full interval $[0, L]$ with an equivalent setting: a pair of fields ϕ_L and ϕ_R living on sub-intervals $[0, \ell]$ and $[\ell, L]$ with an additional boundary condition at ℓ. The figure depicts the case of Neumann boundary conditions at the cut. The boundary conditions at the edges are chosen to be Dirichlet. *Right* Quantization of the fields gives rise to two isomorphic Hilbert spaces $\mathcal{H}$ and $\mathcal{H}_{LR} = \mathcal{H}_L \otimes \mathcal{H}_R$ and a unitary map between them. This maps density matrices to a form suitable for taking partial traces. The cones in the figure represent the exponentially growing number of states with the energy above the ground state. $\mathcal{H}$ and $\mathcal{H}_{LR}$ are generated on top of different vacua (horizontal line below the cone).

A cut at position ℓ divides the system into two subsystems L and R (left and right), as shown in fig. 6.3.1. Similarly to $\mathcal{H}$, we construct $\mathcal{H}_L \otimes \mathcal{H}_R$ by defining two fields ϕ_L and ϕ_R (split fields) living on the two sub-intervals and quantizing them.

The formulation of the fields on the intervals depends on the additional boundary conditions that we introduce at the cut. Throughout the chapter, the outer edges of the system are fixed to be Dirichlet boundary conditions ($\phi(0) = \phi(L) = 0$). In the following paragraph, all boundary conditions describe the boundary conditions at the cut. We choose to study Neumann ($\partial_x \phi|_{x=\ell} = 0$) and Dirichlet ($\phi_L(\ell) = \phi_R(\ell) = 0$) boundary conditions. In the main text, we focus on Neumann boundary conditions ($\partial_x \phi_L(\ell) = \partial_x \phi_R(\ell) = 0$). The treatment of the Dirichlet case is detailed in appendix 6.B. For Neumann boundary conditions at the cut, the fields on the intervals are defined as

$$\phi_L(x,t) = \sqrt{\frac{1}{\ell}} \sum_{m=1}^{\infty} \frac{1}{\sqrt{q_m^{(\ell)}}} \left(a_m^L e^{-iq_m^{(\ell)} t} + a_m^{L,\dagger} e^{iq_m^{(\ell)} t} \right) \sin\left(q_m^{(\ell)} x \right) \tag{6.5}$$

$$\phi_R(x,t) = \sqrt{\frac{1}{L-\ell}} \sum_{m=1}^{\infty} \frac{1}{\sqrt{q_m^{(L-\ell)}}} \left(a_m^R e^{-iq_m^{(L-\ell)} t} + a_m^{R,\dagger} e^{iq_m^{(L-\ell)} t} \right) \sin\left(q_m^{(L-\ell)} (L-x) \right) \tag{6.6}$$

where $q_m^{(\ell)} = \left(m - \frac{1}{2}\right) \frac{\pi}{\ell}$, $q_m^{(L-\ell)} = \left(m - \frac{1}{2}\right) \frac{\pi}{L-\ell}$ and a_m^σ are the bosonic annihilation operators on the two partitions for $\sigma \in \{L, R\}$. Both, the fields ϕ_L, ϕ_R and the modes $a_{L/R}$ defined in eqs. (6.5) and (6.6) fulfill the respective bosonic commutation relations. Fields and modes on different sub-intervals commute. In analogy to the full fields, the modes on the sub-intervals span their respective Hilbert spaces $\mathcal{H}_L$ and $\mathcal{H}_R$. The computational bases for the two sub-intervals are

$$|\vec{n}_\sigma\rangle \equiv \left|n_{1,\sigma}, n_{2,\sigma}, \dots\right\rangle \equiv \frac{1}{N_\sigma} \prod_{m>0} \left(a_m^{\sigma,\dagger}\right)^{n_m} |0\rangle_\sigma , \tag{6.7}$$

with the normalization $N_\sigma = \prod_{m>0} \sqrt{n_{m,\sigma}!}$. The choice of mixed boundary conditions (Dirichlet on the edges and Neumann at the cut) has the advantage that no zero-modes appear in the system. The vacua of the sub-intervals are not equal to each other and in particular they are not equal to the full system vacuum $|0\rangle_L \neq |0\rangle_R \neq |0\rangle$. The product space $\mathcal{H}_L \otimes \mathcal{H}_R$ is then generated by $|\vec{n}_L, \vec{n}_R\rangle \equiv |\vec{n}_L\rangle \otimes |\vec{n}_R\rangle$ on top of the vacuum $|0,0\rangle \equiv |0\rangle_L \otimes |0\rangle_R \neq |0\rangle$.

Before we continue, a couple of words on conventions and notation. Throughout the chapter, we will use k as an index for the full modes A_k and l, m as indices for partial modes a_m^σ. Greek indices always indicate a left or a right partition, $\sigma \in \{L, R\}$.

BOGOLIUBOV TRANSFORMATION

At first glance it might not be obvious that the descriptions of the system in terms of the full field and split fields are equivalent. From an intuitive point of view: for any given field configuration of ϕ, one can find a configuration of ϕ_L and ϕ_R that is arbitrarily close to it and still respects the boundary condition at the cut. We can choose the two functions defined on the subsets to be equal to the function defined on the full set everywhere except for a small neighborhood of the cut. There, they have to deviate in order to satisfy the boundary condition. This neighborhood, however, can be arbitrarily small while still preserving the continuity of the functions and the boundary conditions. Later, we give a more detailed argument for the correspondence on the algebraic level.

We now formally construct the unitary mapping between $\mathcal{H}_F$ and $\mathcal{H}_L \otimes \mathcal{H}_R$ proposed in eq. (6.1)

$$(U_T)_{\vec{n}_L \vec{n}_R; \vec{n}_F} = \langle \vec{n}_L, \vec{n}_R | \vec{n}_F \rangle . \tag{6.8}$$

In order to compute the matrix elements (6.8), we take two distinct steps. First, we express the full modes A_k in terms of the partial modes $\{a_m^\sigma\}_{m,\sigma}$ and $\{a_n^{\sigma\dagger}\}_{n,\sigma}$. Second, we rewrite the full vacuum in terms of the partial vacua and partial modes. The latter is particularly important because the Hilbert spaces are not defined on top of the same vacuum.

We rewrite the full modes as a mixture of modes defined on the sub-intervals

$$A_k = \sum_m \gamma_{km}^{+,L} a_m^L + \sum_m \gamma_{km}^{-,L} a_m^{L,\dagger} + \sum_m \gamma_{km}^{+,R} a_m^R + \sum_m \gamma_{km}^{-,R} a_m^{R,\dagger} , \tag{6.9}$$

where the coefficients γ are to be determined. The coefficients γ are the result of identifying the fields on the full interval with the split fields

$$\phi(x,t) = \begin{cases} \phi_L(x,t) & \text{if } x < \ell, \\ \phi_R(x,t) & \text{if } \ell < x < L \end{cases} . \tag{6.10}$$

This identification, the continuity condition, is the core of the unitary map between the full and the split Hilbert spaces.

We can express the full modes A_k in terms of the fields $\phi(x,t)$ and the canonical momentum operator $\pi(x,t) = \frac{\partial}{\partial t}\phi(x,t)$

$$A_k = \sqrt{\frac{p_k}{L}} \int_0^L \mathrm{d}x \left[\phi(x,t) + \frac{i}{p_k}\pi(x,t) \right] \sin\left(p_k x\right). \tag{6.11}$$

Combining eq. (6.11) with the continuity condition in eq. (6.10) links the full system modes A_k to the partial modes a_m^σ. Evaluating the integral, we obtain the coefficients γ for Neumann boundary conditions at the cut as

$$\gamma_{km}^{+,L} = \begin{cases} \frac{(-1)^m \sqrt{p_k} \cos(p_k \ell)}{\sqrt{L\ell}\sqrt{q_m^{(\ell)}}(p_k - q_m^{(\ell)})} & p_k \neq q_m^{(\ell)} \\ \sqrt{\frac{\ell}{L}} & p_k = q_m^{(\ell)} \end{cases} \tag{6.12}$$

$$\gamma_{km}^{-,L} = \frac{(-1)^m \sqrt{p_k} \cos\left(p_k \ell\right)}{\sqrt{L\ell}\sqrt{q_m^{(\ell)}}\left(p_k + q_m^{(\ell)}\right)} \tag{6.13}$$

$$\gamma_{km}^{+,R} = \begin{cases} \frac{(-1)^{m+1} \sqrt{p_k} \cos(p_k \ell)}{\sqrt{L(L-\ell)}\sqrt{q_m^{(\ell)}}(p_k - q_m^{(L-\ell)})} & p_k \neq q_m^{(L-\ell)} \\ \frac{(-1)^{k+1}\sqrt{L-\ell}}{\sqrt{L}}\left(1 + \frac{\sin(p_k \ell)}{2p_k(L-\ell)}\right) & p_k = q_m^{(L-\ell)} \end{cases} \tag{6.14}$$

$$\gamma_{km}^{-,R} = \frac{(-1)^{m+1} \sqrt{p_k} \cos\left(p_k \ell\right)}{\sqrt{L(L-\ell)}\sqrt{q_m^{(\ell)}}\left(p_k + q_m^{(L-\ell)}\right)}. \tag{6.15}$$

The special cases in eqs. (6.12) and (6.14) are divergences of the integrand. The coefficients are obtained by integrating the special cases separately.

MULTIMODE SQUEEZED COHERENT VACUUM

When expressing the full modes as a superposition of partial modes, we also have to re-express the vacuum of the system. To find a formulation of the full system vacuum in terms of the partial modes, we identify eq. (6.9) as a multi-mode Bogoliubov transformation [210]

$$\begin{bmatrix} A \\ A^\dagger \end{bmatrix} = M \begin{bmatrix} a \\ a^\dagger \end{bmatrix} \tag{6.16}$$

with $A = \left(A_1, \dots, A_{N_F}\right)$, $a = \left(a_1^L, \dots, a_{N_L}^L, \dots, a_{N_R}^R\right)$ and

$$M = \begin{bmatrix} u & v \\ v & u \end{bmatrix} = \begin{bmatrix} \gamma^{L,+} & \gamma^{R,+} & \gamma^{L,-} & \gamma^{R,-} \\ \gamma^{L,-} & \gamma^{R,-} & \gamma^{L,+} & \gamma^{R,+} \end{bmatrix}. \tag{6.17}$$

Note that M is not an operator here, but a matrix of numbers. Since all the coefficients γ in eqs. (6.13) to (6.14) are real, we focus on the case of real u and v. We use the same symbols as in eqs. (6.13) to (6.14) without the subscript indices to refer to matrices of coefficients. For ease of notation, we still express equations in terms of $u = \left[\gamma^{L,+} \quad \gamma^{R,+}\right]$ and $v = \left[\gamma^{L,-} \quad \gamma^{R,-}\right]$.

The transformation (6.17) expresses bosonic modes A in terms of different bosonic modes a. Thus, the transformation must preserve the commutation relations. These are encoded in the symplectic structure of M

$$M^{-1} = KM^{\dagger}K \quad \text{with} \quad K = \begin{bmatrix} \mathbb{1} & \\ & -\mathbb{1} \end{bmatrix}. \tag{6.18}$$

It can be verified that γ coefficients in eqs. (6.12) to (6.15) obey the symplectic structure of the Bogoliubov transformation.

The Bogoliubov transform (6.17) is equivalent to a unitary transformation [210]

$$U \begin{bmatrix} a \\ a^{\dagger} \end{bmatrix} U^{\dagger} = M \begin{bmatrix} a \\ a^{\dagger} \end{bmatrix} \tag{6.19}$$

with

$$U = \exp\left(-\frac{1}{2} \begin{bmatrix} a^{\dagger T} & a^{T} \end{bmatrix} K \ln M \begin{bmatrix} a \\ a^{\dagger} \end{bmatrix} \right). \tag{6.20}$$

In contrast to M, U is an operator and not a matrix of numbers. Thus, the vacuum of the full modes $|0\rangle$ can be expressed in terms of the vacuum of the partial modes $|0,0\rangle$ as

$$|0\rangle = U\, |0,0\rangle\,. \tag{6.21}$$

because then $A_k\, |0\rangle = U^{\dagger} a U U^{\dagger}\, |0,0\rangle = 0$.

The disentangling form transforms U into a more convenient form for actual computations,

$$U = \exp\left(-\operatorname{Tr}(\sigma)\right) \exp\left(-a^{\dagger T} \chi a^{\dagger}\right) \exp\left(-2a^{\dagger T} \sigma a\right) \exp\left(a^{T} \tau a\right) \tag{6.22}$$

with

$$\chi = \frac{1}{2} u^{-1} v, \quad \sigma = \frac{1}{2} \ln u, \quad \tau = \frac{1}{2} v^{*} u^{-1}\,. \tag{6.23}$$

Since we have an expression of the full modes in terms of the partial modes and an expression of the full vacuum in terms of the partial vacua, we can compute the matrix elements of U_T. The elements of U_T are overlaps between states in the full basis $|\vec{n}_F\rangle$ and the split basis $|\vec{n}_L, \vec{n}_R\,\rangle$.

$$\begin{aligned} \langle \vec{n}_L, \vec{n}_R \,|\vec{n}_F\rangle =& \frac{1}{N} \langle 0,0| \left[\prod_{m>0} \left(a^{R}_{m}\right)^{n_{m,R}} \left(a^{L}_{m}\right)^{n_{m,L}} \right] \times \\ & \left[\prod_{k>0} \left[\sum_{\sigma} \sum_{l>0} \left(\gamma^{\sigma,-}_{kl} a^{\sigma}_{l} + \gamma^{\sigma,+}_{kl} a^{\sigma\dagger}_{l} \right) \right]^{n_k} \right] \times \\ & \left[\exp\left(-\sum_{ij} \sum_{\sigma,\chi} a^{\sigma\dagger}_{i} \chi^{\sigma,\xi}_{ij} a^{\xi\dagger}_{j} \right) \right] |0,0\rangle\,, \end{aligned} \tag{6.24}$$

with

$$N = \frac{1}{\exp\left(-\operatorname{Tr}\left(\sigma\right)\right)} \left[\prod_{m>0} \sqrt{\left(n_{m,R}!\right)\left(n_{m,L}!\right)} \right] \left[\prod_{k>0} \sqrt{\left(n_k!\right)} \right]. \tag{6.25}$$

The first bracket in eq. (6.24) builds the occupation number state $\langle \vec{n}_L, \vec{n}_R|$ from the partial vacuum $\langle 0, 0|$. The order of left and right creation operators does not matter here, since they commute as they act on different partitions. The second bracket represents the operators $A_k^\dagger$ which build $|\vec{n}_F\rangle$ on top of the vacuum of the full modes $|0\rangle$. We choose to express the full modes in terms of the partial modes [cf. eq. (6.9)]. The opposite way of expressing the partial modes in terms of full modes would work as well. The last bracket in eq. (6.24) expresses the vacuum of full modes in terms of the split modes. Looking at formulation of the norm in eq. (6.25), we recognize the first term from the transformation of the vacuum; it is constant for all matrix elements. The second and third term are the norms of the partial and the full occupation number states. The contributions of the exponentials with σ and τ in eq. (6.22) vanish due to the order of operators in the exponentials and their action on the vacuum to the right.

EQUIVALENCE OF HILBERT SPACES

We have now defined the unitary transformation between $\mathcal{H}$ and $\mathcal{H}_L \otimes \mathcal{H}_R$. Before we proceed to numerical considerations, we would like to justify why the two descriptions of a physical state are equivalent despite the additional boundary condition at the cut.

We can think about the transformation in terms of Fourier analysis. The sine modes of the split intervals in eqs. (6.5) and (6.6) serve as a functional basis in which a field configuration of the full interval field is expanded. The sine functions build a basis as a consequence of Carleson's theorem for convergence of Fourier series [211, 212].

However, we are dealing with quantum fields not just simple scalar valued functions. Upon quantization, the Fourier coefficients in the expansion become operator valued as indicated in eqs. (6.5) and (6.6). The symplectic structure of the Bogoliubov transform between the two algebras (6.18) guarantees that the two quantizations of the system, the one in terms of the full field in eq. (6.3) and the one in terms of the split fields, are equivalent.

In the complete, infinite dimensional Hilbert spaces, the unitary map between $\mathcal{H}$ and $\mathcal{H}_L \otimes \mathcal{H}_R$ is exact. However, once we introduce a truncation, it becomes an approximation in the same fashion as HT is always an approximation of the quantum state using the low energy sector of the Hilbert space. Using the partial field expansion then becomes in spirit very similar to using a finite Fourier series to approximate a function. In section 6.4 we demonstrate that such an approximation indeed performs well at computing entanglement entropies.

TRUNCATION

The mapping between the full system and the partitioned system formulated without considering the truncation until now. In its current form, we cannot transfer the method to a computer because the sums contain infinitely many terms. We have to consider a finite dimensional approximation of the Hilbert spaces. In HT, it is often important to choose the most suitable truncation scheme for the problem. In our case, we have to introduce three truncations: on for each $\mathcal{H}$, $\mathcal{H}_L$ and $\mathcal{H}_R$. For convenience, we choose the cutoffs such that the Bogoliubov transformation (6.17) becomes a square matrix. This leads to the restriction $s_F = s_L + s_R$, where s_F, s_L and s_R are the number of momentum modes kept in the full system, the left and the right partition, respectively. We truncate all Hilbert spaces, $\mathcal{H}$, $\mathcal{H}_L$ and $\mathcal{H}_R$ with an energy cutoff such that the cutoff

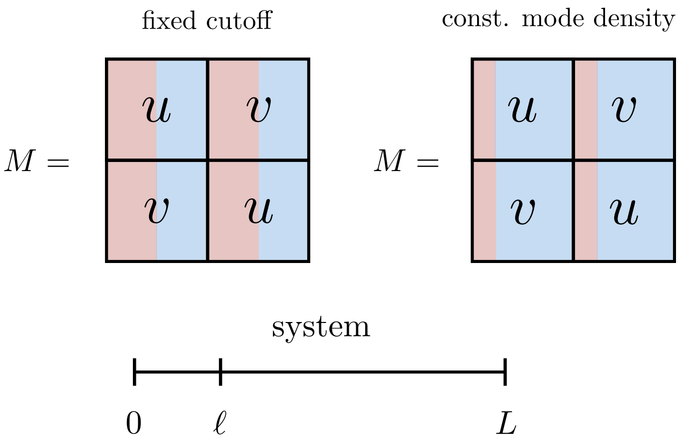

Figure 6.3.2: Illustration of the M matrix for different cut-off schemes. The amount of coefficients for the left and the right partition in the matrices u and v differ depending on the cut-off scheme. The coefficients belonging to the left(right) side are displayed in red(blue).

energy is equal to the energy of the single excitation of the largest momentum mode kept, s_F, s_L and s_R respectively. For a free massless boson Hamiltonian, the energy of the state $|\vec{n}_F\rangle$ defined in eq. (6.3) above the ground state is $\epsilon(\vec{n}_F) - \epsilon(0) = \frac{\pi}{L}\sum_{k=1}^{\infty} k n_k$. We use the formula to determine the cut-off of H_0 as described in section 2.3. The definition of the energy for the states in the split Hilbert spaces in eqs. (6.5) and (6.6) follow analogously: L is replaced by ℓ and $L-\ell$, respectively.

The symplectic structure in eq. (6.18) is fulfilled exactly in the infinite, non-truncated space. By introducing the cut-off this property can be compromised. Different cut-off schemes are benchmarked by checking the bosonic commutation relations, *i.e.* the symplectic structure of the resulting transformation.

We investigate two different cut-off schemes. In the first one, we distribute the number of partial modes equally across the left and the right partition independent of the position of the cut (fixed cutoff): $s_L = s_R = s_F/2$. This leads to an easy implementation but is questionable from a physical standpoint. A short interval with many modes leads to a greater resolution in position space than the same number of modes on a large interval. Furthermore, such a non-uniform UV cut-off leads to a position-dependent non-universal constant in the entanglement entropy that obscures the true functional dependence. The second cut-off scheme takes into account the length of the partition. The number of modes is distributed proportionally to the length of the interval $s_L = \frac{\ell}{L} s_F$ and $s_R = s_F - s_L$ (constant mode density). This scheme keeps a constant density of momentum modes and thus a homogeneous UV cut-off. Both cut-off schemes are illustrated in fig. 6.3.2.

All further considerations use the constant mode density cut-off scheme. Most importantly, it reproduces the bosonic commutation relations more faithfully (cf. appendix 6.A).

6.3.2 ALGORITHM

The evaluation of the overlap as given in eq. (6.24) is difficult because the expression is not normal ordered and the sums in the expression are taken to powers n_k. Its computation in the current form would require an overwhelming number of commutations of individual mode operators.

GENERATING FUNCTIONAL FORMULATION

The expression simplifies if we express it in the spirit of a generating functional. The repeated application of a mode a is equivalent to

$$a^n = \left[\frac{\mathrm{d}^n}{\mathrm{d}\mathcal{J}^n} e^{\mathcal{J} a} \right]_{\mathcal{J}=0}, \tag{6.26}$$

where $\mathcal{J}$ is a scalar variable.

Inserting the identity (6.26) in the formulation of the matrix elements of U_T in eq. (6.24), we obtain an expression resembling a generating functional

$$\langle \vec{n}_L, \vec{n}_R | \vec{n}_F \rangle = \frac{1}{N} \prod_{m>0} \prod_{\sigma} \frac{\mathrm{d}^{n_{m,\sigma}}}{\mathrm{d}j_{m,\sigma}^{n_{m,\sigma}}} \prod_{k>0} \frac{\mathrm{d}^{n_k}}{\mathrm{d}J_L^{n_k}} \langle 0,0| e^S e^F e^V |0,0\rangle \Big|_{J_k=0, j_{m,\sigma}=0}, \tag{6.27}$$

with

$$S = \sum_{m>0} \sum_{\sigma} j_{m,\sigma} a_m^{\sigma} \tag{6.28}$$

$$F = \sum_{k,m>0} \sum_{\xi} J_k \left(\gamma_{k,m}^{+,\xi} a_m^{\xi\dagger} + \gamma_{k,m}^{-,\xi} a_m^{\xi} \right) \tag{6.29}$$

$$V = -\sum_{\kappa,\lambda} \sum_{m,n>0} a_{-m}^{\kappa} \chi_{m,n}^{\kappa,\lambda} a_{-n}^{\lambda} \,. \tag{6.30}$$

Here, S are all terms related to the split modes, F is the term that is associated with the full system modes and V are the terms that build the vacuum. We introduced two kinds of additional, scalar variables: J_k are the additional variables for the full modes and $j_{m,\sigma}$ are defined for the partial modes.

Using the Baker-Campbell-Hausdorff (BCH) relations [213], we can bring this expression into normal order and evaluate the expectation value. The series of commutators in the BCH relations terminate at most at the second order since the highest power of mode operators in the exponent is two. We can write the normal ordered expression as

$$e^S e^F e^V = Z\, e^{[A,V]} \; : e^S e^F e^V : \tag{6.31}$$

with

$$Z = \exp\left[\mathrm{ComF} + \mathrm{ComSF} + \mathrm{ComAV} \right]. \tag{6.32}$$

The terms ComF, ComSF and ComAV are results of the BCH operations. They are defined as

$$\mathrm{ComF} = \frac{1}{2} \sum_{k,k'=1}^{\infty} J_k J_{k'} \sum_{\sigma} \sum_{n>0} \gamma_{k,n}^{+,\sigma} \gamma_{k',n}^{-,\sigma} \tag{6.33}$$

$$\mathrm{ComSF} = \sum_{m>0} \sum_{\sigma} j_{m,\sigma} \sum_{k>0} J_k \gamma_{k,m}^{+,\sigma} \tag{6.34}$$

$$\mathrm{ComAV} = -\frac{1}{2} \sum_{m>0} \sum_{\sigma} \left\{ j_{m,\sigma} + \sum_{k>0} J_k \gamma_{k,m}^{-,\sigma} \right\} \sum_{m'>0} \sum_{\mu} \left\{ j_{m',\mu} + \sum_{k'>0} J_{k'} \gamma_{k',m'}^{-,\mu} \right\} \left(\chi_{m',m}^{\mu,\sigma} + \chi_{m,m'}^{\sigma,\mu} \right). \tag{6.35}$$

The commutator $[A, V]$ is linear in creation operators. The derivation of the commutators is detailed in section 6.C.1.

The problem of computing the overlap reduces to computing multiple derivatives of a scalar expression if we express eq. (6.24) as the derivative of a generating functional

$$\langle \vec{n}_L, \vec{n}_R \,|\vec{n}_F\rangle = \frac{1}{N} \prod_{m>0} \prod_{\sigma} \frac{\mathrm{d}^{n_{m,\sigma}}}{\mathrm{d}j_{m,\sigma}^{n_{m,\sigma}}} \prod_{k>0} \frac{\mathrm{d}^{n_k}}{\mathrm{d}J_L^{n_k}} Z\bigg|_{J_k=0, j_{m,\sigma}=0} . \tag{6.36}$$

TACKLING THE EXPONENTIAL COMPLEXITY OF DIFFERENTIATION

The next goal is the efficient calculation of all derivatives in eq. (6.36). The pure symbolic evaluation of derivatives becomes prohibitively expensive with increasing cut-off. The number of terms to evaluate exponentially with the number of derivatives n. In the following, we show how the structure of the generating functional helps us to make the evaluation more efficient.

From an algorithmic point of view, there are two distinct exponentially scaling problems involved in the computation. On the one hand, the size of the unitary transformation grows with the size of the Hilbert space. We have to evaluate exponentially many terms in order to fill the matrix. It is impossible to circumvent this exponential since the method is based on exact diagonalization. On the other hand, each matrix element needs an increasing number of derivatives with increasing occupation numbers. The number of terms in the derivation scales also exponentially with the occupation number (and thus the cut-off). In the following section, we describe an algorithm to make the evaluation of the derivatives feasible for relevant cut-offs. We are not able to reduce the exponential growth of terms to a polynomial growth. However, we can restrict ourselves to computing only relevant terms which largely reduces the exponential growth. Thus, it is possible to reach HT cut-offs that provide reasonable approximations of interesting physics.

A commonly used alternative to symbolic differentiation is automatic differentiation (AD) [214, 215]. The algorithm of AD tracks the computation of the function and uses predefined derivatives of elementary functions to evaluate the derivative numerically. In our case, it is hard to use AD directly since we have to compute possibly very high derivatives of the function and that we do not need the actual function value. Furthermore, we can exploit the structure of the function to determine which terms must be 0 without computing them. Here, we do not rely on AD, but devise an individual scheme that uses as much information from analytic considerations as possible.

By inspecting the structure of the expressions in eq. (6.36), we note that the derivative always acts on an expression of the form

$$Z = e^T , \tag{6.37}$$

with $T = \text{ComF} + \text{ComSF} + \text{ComAV}$, a summary of all terms in the exponent of Z in eq. (6.32). For the ensuing discussion, we introduce a shorthand notation for the derivatives of Z

$$\begin{aligned} \frac{\mathrm{d}}{\mathrm{d}\mathcal{J}_i} Z &= \frac{\mathrm{d}}{\mathrm{d}\mathcal{J}_i} e^T \\ &= T\left[\mathcal{J}_i, \bullet\right] e^T . \end{aligned} \tag{6.38}$$

The expression $T \equiv T[\bullet, \bullet]$ has two arguments because the commutators in T are always quadratic in J_k and $j_{m,\sigma}$. For the rest of the discussion of the algorithm, we will not distinguish $j_{m,\sigma}$ and J_k. We can always write them in terms of a general $\mathcal{J}_i$ by using i as a multi-index.

This new notation helps us to demonstrate that many terms are 0 and we can drop them. Due to the commutativity of the derivatives and the step of setting $\mathcal{J}_k = 0$ in the end [cf. eq. (6.36)], we find

$$\begin{aligned} T\left[\mathcal{J}_i, \mathcal{J}_{i'}\right] &= T\left[\mathcal{J}_{i'}, \mathcal{J}_i\right] \\ T\left[\bullet, \bullet\right]\rvert_{\mathcal{J}_i=0\,\forall i} &= 0 \\ T\left[\mathcal{J}_k, \bullet\right]\rvert_{\mathcal{J}_i=0\,\forall i} &= 0\,\forall k\,. \end{aligned} \tag{6.39}$$

All expressions that are not derived twice must be zero if we set all $\mathcal{J}_k = 0$ in the end because $\mathcal{J}_k$ appears quadratically in each commutator. Thus, the number of Ts for each derivative is given by $N_T = \frac{\sum_i n_i}{2}$, where n_i are the occupation numbers of the full-system state and the partitioned state.

The restrictions described above lead to a more efficient algorithm in comparison to symbolic derivation of the full expression. Considering the restrictions in eq. (6.39), the result of the derivatives in eq. (6.36) is heavily constrained. Every term must be derived twice (otherwise it is 0). Furthermore, we only sum over unique combinations since we can freely exchange the arguments of T and the order of the $T[\mathcal{J}_{l_1}, \mathcal{J}_{l_2}]$ in the product over l.

The input of the algorithm is a list of $\mathcal{J}_i$ with corresponding powers n_i, and we only compute combinations of fully derived T

$$\prod_i \frac{\mathrm{d}^{n_i}}{\mathrm{d}\mathcal{J}_i^{n_i}} e^T \bigg\rvert_{\mathcal{J}_i=0} = {\sum_k}' c_k \prod_l T^{p_{kl}}\left[\mathcal{J}_{l_1}, \mathcal{J}_{l_2}\right], \tag{6.40}$$

where c_k are the multiplicities of the terms in T. The sum $\sum'$ runs over all unique combinations of T. A combination is unique if it cannot be transformed into another combination of Ts by swapping the arguments of T or commuting Ts. This corresponds to iterating over all pairwise lexicographically ordered tuples of $\mathcal{J}$. The exponents p_{kl} are the powers of certain terms T if the same arguments $(\mathcal{J}_{l_1}, \mathcal{J}_{l_2})$ appear multiple times in the same sequence. Thus, the number of terms in the product over l can vary depending on the number of individual combinations of $(\mathcal{J}_{l_1}, \mathcal{J}_{l_2})$. Since we are not considering the full system and the split modes separately at the moment, the indices k, m, and l are used without further implications here.

For concreteness, we consider a simple example of three modes $\mathcal{J}_1$, $\mathcal{J}_2$ and $\mathcal{J}_3$ to illustrate the procedure. We are interested in the second derivative with respect to each $\mathcal{J}_i$. In terms of occupation numbers, we can write the configuration as $\vec{n} = (2, 2, 2)$, where $\vec{n}$ is the vector of occupations numbers. The primed sum in eq. (6.40) runs over all unique configurations of derivatives. In our example, there are five distinct configurations

$$\begin{aligned} 1 &: (\mathcal{J}_1, \mathcal{J}_1), (\mathcal{J}_2, \mathcal{J}_2), (\mathcal{J}_3, \mathcal{J}_3) \\ 2 &: (\mathcal{J}_1, \mathcal{J}_2), (\mathcal{J}_1, \mathcal{J}_2), (\mathcal{J}_3, \mathcal{J}_3) \\ 3 &: (\mathcal{J}_1, \mathcal{J}_1), (\mathcal{J}_2, \mathcal{J}_3), (\mathcal{J}_2, \mathcal{J}_3) \\ 4 &: (\mathcal{J}_1, \mathcal{J}_3), (\mathcal{J}_1, \mathcal{J}_3), (\mathcal{J}_2, \mathcal{J}_2) \\ 5 &: (\mathcal{J}_1, \mathcal{J}_2), (\mathcal{J}_1, \mathcal{J}_3), (\mathcal{J}_2, \mathcal{J}_3)\,. \end{aligned} \tag{6.41}$$

The tuples in eq. (6.41) represent the arguments of $T[\bullet,\bullet]$. Combinations other than those listed above can either be generated by swapping tuples or by exchanging the arguments inside a tuple. A swap of two tuples is allowed due to the commutativity of multiplication in eq. (6.40). The exchange of arguments is equivalent to exchanging the derivatives of a single T which corresponds to one of the identities in eq. (6.39). Since there are six derivatives in total, we must have three distinct T terms in each string. We can express the five combinations in eq. (6.41) more compactly with powers p_{kl}

$$\begin{aligned}
1 &: (\mathcal{J}_1, \mathcal{J}_1), (\mathcal{J}_2, \mathcal{J}_2), (\mathcal{J}_3, \mathcal{J}_3) \\
2 &: (\mathcal{J}_1, \mathcal{J}_2)^2, (\mathcal{J}_3, \mathcal{J}_3) \\
3 &: (\mathcal{J}_1, \mathcal{J}_1), (\mathcal{J}_2, \mathcal{J}_3)^2 \\
4 &: (\mathcal{J}_1, \mathcal{J}_3)^2, (\mathcal{J}_2, \mathcal{J}_2) \\
5 &: (\mathcal{J}_1, \mathcal{J}_2), (\mathcal{J}_1, \mathcal{J}_3), (\mathcal{J}_2, \mathcal{J}_3) .
\end{aligned} \tag{6.42}$$

Here, k is the index of the overall combination of all pairs $\mathcal{J}$ and l is the index of the tuple in the string. More concretely, $p_{2,1} = 2$ because the second string contains $(\mathcal{J}_1, \mathcal{J}_2)^2$ as first pair.

Some configurations in eq. (6.41) may appear multiple times during the application of the product rule in eq. (6.40). Thus, we have to take care of the multiplicities in front of the terms. In our simple example, we can just list them as $\vec{c} = (1, 2, 2, 2, 8)$. Here, they are calculated by explicitly performing the derivatives on the left side of eq. (6.40). The primed sum in eq. (6.40) can be evaluated given all configurations in eq. (6.41) and the vector $\vec{c}$. All terms of the form $T[\mathcal{J}_{l_1}, \mathcal{J}_{l_2}]$ are numbers that can be evaluated by summing the derivatives of commutators in eq. (6.32) explicitly.

As demonstrated in the example, the computation of eq. (6.40) can be divided into two subproblems. Firstly, we have to determine all unique combinations of pairs $\left(\mathcal{J}_{l_1}, \mathcal{J}_{l_2}\right)$ for a given $\vec{n}$. Secondly, we have to compute the coefficients c_k given p_{kl} and the tuples $(\mathcal{J}_{l_1}, \mathcal{J}_{l_2})$.

The first task can be solved with a tree-based algorithm that is described in detail in section 6.C.2. The idea is to build only the combinations of tuples $(\mathcal{J}_{l_1}, \mathcal{J}_{l_2})$ that adhere to the uniqueness condition defined for the primed sum, i.e. lexicographical ordering of all index tuples. The condition can be checked locally at every node of the tree. Thus, only nodes that can still build valid configurations are expanded in subsequent operations. The trivial approach of listing all combinations of $\mathcal{J}_i$ for a given $\vec{n}$ and filtering for the unique ones gets prohibitively costly already for low cut-offs.

The coefficients c_k have a closed form expression and are given by

$$c_k = \frac{\prod_i (n_i!)}{2^{N_{\mathrm{diag},k}} \prod_l (p_{kl}!)}, \tag{6.43}$$

where n_i are the occupation numbers and $N_{\mathrm{diag},k}$ is the number of identical arguments for T in the string with index k. In our example of $\vec{n} = (2, 2, 2)$, $N_{\mathrm{diag},1} = 3$ and $N_{\mathrm{diag},3} = 1$. The proof of the equation is given in the appendix of [4].

Finally, we can put all the pieces together. An element of U_T corresponds to the calculation of an overlap of the form $\langle \vec{n}_L, \vec{n}_R | \vec{n}_F \rangle$. Each of the states is given as an occupation number vector. Equation (6.36) connects the occupation numbers to derivatives of a scalar function. These derivatives can be computed explicitly by first enumerating all unique configurations of the primed sum in eq. (6.40). Each of the tuples in a configuration represents the arguments of T. The derivatives of T for some tuple $\left(\mathcal{J}_{l_1}, \mathcal{J}_{l_2}\right)$ can be evaluated explicitly. The product of all T values in a string is weighed by a factor [cf. eq. (6.43)] and summed to yield the final value of the matrix element. The explicit expressions for the derivatives of the commutators are given in section 6.C.1.

6.3.3 MODELS

We test the new method to compute entanglement entropies with HT on two well-known models, the free Klein-Gordon theory and the interacting sine-Gordon model. Our aim is to show that the algorithm described in section 6.3.2 is indeed model independent and leads to correct entanglement entropies.

THE KLEIN-GORDON MODEL

One of the most fundamental quantum field theories is the one-dimensional Klein-Gordon (KG) model, the massive free boson theory, described by the Hamiltonian

$$H_{\mathrm{mFB}} = \frac{1}{2}\int_0^L \mathrm{d}x \left[\left(\partial_t \phi(x)\right)^2 + \left(\partial_x \phi(x)\right)^2 + m^2\phi^2(x)\right], \tag{6.44}$$

where $\phi(x)$ is a real-valued quantum field and m is the mass of the boson.

Its entanglement properties are known analytically both from replica trick techniques [197, 199] and from covariance matrix methods [197, 201] including the equilibrium states and the non-equilibrium dynamics. For the massless case, the entanglement entropy can be computed analytically [199]

$$S(\ell) = \frac{c}{6}\log\left(\frac{L}{\pi a}\sin\left(\frac{\pi\ell}{L}\right)\right) + 2g + U(a)\,, \tag{6.45}$$

where the central charge of the CFT $c = 1$, a is a UV cutoff, g is the Affleck-Ludwig boundary entropy [216] and $U(a)$ is a non-universal constant dependent on the precise form of the cutoff.

Due to a finite correlation length $\xi \sim \frac{1}{m}$ the entanglement for $m > \frac{1}{L}$ saturates to an area law plateau where $S(\ell) = \text{const}$. At distance closer than ξ to the boundaries, the vN entropy S_N interpolates smoothly to the zero value at the boundaries. For $m < \frac{1}{L}$, there is a smooth crossover from a log law to an area law scaling of the entanglement entropy.

For thermal states, the vN entanglement entropy becomes the thermodynamic entropy and there is a smooth crossover with increasing temperature to a volume law $S(\ell) \propto \ell$. In non-equilibrium dynamics in the massless case, the vN entropy is expected to grow linearly in time [196]. For finite systems, the growth stops when excitations from the splitting point reach the boundaries of the system and one expects a recurrent dynamics. In the massive case, the linear growth is superposed with an oscillatory component with a frequency given by the boson mass [217].

SINE GORDON MODEL

A paradigmatic model of strongly interacting QFT is the *sine-Gordon* (sG) *model*

$$H_{\mathrm{sG}} = \int \mathrm{d}x \left[\frac{1}{2}\left\{(\partial_t\phi(x))^2 + (\partial_x\phi(x))^2\right\} - \frac{m^2}{\beta^2}\cos(\beta\phi(x))\right] \tag{6.46}$$

with the mass parameter m and the interaction parameter β. The sG model is one of the simplest models displaying confinement and is an integrable model solvable by S-matrix bootstrap techniques [218]. The model has solitonic topological excitations and a rich phase diagram. For $\beta < \sqrt{4\pi}$ the interaction is attractive and the solitons form bound states - breathers. For $\sqrt{4\pi} < \beta < \sqrt{8\pi}$ the interaction is repulsive, for the separating line $\beta = \sqrt{4\pi}$, the model can be mapped to a free Dirac fermion and at $\beta \sim \sqrt{8\pi}$ the model undergoes a Berezinskii–Kosterlitz–Thouless phase transition to a free model [218].

A convenient way to parameterize the sG interaction parameter in the attractive regime $\beta < \sqrt{4\pi}$ is

$$\beta^2 = \frac{8\pi}{1+\lambda} \tag{6.47}$$

where the parameter λ is convenient because $\lfloor\lambda\rfloor$ equals number of breathers present in the sG spectrum. The mass m_n of the n-th breather is given by

$$m_n = 2M \sin\left(\frac{n\pi}{2\lambda}\right), \tag{6.48}$$

where M is the soliton mass. In particular, the mass of the lightest particle, the first breather, m_1 determines the gap of the system. In a finite system, these masses get modified and can be obtained with the form factor and boundary bootstrap formalism [219–222]. Each of the breathers has a tower of excited states as a result of acquiring a nonzero momentum. The set of allowed momentum values is discrete in finite volume. The expressions for finite volume breather energies are given in appendix 6.F.

The entanglement properties of the sG model in the repulsive regime have been studied by spectral form factor and corner transfer matrix techniques [223, 224] and predict the height of the vN entropy area law plateau

$$S = \frac{1}{6}\log\left(\frac{1}{Ma}\right) + \frac{1}{6}\log\left(\frac{\sin\left[\pi\left(1-\frac{\beta^2}{8\pi}\right)\right]}{1-\frac{\beta^2}{8\pi}}\right) + O\left(\frac{1}{\log(a)}\right), \tag{6.49}$$

where M is the soliton mass which is a function of m and β. We are working in the attractive regime, where the entanglement properties are less understood. Based on general arguments for gapped systems, the vN entropy plateau is expected to follow the form [200]

$$S = \frac{c}{3}\log\left(\xi_1\right) + U - \frac{1}{8}\sum_{\alpha=1}^{\ell} K_0\left(2\ell m_\alpha\right) + O\left(e^{-3rm_1}\right), \tag{6.50}$$

where K_0 is the modified Bessel function, c is the central charge of the UV critical point, m_α are the masses of the particles in the spectrum (breathers in the sG case), ξ_1 the correlation length corresponding to the lightest particle and U a constant.

6.4 RESULTS

The following section is structured in two main parts. In the first part, we show results of the method for the Klein Gordon model, both in and out-of equilibrium. These results are compared to covariance matrix calculations and serve as a benchmark. In a second part, we show results for the interacting sine Gordon model to demonstrate that our method works beyond the free regime. As in the Klein Gordon case, we present data for the equilibrium situation and time dynamics of the von Neumann entropy.

All results shown in this section are computed for a finite cut-off $s_F = 18$, corresponding to 1597 states. The boundary conditions at the cut are chosen to be Neumann while the (physical) boundary conditions at the outer edges are Dirichlet. A constant mode density truncation scheme is used in all computations. Further details on the cut-off scheme are described in appendix 6.A. Normalizations (like the global prefactor in eq. (6.25)) are enforced by normalizing the reduced density matrix numerically after the transformation.

6.4.1 KLEIN GORDON MODEL

The Klein Gordon model (6.44) represents a non-trivial check for HT because its Hamiltonian is non-diagonal when expanded in the massless basis for any mass $m \neq 0$.

As an initial check for the splitting procedure, we reproduce the correlations of the Klein Gordon theory in terms of the split modes. The correlations $\langle\phi(x)\phi(L-x)\rangle$ can be either calculated in terms of the full fields ϕ acting on the full interval density matrix ρ or in terms of the split fields of the left and right partition ϕ_L and ϕ_R acting on the partitioned density matrix ρ_{LR}

$$\begin{aligned}\langle\phi(x)\phi(L-x)\rangle &= \mathrm{Tr}(\phi(x)\phi(L-x)\rho) \\ &= \mathrm{Tr}\big(\phi_{L/R}(x)\phi_{L/R}(L-x)\rho_{LR}\big).\end{aligned} \tag{6.51}$$

Here, we use the notation $\phi_{L/R}$ to refer to the field on the sub-interval that x belongs to. If the mapping between the different Hilbert spaces work well, we expect the result to be identical. Figure 6.4.1 compares the correlations across the full range of the system for a cut at position $\ell/L = 1/3$ for Neumann and Dirichlet boundary conditions at the cut. Both of the split field curves agree well with the correlations of the full system. In the case of Neumann boundary conditions at the cut, we only observe deviations at the cut. A plateau forms around the split at ℓ, since we impose $\partial_x\phi = 0$. The Dirichlet boundary conditions enforce $\phi = 0$ at ℓ and we notice that the correlations drop to zero as expected. The figure is symmetric around $\ell/L = 0.5$ due to choice of arguments in the correlator. The overall wavy features in the curve for the full and the partial modes are a feature of the finite cut-off in HT. With an increase in the cut-off, we expect these features to reduce in amplitude. Since correlations with Neumann boundary conditions at the cut agree better with the full correlations, we choose Neumann boundary conditions at the cut for all further entropy computations. We expect Dirichlet boundary conditions at the cut to be eventually equivalent to the choice of Neumann boundary conditions for higher cut-offs (cf. section 6.3.1).

We continue checking the performance of our method by calculating the von Neumann entropy. We compare the von Neumann entropy with an analytic calculation using the covariance matrix approach (cf. fig. 6.4.2). The formalism is explained in detail in appendix 6.E. All covariance matrix computations in this section are performed using 200 momentum modes. HT entropies are calculated at all points $\ell/L = n/s_F$, $n = 1, \dots, s_F - 1$ since the bosonic commutation relations in the truncated split basis are fulfilled best at these points (cf. appendix 6.A). The points $\ell/L = 0$ and $\ell/L = 1$ can be trivially added since they both must yield 0 by construction. We did not add them

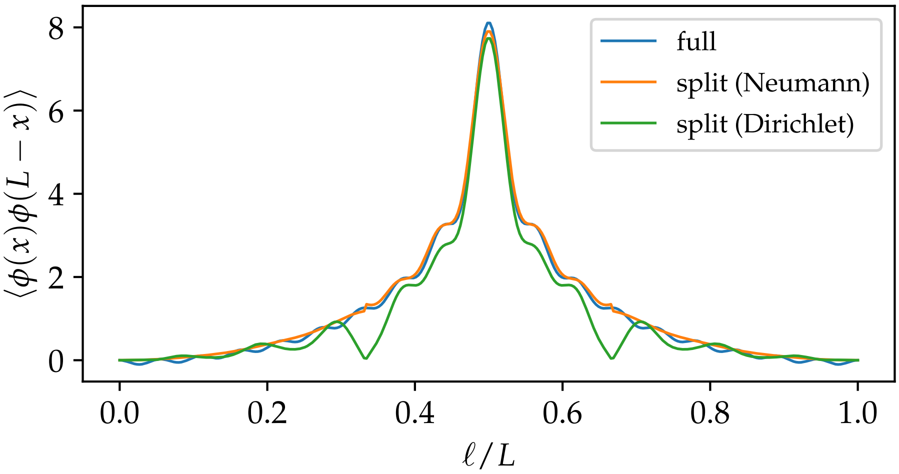

Figure 6.4.1: Correlations $\langle \phi(x)\phi(L-x) \rangle$ of the Klein-Gordon system for mass $m = 1.0$. The plot shows the correlations of the system computed with the original (full) mode decomposition of the fields as a reference. The system is cut at $\ell/L = 1/3$.

in the plots. The calculation of the entropy at other points is possible, but will result in more significant errors due to the truncation effect leading to worse preservation of the canonical commutation relation by the splitting procedure. The covariance matrix results (dashed lines) and the CFT results (solid lines) in the figure are shifted by a constant to coincide with the HT curves at $\ell/L = 0.5$ for ease of comparison. This accounts for the non-universal cutoff dependent constant [cf. eq. (6.45)] which is slightly different in the analytic and the HT case due to the different truncation schemes.

In all cases, our method agrees well with the analytic predictions. The massless boson shows the expected logarithmic growth in entropy. This agrees perfectly with the CFT prediction in eq. (6.45) [199].

With increasing mass, the curve develops a flat plateau in the central region, transitioning to the area law regime as expected for a massive boson. For distances less than a correlation length away from the boundary, the curve undergoes a non-linear behavior before it reaches 0 at the boundaries due to finite size effects.

Similar data can be obtained for Dirichlet boundary conditions at the cut. We present the results for Neumann boundary conditions here since they show better agreement with the expectation. The Dirichlet data has slightly stronger deviations at the boundaries. This is expected since the correlations already agree better for the Neumann than for the Dirichlet case.

In addition to ground state properties, we can also access the von Neumann entropy of thermal states since HT provides access to the reduced density matrix at arbitrary temperatures. Figure 6.4.3 shows the entanglement entropy ($T = 0$) and the thermodynamic entropy ($T > 0$) of a massive ($m = 5$) free boson at different spatial positions. As before, the results obtained by our method agree well with the covariance matrix computation. The dashed curves are again shifted to coincide at $\ell/L = 0.5$ to account for cut-off dependent constants. At $T = 0$, the we see the expected plateau of the area law of the entanglement entropy. This curve is the equivalent plot to fig. 6.4.2 with a higher mass. At a finite temperature, the entropy becomes extensive and grows linear with the system size.

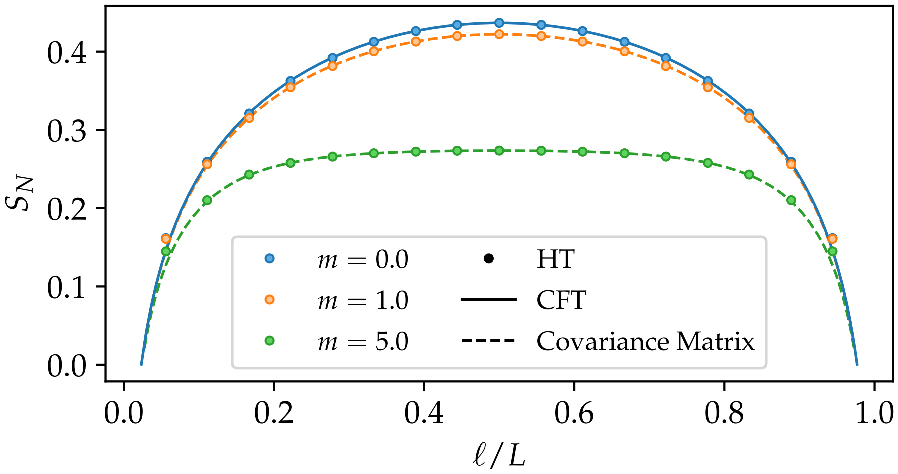

Figure 6.4.2: Spatially resolved von Neumann entropy for the Klein-Gordon model at different masses m (displayed in different colors). Different methods are encoded in the linestyle. The massless case is compared to the CFT result while the massive cases are compared to covariance matrices computations.

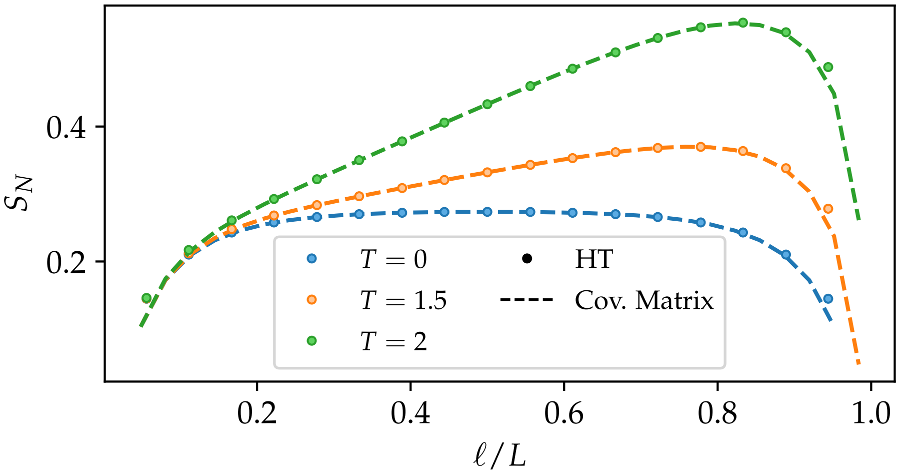

Figure 6.4.3: Von Neumann entropy of thermal states of the Klein-Gordon system with $m = 5$. The dots are the results of HT and the dashed lines are covariance matrix computations. Entropies at finite temperature are computed from a Boltzmann distribution at temperature T. The curve at zero temperature uses the ground state of the system.

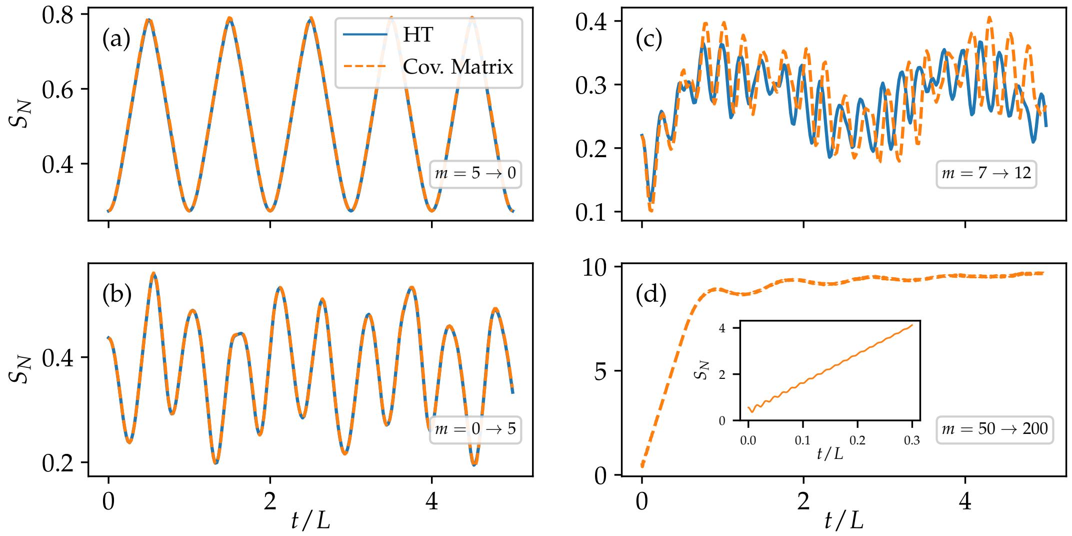

Figure 6.4.4: Time evolution of the von Neumann entropy after quenches in the Klein Gordon model. The system is split at $\ell/L = 0.5$. Different panels show quenches from and to different masses (as indicated in the insets). Solid lines are results from HT and dashed lines represent the covariance matrix results. The inset in panel (d) details the behavior of the quench $m = 50 \to 200$ at short times.

In addition to equilibrium properties, we can study time dynamics as well by quenching a ground state of a system at m_0 to a system with mass m. The resulting time dynamics can be simulated both with the covariance matrix approach and with our method.

Figure 6.4.4 presents several quenches with increasing post-quench. We study the dynamics of the vN entropy between the left and the right half of the system ($\ell = 0.5$) and compare the HT results with the analytical results from the covariance matrix formalism. We displace the curves by a constant such that they start from the same point. This is to account for the non-universal cutoff dependent constant resulting from the difference in truncation schemes in the two methods.

In panel (a) of fig. 6.4.4 we observe the expected CFT linear growth of the vN entropy quenches for a quench to a massless Hamiltonian. The linear growth is interrupted at $t = L/2$ when quasiparticles from the cut are reflected at the system boundaries. At $t = L$ this results in a recurrence and the free dispersionless nature of the model leads to periodic dynamics.

At nonzero mass, the entropy develops an oscillatory component with a frequency proportional to the boson mass m. For a thermodynamically large system $L \gg 1/m$, oscillatory dynamics are expected to be on top of a linear growth before reaching a plateau. This is indeed what we observe in panel (d) with the largest mass case. Because the size of the subsystem that we are computing the entropy of (half of the system) is of the same order as the system size, there are a few oscillations due to reflections at the boundaries before the plateau fully equilibrates. For masses of the order of the system size, the finite size reflections from the boundaries dominate, so the linear growth becomes obscured by them, which is what we see in panel (b). For intermediate masses for which the correlation length is an order of magnitude (but not more) smaller than the system size, linear growth becomes visible (although superposed with signifi-

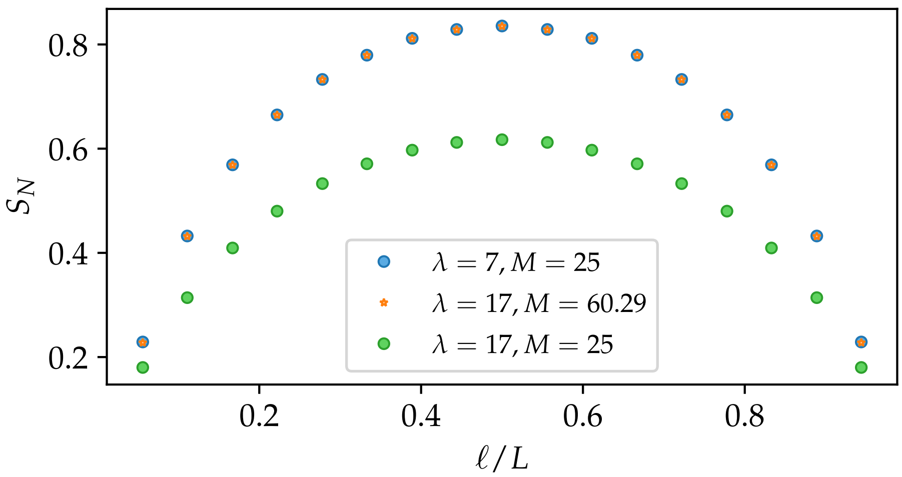

Figure 6.4.5: Spatially resolved von Neumann entropy of the sine Gordon model for Neumann boundary conditions at the cut. The curves are plotted for the interaction parameter $\lambda = 7$ and soliton mass $M = 25$ and for $\lambda = 17$ for two different mass values, $M = 25$ at $M = 60.29$. At $M = 60.29$ the gap (mass of the first breather) agrees with that of the $\lambda = 7$ case.

cant oscillations). However, the plateau keeps undergoing significant oscillations due to reflections from the boundary as shown in panel (c).

The quenches in fig. 6.4.4 expose the limitations of the truncated Hamiltonian approximation. At smaller masses [panels (a) and (b)], the HT results match perfectly the analytic prediction up to times several times longer than the system size. This shows that the HT calculation of real time dynamics can be very reliable up to considerably long times. At higher masses [panel (c)], the real time dynamics start to deviate from the analytic curve for late times and the curve develops a phase shift. This is due to truncation effects – at higher masses the low energy part of the Hilbert space becomes too small to accommodate all the relevant modes for the dynamics. The quality of the time evolution depends also on the amplitude of the quench, the difference between the pre- and the post-quench mass. For small quenches, the HT evolution is reliable even at large masses and for bigger quenches it gets less reliable even at smaller masses. Large quenches excite states high up in the spectrum and exceed the HT truncation. The very high masses shown in panel (d) cannot be reliably simulated with our current implementation of the HT and we show only the analytic curve to support the discussions in the previous paragraphs. The main problem in the simulation is the massless basis chosen for H_0 in the HT procedure. In the massless basis, a large quench excites a sizable number of highly excited states. We expect much better convergence for large quenches in a massive basis.

6.4.2 SINE GORDON MODEL

The basis transformation from a full to a split system is independent of the model. We apply the same methodology to the interacting sine-Gordon Hamiltonian (6.46) as shown in fig. 6.4.5. We compare the spatially resolved vN entropy for two different values of the coupling parameter λ and different values of the soliton mass M. The cases of $\lambda = 7$, $M = 25$ and $\lambda = 17$, $M = 60.29$ are chosen such that the gap of the model

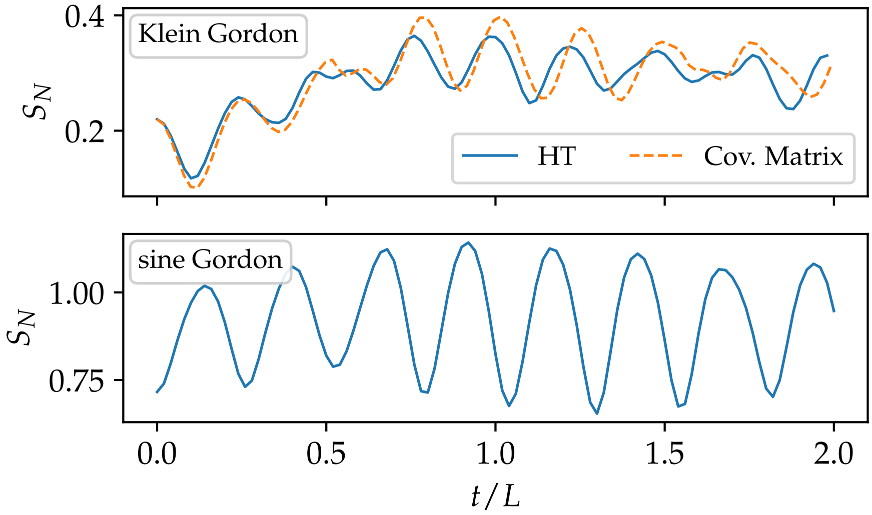

Figure 6.4.6: Time evolution of the von Neumann entropy after quenches. The top panel shows the Klein-Gordon evolution of the entropy at $\ell/L = 0.5$ for a quench from boson mass $m_0 = 7$ to $m = 12$. The bottom panel depicts a quench of the sine Gordon model for $\lambda = 7$ from a soliton mass of $M_0 = 15.73$ to $M = 26.96$. The masses are chosen such that the first breather masses m_1 of the sG model agree with the KG boson masses.

(the mass of the first breather) matches. In comparison to the Klein-Gordon model, we do not see the onset of a plateau in the middle of the curve. For the matching breather mass case, the gap is $m_1 = 11.13L$ meaning that the correlation length is less than one tenth of the system size. At such a short correlation length, an area law plateau would generally be expected. The log-like deviation from that could be indicative of longer range entanglement in the sG case which could be a consequence of the topological nature of solitons or a subtlety of the continuum limit that does not occur in lattice systems. It would be interesting to further understand this surprising scaling with analytical tools.

The perfect overlap of the curves $\lambda = 7$, $M = 25$ and $\lambda = 17$, $M = 60.29$ indicates that the vN entropy scaling in the attractive regime of the sG model is dominated solely by the first breather and not by the higher particles in the spectrum. This is consistent with the general expression (6.50). At large volumes, the K_0 corrections are highly suppressed, resulting in the value of vN entropy depending only on the correlation length.

In addition to equilibrium quantities, we can also study quenches in the sG model. The vN entropy dynamics of the sG quench is shown in Figure 6.4.6 and compared with an equivalent KG quench. The comparison is done at such choices of the parameters that the gaps of the two systems agree. We observe an oscillatory motion as predicted by recent work by Castro-Alvaredo [209]. As known previously in the literature [217] and also demonstrated here in Figure 6.4.4, the oscillating dynamics is a generic consequence of the gap and in not a special feature of interaction. From our present results it is not yet possible to determine whether the oscillations in sG quenches remain undamped at longer times as predicted by [209]. In order to study both questions, the quenches would have to be computed at a much larger post quench soliton mass, allowing to explore larger times before the reflection from the boundaries. Recently,

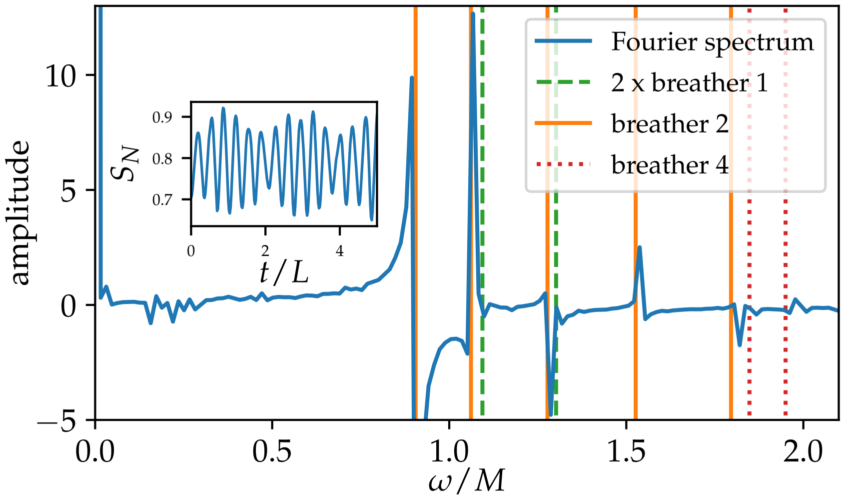

Figure 6.4.7: Frequency spectrum of the von Neumann entropy S_N time evolution after a sine-Gordon mass quench from soliton mass $M_0 = 15$ to $M = 20$ at $\lambda = 7$. The spectrum is obtained using a discrete Fourier transform. The amplitude at frequencies ω is compared against breather masses. The breather masses are computed using reflection factors from reference [222], obtained using boundary bootstrap to include finite size corrections. The inset shows the original time evolution of the von Neumann entropy following the quench.

an advanced HT implementation of the sG model has been developed [208] allowing for calculations with Hilbert space sizes of several hundred thousand states. It would be interesting to combine our method with such an approach to study sG quenches in large volume. This would, however, require even more efficient approaches to deal with the exponential complexity of the derivatives discussed in section 6.3.2.

In Figure 6.4.7 we show the results of a Fourier analysis of the time series and compare the frequency spectra with breather energy levels. In order to have a more reliable time evolution at longer times, we study a small quench in mass - a quench generated by a moderate change of the soliton mass. This reduces the excitations of states high up in the spectrum which are outside of our truncation. The analytical breather energies for comparison are computed using the form factor and boundary bootstrap formalism in references [219–222], for completeness the expressions are listed also in appendix 6.F. The sG ground states which are the prequench states are even under the charge conjugation $C : \phi \to -\phi$ which interchanges solitons with anti-solitons. Therefore, as predicted by [209], only C even states get populated during the quench. These include even breather states and even multiples of odd breathers.

6.5 DISCUSSION

We presented a method to compute reduced density matrices of a quantum field theory using Hamiltonian truncation. Our method constructs a unitary transformation between the Hilbert space of the full interval and a tensor product of Hilbert spaces corresponding to two sub-intervals.

The method enables the direct evaluation of a wide spectrum of entanglement related quantities, including von Neumann and Rényi entropies, mutual information and entanglement Hamiltonians. Most importantly, our method is model-independent and can be applied for any HT that is based on an expansion around a free (massive or massless) theory, which is the most common choice in modern implementations. We studied the entanglement in ground, excited and thermal states as well as the real time evolution of the entanglement entropy. By construction, the method could in principle be applied in any dimension where HT converge.

To check the validity of the approach, we benchmarked the method using the Klein-Gordon Hamiltonian describing a massive free boson. Despite being a free theory, it represents a non-trivial test because its Hamiltonian is a non-diagonal perturbation of the massless free theory. The exact solutions for this model can be obtained using covariance matrix methods [201] making it suitable as a benchmarking model. We found excellent agreement of the von Neumann entropy with theoretical predictions for ground and thermal states. For small quenches, the time dynamics of the Klein-Gordon model are accurately reproduced for up to times several times longer than the system size.

Due to the model independence of the method, we continued by studying an interacting system, the sine-Gordon field theory in the attractive regime. For the scaling of the ground state von Neumann entropy, we found a logarithmic behavior instead of an area-law. At this point, it is unclear whether this is a feature of the model in the continuum or a related to the method. In the large volume regime, the vN entropy depends only on the gap of the system but not the higher particle content. Studying the quench dynamics of the sG model, we found an oscillating behavior, as predicted by [209]. The resonances in the frequency spectrum of the time series matched the masses of the lowest breathers. Whether the oscillations are superimposed with a linear growth needs further investigation. One option would be a more sophisticated implementation of the sG model with a higher cutoff. The recently developed chirally factorized approach [208] could be a suitable candidate.

Our method enables many interesting explorations and can be extended in several directions. The oscillatory time dependence of the vN entropy after quenches could be analyzed. Here, a possible direction is the role of integrability and the effects of integrability breaking. Suitable candidates are non-integrable perturbations of the sG model, like the double sG model and the massive sG model. Another more fundamental possibility would be the ϕ^4 theory which is a non-integrable QFT model and has already been successfully implemented in the HT framework [145, 146]. Our method can be adapted for the ϕ^4 model by computing the Bogoliubov coefficients for the massive field expansion.

Furthermore, it is interesting to study the entanglement Hamiltonian and the Bisognano-Wichmann theorem [225, 226]. Several interesting properties have been established for the CFT case [227–230], and it would be important to explore how they extend to the interacting gapped QFT. The explicit representation of the reduced density matrix in a computational basis given by our method is naturally suited to such a study.

An implementation of our method in $(2+1)$ dimensions is interesting due to the lack of methods in systems with dimension $d > (1+1)$. By construction, our method can be easily generalized to any dimension. The main obstacle would be the quickly growing size of the full and the split system Hilbert spaces. However, HT has already been successfully applied in higher dimensions [148].

Finally, in case of free theories, massless and massive, our construction yields an exact construction of the reduced density matrix of the theory. It could be a fruitful direction to use that to get further analytical insights into the entanglement structure of QFT.

Appendix

6.A Cut-off effects and symplectic structure

The main approximation in our method is the representation of the full system modes in terms of a finite number of partial modes. We have to ensure that the approximation conserves basic properties of the system like the bosonic commutation relations. Equation (6.18) can be reformulated to test the transformation as

$$MKM^{\dagger} = K \tag{6.52}$$

$$M^{\dagger}KM = K\,. \tag{6.53}$$

Equation (6.52) evaluates the commutation relations of the full modes A_k expressed in terms of the partial modes. The structure of K on the diagonal of $\mathbb{1}$ on the first half of the diagonal and $-\mathbb{1}$ on the second half reflects the anti-symmetry of the commutator upon exchanging its arguments. The commutation relations of the reverse transformation (partial modes expressed in full modes) are tested in eq. (6.53). The two equations provide us with an objective quality criterion of the transformation. If the commutation relations of the bosonic modes are not fulfilled, the transformation is invalid.

As described in the main text, we consider two cut-off schemes. The fixed cut-off scheme distributes the partial modes equally across both intervals, irrespective of the size of the interval ($s_L = s_R = s_F/2$). The second scheme, constant mode density, distributes the modes proportionally to the size of the intervals ($s_L = \ell/Ls_F, s_R = s_F - s_L$). The quality of the two schemes can be assessed by checking the commutation relations of the transformed modes. Figure 6.A.1 shows the result of the calculation of eq. (6.52). The top row shows that the fixed cut-off scheme does not reproduce the bosonic commutation relations if the full modes are expressed in terms of partial modes for splits that are not at $x = 0.5$. A cut in the middle represents a special case. Here, the constant mode density scheme and the fixed cut-off scheme coincide. The bottom row illustrates that the constant mode density cut-off schemes reproduces the correct commutation relations for different cuts. All the computations in the main text are performed with this cut-off scheme.

The commutation relations are not exactly fulfilled for all points on the interval $[0, L]$. If we assume s_F full modes, we can split the system at multiples of $1/s_F$ such that we have the exact same density of modes on the left and the right side of the cut. If the mode density is not exactly the same, we have to decide which distribution of partial modes we pick.

The choice of the rounding scheme influences the values for the entropy. We show in fig. 6.A.2 the influence of different rounding schemes. The points in blue always floor the number of modes in the left partition $s_L = \left\lfloor \frac{\ell}{L} s_F \right\rfloor$. This leads to increasingly bad results as we move to the right between commensurate cuts. If we round the number of left modes to the closest integer instead (depicted in orange), the problems get less severe and obtain a symmetric structure around the middle of the intervals.

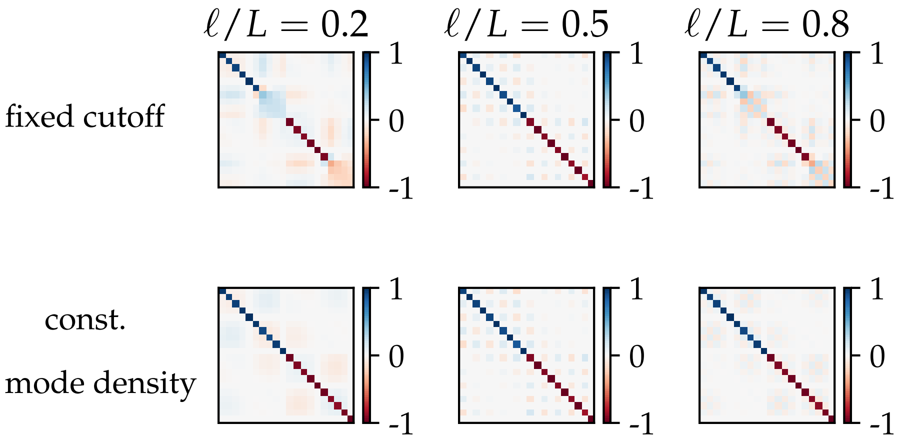

Figure 6.A.1: Check of the symplectic properties of the transformation from full modes to partial modes for $s_F = 10$. The fixed cut-off scheme does not faithfully reproduce the bosonic commutation relations except for the case of $x = 0.5$. In this case, the fixed scheme and the constant mode density scheme coincide.

The commensurate cuts of the system are drawn in green. In the main text, we only calculate points at commensurate splittings to avoid the influence of rounding effects.

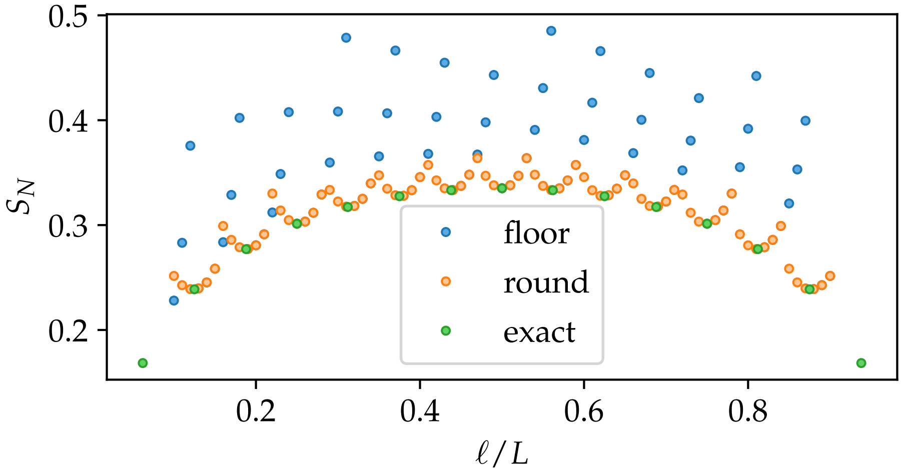

Figure 6.A.2: Effect of rounding schemes for the number of modes in the left and right partition s_L and s_R for Dirichlet boundary conditions at the cut. The system is a Klein-Gordon model with mass $m = 1$. The transformation yields the correct bosonic commutation on commensurate cuts (green) with distance $1/s_F$. If we do not cut at commensurate splits, the s_L can be either floored to the next integer (blue) or rounded (orange).

6.B γ COEFFICIENTS FOR DIRICHLET BOUNDARY CONDITIONS AT THE CUT

Our goal is to find an expression for each full system mode A_k in terms of the partial modes a^R_m and a^L_m. To avoid unnecessary back and forth with the main text, some equations from the main text will be repeated here. The starting point is the mode expansion of the scalar field of the full system [cf. eq. (6.3)]

$$\phi(x,t) = \frac{1}{\sqrt{L}} \sum_{k=1}^{\infty} \frac{1}{\sqrt{p_k}} \left(A_k e^{-ip_k t} + A_k^\dagger e^{ip_k t}\right) \sin(p_k x), \tag{6.54}$$

with $p_k = k\frac{\pi}{L}$ and $[A_k, A_l] = \left[A_k^\dagger, A_l^\dagger\right] = 0$ and $\left[A_k, A_l^\dagger\right] = \delta_{k,l}$. The expression can be inverted with the help of the canonical conjugate momentum field

$$\pi(x,t) = \partial_t \phi(x,t) = -\frac{i}{\sqrt{L}} \sum_{k=1}^{\infty} \sqrt{p_k} \left(A_k e^{-ip_k t} - A_k^\dagger e^{ip_k t}\right) \sin(p_k x)\,. \tag{6.55}$$

By adding the field operator (6.54) and the momentum operator (6.55), we obtain for each k and $t = 0$

$$\left[\phi(x,t) + \frac{i}{p_k}\pi(x,t)\right]_{k,t=0} = \frac{2}{\sqrt{L p_k}} A_k \sin(p_k x)\ . \tag{6.56}$$

Projecting out all except one momentum mode by multiplying the expression on both sides with $\sin(p_k x)$ and integrating, we invert of the mode expansion of the field

$$A_k = \sqrt{\frac{p_k}{L}} \int_0^L \mathrm{d}x \left[\phi(x,t) + \frac{i}{p_k}\pi(x,t)\right] \sin(p_k x)\ . \tag{6.57}$$

Our aim is to express the field operator on the full interval in eq. (6.57) by the fields defined on the sub-intervals. In addition to the full field, we also need the split fields with Dirichlet boundary conditions at the cut

$$\phi_L(x,t) = \frac{1}{\sqrt{\ell}} \sum_{m=1}^{\infty} \frac{1}{\sqrt{p_m^{(\ell)}}} \left(a_m^L e^{-ip_m^{(\ell)} t} + a_m^{L,\dagger} e^{ip_m^{(\ell)} t} \right) \sin\left(p_m^{(\ell)} x \right) \tag{6.58}$$

$$\phi_R(x,t) = \frac{1}{\sqrt{L-\ell}} \sum_{m=1}^{\infty} \frac{1}{\sqrt{p_m^{(L-\ell)}}} \left(a_m^R e^{-ip_m^{(L-\ell)} t} + a_m^{R,\dagger} e^{ip_m^{(L-\ell)} t} \right) \sin\left(p_m^{(L-\ell)} (x-\ell) \right), \tag{6.59}$$

where we have defined $p_m^{(d)} = m\frac{\pi}{d}$. The expression for the canonical momentum on the sub-systems L and R follow analogously to eq. (6.55).

The relationship between the full fields (6.54) and split fields in eq. (6.59) is given by the continuity condition, eq. (6.10) in the main text. Inserting the split field expansions in eqs. (6.58) and (6.59) into eq. (6.57) and performing the integrals yields the Bogoliubov transformation between the full and the split modes, eq. (6.16) in the main text.

The resulting γ coefficients for Dirichlet boundary conditions at the cut are

$$\gamma_{km}^{+,L} = \begin{cases} \frac{(-1)^m \sqrt{p_m^{(\ell)}} \sin(p_k \ell)}{\sqrt{L\ell}\sqrt{p_k}(p_k - p_m^{(\ell)})} & p_k \neq p_m^{(\ell)} \\ \sqrt{\frac{\ell}{L}} & p_k = p_m^{(\ell)} \end{cases} \tag{6.60}$$

$$\gamma_{km}^{-,L} = \frac{(-1)^m \sqrt{p_m^{(\ell)}} \sin(p_k \ell)}{\sqrt{L\ell}\sqrt{p_k}(p_k + p_m^{(\ell)})} \tag{6.61}$$

$$\gamma_{km}^{+,R} = \begin{cases} -\frac{\sqrt{p_m^{(L-\ell)}} \sin(p_k \ell)}{\sqrt{L(L-\ell)}\sqrt{p_k}(p_k - p_m^{(L-\ell)})} & p_k \neq p_m^{(L-\ell)} \\ \frac{\sin(p_k\ell) + p_k(L-\ell)\cos(p_k\ell)}{p_k\sqrt{L}\sqrt{L-\ell}} & p_k = p_m^{(L-\ell)} \end{cases} \tag{6.62}$$

$$\gamma_{km}^{-,R} = -\frac{\sqrt{p_m^{(L-\ell)}} \sin(p_k \ell)}{\sqrt{L(L-\ell)}\sqrt{p_k}(p_k + p_m^{(L-\ell)})} \tag{6.63}$$

The coefficients $\gamma_{km}^{+,L}$ and $\gamma_{km}^{+,R}$ can diverge if the denominator becomes 0. This is impossible for $\gamma_{km}^{-,L}$ or $\gamma_{km}^{-,R}$ since $m, k > 0$. We can compute the integrals again explicitly for the two diverging cases. $\gamma_{km}^{+,L}$ diverges if $k = \frac{Lm}{\ell}$. The integral with this parameter combination yields $\sqrt{\frac{l}{L}}$. The coefficient $\gamma_{km}^{+,R}$ diverges if $k = \frac{Lm}{L-l}$.

6.C ALGORITHM

6.C.1 DERIVATION AND DERIVATIVES OF COMMUTATORS

In order to use the scalar formulation for the matrix elements of U_T in eq. (6.36), we have to bring the terms into normal order. Our starting point is eq. (6.27)

$$\langle \vec{n}_L, \vec{n}_R | \vec{n}_F \rangle = \frac{1}{N} \prod_{m>0} \prod_{\sigma} \frac{\mathrm{d}^{n_{m,\sigma}}}{\mathrm{d}j_{m,\sigma}^{n_{m,\sigma}}} \prod_{k>0} \frac{\mathrm{d}^{n_k}}{\mathrm{d}J_L^{n_k}} \langle 0,0| e^S e^F e^V |0,0\rangle \Big|_{J_k=0, j_{m,\sigma}=0} .$$

with

$$\begin{aligned}
S &\equiv \sum_{m>0} \sum_{\sigma} j_{m,\sigma} a_m^{\sigma} \\
F &\equiv \sum_{k,m>0} \sum_{\xi} J_k \left(\gamma_{k,m}^{+,\xi} a_m^{\xi\dagger} + \gamma_{k,m}^{-,\xi} a_m^{\xi} \right) \\
V &\equiv -\sum_{\xi,\lambda} \sum_{m,n>0} a_m^{\xi,\dagger} \rho_{m,n}^{\xi,\lambda} a_n^{\lambda,\dagger} .
\end{aligned}$$

To avoid unnecessary jumping back and forth between the main text and the appendix, we will repeat some of the equations here. As mentioned in the main text, S creates the excitations of the split modes on the partial vacuum according to the occupation numbers in $|\vec{n}_L, \vec{n}_R\rangle$. F represents the creation operators of the full modes according to $|\vec{n}_F\rangle$ expressed in the split modes. Finally, V transforms the full vacuum into a squeezed state on top of the split vacuum.

We normal order the expression in three steps. First, we normal order the exponential e^F which contains both creation and annihilation operators. In a second step, we commute e^S, which consists of annihilation operators only, past the creation operators of e^F. Finally, we commute all annihilation operators of e^S and e^F past the vacuum transformation e^V.

Normal ordering or e^F is achieved by the application of the Baker-Campbell-Hausdorff formula $e^X e^Y = e^{X+Y+\frac{1}{2}[X,Y]}$ for $[[X,Y],X] = [[X,Y],Y] = 0$. We get

$$\begin{aligned}
e^F &= e^{F^+ + F^-} \\
&= e^{\mathrm{ComF}} e^{F^+} e^{F^-}
\end{aligned} \tag{6.64}$$

where define

$$\begin{aligned}
F_k^+ &\equiv \sum_{k,n>0} \sum_{\xi} J_k \gamma_{k,n}^{+,\xi} a_n^{\xi,\dagger} \\
F_k^- &\equiv \sum_{k,n>0} \sum_{\xi} J_k \gamma_{k,n}^{-,\xi} a_n^{\xi}
\end{aligned}$$

to be the parts containing creation/annihilation operators respectively. The commutator in eq. (6.65) evaluates to

$$\begin{aligned}
\mathrm{ComF} &\equiv -\frac{1}{2} \left[F^+, F^- \right] \\
&= \frac{1}{2} \sum_{k,k'=1}^{\infty} J_k J_{k'} \sum_{\sigma} \sum_{n>0} \gamma_{k,n}^{+,\sigma} \gamma_{k',n}^{-,\sigma} .
\end{aligned} \tag{6.65}$$

In a second step, we commute annihilation operators of partial modes in e^S past e^{F^+}, using BCH in the form $e^X e^Y = e^{Y+[X,Y]} e^X$ for $[[X,Y],X] = [[X,Y],Y] = 0$. We get

$$e^S e^{F^+} = e^{\mathrm{ComSF}} e^{F^+} e^S \tag{6.66}$$

with the commutator

$$\begin{aligned}
\mathrm{ComSF} &\equiv \left[S, F^+ \right] \\
&= \sum_{k,m>0} \sum_{\sigma} j_{m,\sigma} J_k \gamma_{k,m}^{+,\sigma} .
\end{aligned} \tag{6.67}$$

Finally, we commute the annihilation operators in e^{S+F^-} and F^- past the vacuum transformation e^V. For convenience, we rewrite the annihilation operators in S and F^- as A

$$\begin{aligned} A &\equiv S + F^- \\ &= \sum_{m>0} \sum_{\sigma} \left\{ j_{m,\sigma} + \sum_{k>0} J_k \gamma_{k,m}^{-,\sigma} \right\} a_m^{\sigma} . \end{aligned} \tag{6.68}$$

In this commutation, the terms in the exponent of the BCH formula only vanish after the second commutator $[A,[A,V]]$. Thus, using $e^X e^Y = e^{(Y+[X,Y]+\frac{1}{2!}[X,[X,Y]])}\, e^X$, we find

$$e^A e^V = e^{\mathrm{ComAV}} e^{V+[A,V]} e^A \tag{6.69}$$

with the commutators

$$[A,V] = -\sum_{m>0} \sum_{\sigma} \left\{ j_{m,\sigma} + \sum_{k>0} J_k \gamma_{k,m}^{-,\sigma} \right\} \sum_{\xi} \sum_{l>0} \left(\chi_{m,l}^{\sigma,\xi} + \chi_{l,m}^{\xi,\sigma} \right) a_l^{\xi,\dagger} , \tag{6.70}$$

and

$$\begin{aligned} \mathrm{ComAV} &\equiv \frac{1}{2} [A,[A,V]] \\ &= -\frac{1}{2} \sum_{m>0} \sum_{\sigma} \left\{ j_{m,\sigma} + \sum_{k>0} J_k \gamma_{k,m}^{-,\sigma} \right\} \sum_{l>0} \sum_{\xi} \left\{ j_{l,\xi} + \sum_{k'>0} J_{k'} \gamma_{k',l}^{-,\xi} \right\} \left(\chi_{m,l}^{\sigma,\xi} + \chi_{l,m}^{\xi,\sigma} \right) . \end{aligned} \tag{6.71}$$

Finally, the full expression in the normal ordered form is

$$e^S e^F e^V = \exp\left[\mathrm{ComF} + \mathrm{ComSF} + \mathrm{ComAV}\right] e^{[A,V]} \; : e^S e^F e^V : \, . \tag{6.72}$$

For readability, we skipped the derivative and the partial vacua in the expression above. When computing the expectation value in the split vacuum, only the zeroth order in the power expansion of $e^{[A,V]}\; : e^S e^F e^V :$ survives and we obtain

$$\begin{aligned} \langle 0,0| \, e^S e^F e^V \, |0,0\rangle &= \exp\left[\mathrm{ComF} + \mathrm{ComSF} + \mathrm{ComAV}\right] \\ &\equiv e^T . \end{aligned} \tag{6.73}$$

The computation of the matrix elements of U_T in eq. (6.36) does not depend on the form of T directly, but on the second derivatives $T[J_i, J_k]$. All terms that are not derived twice will vanish once we set $J_k = 0$.

The second derivatives are

$$\frac{\mathrm{d}}{\mathrm{d}J_i} \frac{\mathrm{d}}{\mathrm{d}J_p} \mathrm{ComF} = \frac{1}{2} \sum_{\sigma} \sum_{n>0} \left(\gamma_{i,n}^{+,\sigma} \gamma_{p,n}^{-,\sigma} + \gamma_{p,n}^{+,\sigma} \gamma_{i,n}^{-,\sigma} \right) \tag{6.74}$$

$$\frac{\mathrm{d}}{\mathrm{d}j_{l,\xi}} \frac{\mathrm{d}}{\mathrm{d}J_i} \mathrm{ComSF} = \gamma_{i,l}^{+,\xi} \tag{6.75}$$

$$\frac{\mathrm{d}}{\mathrm{d}J_p} \frac{\mathrm{d}}{\mathrm{d}J_i} \mathrm{ComAV} = -\sum_{m,m'>0} \sum_{\sigma,\mu} \gamma_{i,m'}^{-,\sigma} \gamma_{p,m}^{-,\mu} \left(\chi_{m,m'}^{\mu,\sigma} + \chi_{m',m}^{\sigma,\mu} \right) \tag{6.76}$$

$$\frac{\mathrm{d}}{\mathrm{d}j_{p,\alpha}} \frac{\mathrm{d}}{\mathrm{d}j_{l,\xi}} \mathrm{ComAV} = -\left(\chi_{l,p}^{\xi,\alpha} + \chi_{p,l}^{\alpha,\xi} \right) \tag{6.77}$$

$$\frac{\mathrm{d}}{\mathrm{d}J_i} \frac{\mathrm{d}}{\mathrm{d}j_{l,\xi}} \mathrm{ComAV} = -\sum_{m>0} \sum_{\sigma} \gamma_{i,m}^{-,\sigma} \left(\chi_{l,m}^{\xi,\sigma} + \chi_{m,l}^{\sigma,\xi} \right) . \tag{6.78}$$

All other derivatives vanish.

6.C.2 TREE BUILDING ALGORITHM

The primed sum in eq. (6.40) runs over all lexicographically unique configurations of the arguments $(\mathcal{J}_1, \mathcal{J}_2)$ of T. Lexicographically unique implies that all tuples are sorted internally $\mathcal{J}_1 < \mathcal{J}_2$ and the string of tuples is sorted as well. Two tuples are sorted by sorting them first by their first entry and then by second entry.

The generation of all unique pairs can be approached in at least two ways. We could take all Js independently and find all possible ways of distributing them as pairs. In this case, we would have to filter out all the repeated configurations due to ordering in the arguments of T and in the string. Alternatively, we can incrementally create all orderings in a tree-like structure. By tracking the ordering as we progress, we can avoid the generation of forbidden configurations. We will only consider the latter alternative since the generation of all permutations scales with $n!$ where $n = \sum_i n_i$, *i.e.*the number derivatives.

We start with vector $\vec{n} = (n_1, n_2, \ldots, r_N)$. Since we consider only sorted tuples and a globally sorted string of tuples, we build all valid pairs $(\mathcal{J}_i, \mathcal{J}_k)$ with the first $\mathcal{J}_i$ corresponding to the smallest non-zero n_i. A pair is valid if the $\mathcal{J}_i < \mathcal{J}_k$ for a pair $(\mathcal{J}_i, \mathcal{J}_k)$ and the pair is greater or equal to the previous selected pair. We proceed in a recursive manner and modify the vector $\vec{n}$ by subtracting one from n_i and n_k and select again all valid pairs in the next step of the tree. In total, we build a tree of the form in fig. 6.C.1. We start on the left with the full string of the example that is also used in the main text $\vec{n} = (2, 2, 2)$. Lists in round brackets describe the occupation numbers of the state. Each level of the tree represents one level of recursion. In each level, the vectors in round parentheses represent the vector $\vec{n}$ after picking the tuple in brackets. The topmost entry on the second level describes the case of picking $[1, 3]$ from the tuple as first argument for T. Thus, the first and the third entry are decreased by one. All valid combinations of T can be enumerated by following the branches of the tree. If we pick up all tuples in brackets, we obtain the full string of arguments for T. The algorithm stops if no valid pair can be found for a given vector $\vec{n}$ or if $\vec{n} = \vec{0}$. In the example, the second condition is met after 3 iterations. Some branches are not continued because the following tuple is smaller than the previous one (first termination condition). In the example, $[1, 2] < [1, 3]$ in the third level and we abort the branch. This step would not result in a sorted combination of tuples. In total, the tree in fig. 6.C.1 has five leafs. Following all the paths leading to those leafs, we obtain the five configurations that are listed in eq. (6.41).

The number of strings still scales exponentially, but the approach allows us to generate all tuples with a local condition. Given the current occupation number vector, we can call the same function recursively and obtain the next level. We do not have to store a global state in order to decide which pairs to build. Thus, we never have to store all tuples at the same time. This significantly decreases the memory requirements of the algorithm. More concretely, the algorithm is implemented in terms of a recursive generator in Python[184].

As we can see in the tree, the generated strings depend only on the initial occupation number vector $\vec{n}$. The allowed occupation number vectors, in turn, depend only on the cut-offs that are chosen for the subsystems. Thus, we can generate all the strings once and write them directly to disk. These files can be stored in a compressed format and can be loaded as a stream when the actual unitary matrices are evaluated. Again, we can avoid loading the entire file into main memory. The unitary demands much less memory than storing all T contributions.

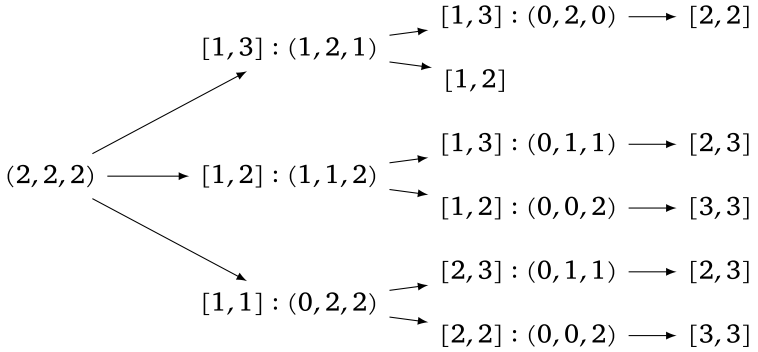

Figure 6.C.1: Tree to build all tuples of configurations of $\vec{n} = (2,2,2)$. The expression in parentheses are the $\mathcal{J}_i$ that still have to be distributed. The tuple that is added to the configuration at every step is noted in brackets. The final configuration of every path can be assembled by following the arrows and collecting the entries of all brackets. The missing leaf in the last layer on the right indicates a configuration that cannot be build due to the restrictions on the tuples.

6.D HT MATRIX ELEMENTS

The HT computations use the matrix elements from the methods developed in [222, 231]. In this work, we use the explicit parameterizations of the Klein Gordon model and the sine Gordon model in terms of massless, bosonic fields. The boundary conditions at the edges of the physical system ($x = 0, x = L$) are chosen to be Dirichlet.

For an operator O, we list matrix elements

$$O^{\vec{n}',\vec{n}} = \langle \vec{n}' | \, O \, | \vec{n} \rangle \tag{6.79}$$

with states spanning the computational basis, the Hilbert space of the massless free boson

$$|\vec{n}\rangle \equiv |n_1, n_2, \ldots\rangle \equiv \frac{1}{N_{\vec{n}}} \prod_{k>0} \left(A_k^\dagger\right)^{n_k} |0\rangle \tag{6.80}$$

with A_k, $k = 1, 2, \ldots$ the bosonic modes fulfilling the canonical commutation relations $\left[A_k, A_l\right] = \left[A_k^\dagger, A_l^\dagger\right] = 0$ and $\left[A_k, A_l^\dagger\right] = \delta_{k,l}$. The normalization is defined as $N_{\vec{n}} = \prod_{k>0} \sqrt{n_k!}$ and $A_k \, |0\rangle = 0 \; \forall k$ the vacuum of the massless free boson theory.

The massless free boson Hamiltonian for Dirichlet boundary conditions

$$H_{0\mathrm{FB}} = \frac{1}{2} \int_0^L \mathrm{d}x \left[\left(\partial_t \phi\right)^2 + \left(\partial_x \phi\right)^2 \right]. \tag{6.81}$$

is diagonal with matrix elements

$$H_{0\mathrm{FB}}^{\vec{n}',\vec{n}} = \frac{\pi}{L} \left(\sum_{k=1}^{\infty} k n_k - \frac{1}{24} \right) \delta_{\vec{n}',\vec{n}} \, . \tag{6.82}$$

The Hamiltonian of the massive free boson

$$H_{m\mathrm{FB}} = \frac{1}{2} \int_0^L \mathrm{d}x \left[\left(\partial_t \phi\right)^2 + \left(\partial_x \phi\right)^2 + m^2 \phi^2 \right] \tag{6.83}$$

has the matrix elements

$$\begin{aligned} H_{\mathrm{mFB}}^{\vec{n}',\vec{n}} =& \frac{\pi}{L}\left\{\delta_{\vec{n}',\vec{n}}\left(\sum_{k=1}^{\infty}\left(1+\frac{m^2L^2}{2\pi^2k^2}\right)kn_k-\frac{1}{24}\right)\right. \\ &+\frac{m^2L^2}{4\pi^2}\sum_{k=1}^{\infty}\left(\prod_{\substack{j=1\\ j\neq k}}^{\infty}\delta_{n'_j,n_j}\right)\frac{1}{k^2}\left(\sqrt{n_k k}\sqrt{(n_k-1)k}\,\delta_{n'_k+2,n_k}\right. \\ &\left.\left.+\sqrt{(n_k+2)k}\sqrt{(n_k+1)k}\,\delta_{n'_k-2,n_k}\right)\right\} . \end{aligned} \tag{6.84}$$

The Hamiltonian of the sine-Gordon model can be expressed as

$$\begin{aligned} H_{\mathrm{sG}} =& \int_0^L \mathrm{d}x\left[\frac{1}{2}\left\{(\partial_t\phi(x))^2+(\partial_x\phi(x))^2\right\}-2\kappa(\Delta)M_S^{2-2\Delta}\cos\left(\beta\phi(x)\right)\right] \\ =& H_{0\mathrm{FB}}-\kappa(\Delta)M_S^{2-2\Delta}\int_0^L\mathrm{d}x\left(V_1(x)+V_{-1}(x)\right) \end{aligned} \tag{6.85}$$

where

$$V_p(x)\equiv e^{iq\phi(x)}, \quad p\in\mathbb{Z} \tag{6.86}$$

for $q\equiv p\beta$ is the *vertex operator*, M is the semi-classical soliton mass, the interaction related coefficient Δ is defined as

$$\Delta\equiv\frac{\beta^2}{8\pi} \tag{6.87}$$

and the coupling-mass ratio $\kappa(\Delta)$ [232],

$$\kappa(\Delta)=\frac{1}{\pi}\frac{\gamma_b\left(\Delta\right)}{\gamma_b\left(1-\Delta\right)}\left[\frac{\sqrt{\pi}\gamma_b\left(\frac{1}{2-2\Delta}\right)}{2\gamma_b\left(\frac{\Delta}{2-2\Delta}\right)}\right]^{2-2\Delta} . \tag{6.88}$$

The vertex operator can be written in normal ordered form as

$$V_p(z,\bar{z})=e^{iq\phi(z,\bar{z})}=|z-\bar{z}|^{-q^2}:e^{iq\phi(z,\bar{z})}: \tag{6.89}$$

where for convenience we have introduced $z\equiv e^{i\frac{\pi}{L}x}$. The matrix elements are

$$V_p^{\psi',\psi}\left(z,\bar{z}\right)=N_{\vec{n}'}^{-1}N_{\vec{n}}^{-1}\left[2\sin\left(\frac{\pi x}{L}\right)\right]^{-q^2}\prod_{k=1}^{\infty}\langle 0|A_k^{n'_k}e^{-q\frac{A_k^\dagger}{\sqrt{k}}(z^k-\bar{z}^k)}e^{q\frac{A_k}{\sqrt{k}}(z^{-k}-\bar{z}^{-k})}\left(A_k^\dagger\right)^{n_k}|0\rangle , \tag{6.90}$$

with

$$\begin{aligned} &\langle 0|A_k^{n'_k}e^{-q\frac{A_k^\dagger}{\sqrt{k}}(z^k-\bar{z}^k)}e^{q\frac{A_k}{\sqrt{k}}(z^{-k}-\bar{z}^{-k})}\left(A_k^\dagger\right)^{n_k}|0\rangle \\ &=\sum_{j'=0}^{\infty}\sum_{j=0}^{\infty}\frac{(-1)^{j'}}{j'!j!}\left(\frac{2q}{\sqrt{k}}\right)^{j'+j}\left[\frac{\bar{z}^k-z^k}{2}\right]^{j'+j}\left\langle 0\middle|A_k^{n'_k}\left(A_k^\dagger\right)^{j'}A_k^j\left(A_k^\dagger\right)^{n_k}\middle|0\right\rangle \end{aligned} \tag{6.91}$$

and

$$\left\langle 0\middle|A_k^{n'_k}\left(A_k^\dagger\right)^{j'}A_k^j\left(A_k^\dagger\right)^{n_k}\middle|0\right\rangle=\left(\begin{array}{c} n'_k \\ j' \end{array}\right)\left(\begin{array}{c} n_k \\ j \end{array}\right)j'!j!(n_k-j)!\delta_{n'_k-j',n_k-j}\Theta(n_k\geq j) \tag{6.92}$$

with the Heaviside step function Θ.

To get the matrix elements of the spatially integrated vertex operator that appears in the sine-Gordon Hamiltonian, the following relation is useful

$$\int_0^{\pi} \mathrm{d}u \, [2\sin(u)]^{-q^2} e^{-iku} = \frac{e^{-i\frac{\pi}{2}k}\pi}{(1-q^2)\, B\left(\frac{1}{2}(2-q^2-k), \frac{1}{2}(2-q^2+k)\right)}. \tag{6.93}$$

Here, $B(x,y) = \frac{\Gamma(x)\Gamma(y)}{\Gamma(x+y)}$ is the beta function.

6.E COVARIANCE MATRIX FORMALISM FOR FREE THEORIES

Eigen, thermal and time-evolved states of free theories are Gaussian and the computation of their entanglement properties can be simply achieved by means of the covariance matrix formalism [201].

A Gaussian state is completely determined by its covariance matrix

$$\Gamma = \begin{bmatrix} Q & R \\ R^T & P \end{bmatrix} \tag{6.94}$$

with

$$\begin{aligned} Q_{mn} &= \langle \phi_m \phi_n \rangle \\ P_{mn} &= \langle \pi_m \pi_n \rangle \\ R_{mn} &= \left\langle \frac{1}{2} \{\phi_m, \pi_n\} \right\rangle \end{aligned} \tag{6.95}$$

where $[\phi_m, \phi_n] = [\pi_m, \pi_n] = 0$, $[\phi_m, \pi_n] = i\delta_{m,n}$ are harmonic oscillator conjugate pairs. All higher order correlations are given by Wick's theorem.

In the case of a bosonic field theory, we have to introduce an IR (finite volume L) and UV (maximal momentum mode kept, K) cutoff in order to keep the covariance matrix finite. Then, the harmonic oscillators are finitely many, and we can treat the covariance matrix either in momentum space or position space. For covariance matrix calculations it is convenient to go back and forth between those representations using a discrete sine transform. The field expansion can be written as

$$\begin{aligned} \phi(x_n, t) &= \sqrt{\frac{2}{L}} \sum_{k=1}^{K} \phi_k(t) \sin\left(\frac{k\pi}{L} x_n\right) \\ \pi(x_n, t) &= \sqrt{\frac{2}{L}} \sum_{k=1}^{K} \pi_k(t) \sin\left(\frac{k\pi}{L} x_n\right) \end{aligned} \tag{6.96}$$

with $x_n = na$ for $n = 1, \ldots, K$ with the lattice spacing $a = \frac{L}{K+1}$. The inverse discrete sine transform is achieved by

$$\begin{aligned} \phi_k(t) &= a\sqrt{\frac{2}{L}} \sum_{n=1}^{K} \phi(x_n, t) \sin\left(\frac{k\pi}{L} x_n\right) \\ \pi_k(t) &= a\sqrt{\frac{2}{L}} \sum_{n=1}^{K} \pi(x_n, t) \sin\left(\frac{k\pi}{L} x_n\right). \end{aligned} \tag{6.97}$$

Such definitions of fields correspond to approximating the field theory with a lattice system. We shall be keeping the relativistic dispersion, however.

For the calculation of entanglement entropy it is most convenient to take the position space covariance matrix of the bosonic degrees multiplied by the lattice spacing a, that is $\phi_n = a\phi(x_n)$ and $\pi_n = a\pi(x_n)$ to keep the correct dimensions. In position space, the covariance matrix of a reduced density matrix corresponding to a subsystem is achieved by taking only those matrix elements corresponding to the lattice points that lie within the subsystem. For example if we are interested in the entanglement between the interval $[0, \ell]$ and the rest of the system, we take the covariance matrix of the lattice sites $x_n \in [0, \ell]$.

Then, the von Neumann entanglement entropy is computed by calculating the symplectic spectrum of the covariance matrix Γ. This is achieved by diagonalizing

$$iJ\Gamma \tag{6.98}$$

with the symplectic unit

$$J = \begin{bmatrix} 0 & I \\ -I & 0 \end{bmatrix}. \tag{6.99}$$

The eigenvalues appear in pairs $\pm\gamma_k$, $k = 1, \ldots, K$. This maps the problem to computing the entropy of K harmonic oscillators at inverse temperatures

$$\beta = \log \frac{\gamma_k + \frac{1}{2}}{\gamma_k - \frac{1}{2}}. \tag{6.100}$$

The von Neumann entropy is then

$$S(\Gamma) = \sum_{k=1}^{K} \left[\left(\gamma_k + \frac{1}{2}\right) \log\left(\gamma_k + \frac{1}{2}\right) - \left(\gamma_k - \frac{1}{2}\right) \log\left(\gamma_k - \frac{1}{2}\right) \right] \tag{6.101}$$

and the Rényi entropies are

$$S^\alpha(\Gamma) = \frac{1}{\alpha - 1} \sum_{k=1}^{K} \log\left[\left(\gamma_k + \frac{1}{2}\right)^\alpha - \left(\gamma_k - \frac{1}{2}\right)^\alpha \right]. \tag{6.102}$$

The covariance matrix approach to computing the entanglement entropies is convenient because it lets us model also the truncation effects by taking finite K. The results are not exactly comparable to the HT cutoff at the same maximal momentum, because in the HT case, we have an energy cutoff which implies also a maximal occupation number for a mode. But it is the closest approximation of the cutoff effect that we can get. Taking K large, we can recover the exact analytical results in the continuum limit.

The concrete results presented in the main text for the thermal states of the Klein-Gordon model

$$H_{\text{mFB}} = \frac{1}{2} \int_0^L \mathrm{d}x \left[\Pi^2(x) + (\partial_x \phi(x))^2 + m^2 \phi^2(x) \right] \tag{6.103}$$

can be recovered using the thermal covariance matrix of the model

$$\begin{aligned}
\langle \phi(x_m)\phi(x_n) \rangle &= \frac{1}{L} \sum_{k=1}^{K} \frac{1}{\epsilon_k} \coth\left(\frac{\epsilon_k}{2T}\right) \sin\!\left(\frac{k\pi}{L} x_m\right) \sin\!\left(\frac{k\pi}{L} x_n\right) \\
\langle \pi(x_m)\pi(x_n) \rangle &= \frac{1}{L} \sum_{k=1}^{K} \epsilon_k \coth\left(\frac{\epsilon_k}{2T}\right) \sin\!\left(\frac{k\pi}{L} x_m\right) \sin\!\left(\frac{k\pi}{L} x_n\right) \\
\frac{1}{2} \langle \{ \phi(x_m), \pi(x_n) \} \rangle &= 0
\end{aligned} \tag{6.104}$$

with the dispersion relation $E_{0q} = \sqrt{\left(\frac{k\pi}{L}\right)^2 + M^2}$.

The quench dynamics can be computed using the equations of motion $\dot{O} = i[H, O]$, yielding for the KG model

$$\phi_k(t) = \cos(\epsilon_k t)\, \phi_k(0) + \frac{\sin(\epsilon_k t)}{\epsilon_k} \pi_k(0) \tag{6.105}$$

$$\pi_k(t) = -\epsilon_k \sin(\epsilon_k t)\, \phi_k(0) + \cos(\epsilon_k t)\, \pi_k(0)\,. \tag{6.106}$$

The procedure for a KG mass quench from the pre-quench mass m_0 to the post-quench mass m is the following: take the momentum space representation of the thermal correlations (6.104) for the pre-quench mass m_0 and propagate them using the equations of motion (6.106) for the post-quench mass m. The covariance matrix is transformed back to position space, the reduced covariance matrix corresponding to the subsystem taken as described above and the entanglement entropies computed.

6.F FINITE SIZE SINE-GORDON BREATHER MASSES

The corrections to infinite size sine-Gordon breather masses to obtain their finite volume counterparts can be computed using the boundary bootstrap [219–222]. The finite size energy E_n of the (excited) n-the breather can be written in the parametric form

$$(ML(\theta), \epsilon(\theta) - \epsilon_0) = \left(\frac{2\pi I_n + 2i \log\left(R^{(n)}(\theta)\right)}{2\frac{m_n}{M} \sinh(\theta)}, \frac{m_n}{M} \cosh(\theta) \right), \tag{6.107}$$

where $\theta \in [0, \infty)$ is the parameter of the parameterization and $I_n \in \mathbb{Z}$ is the quantum number labeling the breather lines. Each value of I_n corresponds to one of the excited states of the n-th breather. These are moving breathers whose momentum has a discrete set of possible values due to the finite volume. In the $L \to \infty$ limit, all breather lines converge to the infinite volume breather mass m_n. Further, λ is the sine-Gordon interaction parameter [eq. (6.47) in the main text], M is the soliton mass and the infinite volume breather mass of the n-th breather m_n is given by

$$m_n = 2M \sin\left(\frac{n\pi}{2\lambda}\right)\,. \tag{6.108}$$

The functions $R^{(n)}$ are the boundary breather reflection factors.

In case of Dirichlet boundary conditions at the edges the reflection factors are given by [219–222]

$$R^{(n)}(\theta) = R_0^{(n)}(\theta) S^{(n)}(0, \theta)\,, \tag{6.109}$$

with

$$\begin{aligned} R_0^{(n)}(\theta) &= \frac{\left(\frac{1}{2}\right)_\theta \left(\frac{n}{2\lambda} + 1\right)_\theta}{\left(\frac{n}{2\lambda} + \frac{3}{2}\right)_\theta} \prod_{k=1}^{n-1} \frac{\left(\frac{k}{2\lambda}\right)_\theta \left(\frac{k}{2\lambda} + 1\right)_\theta}{\left(\frac{k}{2\lambda} + \frac{3}{2}\right)_\theta^2}, \\ S^{(n)}(x, \theta) &= \prod_{k=0}^{n-1} \frac{\left(\frac{x}{\pi\lambda} - \frac{1}{2} + \frac{n-2k-1}{2\lambda}\right)_\theta}{\left(\frac{x}{\pi\lambda} + \frac{1}{2} + \frac{n-2k-1}{2\lambda}\right)_\theta}, \end{aligned} \tag{6.110}$$

where we introduced the following shorthand notation

$$(x)_\theta \equiv \frac{\sin\left[\frac{i\theta}{2} - \frac{\pi x}{2}\right]}{\sin\left[\frac{i\theta}{2} + \frac{\pi x}{2}\right]} \,. \tag{6.111}$$

ACKNOWLEDGEMENTS

During the past years, I have been supported by many people, both scientifically and personally. On both counts, I am very glad that I have had the opportunity to learn from and work with my supervisor Ignacio Cirac. His scientific guidance and original thinking made my time as a Ph.D. student at MPQ a very exciting, insightful and a highly enjoyable journey. I feel grateful for his invaluable support as a mentor, his kindness and the possibility to work in an inspiring environment, together with many great scientists from around the world.

In an equal way, I am thankful to Erez Zohar for patiently answering all my questions and guiding me through my PhD. From a co-supervisor, you became a friend who introduced me to the cinematic world of Woody Allen and showed me the most beautiful corners of Tel Aviv. I wish him, Na'ama and Noga all the best.

I am grateful to Mari Carmen Bañuls for her guidance as my mentor and many discussions about physics.

Science is a team effort, and much of the work that was presented in this thesis would not have been possible without my collaborators. It was a pleasure to get to know Antoine Tilloy and the many discussions that we had about physics and life in general. I am grateful to have had the opportunity to work with Teresa Karanikolaou. Thank you to Ivan Kukuljan for the intense collaboration on quantum field theories and Hamiltonian truncation. Julian Bender answered more questions about lattice gauge theories than I thought that I could possibly have. I would like to thank you for one of the smoothest collaborations that I ever experienced. If I ever have to stay in lockdown in Israel again, I will choose you again as my flatmate.

Thank you to my office mate Giacomo Giudice who never tolerated any nonsense in discussions about physics and who made sure that I do not take my self too seriously. And yes, we can always fit in another hang board session.

I am grateful to Johannes Knörzer for many discussions about more topics than I can count and the insight that uphill cycling can be fun. And that there is always someone quicker than oneself. I would like to thank Anna Hackenbroich, Antoine Sterdyniak, and Clemens Herkommer for their friendship and saving my life during climbing from time to time.

I would like to thank Albert Gasull for proofreading and discussing many of my texts and for showing my how to make a proper tortilla. This thesis would sound very different without him.

Thank you to Jeanne Colbois and Gertian Roose for making Benasque one of the most fun conferences that I ever visited.

I would like to thank Sonya Gzyl for her excellent support via the International Max Planck Research School for Quantum Science and Technology. Your organizational skills made many events possible and allowed us to focus on the scientific part of summer schools and conferences.

It was a pleasure to get to know Caroline de Groot, Tommaso Guiana, David Castells, Asli Cebe, Arthur Christianen, Esther Cruz, Cosimo Rusconi, Benjamin Schiffer, David

Stephen, Dominik Wild, Bennet Windt and all the others from the theory division at MPQ. In particular, I am grateful for the support by Andrea Kluth, Regina Jasny, and Elena Wiggert in many administrative matters and beyond.

Special thanks to my family, who always support me. It is encouraging to know that I can always count on you.

Funding from the International Max-Planck Research School, and the Max Planck Society is gratefully acknowledged.

BIBLIOGRPAHY

[1] Patrick Emonts et al. “Variational Monte Carlo Simulation with Tensor Networks of a Pure $\mathbb{Z}_3$ Gauge Theory in $(2 + 1)$ D”. In: *Physical Review D* 102.7 (Oct. 1, 2020), p. 074501. DOI: `10.1103/PhysRevD.102.074501`.

[2] Julian Bender et al. “Real-Time Dynamics in 2 + 1D Compact QED Using Complex Periodic Gaussian States”. In: *Physical Review Research* 2.4 (Oct. 27, 2020), p. 043145. DOI: `10.1103/PhysRevResearch.2.043145`.

[3] Teresa D. Karanikolaou, Patrick Emonts, and Antoine Tilloy. “Gaussian Continuous Tensor Network States for Simple Bosonic Field Theories”. In: *Physical Review Research* 3.2 (Apr. 19, 2021), p. 023059. DOI: `10.1103/PhysRevResearch.3.023059`.

[4] Patrick Emonts and Ivan Kukuljan. “Reduced Density Matrix and Entanglement in Interacting Quantum Field Theory with Hamiltonian Truncation”. Feb. 22, 2022. arXiv: `2202.11113 [hep-th, physics:quant-ph]`.

[5] Patrick Emonts and Stefan Wessel. “Monte Carlo Study of the Discontinuous Quantum Phase Transition in the Transverse-Field Ising Model on the Pyrochlore Lattice”. In: *Physical Review B* 98.17 (Nov. 27, 2018). DOI: `10.1103/PhysRevB.98.174433`.

[6] Patrick Emonts and Erez Zohar. “Gauss Law, Minimal Coupling and Fermionic PEPS for Lattice Gauge Theories”. In: *SciPost Physics Lecture Notes* (Jan. 17, 2020), p. 12. DOI: `10.21468/SciPostPhysLectNotes.12`.

[7] Andrew M. Steane. *Relativity Made Relatively Easy*. Oxford, United Kingdom: Oxford University Press, 2012. 419 pp.

[8] Max Karl Ernst Ludwig Planck. “Zur Theorie Des Gesetzes Der Energieverteilung Im Normalspectrum”. In: *Verhandlungen der Deutschen Physikalischen Gesellschaft* 2 (1900).

[9] A. Einstein. “Über einen die Erzeugung und Verwandlung des Lichtes betreffenden heuristischen Gesichtspunkt”. In: *Annalen der Physik* 322.6 (1905), pp. 132–148. DOI: `10.1002/andp.19053220607`.

[10] W. Heisenberg. “Über Quantentheoretische Umdeutung Kinematischer Und Mechanischer Beziehungen.” In: *Zeitschrift für Physik* 33.1 (Dec. 1925), pp. 879–893. DOI: `10.1007/BF01328377`.

[11] A. Einstein, B. Podolsky, and N. Rosen. “Can Quantum-Mechanical Description of Physical Reality Be Considered Complete?” In: *Physical Review* 47.10 (May 15, 1935), pp. 777–780. DOI: `10.1103/PhysRev.47.777`.

[12] J. S. Bell. “On the Einstein Podolsky Rosen Paradox”. In: *Physics Physique Fizika* 1.3 (Nov. 1, 1964), pp. 195–200. DOI: `10.1103/PhysicsPhysiqueFizika.1.195`.

[13] B. Hensen et al. “Loophole-Free Bell Inequality Violation Using Electron Spins Separated by 1.3 Kilometres”. In: *Nature* 526.7575 (Oct. 2015), pp. 682–686. DOI: `10.1038/nature15759`.

[14] Nicholas Metropolis et al. “Equation of State Calculations by Fast Computing Machines”. In: *The Journal of Chemical Physics* 21.6 (June 1953), pp. 1087–1092. DOI: `10.1063/1.1699114`.

[15] Simon Duane et al. “Hybrid Monte Carlo”. In: *Physics Letters B* 195.2 (Sept. 1987), pp. 216–222. DOI: `10.1016/0370-2693(87)91197-X`.

[16] Jonathan P. Dowling and Gerard J. Milburn. “Quantum Technology: The Second Quantum Revolution”. In: *Philosophical Transactions of the Royal Society of London. Series A: Mathematical, Physical and Engineering Sciences* 361.1809 (Aug. 15, 2003). Ed. by A. G. J. MacFarlane, pp. 1655–1674. DOI: `10.1098/rsta.2003.1227`.

[17] Richard P. Feynman. “Simulating Physics with Computers”. In: *International Journal of Theoretical Physics* 21.6-7 (June 1982), pp. 467–488. DOI: `10.1007/BF02650179`.

[18] Andreas Trabesinger. “Quantum Simulation”. In: *Nature Physics* 8.4 (Apr. 2012), pp. 263–263. DOI: `10.1038/nphys2258`.

[19] John Preskill. “Quantum Computing 40 Years Later”. June 25, 2021. arXiv: `2106.10522 [quant-ph]`.

[20] FLAG Working Group et al. “Review of Lattice Results Concerning Low-Energy Particle Physics”. In: *The European Physical Journal C* 74.9 (Sept. 2014). DOI: `10.1140/epjc/s10052-014-2890-7`.

[21] M. Fannes, B. Nachtergaele, and R. F. Werner. “Finitely Correlated States on Quantum Spin Chains”. In: *Communications in Mathematical Physics* 144.3 (Mar. 1992), pp. 443–490. DOI: `10.1007/BF02099178`.

[22] Guifré Vidal. “Efficient Simulation of One-Dimensional Quantum Many-Body Systems”. In: *Physical Review Letters* 93.4 (July 2004), p. 040502. DOI: `10.1103/PhysRevLett.93.040502`.

[23] F. Verstraete and J.I. Cirac. “Renormalization Algorithms for Quantum-Many Body Systems in Two and Higher Dimensions”. July 2004. arXiv: `cond-mat/0407066`.

[24] F. Verstraete et al. “Criticality, the Area Law, and the Computational Power of Projected Entangled Pair States”. In: *Physical Review Letters* 96.22 (June 2006). DOI: `10.1103/physrevlett.96.220601`.

[25] Norbert Schuch, Ignacio Cirac, and David Pérez-García. “PEPS as Ground States: Degeneracy and Topology”. In: *Annals of Physics* 325.10 (Oct. 2010), pp. 2153–2192. DOI: `10.1016/j.aop.2010.05.008`.

[26] Ulrich Schollwöck. “The Density-Matrix Renormalization Group in the Age of Matrix Product States”. In: *Annals of Physics* 326.1 (Jan. 2011), pp. 96–192. DOI: `10.1016/j.aop.2010.09.012`.

[27] Jacob C. Bridgeman and Christopher T. Chubb. “Hand-Waving and Interpretive Dance: An Introductory Course on Tensor Networks”. In: *Journal of Physics A: Mathematical and Theoretical* 50.22 (June 2, 2017), p. 223001. DOI: `10.1088/1751-8121/aa6dc3`.

[28] Román Orús. “A Practical Introduction to Tensor Networks: Matrix Product States and Projected Entangled Pair States”. In: *Annals of Physics* 349 (Oct. 2014), pp. 117–158. DOI: `10.1016/j.aop.2014.06.013`.

[29] Ignacio Cirac et al. “Matrix Product States and Projected Entangled Pair States: Concepts, Symmetries, and Theorems”. Nov. 24, 2020. arXiv: `2011.12127 [cond-mat, physics:hep-th, physics:quant-ph]`.

[30] Steven R. White. “Density Matrix Formulation for Quantum Renormalization Groups”. In: *Physical Review Letters* 69.19 (Nov. 9, 1992), pp. 2863–2866. DOI: `10.1103/PhysRevLett.69.2863`.

[31] Lars Grasedyck. “Hierarchical Singular Value Decomposition of Tensors”. In: *SIAM Journal on Matrix Analysis and Applications* 31.4 (Jan. 2010), pp. 2029–2054. DOI: `10.1137/090764189`.

[32] I. V. Oseledets. “Tensor-Train Decomposition”. In: *SIAM Journal on Scientific Computing* 33.5 (Jan. 2011), pp. 2295–2317. DOI: `10.1137/090752286`.

[33] Wolfgang Hackbusch. *Tensor Spaces and Numerical Tensor Calculus*. Second edition. Springer Series in Computational Mathematics volume 56. Cham, Switzerland: Springer, 2019. 605 pp. DOI: `10.1007/978-3-03035554-8`.

[34] Ian Affleck et al. “Rigorous Results on Valence-Bond Ground States in Antiferromagnets”. In: *Physical Review Letters* 59.7 (Aug. 17, 1987), pp. 799–802. DOI: `10.1103/PhysRevLett.59.799`.

[35] D. Perez-Garcia et al. “Matrix Product State Representations”. May 14, 2007. arXiv: `quant-ph/0608197`.

[36] J. Eisert, M. Cramer, and M. B. Plenio. “*Colloquium* : Area Laws for the Entanglement Entropy”. In: *Reviews of Modern Physics* 82.1 (Feb. 4, 2010), pp. 277–306. DOI: `10.1103/RevModPhys.82.277`.

[37] Norbert Schuch, David Pérez-García, and Ignacio Cirac. “Classifying Quantum Phases Using Matrix Product States and Projected Entangled Pair States”. In: *Physical Review B* 84.16 (Oct. 2011). DOI: `10.1103/physrevb.84.165139`.

[38] Michael Lubasch, J. Ignacio Cirac, and Mari-Carmen Bañuls. “Algorithms for Finite Projected Entangled Pair States”. In: *Physical Review B* 90.6 (Aug. 2014). DOI: `10.1103/physrevb.90.064425`.

[39] J. Jordan et al. “Classical Simulation of Infinite-Size Quantum Lattice Systems in Two Spatial Dimensions”. In: *Physical Review Letters* 101.25 (Dec. 18, 2008), p. 250602. DOI: `10.1103/PhysRevLett.101.250602`.

[40] Ho N. Phien et al. “Infinite Projected Entangled Pair States Algorithm Improved: Fast Full Update and Gauge Fixing”. In: *Physical Review B* 92.3 (July 24, 2015), p. 035142. DOI: `10.1103/PhysRevB.92.035142`.

[41] Tomotoshi Nishino and Kouichi Okunishi. “Corner Transfer Matrix Renormalization Group Method”. In: *Journal of the Physical Society of Japan* 65.4 (Apr. 15, 1996), pp. 891–894. DOI: `10.1143/JPSJ.65.891`.

[42] V. Murg, F. Verstraete, and J. I. Cirac. “Variational Study of Hard-Core Bosons in a Two-Dimensional Optical Lattice Using Projected Entangled Pair States”. In: *Physical Review A* 75.3 (Mar. 13, 2007), p. 033605. DOI: `10.1103/PhysRevA.75.033605`.

[43] Román Orús and Guifré Vidal. “Simulation of Two-Dimensional Quantum Systems on an Infinite Lattice Revisited: Corner Transfer Matrix for Tensor Contraction”. In: *Physical Review B* 80.9 (Sept. 8, 2009), p. 094403. DOI: `10.1103/PhysRevB.80.094403`.

[44] Y.-Y. Shi, L.-M. Duan, and G. Vidal. “Classical Simulation of Quantum Many-Body Systems with a Tree Tensor Network”. In: *Physical Review A* 74.2 (Aug. 23, 2006), p. 022320. DOI: `10.1103/PhysRevA.74.022320`.

[45] Simone Montangero, Enrique Rico, and Pietro Silvi. “Loop-Free Tensor Networks for High-Energy Physics”. In: *Philosophical Transactions of the Royal Society A: Mathematical, Physical and Engineering Sciences* 380.2216 (Feb. 7, 2022), p. 20210065. DOI: `10.1098/rsta.2021.0065`.

[46] Cécilia Lancien and David Pérez-García. “Correlation Length in Random MPS and PEPS”. In: *Annales Henri Poincaré* 23.1 (Jan. 1, 2022), pp. 141–222. DOI: `10.1007/s00023-021-01087-4`.

[47] G. Vidal. “Entanglement Renormalization”. In: *Physical Review Letters* 99.22 (Nov. 2007), p. 220405. DOI: `10.1103/PhysRevLett.99.220405`.

[48] Christina V. Kraus et al. “Fermionic Projected Entangled Pair States”. In: *Physical Review A* 81.5 (May 26, 2010). DOI: `10.1103/PhysRevA.81.052338`.

[49] Erez Zohar and Michele Burrello. “Building Projected Entangled Pair States with a Local Gauge Symmetry”. In: *New Journal of Physics* 18.4 (Apr. 8, 2016), p. 043008. DOI: `10.1088/1367-2630/18/4/043008`.

[50] Philippe Corboz and Guifré Vidal. “Fermionic Multiscale Entanglement Renormalization Ansatz”. In: *Physical Review B* 80.16 (Oct. 29, 2009), p. 165129. DOI: `10.1103/PhysRevB.80.165129`.

[51] Philippe Corboz et al. “Simulation of Interacting Fermions with Entanglement Renormalization”. In: *Physical Review A* 81.1 (Jan. 21, 2010), p. 010303. DOI: `10.1103/PhysRevA.81.010303`.

[52] Philippe Corboz et al. “Simulation of Strongly Correlated Fermions in Two Spatial Dimensions with Fermionic Projected Entangled-Pair States”. In: *Phys. Rev. B* 81.16 (Apr. 2010), p. 165104. DOI: `10.1103/PhysRevB.81.165104`.

[53] Ashley Milsted, Jutho Haegeman, and Tobias J. Osborne. “Matrix Product States and Variational Methods Applied to Critical Quantum Field Theory”. In: *Physical Review D* 88.8 (Oct. 24, 2013), p. 085030. DOI: `10.1103/PhysRevD.88.085030`.

[54] Bram Vanhecke et al. “Scaling Hypothesis for Matrix Product States”. In: *Physical Review Letters* 123.25 (Dec. 2019), p. 250604. DOI: `10.1103/PhysRevLett.123.250604`.

[55] Clement Delcamp and Antoine Tilloy. “Computing the Renormalization Group Flow of Two-Dimensional ϕ^4 Theory with Tensor Networks”. In: *Physical Review Research* 2.3 (Aug. 20, 2020), p. 033278. DOI: `10.1103/PhysRevResearch.2.033278`.

[56] F. Verstraete and J. I. Cirac. “Continuous Matrix Product States for Quantum Fields”. In: *Physical Review Letters* 104.19 (May 14, 2010), p. 190405. DOI: `10.1103/PhysRevLett.104.190405`.

[57] Jutho Haegeman et al. “Applying the Variational Principle to $(1+1)$-Dimensional Quantum Field Theories”. In: *Physical Review Letters* 105.25 (Dec. 2010). DOI: `10.1103/physrevlett.105.251601`.

[58] Vid Stojevic et al. “Conformal Data from Finite Entanglement Scaling”. In: *Physical Review B* 91.3 (Jan. 2015), p. 035120. DOI: `10.1103/PhysRevB.91.035120`.

[59] Julián Rincón, Martin Ganahl, and Guifre Vidal. “Lieb-Liniger Model with Exponentially Decaying Interactions: A Continuous Matrix Product State Study”. In: *Physical Review B* 92.11 (Sept. 2015), p. 115107. DOI: `10.1103/PhysRevB.92.115107`.

[60] Jutho Haegeman et al. “Calculus of Continuous Matrix Product States”. In: *Physical Review B* 88.8 (Aug. 20, 2013), p. 085118. DOI: `10.1103/PhysRevB.88.085118`.

[61] Antoine Tilloy and J. Ignacio Cirac. “Continuous Tensor Network States for Quantum Fields”. In: *Physical Review X* 9.2 (May 28, 2019), p. 021040. DOI: `10.1103/PhysRevX.9.021040`.

[62] Tom Shachar and Erez Zohar. “Approximating Relativistic Quantum Field Theories with Continuous Tensor Networks”. Oct. 4, 2021. arXiv: `2110.01603 [hep-th, physics:quant-ph]`.

[63] Michael Edward Peskin and Daniel V. Schroeder. *An Introduction to Quantum Field Theory*. Reading, Mass: Addison-Wesley Pub. Co, 1995. 842 pp.

[64] A. Pais and S. B. Treiman. “How Many Charm Quantum Numbers Are There?” In: *Physical Review Letters* 35.23 (Dec. 8, 1975), pp. 1556–1559. DOI: `10.1103/PhysRevLett.35.1556`.

[65] Steven Weinberg. *The Quantum Theory of Fields*. Cambridge ; New York: Cambridge University Press, 1995. 3 pp.

[66] Franz J. Wegner. “Duality in Generalized Ising Models and Phase Transitions without Local Order Parameters”. In: *Journal of Mathematical Physics* 12.10 (Oct. 1971), pp. 2259–2272. DOI: `10.1063/1.1665530`.

[67] E. Fradkin and S. H. Shenker. “Phase Diagrams of Lattice Gauge Theories with Higgs Fields”. In: *Phys. Rev. D* 19.12 (June 1979), pp. 3682–3697. DOI: `10.1103/PhysRevD.19.3682`.

[68] David J. Gross and Frank Wilczek. “Asymptotically Free Gauge Theories. I”. In: *Physical Review D* 8.10 (Nov. 15, 1973), pp. 3633–3652. DOI: `10.1103/PhysRevD.8.3633`.

[69] H. David Politzer. “Reliable Perturbative Results for Strong Interactions?” In: *Physical Review Letters* 30.26 (June 1973), pp. 1346–1349. DOI: `10.1103/PhysRevLett.30.1346`.

[70] Kenneth G. Wilson. “Confinement of Quarks”. In: *Physical Review D* 10.CLNS-262 (8 Oct. 15, 1974), pp. 2445–2459. DOI: `10.1103/PhysRevD.10.2445`.

[71] Michael Creutz. “Monte Carlo Study of Quantized SU(2) Gauge Theory”. In: *Physical Review D* 21.8 (Apr. 15, 1980), pp. 2308–2315. DOI: `10.1103/PhysRevD.21.2308`.

[72] J. Greensite. “The Confinement Problem in Lattice Gauge Theory”. In: *Prog. Part. Nucl. Phys.* 51 (2003), p. 1. arXiv: `hep-lat/0301023`.

[73] Franco Strocchi. *An Introduction to Non-Perturbative Foundations of Quantum Field Theory*. 2016.

[74] Richard P. Feynman and Albert R. Hibbs. *Quantum Mechanics and Path Integrals*. 20. [pr.] International Series in Pure and Applied Physics. New York, NY: McGraw-Hill, 1995. 365 pp.

[75] Alexandre Deur, Stanley J. Brodsky, and Guy F. de Téramond. “The QCD Running Coupling”. In: *Progress in Particle and Nuclear Physics* 90 (Sept. 2016), pp. 1–74. DOI: `10.1016/j.ppnp.2016.04.003`.

[76] S. Ben-Menahem. “Confinement in Compact QED for Low Couplings”. In: *Phys. Rev. D* 20.8 (Oct. 1979), pp. 1923–1933. DOI: `10.1103/PhysRevD.20.1923`.

[77] Michael Creutz, Laurence Jacobs, and Claudio Rebbi. “Monte Carlo Study of Abelian Lattice Gauge Theories”. In: *Physical Review D* 20.8 (Oct. 15, 1979), pp. 1915–1922. DOI: `10.1103/PhysRevD.20.1915`.

[78] G. Bhanot and Michael Creutz. “Phase Diagram of Z(N) and U(1) Gauge Theories in Three Dimensions”. In: *Phys. Rev. D* 21.10 (May 1980), pp. 2892–2902. DOI: `10.1103/PhysRevD.21.2892`.

[79] Michael Creutz, Laurence Jacobs, and Claudio Rebbi. “Monte Carlo Computations in Lattice Gauge Theories”. In: *Physics Reports* 95.4 (Apr. 1983), pp. 201–282. DOI: `10.1016/0370-1573(83)90016-9`.

[80] Matthias Troyer and Uwe-Jens Wiese. “Computational Complexity and Fundamental Limitations to Fermionic Quantum Monte Carlo Simulations”. In: *Physical Review Letters* 94.17 (May 4, 2005). DOI: `10.1103/PhysRevLett.94.170201`.

[81] Mari Carmen Bañuls et al. “Density Induced Phase Transitions in the Schwinger Model: A Study with Matrix Product States”. In: *Phys. Rev. Lett.* 118.7 (Feb. 2017), p. 071601. DOI: `10.1103/PhysRevLett.118.071601`.

[82] Boye Buyens et al. “Finite-Representation Approximation of Lattice Gauge Theories at the Continuum Limit with Tensor Networks”. In: *Physical Review D: Particles and Fields* 95 (2017), p. 094509. DOI: `10.1103/PhysRevD.95.094509`.

[83] John Kogut and Leonard Susskind. “Hamiltonian Formulation of Wilson’s Lattice Gauge Theories”. In: *Physical Review D* 11.2 (Jan. 15, 1975), pp. 395–408. DOI: `10.1103/PhysRevD.11.395`.

[84] Leonard Susskind. “Lattice Fermions”. In: *Physical Review D* 16.10 (Nov. 15, 1977), pp. 3031–3039. DOI: `10.1103/PhysRevD.16.3031`.

[85] H.B. Nielsen and M. Ninomiya. “A No-Go Theorem for Regularizing Chiral Fermions”. In: *Physics Letters B* 105.23 (1981), pp. 219–223. DOI: `http://dx.doi.org/10.1016/0370-2693(81)91026-1`.

[86] John B. Kogut. “An Introduction to Lattice Gauge Theory and Spin Systems”. In: *Reviews of Modern Physics* 51.4 (Oct. 1, 1979), pp. 659–713. DOI: `10.1103/RevModPhys.51.659`.

[87] D. Horn. “Finite Matrix Models with Continuous Local Gauge Invariance”. In: *Physics Letters B* 100.2 (Mar. 1981), pp. 149–151. DOI: `10.1016/0370-2693(81)90763-2`.

[88] P. Orland and D. Rohrlich. “Lattice Gauge Magnets: Local Isospin from Spin”. In: *Nuclear Physics B* 338.3 (1990), pp. 647–672. DOI: `10.1016/0550-3213(90)90646-U`.

[89] S Chandrasekharan and U.-J Wiese. “Quantum Link Models: A Discrete Approach to Gauge Theories”. In: *Nuclear Physics B* 492.1-2 (May 1997), pp. 455–471. DOI: `10.1016/S0550-3213(97)80041-7`.

[90] R. Brower, S. Chandrasekharan, and U.-J. Wiese. “QCD as a Quantum Link Model”. In: *Physical Review D* 60.9 (Sept. 27, 1999). DOI: `10.1103/PhysRevD.60.094502`.

[91] M. Mathur. “Harmonic Oscillator Pre-Potentials in SU (2) Lattice Gauge Theory”. In: *Journal of Physics A: Mathematical and General* 38.46 (2005), p. 10015.

[92] S. D. Drell et al. “Quantum Electrodynamics on a Lattice: A Hamiltonian Variational Approach to the Physics of the Weak-Coupling Region”. In: *Phys. Rev. D* 19.2 (Jan. 1979), pp. 619–638. DOI: `10.1103/PhysRevD.19.619`.

[93] David B. Kaplan and Jesse R. Stryker. “Gauss’s Law, Duality, and the Hamiltonian Formulation of U(1) Lattice Gauge Theory”. In: *Physical Review D* 102.9 (Nov. 20, 2020), p. 094515. DOI: `10.1103/PhysRevD.102.094515`.

[94] D. Horn, M. Weinstein, and S. Yankielowicz. “Hamiltonian Approach to Z (N) Lattice Gauge Theories”. In: *Physical Review D* 19.12 (June 15, 1979), pp. 3715–3731. DOI: `10.1103/PhysRevD.19.3715`.

[95] Julian Schwinger. “Gauge Invariance and Mass. II”. In: *Physical Review* 128.5 (Dec. 1, 1962), pp. 2425–2429. DOI: `10.1103/PhysRev.128.2425`.

[96] Sidney Coleman. “More about the Massive Schwinger Model”. In: *Annales de Physique* 101 (1976), pp. 239–267. DOI: `10.1016/0003-4916(76)90280-3`.

[97] T. M. R. Byrnes et al. “Density Matrix Renormalization Group Approach to the Massive Schwinger Model”. In: *Phys. Rev. D* 66.1 (July 2002), p. 013002. DOI: `10.1103/PhysRevD.66.013002`.

[98] T. Banks, L. Susskind, and J. Kogut. “Strong-Coupling Calculations of Lattice Gauge Theories: (1 + 1)-Dimensional Exercises”. In: *Phys. Rev. D* 13.CLNS-318 (4 Feb. 1976), pp. 1043–1053. DOI: `10.1103/PhysRevD.13.1043`.

[99] M.C. Bañuls et al. “The Mass Spectrum of the Schwinger Model with Matrix Product States”. In: *Journal of High Energy Physics* 2013.11 (Nov. 2013). DOI: `10.1007/JHEP11(2013)158`.

[100] Mari Carmen Bañuls et al. “Chiral Condensate in the Schwinger Model with Matrix Product Operators”. In: *Physical Review D* 93.9 (May 24, 2016), p. 094512. DOI: `10.1103/PhysRevD.93.094512`.

[101] Boye Buyens, Frank Verstraete, and Karel Van Acoleyen. “Hamiltonian Simulation of the Schwinger Model at Finite Temperature”. In: *Physical Review D* 94.8 (Oct. 21, 2016). DOI: `10.1103/PhysRevD.94.085018`.

[102] T. Pichler et al. “Real-Time Dynamics in U(1) Lattice Gauge Theories with Tensor Networks”. In: *Phys. Rev. X* 6.1 (Mar. 2016), p. 011023. DOI: `10.1103/PhysRevX.6.011023`.

[103] Mari Carmen Bañuls et al. “Efficient Basis Formulation for (1 + 1)-Dimensional SU(2) Lattice Gauge Theory: Spectral Calculations with Matrix Product States”. In: *Physical Review X* 7.4 (Nov. 28, 2017). DOI: `10.1103/PhysRevX.7.041046`.

[104] Daniel Robaina, Mari Carmen Bañuls, and J. Ignacio Cirac. “Simulating $2+1$D Z3 Lattice Gauge Theory with an Infinite Projected Entangled-Pair State”. In: *Physical Review Letters* 126.5 (Feb. 2021). DOI: `10.1103/physrevlett.126.050401`.

[105] P. Sala et al. “Variational Study of U(1) and SU(2) Lattice Gauge Theories with Gaussian States in 1 + 1 Dimensions”. In: *Physical Review D* 98.3 (Aug. 27, 2018), p. 034505. DOI: `10.1103/PhysRevD.98.034505`.

[106] Roger G. Melko et al. “Restricted Boltzmann Machines in Quantum Physics”. In: *Nature Physics* 15.9 (Sept. 2019), pp. 887–892. DOI: `10.1038/s41567-019-0545-1`.

[107] Juan Carrasquilla. “Machine Learning for Quantum Matter”. In: *Advances in Physics: X* 5.1 (Jan. 1, 2020), p. 1797528. DOI: `10.1080/23746149.2020.1797528`.

[108] Di Luo et al. “Gauge Equivariant Neural Networks for Quantum Lattice Gauge Theories”. Dec. 9, 2020. arXiv: `2012.05232 [cond-mat, physics:hep-lat, physics:quant-ph]`.

[109] Di Luo et al. “Gauge Invariant Autoregressive Neural Networks for Quantum Lattice Models”. Jan. 18, 2021. arXiv: `2101.07243 [cond-mat, physics:hep-lat, physics:quant-ph]`.

[110] U.-J. Wiese. “Ultracold Quantum Gases and Lattice Systems: Quantum Simulation of Lattice Gauge Theories”. In: *Annalen der Physik* 525.10-11 (2013), pp. 777–796. DOI: `10.1002/andp.201300104`. arXiv: `1305.1602 [quant-ph]`.

[111] Philipp Hauke et al. “Non-Abelian Gauge Fields and Topological Insulators in Shaken Optical Lattices”. In: *Physical Review Letters* 109 (2012), p. 145301.

[112] P. Hauke et al. “Quantum Simulation of a Lattice Schwinger Model in a Chain of Trapped Ions”. In: *Phys. Rev. X* 3.4 (Nov. 2013), p. 041018. DOI: `10.1103/PhysRevX.3.041018`.

[113] Marlon Brenes et al. “Many-Body Localization Dynamics from Gauge Invariance”. In: *Physical Review Letters* 120.3 (Jan. 19, 2018), p. 030601. DOI: `10.1103/PhysRevLett.120.030601`. arXiv: `1706.05878`.

[114] Irene Papaefstathiou, Adam Smith, and Johannes Knolle. “Disorder-Free Localization in a Simple $U(1)$ Lattice Gauge Theory”. In: *Physical Review B* 102.16 (Oct. 16, 2020), p. 165132. DOI: `10.1103/PhysRevB.102.165132`.

[115] Jad C. Halimeh et al. “Stabilizing Disorder-Free Localization”. Jan. 6, 2022. arXiv: `2111.02427 [cond-mat, physics:quant-ph]`.

[116] Michael Levin and Cody P. Nave. “Tensor Renormalization Group Approach to Two-Dimensional Classical Lattice Models”. In: *Physical Review Letters* 99.12 (Sept. 19, 2007), p. 120601. DOI: `10.1103/PhysRevLett.99.120601`.

[117] Yannick Meurice et al. “Comparing Tensor Renormalization Group and Monte Carlo Calculations for Spin and Gauge Models”. In: *PoS(LATTICE 2013)* (2013).

[118] Yannick Meurice et al. “Approaching Conformality with the Tensor Renormalization Group Method”. In: *PoS(LATTICE 2015)* (2015), p. 285.

[119] Alexei Bazavov et al. “Tensor Renormalization Group Study of the Non-Abelian Higgs Model in Two Dimensions”. In: *Physical Review D* 99.11 (June 24, 2019), p. 114507. DOI: `10.1103/PhysRevD.99.114507`.

[120] I. M. Georgescu, S. Ashhab, and Franco Nori. “Quantum Simulation”. In: *Reviews of Modern Physics* 86.1 (Mar. 2014), pp. 153–185. DOI: `10.1103/RevModPhys.86.153`.

[121] Mari Carmen Bañuls and Krzysztof Cichy. “Review on Novel Methods for Lattice Gauge Theories”. In: *Reports on Progress in Physics* 83.2 (Feb. 1, 2020), p. 024401. DOI: `10.1088/1361-6633/ab6311`.

[122] Mari Carmen Bañuls et al. “Simulating Lattice Gauge Theories within Quantum Technologies”. In: *The European Physical Journal D* 74.8 (Aug. 2020), p. 165. DOI: `10.1140/epjd/e2020-100571-8`.

[123] H. P. Büchler et al. “Atomic Quantum Simulator for Lattice Gauge Theories and Ring Exchange Models”. In: *Phys. Rev. Lett.* 95.4 (July 2005), p. 040402. DOI: `10.1103/PhysRevLett.95.040402`.

[124] J. Ignacio Cirac, Paolo Maraner, and Jiannis K. Pachos. “Cold Atom Simulation of Interacting Relativistic Quantum Field Theories”. In: *Physical Review Letters* 105.19 (Nov. 2010). DOI: `10.1103/physrevlett.105.190403`.

[125] E. Zohar and B. Reznik. “Confinement and Lattice Quantum-Electrodynamic Electric Flux Tubes Simulated with Ultracold Atoms”. In: *Phys. Rev. Lett.* 107.27 (Dec. 2011), p. 275301. DOI: `10.1103/PhysRevLett.107.275301`.

[126] D. Marcos et al. “Superconducting Circuits for Quantum Simulation of Dynamical Gauge Fields”. In: *Phys. Rev. Lett.* 111.11 (Sept. 2013), p. 110504. DOI: `10.1103/PhysRevLett.111.110504`.

[127] Christian Schweizer et al. “Floquet Approach to $\mathbb{Z}_2$ Lattice Gauge Theories with Ultracold Atoms in Optical Lattices”. In: *Nature Physics* 15.11 (Nov. 2019), pp. 1168–1173. DOI: `10.1038/s41567-019-0649-7`.

[128] Alexander Mil et al. “A Scalable Realization of Local U(1) Gauge Invariance in Cold Atomic Mixtures”. In: *Science* 367.6482 (Mar. 6, 2020), pp. 1128–1130. DOI: `10.1126/science.aaz5312`.

[129] John Preskill. “Quantum Computing in the NISQ Era and Beyond”. In: *Quantum* 2 (Aug. 6, 2018), p. 79. DOI: `10.22331/q-2018-08-06-79`.

[130] S. P. Jordan, K. S. M. Lee, and J. Preskill. “Quantum Algorithms for Quantum Field Theories”. In: *Science* 336 (2012), pp. 1130–1133.

[131] Martin Luscher. “Volume Dependence of the Energy Spectrum in Massive Quantum Field Theories. 2. Scattering States”. In: *Communications in Mathematical Physics* 105 (DESY-86-034 1986), pp. 153–188.

[132] U-J Wiese. “Identification of Resonance Parameters from the Finite Volume Energy Spectrum”. In: *Nuclear Physics B-Proceedings Supplements* 9 (1989), pp. 609–613.

[133] Martin Lüscher. “Signatures of Unstable Particles in Finite Volume”. In: *Nuclear Physics B* 364.1 (1991), pp. 237–251.

[134] Hsuan-Hao Lu et al. “Simulations of Subatomic Many-Body Physics on a Quantum Frequency Processor”. In: *Physical Review A* 100.1 (July 15, 2019), p. 012320. DOI: `10.1103/PhysRevA.100.012320`.

[135] E. A. Martinez et al. “Real-Time Dynamics of Lattice Gauge Theories with a Few-Qubit Quantum Computer”. In: *Nature* 534 (2016), pp. 516–519. DOI: `10.1038/nature18318`.

[136] Seth Lloyd. “Universal Quantum Simulators”. In: *Science* 273.5278 (Aug. 23, 1996), pp. 1073–1078. DOI: `10.1126/science.273.5278.1073`.

[137] A. Mezzacapo et al. “Non-Abelian SU(2) Lattice Gauge Theories in Superconducting Circuits”. In: *Phys. Rev. Lett.* 115.24 (Dec. 2015), p. 240502. DOI: `10.1103/PhysRevLett.115.240502`.

[138] H. Weimer et al. “A Rydberg Quantum Simulator”. In: *Nat Phys* 6.5 (May 2010), pp. 382–388.

[139] L. Tagliacozzo et al. “Optical Abelian Lattice Gauge Theories”. In: *Annals of Physics* 330 (Mar. 2013), pp. 160–191. DOI: `10.1016/j.aop.2012.11.009`.

[140] L. Tagliacozzo et al. “Simulation of Non-Abelian Gauge Theories with Optical Lattices”. In: *Nature Communications* 4.1 (Dec. 2013), p. 2615. DOI: `10.1038/ncomms3615`.

[141] Erez Zohar et al. “Digital Quantum Simulation of Z 2 Lattice Gauge Theories with Dynamical Fermionic Matter”. In: *Physical Review Letters* 118.7 (Feb. 17, 2017). DOI: `10.1103/PhysRevLett.118.070501`.

[142] Erez Zohar et al. “Digital Lattice Gauge Theories”. In: *Physical Review A* 95.2 (Feb. 6, 2017), p. 023604. DOI: `10.1103/PhysRevA.95.023604`.

[143] V. P. Yurov and Al. B. Zamolodchikov. “Truncated Conformal Space Approach to the Sacling Lee-Yang Model”. In: *International Journal of Modern Physics A* 05.16 (Aug. 20, 1990), pp. 3221–3245. DOI: `10.1142/S0217751X9000218X`.

[144] V.P. Yurov and Al.B. Zamolodchikov. “Truncated-Fermionic-Space Approach to the Critical 2D Ising Model with Magnetic Field”. In: *International Journal of Modern Physics A* 06.25 (Oct. 20, 1991), pp. 4557–4578. DOI: `10.1142/S0217751X91002161`.

[145] Slava Rychkov and Lorenzo G. Vitale. “Hamiltonian Truncation Study of the ϕ^4 Theory in Two Dimensions”. In: *Physical Review D* 91.8 (Apr. 8, 2015), p. 085011. DOI: `10.1103/PhysRevD.91.085011`.

[146] Slava Rychkov and Lorenzo G. Vitale. “Hamiltonian Truncation Study of the ϕ^4 Theory in Two Dimensions. II. The Z 2 -Broken Phase and the Chang Duality”. In: *Physical Review D* 93.6 (Mar. 7, 2016), p. 065014. DOI: `10.1103/PhysRevD.93.065014`.

[147] Anders W. Sandvik. “Computational Studies of Quantum Spin Systems”. In: *AIP Conference Proceedings*. Ed. by Adolfo Avella and Ferdinando Mancini. Vol. 1297. 2010, pp. 135–338. DOI: `10.1063/1.3518900`.

[148] Matthijs Hogervorst, Slava Rychkov, and Balt C. van Rees. “Truncated Conformal Space Approach in d Dimensions: A Cheap Alternative to Lattice Field Theory?” In: *Physical Review D* 91.2 (Jan. 6, 2015), p. 025005. DOI: `10.1103/PhysRevD.91.025005`.

[149] Robert M. Konik and Yury Adamov. “Numerical Renormalization Group for Continuum One-Dimensional Systems”. In: *Physical Review Letters* 98.14 (Apr. 6, 2007), p. 147205. DOI: `10.1103/PhysRevLett.98.147205`.

[150] Kenji Fukushima and Tetsuo Hatsuda. “The Phase Diagram of Dense QCD”. In: *Reports on Progress in Physics* 74.1 (Jan. 1, 2011), p. 014001. DOI: `10.1088/0034-4885/74/1/014001`.

[151] Marc Daniel Schulz et al. “Breakdown of a Perturbed $\boldsymbol{\mathbbm{Z}}_N$ Topological Phase”. In: *New Journal of Physics* 14.2 (Feb. 17, 2012), p. 025005. DOI: `10.1088/1367-2630/14/2/025005`.

[152] L. Tagliacozzo and G. Vidal. “Entanglement Renormalization and Gauge Symmetry”. In: *Physical Review B* 83.11 (Mar. 16, 2011), p. 115127. DOI: `10.1103/PhysRevB.83.115127`.

[153] Timo Felser et al. “Two-Dimensional Quantum-Link Lattice Quantum Electrodynamics at Finite Density”. In: *Physical Review X* 10.4 (Nov. 25, 2020), p. 041040. DOI: `10.1103/PhysRevX.10.041040`.

[154] L. Tagliacozzo, A. Celi, and M. Lewenstein. “Tensor Networks for Lattice Gauge Theories with Continuous Groups”. In: *Phys. Rev. X* 4.4 (Nov. 2014), p. 041024. DOI: `10.1103/PhysRevX.4.041024`.

[155] Jutho Haegeman et al. “Gauging Quantum States: From Global to Local Symmetries in Many-Body Systems”. In: *Physical Review X* 5.1 (Feb. 2015). DOI: `10.1103/physrevx.5.011024`.

[156] Erez Zohar et al. “Fermionic Projected Entangled Pair States and Local U(1) Gauge Theories”. In: *Annals of Physics* 363 (Dec. 2015), pp. 385–439. DOI: `10.1016/j.aop.2015.10.009`.

[157] Erez Zohar et al. “Projected Entangled Pair States with Non-Abelian Gauge Symmetries: An SU(2) Study”. In: *Annals of Physics* 374 (Nov. 2016), pp. 84–137. DOI: `10.1016/j.aop.2016.08.008`.

[158] Erez Zohar and J. Ignacio Cirac. “Combining Tensor Networks with Monte Carlo Methods for Lattice Gauge Theories”. In: *Physical Review D* 97.3 (Feb. 2018). DOI: `10.1103/physrevd.97.034510`.

[159] G. ’t Hooft. “On the Phase Transition towards Permanent Quark Confinement”. In: *Nuclear Physics B* 138.1 (June 5, 1978), pp. 1–25. DOI: `10.1016/0550-3213(78)90153-0`.

[160] John M. Cornwall. “Quark Confinement and Vortices in Massive Gauge-Invariant QCD”. In: *Nuclear Physics B* 157.3 (Oct. 1, 1979), pp. 392–412. DOI: `10.1016/0550-3213(79)90111-1`.

[161] J. Ambjørn and P. Olesen. “A Color Magnetic Vortex Condensate in QCD”. In: *Nuclear Physics B*. Volume B170 [FSI] No. 3 to Follow in Approximately Two Months 170.2 (Oct. 20, 1980), pp. 265–282. DOI: `10.1016/0550-3213(80)90150-9`.

[162] H. B. Nielsen and P. Olesen. “A Quantum Liquid Model for the QCD Vacuum: Gauge and Rotational Invariance of Domained and Quantized Homogeneous Color Fields”. In: *Nuclear Physics B* 160.2 (Dec. 3, 1979), pp. 380–396. DOI: `10.1016/0550-3213(79)90065-8`.

[163] Gerhard Mack. “Properties of Lattice Gauge Theory Models at Low Temperatures”. In: *Recent Developments in Gauge Theories*. Ed. by G.’t Hooft et al. NATO Advanced Study Institutes Series. Boston, MA: Springer US, 1980, pp. 217–263. DOI: `10.1007/978-1-4684-7571-5_14`.

[164] Richard P. Feynman. “The Qualitative Behavior of Yang-Mills Theory in 2 + 1 Dimensions”. In: *Nuclear Physics B* 188.3 (Oct. 5, 1981), pp. 479–512. DOI: `10.1016/0550-3213(81)90005-5`.

[165] H. W. J. Blöte and R. H. Swendsen. “First-Order Phase Transitions and the Three-State Potts Model”. In: *Physical Review Letters* 43.11 (Sept. 10, 1979), pp. 799–802. DOI: `10.1103/PhysRevLett.43.799`.

[166] Sandro Sorella. “Generalized Lanczos Algorithm for Variational Quantum Monte Carlo”. In: *Physical Review B* 64.2 (June 19, 2001). DOI: `10.1103/PhysRevB.64.024512`.

[167] Sandro Sorella. “Wave Function Optimization in the Variational Monte Carlo Method”. In: *Physical Review B* 71.24 (June 22, 2005). DOI: `10.1103/PhysRevB.71.241103`.

[168] A. W. Sandvik and G. Vidal. “Variational Quantum Monte Carlo Simulations with Tensor-Network States”. In: *Physical Review Letters* 99.22 (Nov. 29, 2007). DOI: `10.1103/PhysRevLett.99.220602`.

[169] Sergey Bravyi. “Lagrangian Representation for Fermionic Linear Optics”. In: *Quantum Inf. and Comp.* 5.3 (2005), pp. 216–238. arXiv: `0404180v2 [quant-ph]`.

[170] William H. Press, ed. *Numerical Recipes: The Art of Scientific Computing*. 3rd ed. Cambridge, UK ; New York: Cambridge University Press, 2007. 1235 pp.

[171] S. Elitzur. “Impossibility of Spontaneously Breaking Local Symmetries”. In: *Physical Review D* 12.12 (Dec. 15, 1975), pp. 3978–3982. DOI: `10.1103/PhysRevD.12.3978`.

[172] A. M. Polyakov. “Quark Confinement and Topology of Gauge Theories”. In: *Nucl. Phys. B* 120.3 (1977), pp. 429–458. DOI: `DOI : 10.1016/0550-3213(77)90086-4`.

[173] Ulli Wolff. “Collective Monte Carlo Updating for Spin Systems”. In: *Physical Review Letters* 62.4 (Jan. 23, 1989), pp. 361–364. DOI: `10.1103/PhysRevLett.62.361`.

[174] Robert H. Swendsen and Jian-Sheng Wang. “Nonuniversal Critical Dynamics in Monte Carlo Simulations”. In: *Physical Review Letters* 58.2 (Jan. 12, 1987), pp. 86–88. DOI: `10.1103/PhysRevLett.58.86`.

[175] Tobias J. Osborne. “Efficient Approximation of the Dynamics of One-Dimensional Quantum Spin Systems”. In: *Physical Review Letters* 97.15 (Oct. 2006), p. 157202. DOI: `10.1103/PhysRevLett.97.157202`.

[176] Norbert Schuch et al. “Entropy Scaling and Simulability by Matrix Product States”. In: *Physical Review Letters* 100.3 (Jan. 2008). DOI: `10.1103/physrevlett.100.030504`.

[177] Vincenzo Alba and Pasquale Calabrese. “Entanglement and Thermodynamics after a Quantum Quench in Integrable Systems”. In: *Proceedings of the National Academy of Sciences* 114.30 (July 25, 2017), pp. 7947–7951. DOI: `10.1073/pnas.1703516114`.

[178] C. J. Hamer, Zheng Weihong, and J. Oitmaa. “Series Expansions for the Massive Schwinger Model in Hamiltonian Lattice Theory”. In: *Physical Review D* 56.1 (July 1, 1997), pp. 55–67. DOI: `10.1103/PhysRevD.56.55`.

[179] Barak Bringoltz. “Volume Dependence of Two-Dimensional Large- N QCD with a Nonzero Density of Baryons”. In: *Physical Review D* 79.10 (May 22, 2009), p. 105021. DOI: `10.1103/PhysRevD.79.105021`.

[180] Valentin Kasper et al. “From the Jaynes–Cummings Model to Non-Abelian Gauge Theories: A Guided Tour for the Quantum Engineer”. In: *New Journal of Physics* 22.10 (Oct. 2020), p. 103027. DOI: `10.1088/1367-2630/abb961`.

[181] Bernard Deconinck et al. “Computing Riemann Theta Functions”. In: *Mathematics of Computation* 73.247 (Dec. 19, 2003), pp. 1417–1443. DOI: `10.1090/S0025-5718-03-01609-0`.

[182] Lucas Hackl et al. “Geometry of Variational Methods: Dynamics of Closed Quantum Systems”. Apr. 2, 2020. arXiv: `2004.01015 [cond-mat, physics:quant-ph]`.

[183] Aaron Williams. “Loopless Generation of Multiset Permutations Using a Constant Number of Variables by Prefix Shifts”. In: *Proceedings of the Twentieth Annual ACM-SIAM Symposium on Discrete Algorithms*. Society for Industrial and Applied Mathematics, Jan. 4, 2009, pp. 987–996. DOI: `10.1137/1.9781611973068.107`.

[184] *Generators - Python Wiki*. URL: `https://wiki.python.org/moin/Generators` (visited on 03/07/2022).

[185] *Multiprocessing — Process-based Parallelism — Python 3.10.2 Documentation*. URL: `https://docs.python.org/3/library/multiprocessing.html` (visited on 03/09/2022).

[186] *GlobalInterpreterLock - Python Wiki*. URL: `https://wiki.python.org/moin/GlobalInterpreterLock` (visited on 03/09/2022).

[187] Paul D. Coddington et al. “The Deconfining Transition for Finite-Temperature U(1) Lattice Gauge Theory in (2 + 1) Dimensions”. In: *Physics Letters B* 175.1 (July 1986), pp. 64–68. DOI: `10.1016/0370-2693(86)90332-1`.

[188] M. N. Chernodub, E.-M. Ilgenfritz, and A. Schiller. “Lattice Study of 3 D Compact QED at Finite Temperature”. In: *Physical Review D* 64.5 (Aug. 10, 2001), p. 054507. DOI: `10.1103/PhysRevD.64.054507`.

[189] Julian Bender and Erez Zohar. “Gauge Redundancy-Free Formulation of Compact QED with Dynamical Matter for Quantum and Classical Computations”. In: *Physical Review D* 102.11 (Dec. 23, 2020), p. 114517. DOI: `10.1103/PhysRevD.102.114517`.

[190] Richard P. Feynman. “Difficulties in Applying the Variational Principle to Quantum Field Theories”. In: *Variational Calculations in Quantum Field Theory*. World Scientific Publishing, Singapore, 1987, pp. 28–40. DOI: `10.1142/9789814390187_0003`.

[191] Boye Buyens et al. “Matrix Product States for Gauge Field Theories”. In: *Physical Review Letters* 113.9 (Aug. 25, 2014). DOI: `10.1103/PhysRevLett.113.091601`.

[192] Zoran Ristivojevic. “Conjectures about the Ground-State Energy of the Lieb-Liniger Model at Weak Repulsion”. In: *Physical Review B* 100.8 (Aug. 2019), p. 081110. DOI: `10.1103/PhysRevB.100.081110`.

[193] Anna Minguzzi Guillaume Lang Frank Hekking. “Ground-State Energy and Excitation Spectrum of the Lieb-Liniger Model : Accurate Analytical Results and Conjectures about the Exact Solution”. In: *SciPost Phys.* 3.1 (2017), p. 003. DOI: `10.21468/SciPostPhys.3.1.003`.

[194] Tommaso Guaita et al. “Gaussian Time-Dependent Variational Principle for the Bose-Hubbard Model”. In: *Physical Review B* 100.9 (Sept. 24, 2019), p. 094529. DOI: `10.1103/PhysRevB.100.094529`.

[195] Jiajun Chen. “Review on Quantum Communication and Quantum Computation”. In: *Journal of Physics: Conference Series* 1865.2 (Apr. 1, 2021), p. 022008. DOI: `10.1088/1742-6596/1865/2/022008`.

[196] Pasquale Calabrese and John Cardy. “Entanglement Entropy and Conformal Field Theory”. In: *Journal of Physics A: Mathematical and Theoretical* 42.50 (Dec. 2009), p. 504005. DOI: `10.1088/1751-8113/42/50/504005`.

[197] H. Casini and M. Huerta. “Entanglement Entropy in Free Quantum Field Theory”. In: *Journal of Physics A: Mathematical and Theoretical* 42.50 (Dec. 18, 2009), p. 504007. DOI: `10.1088/1751-8113/42/50/504007`.

[198] J. L. Cardy, O. A. Castro-Alvaredo, and B. Doyon. “Form Factors of Branch-Point Twist Fields in Quantum Integrable Models and Entanglement Entropy”. In: *Journal of Statistical Physics* 130.1 (Nov. 28, 2007), pp. 129–168. DOI: `10.1007/s10955-007-9422-x`.

[199] Pasquale Calabrese and John Cardy. “Entanglement Entropy and Quantum Field Theory”. In: *Journal of Statistical Mechanics: Theory and Experiment* 2004.06 (June 12, 2004), P06002. DOI: `10.1088/1742-5468/2004/06/P06002`.

[200] Benjamin Doyon. “Bipartite Entanglement Entropy in Massive Two-Dimensional Quantum Field Theory”. In: *Physical Review Letters* 102.3 (Jan. 23, 2009), p. 031602. DOI: `10.1103/PhysRevLett.102.031602`.

[201] Alessio Serafini. *Quantum Continuous Variables: A Primer of Theoretical Methods*. Boca Raton: CRC Press, Taylor & Francis Group, CRC Press is an imprint of the Taylor & Francis Group, an informa business, 2017. 349 pp.

[202] Andrew J A James et al. “Non-Perturbative Methodologies for Low-Dimensional Strongly-Correlated Systems: From Non-Abelian Bosonization to Truncated Spectrum Methods”. In: *Reports on Progress in Physics* 81.4 (Apr. 1, 2018), p. 046002. DOI: `10.1088/1361-6633/aa91ea`.

[203] T. Palmai. “Entanglement Entropy from the Truncated Conformal Space”. In: *Physics Letters B* 759 (Aug. 2016), pp. 439–445. DOI: `10.1016/j.physletb.2016.06.012`.

[204] Sara Murciano, Pasquale Calabrese, and Robert M. Konik. “Post-Quantum Quench Growth of Renyi Entropies in Perturbed Luttinger Liquids”. Dec. 8, 2021. arXiv: `2112.04412 [cond-mat, physics:quant-ph]`.

[205] G. Feverati, F. Ravanini, and G. Takács. “Scaling Functions in the Odd Charge Sector of Sine-Gordon/Massive Thirring Theory”. In: *Physics Letters B* 444.3-4 (Dec. 1998), pp. 442–450. DOI: `10.1016/S0370-2693(98)01406-3`.

[206] Z. Bajnok, L. Palla, and G. Takács. “Boundary States and Finite Size Effects in Sine-Gordon Model with Neumann Boundary Condition”. In: *Nuclear Physics B* 614.3 (Nov. 2001), pp. 405–448. DOI: `10.1016/S0550-3213(01)00391-1`.

[207] Joan Elias-Miró, Slava Rychkov, and Lorenzo G. Vitale. “NLO Renormalization in the Hamiltonian Truncation”. In: *Physical Review D* 96.6 (Sept. 27, 2017), p. 065024. DOI: `10.1103/PhysRevD.96.065024`.

[208] D. X. Horvath, K. Hodsagi, and G. Takacs. “Chirally Factorised Truncated Conformal Space Approach”. Feb. 1, 2022. arXiv: `2201.06509 [cond-mat, physics:hep-th, physics:physics]`.

[209] Olalla A. Castro-Alvaredo and David X. Horvath. “Branch Point Twist Field Form Factors in the Sine-Gordon Model I: Breather Fusion and Entanglement Dynamics”. In: *SciPost Physics* 10.6 (June 4, 2021), p. 132. DOI: `10.21468/SciPostPhys.10.6.132`.

[210] Gan Qin, Ke-lin Wang, and Tong-zhong Li. “General Multimode Squeezed States”. Sept. 4, 2001. arXiv: `quant-ph/0109020`.

[211] A.M. Trembinska. *Variations on Carlson’s Theorem*. Northwestern University, 1985.

[212] Edward C. Titchmarsh. *The Theory of Functions*. 2. ed., reprinted. Oxford Science Publications. Oxford: Oxford Univ. Press, 2002. 454 pp.

[213] F Hausdorff. “Die Symbolische Exponentialformel in Der Gruppentheorie”. In: *Ber. Verh. Kgl. Sächs. Ges. Wiss. Leipzig., Math.-phys. Kl.* 58 (1906), pp. 19–48.

[214] R. E. Wengert. “A Simple Automatic Derivative Evaluation Program”. In: *Communications of the ACM* 7.8 (Aug. 1964), pp. 463–464. DOI: `10.1145/355586.364791`.

[215] Michael Bartholomew-Biggs et al. “Automatic Differentiation of Algorithms”. In: *Journal of Computational and Applied Mathematics* 124.1-2 (Dec. 2000), pp. 171–190. DOI: `10.1016/S0377-0427(00)00422-2`.

[216] Ian Affleck and Andreas W. W. Ludwig. “Universal Noninteger “Ground-State Degeneracy” in Critical Quantum Systems”. In: *Physical Review Letters* 67.2 (July 8, 1991), pp. 161–164. DOI: `10.1103/PhysRevLett.67.161`.

[217] Vincenzo Alba and Pasquale Calabrese. “Entanglement Dynamics after Quantum Quenches in Generic Integrable Systems”. In: *SciPost Physics* 4.3 (Mar. 27, 2018), p. 017. DOI: `10.21468/SciPostPhys.4.3.017`.

[218] Giuseppe Mussardo. *Statistical Field Theory: An Introduction to Exactly Solved Models in Statistical Physics*. 2nd ed. Oxford University Press, Mar. 26, 2020. DOI: `10.1093/oso/9780198788102.001.0001`.

[219] Subir Ghoshal and Alexander Zamolodchikov. “Boundary S Matrix and Boundary State Int Two-Dimensional Integrable Quantum Field Theory”. In: *International Journal of Modern Physics A* 09.21 (Aug. 20, 1994), pp. 3841–3885. DOI: `10.1142/S0217751X94001552`.

[220] Subir Ghoshal. “Bound State Boundary S Matrix of the Sine-Gordon Model”. In: *International Journal of Modern Physics A* 09.27 (Oct. 30, 1994), pp. 4801–4810. DOI: `10.1142/S0217751X94001941`.

[221] Peter Mattsson and Patrick Dorey. “Boundary Spectrum in the Sine-Gordon Model with Dirichlet Boundary Conditions”. In: *Journal of Physics A: Mathematical and General* 33.49 (Dec. 15, 2000), pp. 9065–9093. DOI: `10.1088/0305-4470/33/49/304`.

[222] Z. Bajnok, L. Palla, and G. Takács. “Finite Size Effects in Boundary Sine-Gordon Theory”. In: *Nuclear Physics B* 622.3 (Feb. 2002), pp. 565–592. DOI: `10.1016/S0550-3213(01)00616-2`.

[223] O A Castro-Alvaredo and B Doyon. “Bi-Partite Entanglement Entropy in Integrable Models with Backscattering”. In: *Journal of Physics A: Mathematical and Theoretical* 41.27 (July 11, 2008), p. 275203. DOI: `10.1088/1751-8113/41/27/275203`.

[224] Elisa Ercolessi, Stefano Evangelisti, and Francesco Ravanini. “Exact Entanglement Entropy of the XYZ Model and Its Sine-Gordon Limit”. In: *Physics Letters A* 374.21 (Apr. 2010), pp. 2101–2105. DOI: `10.1016/j.physleta.2010.03.014`.

[225] Joseph J. Bisognano and Eyvind H. Wichmann. “On the Duality Condition for a Hermitian Scalar Field”. In: *Journal of Mathematical Physics* 16.4 (Apr. 1975), pp. 985–1007. DOI: `10.1063/1.522605`.

[226] Joseph J. Bisognano. “On the Duality Condition for Quantum Fields”. In: *Journal of Mathematical Physics* 17.3 (1976), p. 303. DOI: `10.1063/1.522898`.

[227] John Cardy and Erik Tonni. “Entanglement Hamiltonians in Two-Dimensional Conformal Field Theory”. In: *Journal of Statistical Mechanics: Theory and Experiment* 2016.12 (Dec. 23, 2016), p. 123103. DOI: `10.1088/1742-5468/2016/12/123103`.

[228] Xueda Wen, Shinsei Ryu, and Andreas W W Ludwig. “Entanglement Hamiltonian Evolution during Thermalization in Conformal Field Theory”. In: *Journal of Statistical Mechanics: Theory and Experiment* 2018.11 (Nov. 19, 2018), p. 113103. DOI: `10.1088/1742-5468/aae84e`.

[229] G. Giudici et al. “Entanglement Hamiltonians of Lattice Models via the Bisognano-Wichmann Theorem”. In: *Physical Review B* 98.13 (Oct. 1, 2018), p. 134403. DOI: `10.1103/PhysRevB.98.134403`.

[230] Ananda Roy, Frank Pollmann, and Hubert Saleur. “Entanglement Hamiltonian of the $1+1$-Dimensional Free, Compactified Boson Conformal Field Theory”. In: *Journal of Statistical Mechanics: Theory and Experiment* 2020.8 (Aug. 4, 2020), p. 083104. DOI: `10.1088/1742-5468/aba498`.

[231] I. Kukuljan, S. Sotiriadis, and G. Takacs. “Correlation Functions of the Quantum Sine-Gordon Model in and out of Equilibrium”. In: *Physical Review Letters* 121.11 (Sept. 13, 2018), p. 110402. DOI: `10.1103/PhysRevLett.121.110402`.

[232] Al. B. Zamolodchikov. “Mass Scale in the Sine–Gordon Model and Its Reductions”. In: *International Journal of Modern Physics A* 10.08 (Mar. 30, 1995), pp. 1125–1150. DOI: `10.1142/S0217751X9500053X`.